
Universitat
de les Illes Balears



Instituto de Física Interdisciplinar y Sistemas Complejos

# DOCTORAL THESIS

## 2016

# PHOTONIC SYSTEMS WITH MULTIPLE DELAY TIMES: SYNCHRONIZATION, SQUARE-WAVE SWITCHING AND STATE-DEPENDENT DELAY

Jade Martínez Llinàs


Universitat
de les Illes Balears



Instituto de Física Interdisciplinar y Sistemas Complejos

# DOCTORAL THESIS

## 2016

## Doctoral Program in Physics

# PHOTONIC SYSTEMS WITH MULTIPLE DELAY TIMES: SYNCHRONIZATION, SQUARE-WAVE SWITCHING AND STATE-DEPENDENT DELAY

**Jade Martínez Llinàs**

**Supervisor: Prof. Pere Colet Rafecas**

**Doctor by the Universitat de les Illes Balears**

Tesi doctoral presentada per Jade Martínez Llinàs per a l'obtenció del títol de Doctora, en el Programa de Doctorat de Física de la Universitat de les Illes Balears, realitzada a l'Institut de Física Interdisciplinària i Sistemes Complexos (IFISC, CSIC-Universitat de les Illes Balears) sota la direcció de Pere Colet Rafecas.

Vist i plau

Director de la tesi

Prof. Pere Colet Rafecas

Doctoranda

Jade Martínez Llinàs

Palma, 25 d'agost de 2016

*To my family and friends*

# Acknowledgements

I am indebted to Professor Pere Colet for the supervision of this thesis. Thanks, Pere, for your entire availability and implication for the development of this work, for sharing with me your enthusiasm for science and your knowledge, for being always receptive to discuss, for teaching me how to do science, for giving me freedom to explore my own ideas and for building on them. Thanks, also, for the organization of the Summer School of Complex and Small Systems, where I learnt a lot, and for encouraging me to participate in other courses and conferences.

I am also indebted to my family and friends, for their help and encouragement for the development of this work and for being there in good and bad times. Thanks to my father, my mother, and my grandmother, for the education and love that they provided me, and for giving me freedom to decide and experiment at any moment of my life. Thanks to my son Martí and my partner Facundo for providing me love, peace and fun. Thanks to my sister and my mother for taking always care of me and for helping me in whatever I need. I especially thank my sister Diana and my friend Prof. Manuel Matías for revising the writing of this thesis.

I would also like to express my gratitude to other professors and researchers who have generously shared with me their knowledge, ideas and expertise. Among them, I am especially grateful to Prof. Thomas Erneux, Prof. Ingo Fischer, Dr. Xavi Porte, Dr. Lionel Weicker, and Dr. Miguel C. Soriano, for the fruitful discussions with them and their contributions to this work.

I am extremely grateful to Prof. Claudio Mirasso for proposing me to join one of the IFISC groups with an exciting research project, for introducing me Prof. Pere Colet and Prof. Ingo Fischer, for helping me to obtain funding for this thesis and other future projects, and for allowing me to participate in the organization of many outreach activities such as the *Fira de la Ciència* and the project *Investiga a la UIB*.

I also thank Prof. Maxi San Miguel for the creation of the IFISC and for providing me financial support.

Thanks to other IFISC members who have shared some time with me. I am especially grateful to my colleagues of the S007 for their help and company, to Prof. Roberta Zambrini and other past members of the IFISC OSA students Chapter for their collaboration

in the organization of many outreach activities, to Rubén and Antònia for providing a fast solution to any computer problem, and to Inma and Marta for their help in the administrative tasks.

I also thank Prof. Axelle Amon, Prof. Mariana Haragus, Prof. Laurent Larger, Prof. Stéphane Metens and Prof. Luc Pastur for the organization of the Summer School for Nonlinear Dynamics in Peyresq, where I not only learnt a lot about nonlinear dynamical systems, but also had the opportunity to meet Prof. Thomas Erneux and Dr. Lionel Weicker and to start a fruitul collaboration with Prof. Thomas Erneux.

Finally, I acknowledge the financial support of Ministerio de Economía y Competitividad (Spain) and Fondo Europeo de Desarrollo Regional (FEDER) under the projects No. FIS2012-30634 (INTENSE@COSYP) and No. TEC2012-36335 (TRIPHOP), the European Social Fund and the Govern de les Illes Balears under the programs Grups Competitius and Formació de Personal Investigador, and the Universitat de les Illes Balears.







# Resum

Aquesta tesi doctoral se centra en l'estudi teòric i numèric de sistemes fotònics amb retroacció i múltiples línies de retard, en el límit en el que els temps de retard són molt més grans que les escales de temps intrínseques del sistema.

Es consideren dos sistemes òptics amb retroacció: i) dos oscil ladors optoelèctronics (OEOs) acoblats mútuament amb retard i ii) un làser de semiconductor amb retard que depèn de l'estat mitjançant el filtrat freqüencial des de dues cavitats amb diferents longituds i freqüències centrals.

Tot i que els dos sistemes tenen en comú la presència de múltiples línies de retard, es tracta de dos sistemes ben diferents. En el primer, intevenen en tot moment dos temps de retard. En el segon, en canvi, la llum pren una única línia de retard a cada moment; en aquest sistema, el valor del retard és seleccionat intrínsicament per l'estat del sistema d'entre dos valors diferents mitjançant el filtrat freqüencial de la llum des de dos filtres de diferents freqüències centrals col locats en dues cavitats de diferent longitud.

D'una banda, es modelitzen aquests sistemes i es desenvolupen mètodes analítics per trobar solucions aproximades. Aquests mètodes es podrien emprar per entendre la dinàmica d'altres sistemes amb retard. D'altra banda, es comparen els resultats analítics o experimentals amb simulacions numèriques.

La tesi està dividida en quatre parts. Les parts I, II i IV contenen diversos capítols, mentre que la part III està formada per un únic capítol.

La part I, **Introducció, objectius, eines i resultats anteriors** , està dividida en tres capítols:

En el **Capítol 1**, primer s'introdueixen alguns exemples de sistemes en els quals la presència de retards determina les propietats dinàmiques del sistema i en alguns casos origina un comportament complex. A continuació, s'introdueix el problema genèric d'un sistema amb retard i la seva modelització mitjançant equacions diferencials amb retard. S'expliquen dos exemples en detall, incloent la seva modelització amb equacions diferencials amb retard. Més endavant, s'introdueixen les ones quadrades que es poden obtenir amb sistemes d'OEOs i altres sistemes amb retard, i es presenten algunes aplicacions de les solucions tipus ona quadrada

obtingudes amb OEOs, com són el control del període o la codificació d'informació. Finalment es resumeixen els objectius de la tesi.

En el **Capítol 2**, es presenten alguns mètodes analítics i numèrics emprats en aquesta tesi, com són el mètode d'estabilitat lineal, l'estudi de l'estabilitat de solucions periòdiques, i algoritmes per integrar numèricament equacions diferencials amb retard.

El **Capítol 3** està dedicat a l'estudi de la dinàmica de sistemes senzills en els quals els sistemes d'estudi d'aquesta tesi estan basats: un oscil·lador optoelectrònic i un làser de semiconductor amb retroacció òptica. En cada cas, es descriu el sistema en detall, s'introdueix la seva modelització mitjançant equacions diferencials amb retard, i es presenten els diferents tipus de dinàmica i possibles aplicacions.

La part II està dedicada a la **Sincronització en oscil·ladors optoelectrònics mútuament acoblats amb retard** i conté quatre capítols:

En el **Capítol 4**, es descriu el sistema de dos OEOs mútuament acoblats i amb dos temps de retard diferents, el de la retroacció i el de l'acoblament. Primer s'obtenen les equacions dinàmiques del sistema. A continuació, s'escriuen les equacions dinàmiques de manera adimensional i es troba l'estat estacionari estàtic (punt fix) del sistema. Per acabar, s'introdueix el cas d'OEOs idèntics, se simplifiquen les equacions dinàmiques i es demostra l'existència de solucions periòdiques sincronitzades en fase i en antifase a partir de l'anàlisi d'estabilitat lineal de la solució zero.

El **Capítol 5** se centra en la generació de solucions periòdiques quadrades mitjançant el sistema de dos OEOs idèntics mútuament acoblats descrit en el capítol 4, en el cas de retroacció negativa, la qual tendeix a reduir l'efecte de les pertorbacions de l'estat estacionari estàtic. Primer s'aplica el mètode d'estabilitat lineal per trobar el període de les solucions oscil·lants en funció de la relació entre els dos temps de retard diferents. Es demostra la coexistència de múltiples solucions periòdiques de tipus ona quadrada sincronitzades en fase quan la raó entre el temps de retard intrínsec i el de l'acoblament satisfà una relació racional entre dos nombres senars. De manera similar, múltiples ones quadrades en antifase i amb diferents períodes poden coexistir quan la raó entre el temps de retard intrínsec i el de l'acoblament és un racional senar/parell. A continuació, s'apliquen mètodes assimptòtics per obtenir mapes per a l'amplada de les solucions. Es demostra que les solucions periòdiques quadrades experimenten una ruta al caos del tipus *doblament de període*. Després s'analitza l'efecte de canviar lleugerament els paràmetres en la forma de les solucions. Finalment, a partir del càlcul precís del període de les solucions, s'observa un fenomen de divisió del període en diferents valors.

El **Capítol 6** està dedicat a l'aparició de solucions quadrades estables amb el mateix model que en el Capítol 5, però en el cas de retroacció positiva, la qual tendeix a augmentar l'efecte de les pertorbacions de l'estat estacionari estàtic. Les solucions quadrades que apareixen amb retroacció positiva tenen un cicle asimètric

i són més flexibles i robustes que les que s'obtenen amb retroacció negativa; en concret, l'asimetria del seu cicle permet que puguin adaptar la seva forma com a resposta a canvis en els valors dels paràmetres. Primer s'aplica l'anàlisi d'estabilitat lineal de l'estat estacionari estàtic per obtenir el període de les ones quadrades de freqüència més gran en funció de la relació entre els dos temps de retard diferents. Es demostra que el sistema té solucions sincronitzades en fase i en antifase, i que múltiples solucions poden coexistir, de manera similar al cas de retroacció negativa. No obstant això, a diferència del cas de retroacció negativa, aquí les solucions en antifase sempre coexisteixen amb solucions en fase amb diferents períodes. A més, aquest sistema té solucions periòdiques de freqüència més baixa, sincronitzades en fase i que coexisteixen amb les ones quadrades de freqüència alta per als mateixos valors dels paràmetres. A continuació, s'aplica un mètode assimptòtic per caracteritzar l'amplitud i la forma de les ones quadrades. Es demostra que el cicle de les solucions quadrades generades amb retroacció positiva es pot controlar canviant el voltatge constant aplicat als OEOs, sense que canviï el període. També s'analitza l'efecte de canviar lleugerament els valors dels paràmetres en la forma de les solucions. Es demostra que les ones quadrades generades amb retroacció positiva són més robustes a canvis en els valors dels paràmetres. Finalment, a partir del càlcul precís del període de les solucions, s'observa un fenomen de divisió del període en diferents valors.

En el **Capítol 7**, s'estudia el cas de dos oscil ladors no-idèntics, incloent les possibilitats de retroacció negativa, positiva i mixta. Es demostra que aquest sistema pot generar múltiples solucions de tipus ona quadrada, amb diferents tipus de sincronització (en fase, en antifase i a un quart del període) depenent del signe de la retroacció de cada oscil lador. Les ones quadrades amb sincronització a un quart del període apareixen principalment quan la retroacció és negativa per a un oscil lador i positiva per a l'altre. Finalment, s'analitza la robustesa de les solucions sincronitzades a un quart del període a petits canvis en els valors dels paràmetres.

La part III se centra en el tema **Sistemes fotònics amb retards que depenen de l estat** i està formada per un capítol:

En el **Capítol 8**, es considera un sistema de làser de semiconductor amb filtrat freqüencial des de dues cavitats de longituds i freqüències centrals diferents, com a model per a estudiar la dinàmica d'un sistema amb retard que depèn de l'estat. Primer s'introdueix el disseny experimental, que està basat en un làser de semiconductor i dos filtres de Bragg amb diferents freqüències centrals col locats en dues cavitats de diferents longituds, i per tant associats a dos temps de retard diferents. Es demostra que la dinàmica d'aquest sistema es caracteritza per salts erràtics entre els dos valors del temps de retard. A continuació, s'introdueix un model teòric amb filtrat lorentzià des de dues cavitats diferents. Es calculen les solucions estacionàries i s'analitza la dinàmica erràtica amb retard que depèn de l'estat per a diferents valors dels paràmetres. Es demostra que els resultats numèrics en el règim erràtic coincideixen qualitativament amb els experiments. També es demostra que aquest sistema té solucions més regulars, similars a les ones quadrades periòdiques,

amb retard que depèn de l'estat. Finalment, s'analitza l'estadística dels temps de residència durant els quals el retard pren un valor constant.

La part IV, **Resum i perspectives de treball** , conté dos capítols de conclusions: el **Capítol 9**, corresponent a la part dels OEOs; i el **Capítol 10**, referit a la part dels retards depenents de l'estat. En aquests capítols es resumeixen els principals resultats obtinguts i es proposen algunes perspectives per a futures investigacions.

# Resumen

Esta tesis doctoral se centra en el estudio teórico y numérico de sistemas fotónicos con realimentación y múltiples líneas de retardo, en el límite en el que los tiempos de retardo son mucho más grandes que las escalas de tiempo intrínsecas del sistema.

Se consideran dos sistemas ópticos con realimentación: i) dos osciladores optoelectrónicos (OEOs) mutuamente acoplados con retardo y ii) un láser de semiconductor con retardo dependiente del estado mediante el filtrado frecuencial desde dos cavidades con diferentes longitudes y frecuencias centrales.

Aunque estos dos sistemas tienen en común la presencia de múltiples líneas de retardo, se trata de dos sistemas bastante diferentes. En el primero en todo momento intervienen dos tiempos de retardo. En el segundo, en cambio, la luz toma una única línea de retardo en cada momento; en este sistema, el valor del retardo es seleccionado intrínsicamente por el estado del sistema entre dos valores diferentes mediante el filtrado frecuencial de la luz desde dos filtros con diferentes frecuencias centrales colocados en dos cavidades de diferente longitud.

Por un lado, se modelizan estos sistemas y se desarrollan métodos analíticos para encontrar soluciones aproximadas. Estos métodos podrían utilizarse para comprender la dinámica de otros sistemas con retardo. Por otro lado, se contrastan los resultados analíticos o experimentales con simulaciones numéricas.

La tesis está dividida en cuatro partes. Las partes I, II y IV contienen varios capítulos, mientras que la parte III está formada por un solo capítulo.

La parte I, **Introducción, objectivos, herramientas y resultados anteriores** , está dividida en tres capítulos:

> En el **Capítulo 1**, primero se introducen algunos ejemplos de sistemas en los cuales la presencia de retardos determina las propiedades dinámicas del sistema, en algunos casos dando lugar a comportamiento complejo. A continuación se presenta el problema general de un sistema con retardo y su modelización con ecuaciones diferenciales con retardo. Se explican dos ejemplos en detalle, incluyendo su modelización con ecuaciones diferenciales con retardo. Luego se introduce el régimen dinámico de oscilación periódica de tipo onda cuadrada que se puede obtener con OEOs y otros sistemas con retardo, y se resaltan algunas aplicaciones de estas

ondas cuadradas, como el control del período y la codificación de información. El capítulo termina con un resumen de los objetivos de la tesis.

En el **Capítulo 2**, se introducen algunos métodos numéricos y teóricos usados en esta tesis, como el análisis de estabilidad lineal, métodos y herramientas para el estudio de la estabilidad de soluciones periódicas, y algoritmos para integrar numéricamente las ecuaciones diferenciales con retardo.

El **Capítulo 3** está dedicado al estudio de la dinámica de sistemas sencillos en los que se basan los sistemas estudiados en esta tesis: un único OEO y un láser de semiconductor con realimentación óptica. En cada caso, se describe en detalle el sistema, se introduce su modelización con ecuaciones diferenciales con retardo, y se presentan sus diferentes regímenes dinámicos y posibles aplicaciones.

La parte II está dedicada a la **Sincronización en osciladores optoelectrónicos mutuamente acoplados con retardo** y contiene cuatro capítulos:

En el **Capítulo 4**, se describe el sistema de dos OEOs mutuamente acoplados y con dos tiempos de retardo diferentes, el de la propia realimentación y el del acoplamiento. Primero se derivan las ecuaciones dinámicas del sistema. A continuación se escriben las ecuaciones dinámicas en forma adimensional y se calcula la solución estacionaria estática (punto fijo) del sistema. Finalmente se introduce el caso de OEOs idénticos, se simplifican las ecuaciones dinámicas y se demuestra que el análisis de estabilidad lineal de la solución cero da lugar a soluciones periódicas sincronizadas en fase y en antifase.

El **Capítulo 5** se centra en la generación de pulsos simétricos de onda cuadrada mediante el sistema de dos OEOs idénticos mutuamente acoplados con retardo descrito en el capítulo 4, en el caso de realimentacion negativa, la cual tiende a reducir el efecto de las perturbaciones del estado etacionario estático. Primero se aplica el método de estabilidad lineal para obtener el período de las soluciones oscilatorias en función de la relación entre los dos tiempos de retardo diferentes. Se demuestra que múltiples soluciones periódicas de tipo onda cuadrada en fase coexisten cuando la razón entre el tiempo de retardo intrínseco y el del acoplamiento satisface una relación racional entre dos números impares. De manera similar, múltiples ondas cuadradas en antifase con diferentes períodos pueden coexistir cuando la razón entre el tiempo de retardo intrínseco y el del acoplamiento es un racional impar/-par. A continuación, se aplican métodos asintóticos para obtener mapas para la amplitud de las soluciones. Se demuestra que las ondas cuadradas periódicas experimentan una ruta al caos del tipo *doblamiento de período*. Después se analiza el efecto de cambiar ligeramente los valores de los parámetros en la forma de las soluciones. Finalmente, a partir del cálculo preciso del período de las soluciones, se observa un fenómeno de división del período en diferentes valores.

El **Capítulo 6** está dedicado a la aparición de pulsos de onda cuadrada estables con el mismo modelo que en el Capítulo 5 pero en el caso de realimentación positiva, la cual tiende a aumentar el efecto de las perturbaciones del estado etacionario

estático. Las ondas cuadradas que surgen con realimentación positiva tienen un ciclo asimétrico y son más flexibles y robustas que las obtenidas con realimentación negativa; en particular, la asimetría de su ciclo les permite adaptar su forma en respuesta a cambios en los valores de los parámetros en vez de experimentar un doblamiento de período. Primero se aplica el análisis de estabilidad lineal del estado estacionario estático para obtener el período de las ondas cuadradas de mayor frecuencia en función de la relación entre los dos tiempos de retardo diferentes. Se demuestra que el sistema tiene soluciones sincronizadas en fase y en antifase, y que múltiples soluciones pueden coexistir, de manera similar al caso de realimentación negativa. Sin embargo, a diferencia del caso de realimentación negativa, aquí las soluciones en antifase siempre coexisten con soluciones en fase con diferentes períodos. Además, este sistema tiene soluciones periódicas de menor frecuencia, sincronizadas en fase y coexistiendo con las soluciones cuadradas rápidas para los mismos valores de los parámetros. A continuación se aplica un método asintótico para determinar la amplitud y forma de las ondas cuadradas. Se demuestra que el ciclo de las ondas cuadradas generadas con realimentación positiva se puede controlar cambiando el voltaje constante aplicado a los OEOs, manteniendo el período constante. También se analiza el efecto de variar ligeramente los valores de los parámetros en la forma de las soluciones. Se demuestra que las ondas cuadradas generadas con realimentación positiva son más robustas frente a cambios en los valores de los parámetros que las obtenidas con realimentación negativa. Finalmente, a partir del cálculo preciso del período de las soluciones, se demuestra que el período de las soluciones se divide en diferentes valores.

En el **Capítulo 7**, se considera el caso de OEOs no idénticos, incluyendo las posibilidades de realimentación negativa, positiva y mixta. Se demuestra que este sistema puede generar múltiples ondas cuadradas, con diferentes tipos de sincronización (en fase, en antifase y a un cuarto del período) dependiendo del signo de la realimentación de cada oscilador. Las ondas cuadradas con sincronización a un cuarto del período aparecen principalmente cuando la realimentación es negativa para un oscilador y positiva para el otro. Finalmente se analiza la robustez de las soluciones sincronizadas a un cuarto del período frente a pequeños cambios en los valores de los parámetros.

La parte III se centra en el tema **Sistemas fotónicos con retardos que dependen del estado** y está formada per un único capítulo:

En el **Capítulo 8**, se considera un sistema de láser de semiconductor con filtrado frecuencial desde dos cavidades de longitudes y frecuencias centrales diferentes, como prototípico para estudiar la dinámica de un sistema con retardo que depende del estado. Primero se introduce el diseño experimental, basado en un láser de semiconductor con realimentación filtrada desde dos filtros de Bragg con diferentes frecuencias centrales y situados en dos cavidades de diferetes longitudes, y por lo tanto asociados a diferentes tiempos de retardo. Se demuestra que la dinámica de este sistema se caracteriza por saltos erráticos entre los dos valores del tiempo de retardo. A continuación se introduce un modelo teórico con filtrado lorenciano

desde dos cavidades diferentes. Se calculan las soluciones estacionarias y se analiza la dinámica errática con retardo que depende del estado para diferentes valores de los parámetros. Se demuestra que los resultados numéricos en el régimen errático concuerdan de forma cualitativa con los resultados experimentales. También se demuestra que este sistema tiene soluciones más regulares, similares a las ondas cuadradas, con retardo dependiente del estado. Finalmente se analiza la estadística de los tiempos de residencia durante los que el retardo toma un valor constante.

La parte IV, **Resumen y perspectivas de trabajo** , contiene dos capítulos de conclusiones: el **Capítulo 9**, correspondiente a la parte de los OEOs; y el **Capítulo 10**, referido a la parte de sistemas fotónicos con retardos dependientes del estado. En estos capítulos, se resumen los principales resultados obtenidos y se proponen algunas perspectivas de trabajo para futuras investigaciones.

# Summary

This PhD thesis focuses on the theoretical and numerical study of photonic systems with feedback from multiple delay lines, in the limit in which the delay times are much longer than the intrinsic time scales of the system.

Two optical systems with feedback are considered: i) two mutually delay-coupled optoelectronic oscillators (OEOs) and ii) a semiconductor laser with a delay time that depends on the state of the system via the filtered feedback from two cavities with different length and central frequency.

Although these two systems have in common the presence of multiple delay lines, they are indeed quite different. In the former, two different delay times take part at any time. In the latter, in contrast, light takes a single delay line at any time; in this system, the delay time value is intrinsically selected among two different values by the state of the system since the frequency of light is selectively filtered by using two filters of different central frequencies placed in two cavities of different lengths.

On the one hand, these systems are modelled and analytical methods are developed to find approximate solutions. These methods could be used to understand the dynamics of other systems with delay. On the other hand, extensive numerical simulations are compared to analytical or experimental results.

The thesis is divided into four parts. Parts I, II and IV contain several chapters, whereas part III has a single chapter.

Part I, **Introduction, objectives, tools and previous results** , is divided in three chapters:

In **Chapter 1**, some examples of systems in which the presence of delays determines the dynamical properties of the system, often giving rise to complex behavior, are first introduced. After that, the generic problem of a system with delay and its modelling with delay differential equations is presented. Two examples are explained in detail, including their modelling with delay differential equations. Then, the square-wave periodic regime that can be obtained with OEOs and other systems with delay is introduced, and some applications of the square-wave regime are highlighted, such as the control of the period and information encoding. The chapter ends with a summary of the objectives of the thesis.

**Chapter 2** introduces some analytical and numerical methods and tools used in this thesis, such as the linear stability analysis, methods and tools for the study of the stability of periodic solutions, and algorithms to integrate numerically delay differential equations.

**Chapter 3** is devoted to the study of the dynamics of simple systems in which the systems studied in this thesis are based: a single OEO and a semiconductor laser with optical feedback. In each case, the system is described in detail, its modelling with delay-defferential equations is introduced, and its different dynamical regimes and possible applications are presented.

Part II is devoted to the **Synchronization in mutually delay-coupled optoelectronic oscillators** and contains four chapters:

**Chapter 4** describes the system of two mutually delay-coupled OEOs with two different delay times, the self-feedback delay time and the coupling delay time. First, the dynamical equations of the system are derived. After that, the equations are writen in non-dimensional form and the steady state (fixed point) of the system is found. Finally, the case of identical OEOs is introduced, the dynamical equations are simplified and it is shown that the linear stability analysis of the zero solution gives rise to periodic solutions synchronized in phase and out of phase.

**Chapter 5** focuses on the generation of symmetric square-wave pulses by the system of two identical mutually delay-coupled OEOs described in Chapter 4, in the case of negative feedback, which tends to reduce the effect of the perturbations of the steady state solution. First, linear stability analysis is applied to obtain the period of the solutions as a function of the ratio between the two different delay times. It is shown that multiple in-phase square waves with different periods can coexist when the ratio between the self-feedback and the cross-feedback delay times satisfies a rational relationship involving two odd numbers. Similarly, multiple out-of-phase square waves with different periodicity can coexist when the ratio between the self- and the cross-delay times is an odd/even rational. After that, asymptotic methods are applied to obtain maps for the amplitude of the solutions. It is found that the symmetric square-wave periodic solutions undergo a period doubling route to chaos. Then, the effect of the parameter mismatch in the form of the solutions is analyzed. Finally, a splitting of the period in different values is demonstrated by performing a precise calculation of the period of the solutions.

**Chapter 6** is devoted to the emergence of stable square-wave pulses with the system described in Chapter 4 in the case of positive feedback, which tends to amplify the effect of the perturbations of the steady state solution. The square waves arising with positive feedback have an asymmetric duty cycle and turn out to be more flexible and robust than those obtained with negative feedback; in particular, the asymmetry of their duty cycle allows them to adapt their shape in response to changes in the parameter values instead of undergoing a period doubling. First, the linear stability analysis of the steady state is applied to obtain the period of the oscillatory solutions as a function of the two different delay times.

It is shown that the system has stable in- and out-of-phase synchronized solutions, and that several solutions can coexist, similarly to the case of negative feedback. Nevertheless, in contrast to the negative feedback case, here out-of-phase solutions always coexist with in-phase solutions with different periods. Furthermore, this system has limit cycles of lower frequency, synchronized in phase and coexisting with the aforementioned fast square waves for the same values of the parameters. After that, an asymptotic method is applied to determine the amplitude and the shape of the square waves. It is shown that the duty cycle of the square waves generated with positive feedback can be tuned with the constant voltage applied to the OEOs, while the total period remains constant. The effect of the parameter mismatch on the form of the solutions is also analyzed. It is found that the square waves generated with positive feedback are more robust to parameter mismatch than those obtained with negative feedback. Finally, a splitting of the period in different values is demonstrated by performing a precise calculation of the period of the solutions.

**Chapter 7** addresses the case of two non-identical OEOs, including the possibilities of negative, positive, and mixed feedback. It is shown that this system can generate multiple square-wave solutions, with different kinds of synchronization (in-phase, out-of-phase, or at a quarter of the period) depending on the sign of the feedback on each oscillator. The square waves with synchronization at a quarter of the period mainly appear when the feedback is negative for one oscillator and positive for the other one. Finally, the robustness of the solutions synchronized at a quarter of the period to parameter mismatch is analyzed.

Part III focuses on the topic **Photonic systems with state-dependent delays** and contains a single chapter:

In **Chapter 8**, a semiconductor laser system with frequency filtering from two cavities of different lengths and central frequencies is considered as prototypical to study the dynamics of a system with state-dependent delay. First, the experimental setup is presented. It is based on a semiconductor laser with filtered feedback from two Bragg filters of different central frequencies placed in two cavities of different lengths, and thus associated to different delay times, experiencing erratic jumps between the two delay-time values. Then, a theoretical model with lorentzian filtering from different cavities is introduced. The stationary solutions are calculated and the erratic dynamics with state-dependent delay is analyzed for different parameter values. It is shown that numerical results in the erratic regime are in qualitative agreement with the experiments. It is also shown that this system has more regular solutions, similar to the square waves, with state-dependent delay. Finally, the switching statistics is analyzed from the residence times during which the delay time remains constant.

Part IV, **Summary and future work** , contains two concluding chapters: **Chapter 9**, corresponding to the part of OEOs; and **Chapter 10**, associated to the part of photonic systems with state-dependent delays. In these chapters, the main results are summarized and some perspectives of future work are proposed.

# Publications

The work carried out during the PhD has lead to the following publications:

## Journal articles

[1] J. Martínez-Llinàs and P. Colet, In-phase, out-of-phase and T/4 synchronization of square waves in delay-coupled non-identical optoelectronic oscillators, *Opt. Express*, vol. 23, no. 19, pp. 24785 24799, 2015.

[2] J. Martínez-Llinàs, X. Porte, M.C. Soriano, P. Colet and I. Fischer, Dynamical properties induced by state-dependent delays in photonic systems, *Nature Communications* 6:7425 p. 7425(9), 2015.

[3] J. Martínez-Llinàs, P. Colet, and T. Erneux, Synchronization of tunable asymmetric square-wave pulses in delay-coupled optoelectronic oscillators, *Phys. Rev. E*, vol. 91, no. 3, p. 032911, 2015.

[4] J. Martínez-Llinàs, P. Colet, and T. Erneux, Tuning the period of square-wave oscillations for delay-coupled optoelectronic systems, *Phys. Rev. E*, vol. 89, p. 42908, 2014.

## Conference papers

[1] J. Martínez-Llinàs, X. Porte, M.C. Soriano, P. Colet and I. Fischer, State-dependent delay dynamics in photonic systems, FISES 2015, XX Congreso de Física Estadística, 2015.

[2] X. Porte, J. Martínez-Llinàs, M.C. Soriano, P. Colet and I. Fischer, External-cavity semiconductor laser with state-dependent delay, *European Quantum Electronics Con-*

*ference*, European Physical Society, 2015. http://www.cleoeurope.org/documents/CLEO 2015 advance programme web.pdf

[3] J. Martínez-Llinàs, P. Colet, and T. Erneux, Tuning Synchronized Square-wave Pulses With Optoelectronic Oscillators, *European Quantum Electronics Conference*, European Physical Society, 2015. http://www.cleoeurope.org/documents/CLEO2015 advance programme web.pdf

[4] J. Martínez-Llinàs, P. Colet, and T. Erneux, Tuning the period of square-wave oscillations in delay-coupled optoelectronic oscillators, FISES 2014, XIX Congreso de Física Estadística, 2014.

[5] J. Martínez-Llinàs, P. Colet, and T. Erneux, Tuning the period of square-wave oscillations in two delay coupled systems with delay feedback, XXXIII Dynamics Days Europe, 2013.

[6] J. Martínez-Llinàs and P. Colet, Synchronization in delayed mutually coupled optoelectronic oscillators, FISES 2012, XIX Congreso de Física Estadística, 2012.

[7] J. Martínez-Llinàs and P. Colet, Synchronization in delayed mutually coupled optoelectronic oscillators, FISES 2011, XVIII Congreso de Física Estadística, 2011.

# Contents

# List of Figures

# List of Tables

# Abbreviations

EEL: edge-emitting laser

VCSEL: vertical-cavity surface-emitting laser

PROF: polarization-rotated optical feedback

TM: transversal magnetic

TE: transversal electric

DDE: delay differential equation

ODE: ordinary differential equation

MZI: Mach-Zhender interferometer

OEO: optoelectronic oscillator

SHG: second-harmonic generation

AC: alternating current

DC: direct current

RF: radio-frequency

SL: semiconductor laser

LD: laser diode

LFF: low-frequency fluctuations

ASE: amplified spontaneous emission

SASE: self-amplified spontaneous emission

ECM: external cavity mode

FCM: filtered cavity mode

FBG: fiber Bragg grating

SDD: state-dependent delay

# Part I

# Introduction, objectives, tools and previous results

Chapter 1

# Introduction

1.1

## Dynamical systems with delay

*"The law of force connecting the motion of one charge with another would just involve a delay. Shake this one, that one shakes later. The sun atom shakes; my eye electron shakes eight minutes later, because of a direct interaction across."*

Richard P. Feynman. Nobel Lecture, December 11, 1965.

Dynamical systems with delay are ubiquitous in nature, and they have been a topic of intense research in science and technology during the last decades. Any system in which the future depends not only on the present but also on the past will indeed involve a delay time. Time delays naturally appear in systems in which signals are propagated classically through space at finite speed. For instance, in coupled systems with delay, information is transferred between two different points, whereas in self-feedback systems the signal travels through a delay loop and is reinjected into the original point after a finite time. Systems with intrinsic self-feedback can in turn be coupled with delay, as in the graphical example shown in Fig. 1.1.

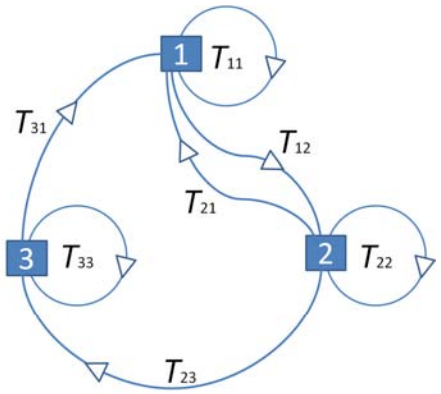


**Figure 1.1:** Delay-coupled units with feedback delay times $T_{ii}$ and coupling delay times $T_{ij,j\neq i}$.

When the delay times are similar or larger than the intrinsic time scales of the system, they can have a dramatic impact on the dynamics [11]. We next introduce some dynamical systems in which the delays cannot be neglected.

### 1.1.1 The shower temperature control

A familiar situation in which the delay plays a crucial role is the shower temperature control. Because the water takes a finite time $\tau$ to travel from the faucet to the shower head, any adjustment will take a time $\tau$ to be perceived. Reacting too fast to a non-desired temperature can give rise to large delay-induced oscillations, causing unpleasant low and high temperatures. This example is analyzed in more detail in the subsection 1.3.1.

### 1.1.2 Delays in economics

Delay-induced cyclic behaviours also take place in economic systems. The first detailed economic model predicting delay-induced oscillations was formulated by M. Kalecki. In his business cycle model (1935) [12], Kalecki defined the gestation period of any investment as the time between the investment decision and the delivery of goods, in such a way that an increase of capital at time $t$ depends upon an investment order at time $t -$ .

### 1.1.3 Delays in transportation systems

Another example in which the delays play an important role is the transportation system. Delays in transportation systems have important economic and environmental consequences. Besides the excess of fuel consumption causing an increase of air pollution and contributing to climatic change, delay propagation in transportation systems has a huge economic impact.

For air transportation systems in particular, such impact is expected to grow in the next decade due to the increasing number of flights. In these systems, characterized by a network connecting different airports, delays arise due to meteorological, technical or operational conditions affecting some flights; if the condition responsible of the primary delays continues, delays can be propagated through the network and eventually affect a large part of the system.

In road transportation, drivers following each other in a traffic stream represent a system in which delay-induced oscillations in the spaces between the vehicles can arise due to the finite human reaction time to respond to an obstacle, giving rise to the formation of jams when the number of vehicles on a road reaches a critical level.

Regarding the modelling of transportation systems, since the first traffic flow theory for road traffic on a highway developed in the 1930s, several approaches such as car-following models [13, 14], traffic wave theory [13, 15] and queueing theory [16] have been introduced. More recently, data-driven models, which are based on real data, have been

proven to succeed in understanding the delay-spreading dynamics in air transportation networks (see for instance [17] and references therein).

### 1.1.4 Delays in ecology

Delays also exist in population dynamics. On the one hand, organisms' birth and death rates do not change instantaneously with variations in population size, as would predict the well-known logistic equation, but do exhibit delays due to nutrient storage by the organism, the cell cycle or environmental conditions. Hutchiston was one of the first scientists to introduce delays in the logistic equation to account for hatching and maduration periods [18]. On the other hand, in predator-pray systems, species' growth can be modelled with several delays, including the hunting delay and maduration delays [19].

### 1.1.5 Delays in optics

In optics, an example of a system with delay-induced dynamics is a semiconductor laser subject to optical feedback from a distant mirror. In this system, the delay $\tau$ is given by the time the light needs to come back to the laser after reflection from the mirror, in such a way that the laser output at time $t$ depends on the reflected light that was emitted at time $t-\tau$. The fastest intrinsic time scale of a semiconductor laser is of the order of tens of picoseconds [20] or even lower [11]. Another important intrinsic time scale in semiconductor lasers is the so called relaxation oscillation frequency, a resonance resulting from the interplay between photon and carrier number, which is damped for the solitary laser but can be easily excited with delayed feedback [21].

In the study of the dynamics of semiconductor lasers subject to delayed optical feedback, two different regimes have been considered depending on the ratio $_{\mathrm{EC}}/\ _{\mathrm{RO}}$ between the roundtrip frequency of the light, $_{\mathrm{EC}} = \tau\ ^{1} = c/(2L)$, and the relaxation oscillation frequency, $_{\mathrm{RO}}$: the long-cavity regime and the short-cavity regime.

In the long-cavity regime or large-delay limit, the external cavity length $L$ is chosen in such a way that the roundtrip frequency of the light is of the order of several MHz, much larger than the relaxation oscillation frequency, which is in the range of GHz. An example of a large-delay-induced dynamical regime in semiconductor lasers subject to optical feedback is low-frequency fluctuations (LFFs). As shown in Fig. 1.2, the LFF dynamics consists of irregular intensity dropouts on a slow time scale on the top of fast irregular fluctuations at an average frequency given by the relaxation oscillation frequency [1]. The LFF regime is explained in more detail in the subsection 3.3.4.

Another example of semiconductor laser dynamics arising from a large delayed feedback is square-wave switching, namely periodic output with two different constant plateaus connected by fast transition layers. This periodic regime is introduced in Sec. 1.4. Semiconductor lasers in the long-cavity regime are used in optical communication systems and data storage technologies. However, in many applications such as fiber couplers or compact discs, the external cavity is only several cm long. In this short-cavity regime, the ratio $_{\mathrm{EC}}/\ _{\mathrm{RO}}$ is reversed; nevertheless, the delay time is still much longer than the fastest intrinsic time scale and thus the delay also plays an important role in the

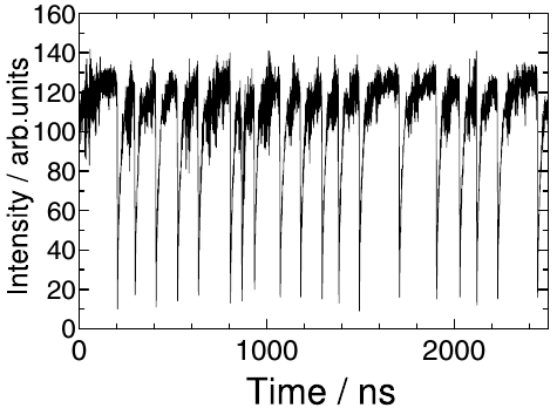


**Figure 1.2:** Output intensity of a semiconductor laser in the long-cavity regime with a delay time of 4 ns corresponding to $_{EC}$ 0.25 GHz. From [1].

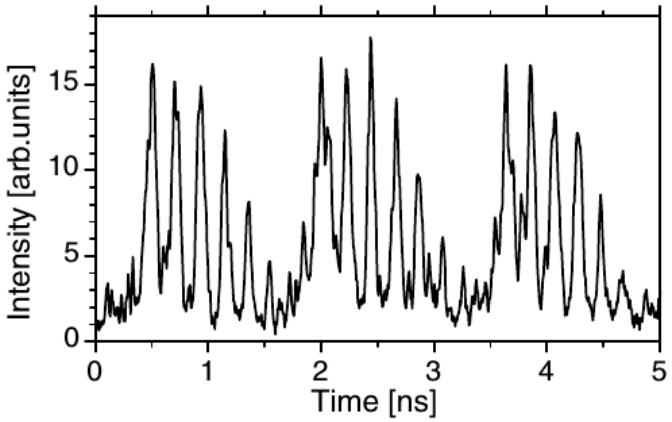


**Figure 1.3:** Output intensity of a semiconductor laser in the short-cavity regime with an external cavity of 3.2 cm long corresponding to $_{EC}$ 4.7 GHz. From [2].

dynamics, as it can be seen in Fig. 1.3, where regular pulse packages are observed in the laser output intensity [2].

### 1.1.6 Delays in neuroscience

One of the most fascinating systems in which time delays cannot be neglected is the human nervous system, a network of tens of billions of neurons connected by synapses. The brain is a multiscale complex network both in the spatial and temporal structure [22]. In the temporal structure alone, the human brain works in the range from milliseconds to several years. In particular, memory has time scales ranging from seconds (working memory) to years and decades (long-term memory). The representation of time in the brain is fundamental for organizing the information of experience into coherent memories [23]. The fact that time delays are related to the memory in the human brain [23] has inspired a new kind of computation called reservoir computing, in which the transient

dynamics of a system with delay provides memory useful to train the system in such a way that once trained it can successfully differentiate between different inputs [24].

### 1.1.7 State-dependent delays

A topic in dynamical systems with delay which is now attracting much attention is state-dependent delays (SDDs), in which the delay time depends on the dynamical variables of the system. Although variable delays represent an old topic, which was studied for the first time by Poisson in 1806 [25, 26], intense studies in SDD systems did not start until the 1980ies. SDDs appear in many physical systems. For example, SDDs are involved in systems using echo for position control; in these systems the delay depends on the position when the signal is emitted and on the position when the echo is received [27]. Other examples in which the delay depends on the state are found in the Wheeler-Feynman equations for the motion of charged point masses interacting through their electromagnetic fields [28, 29, 30, 31], and in the vibrations of a tool cutting into a rotating workpiece [32].

### 1.1.8 Outline of Part I of the thesis

The outline of Part I of this thesis is the following. In the next sections we first focus on the modelling of dynamical systems with delay using delay differential equations and introduce two simple examples: the shower temperature control and the Ikeda equation. After that, we introduce an interesting dynamical regime that can be obtained with photonic systems with delay, square-wave switching, and briefly review some applications and schemes for generation of square-wave pulsating dynamics. In Chapter 2, we describe the tools used in this work, including stability analysis and numerical integration methods. In Chapter 3, we introduce and review some previous results obtained with two photonic systems in which the systems studied in this thesis are based: optoelectronic oscillators (OEOs) with nonlinear delayed feedback and semiconductor lasers subject to delayed optical feedback.

## 1.2 Delay di erential equations

Dynamical systems with delay can be modelled with delay differential equations (DDEs). DDEs were introduced in the 1940ies in the former Soviet Union, motivated by problems of automatic control, such as stabilizing the position of a ship [33]. A large compilation of DDEs arising in applications in mechanical engineering, physics, chemistry, economics, and biology can be found in the book *Applied Delay Di erential Equations* by Erneux [11]. The first mathematical works on DDE are due to Myshkis [34], Bellman and Danskin [35], Bellman and Cooke [36], and Krasovskii [37]. These works set the basis for a basic theory for DDEs from a dynamical systems point of view [38], presented by Hale in 1977.

In this section, we present some properties of DDEs that make these equations different from ODEs. To facilitate the understanding of these differences, we compare the following first-order linear ODE and DDE for a real variable $x$,

$$ODE: \qquad \dot{x}(t) = -\alpha x(t), \tag{1.1}$$

$$DDE: \qquad \dot{x}(t) = -\alpha x(t-\tau), \tag{1.2}$$

where overdot stands for differentiation with respect to time $t$ and $\alpha$ .

Eq. (1.1) with the initial condition $x(0) = 1$ admits the exponential solution $x(t) = \exp(-\alpha t)$, which predicts the evolution of $x$ without involving any time before the initial time $t = 0$. In contrast with ODEs, in DDEs the future depends not only on the present but also on the history.

### 1.2.1 Positive and negative feedback

Eq. (1.2) can be interpreted as a system with feedback with a time lag $\tau$. With $\alpha > 0$, the sign of the feedback is opposite to the sign of the perturbations to the zero solution and thus the feedback is negative in the sense that it tends to reduce small disturbances. For $\alpha < 0$, the feedback is positive because it has the same sign than the perturbations. Positive feedback amplifies the effect of perturbations, as opposed to negative feedback which tends to reduce them.

An example of positive feedback mechanism is the regulation of oxytocine in a baby birth: oxytocine release induces contractions, which in turn induce more oxytocine release, and this cycle continues until the baby is born. Examples of negative feedback mechanisms encountered in nature are the carbon cycle, the photosynthesis in plants, and equilibrium processes in human body such as homeostasis and the metabolic slowdown when reducing food intake.

Eq. (1.2) is linear and, for positive feedback, it has no physical solutions but it diverges for any initial condition. In nonlinear systems, the higher-order terms can compensate the growth of the perturbations generated by positive feedback and therefore, in general, one can have physical solutions both for positive and negative feedback.

### 1.2.2 Initial history

One of the differences between DDEs and ODEs is the initial history required to predict the future. In contrast to an ODE, for which the temporal evolution depends uniquely on the value of the variable at a given time, to obtain a solution of a DDE the initial condition must be defined on a continuous interval of time equal to the length of the delay, that is on the interval $[-\tau, 0]$. This represents the most obvious difference between ODEs and DDEs, and has several implications.

First, the continuity of the interval makes DDEs an infinite-dimensional problem because an infinite-dimensional set of initial conditions must be provided. Such infinite-dimensional equations are associated to more complicated analysis than ODEs. For instance, as discussed in Chapter 2, the characteristic equation which determines the

stability of a steady state becomes transcendental and often does not have an analytical solution. In numerical simulations, however, due to the discretization of time with a small step size $h$, the dimension of the discretized equations is finite and it is given by $\tau/h$.

Second, DDE can have discontinuities that propagate through time due to the initial history. Although discontinuities can also arise in ODEs in certain circumstances [39, 40], one or more discontinuities are almost always present in DDEs and the propagation of discontinuities in time is a feature of DDEs which does not take place in ODEs [40]. For example, for Eq. (1.2) with $\alpha = 1$ and initial condition $x = 1$ for $t \quad [-\tau, 0]$, we have a discontinuity of the first derivative at time $t = 0$,

$$x'(0 \ \ ) = 0 \neq x'(0^+) = -1. \tag{1.3}$$

The discontinuity of the first derivative at time $t = 0$ is a general property of DDEs. Furthermore, DDEs can also have discontinuities at times prior to $t = 0$ [41]. Due to the delay, the discontinuity in $x'(t)$ at $t = 0$ is propagated to the other derivatives $d^{n+1}x(t)/dt$ at times $t = n\tau$. This can be seen derivating $n$ times Eq. (1.2) and making the change of variables $t - n\tau \quad t$, which leads to the following equation:

$$\frac{d^{n+1}x(t + n\tau)}{dt} = (-\alpha)^n x'(t). \tag{1.4}$$

The propagation of discontinuities has to be taken into account to ensure convergence in numerical integration algorithms. However, the discontinuities smoothen as they propagate to higher-order derivatives, in such a way that for high enough order of the derivatives do not interfere with the numerical algorithm and thus can be neglected [41].

Besides the propagation of discontinuities, information is propagated in time in any system governed by DDEs. For this reason, delay systems are good candidates for applications requiring memory such as reservoir computing [24].

### 1.2.3 Periodic solutions

Another property of DDEs, which has no counterpart in scalar autonomous ODEs, for which the solutions are all monotonic, is the existence of oscillatory solutions for particular values of the parameters. For example, Eq. (1.2) admits multiple periodic solutions

$$x_k(t) = A\cos(\omega_k t), \tag{1.5}$$

at particular values of $\alpha$,

$$\alpha = \alpha_k. \tag{1.6}$$

This can be verified inserting (1.5) and (1.6) into (1.2),

$$\begin{aligned} -A\omega_k \sin(\omega_k t) &= -\alpha_k A\cos(\omega_k t - \omega_k \tau) \\ &= -\alpha_k A[\cos(\omega_k t)\cos(\omega_k \tau) + \sin(\omega_k t)\sin(\omega_k \tau)], \end{aligned} \tag{1.7}$$

and equating to zero the coefficients multiplying $\sin(\omega_k t)$ and $\cos(\omega_k t)$,

$$\alpha_k \sin(\omega_k \tau) = \omega_k, \tag{1.8}$$
$$\cos(\omega_k \tau) = 0. \tag{1.9}$$

The second condition is satisfied for $\omega_k \tau = \quad \frac{\pi}{2} \quad k\pi$ with $k = 0, 1, 2, ....$ However, not all the frequencies are compatible with the first condition. We now consider $\alpha_k > 0$ since $\alpha_k < 0$ gives rise to non physical solutions as discussed before. From (1.8), we obtain $\sin(\omega_k \tau) > 0$ for $\omega_k > 0$ and $\sin(\omega_k \tau) < 0$ for $\omega_k < 0$; thus

$$\omega_k \tau = \quad \frac{\pi}{2} \quad 2k\pi = \quad \frac{4k+1}{2}\pi. \tag{1.10}$$

Introducing Eq. (1.10) into Eq. (1.8), we obtain

$$\alpha_k \tau = \ \omega_k \ \tau = \frac{4k+1}{2}\pi. \tag{1.11}$$

A general characteristic of DDEs is the coexistence of multiple stable periodic solutions with the same amplitude and different periods for particular values of the parameters. The fundamental solution of Eq. (1.5), corresponding to $k = 0$, has period $T_0 = 4\tau$, while harmonics of shorter periods $T_k = \frac{T_0}{4k+1}$ are found with $k = 1, 2, 3, ....$

## 1.3 Examples

In this section, we introduce two illustrative examples of dynamical systems in which time delays induce oscillatory behaviour: i) the control of the shower temperature, and ii) the Ikeda equation.

### 1.3.1 Shower temperature dynamics

The adjustment of the desired shower temperature represents an everyday DDE problem with delay-induced oscillations, in which the delay arises because the water takes a time $\tau$ to go from the faucet to the shower head. Assuming that water is an incompressible fluid and a stationary flow, according to Poiseuille law for a cylindrical pipe, the flow rate of water is [42]

$$F = \frac{\pi R^4 \Delta p}{8 \ l}, \tag{1.12}$$

where is the dynamic viscosity of water, $R$ the radius of the pipe, $l$ the length of the pipe, and $\Delta p$ the pressure difference between the two ends of the pipe. Then, the delay time can be derived from the definition of flow rate, liquid volume per time [42],

$$\tau = \frac{\pi R^2 l}{F} = \frac{8}{\Delta p} \quad \frac{l}{R} \quad ^2. \tag{1.13}$$

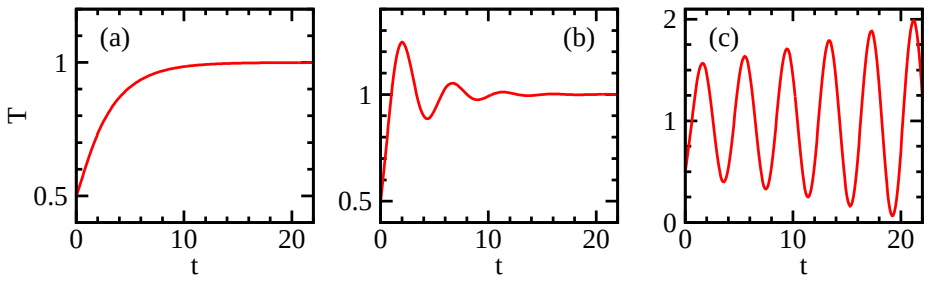


**Figure 1.4:** Solution of Eq. (1.14) for an initial temperature $T_0 = 0.5$, a desired temperature $T_d = 1$, a delay $\tau = 1$ and different values of : (a) = 0.25, below the onset of oscillations $\tau = 1/e$ 0.36, being $e$ the Euler constant; (a) = 1, in the region of damped oscillations $1/e$ 0.36 $< \tau < \pi/2$ 1.57; and (c) = 1.65, in the region of growing oscillations $\tau >$ $\pi/2$ 1.57.

We adjust the faucet temperature based on the temperature of the water at the time of the measurement. Neglecting the time it takes the water to fall from the shower head into the individual, the water used for the measurement is the one that was at the faucet $\tau$ seconds before. Considering $T(t)$ the temperature at the faucet at time $t$, and $T_d$ the desired temperature, the evolution of the temperature can be described by

$$T = - \ [T(t-\tau) - T_d], \tag{1.14}$$

where overdot stands for differentiation with respect to time and represents the human reaction rate to a non-desired temperature. If is very small, the temperature is adjusted slowly, whereas if is too large, oscillations can give rise to unpleasant low and high temperatures [11]. It can be shown that increasing the onset of damped oscillations is $\tau = 1/e$ 0.36, and that for $\tau > \pi/2$ 1.57 the amplitude of the oscillations grows exponentially with time. As an example, the numerical solution of (1.14) is shown in Fig. 1.4 for an initial value of temperature $T_0 = 0.5$, a desired temperature $T_d = 1$, a delay $\tau = 1$ and different values of .

In this example, we have considered that the dynamic viscosity of water is constant. However, this is an approximation and in fact the viscosity of water depends on the temperature. The variation of viscosity of water upon temperature can be described with empirical and semiempirical equations obtained from correlation analysis of experimental data [43, 44, 3]. An example of viscosity model is the Vogel Fulcher Tammann-Hesse equation [43],

$$= \ _0 e^{A + \frac{B}{T - T_0}}, \tag{1.15}$$

where A, B and and $T_0$ are parameters that can be obtained by fitting Eq. (1.15) to experimentally measured viscosity data, and $_0$ accounts for the units of viscosity. The viscosity of water decreases with increasing temperature, as it can be seen in Fig. 1.5, where red dots correspond to experimental data obtained from [3, 4] and the blue line has been obtained by fitting of experimental data to Eq. (1.15) with $A = -3.7188$, $B = 578.919\,\mathrm{K}$, $T_0 = 137.546\,\mathrm{K}$ and $_0 = 1\,\mathrm{mPa\,s}$ [5].

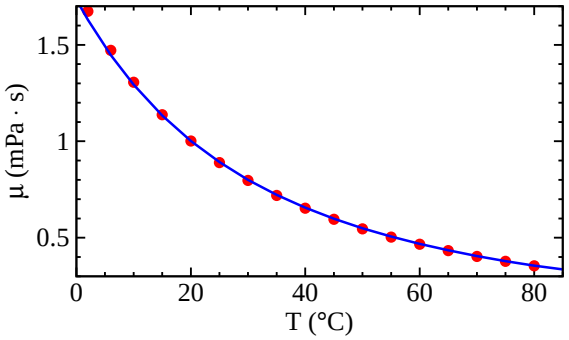


**Figure 1.5:** Viscosity of water at 0.1 MPa as a function of temperature. Red dots correspond to experimental data obtained from [3, 4], whereas the blue line is the fitting of the data to the Vogel Fulcher Tammann-Hesse equation with $A = -3.7188$, $B = 578.919\,\mathrm{K}$, $T_0 = 137.546\,\mathrm{K}$ and $_0 = 1\,\mathrm{mPa\ s}$ [5].

Considering the dependence of the viscosity on the temperature gives rise to a SDD equation,

$$T' = - \ [T(t - \tau(T)) - T_d]. \tag{1.16}$$

We will consider SDD systems in Part III of this thesis (Chapter 8).

### 1.3.2 Ikeda-type delay dynamics

The Ikeda equation is introduced here as an illustrative example which will be useful to understand the OEOs system considered in Part II of this thesis. In 1979, Kensuke Ikeda studied the propagation of light across a nonlinear absorbing medium containing two-level atoms placed in a ring cavity and subject to a constant input of light, and derived a set of DDEs from the Maxwell-Bloch equations [45]. One year later, starting from the Maxwell-Debie equations, he simplified the problem and introduced more assumptions, giving rise to the following scalar DDE,

$$\tau\phi(t) = -\phi(t) + A^2 \ \ 1 + 2B\cos[\phi(t - t_D) - \phi_0)] \ \ , \tag{1.17}$$

where $\phi$ represents the phase shift of the electric field in the medium due to absorption of light by the molecules, $\phi_0$ is the linear phase shift across the medium, $\tau$ is the Debie relaxation time, $t_D$ is the delay time originated from the propagation of light, $A$ is proportional to the amplitude of the incident field, and $B$ characterizes the dissipation of the electric field in the cavity. With this equation, which is well-known as the Ikeda DDE, Ikeda and coworkers demonstrated for the first time chaotic behavior in an optical system [46].

The Ikeda equation was soon generalized to other systems with time-delayed feedback [47]. A whole family of Ikeda-like systems can be described with a DDE of the form

$$\tau x(t) = -x(t) + f(\lambda_i, x(t - t_D)), \tag{1.18}$$

where $\lambda_i$ are control parameters, $t_D$ is the delay time and $\tau$ is the linear decay time of $x$.

### Bifurcations and harmonics

In 1987, Ikeda and coworkers analyzed Eq. (1.17) with delayed nonlinear feedback given by

$$f = \quad \sin[x(t - t_D) - x_0], \tag{1.19}$$

with $\quad > 0$ and $x_0 > 0$. Increasing $\quad$, the stationary solution becomes unstable leading to multiple periodic solutions. For sufficiently large $t_D$, the fundamental solution has the shape of a square wave with period $T = 2t_D + R$, being $R$ small, and multiple harmonics of frequencies odd multiples of the fundamental frequency coexist for the same values of the parameters. Increasing $\quad$, a usual period doubling route to chaos takes place on the fundamental branch. Higher harmonics, however, bifurcate into multiple solutions giving rise to multiple routes to chaos, as illustrated in Fig. 1.6.

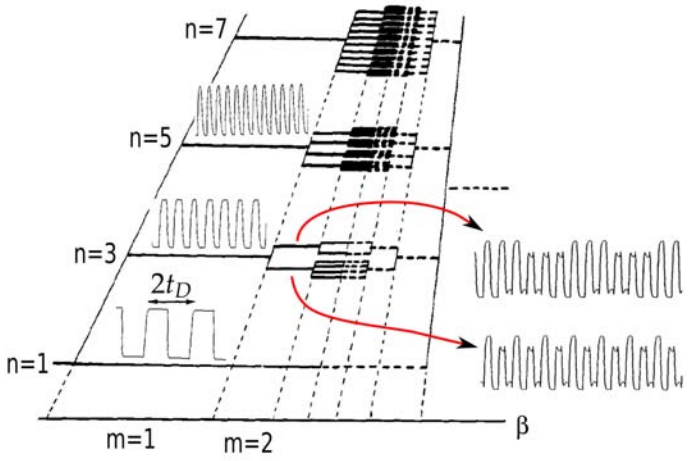


**Figure 1.6:** Hierarchical structure of bifurcated isomers increasing $\quad$. The arrow indicates the interval $2t_D$. Solid and broken lines represent periodic and chaotic solutions, respectively. Modified from [6].

Ikeda and coworkers called the multiple solutions with different forms isomers, and soon realized that, by storing complex information as temporal patterns using different isomers, such multiple periodic regimes could be used for encoding of information in high-capacity memory devices [6]. They showed that there are $2^{n(m\ \ 1)}$ different isomers, where $n$ is the order of the harmonic of larger order and $m$ the order of the bifurcation. Therefore, the capacity of this device is $n(m-1)$ bits. Because the capacity increases with $m$ and $n$, the closer to the edge of chaos or the order of the harmonic the larger the capacity of the system. Furthermore, besides the period doubling bifurcation explained above, that takes place increasing $\quad$, other bifurcations can take place changing $x_0$. Then, encoding is possible for each $n$ harmonic branch, by varying the control parameters $\quad$ and $x_0$. In Part II of this thesis we explore similar bifurcations in a prototypical model of two mutually delay-coupled OEOs. Besides the application of encoding of information, such multistable periodic solutions can be used for signal processing, optical sensing or optical clocks.

One fundamental question raised by Ikeda's work [46, 6, 48] is the possibility to generate oscillations with a desired period. Experiments showed that an electro-optical hybrid bistable system with a fiber delay loop could indeed sustain a large number of oscillatory states [48, 49]. However, the experiments also produced evidence that such systems were very sensitive to spurious resonances. Particularly disturbing was the fact that a large number of harmonics predicted by numerical simulations were not observed in physical implementations. This raised the question of the stability of all the bifurcating time-periodic modes and their robustness with respect to external perturbations. Ikeda and coworkers were able to recover the desired harmonics introducing a suitable periodic perturbation on the system. This idea has recently been implemented again by Weicker et al. in an experimental demonstration of multiple periodic solutions in an improved optoelectronic oscillator [8], as discussed in the subsection 3.2.6.

## 1.4 Square-wave switching

A particular kind of solution that is interesting for the aforementioned applications is a square-wave pulse, which arises under large delayed feedback [50, 51].

In optical and optoelectronic systems with feedback, in which the time scale associated to the feedback is generally much larger than the intrinsic time scales of the dynamical system, the generation of tunable pulsating dynamics has been studied during the past few years [52, 53, 7, 54, 55, 56, 57, 58, 59], not only for its fundamental interest but also motivated by applications such as optical clocks [52] or optical sensing [53]. In particular, stable square-wave switching has been observed in edge-emitting diode lasers (EELs) [7, 54, 55], vertical-cavity surface-emitting lasers (VCSELs) [56, 57, 60], OEOs [61, 62, 63], ring lasers [58] and mode-locked fiber lasers [59, 64].

Square-wave switching between the two natural polarization states of a laser can be realized by injecting light with one polarization mode to the orthogonal mode. A quarter-wave plate has been typically used to achieve such polarization self-modulation regime [65]. Nevertheless, this configuration allows mutual coupling between the polarization modes and multiple cavity round-trips.

In [7], a Faraday rotator has been used instead. A Faraday rotator is a Faraday isolator with its input polarized removed and its output polarizer at 45° from horizontal. It avoids multiple round-trip reflections and allows only unidirectional coupling between the natural TE mode and the unsupported orthogonal TM mode. In the polarization-rotated optical feedback (PROF) setup depicted in Fig. 1.7, the polarization state of the feedback of an EEL is rotated by 90°, in such a way that the natural horizontal polarization TE mode, which is normally supported by the laser cavity, is coupled to the normally unsopported orthogonal TM mode. This configuration prevents the influence of the TM mode on the TE mode directly via optical injection, and this simplifies the analysis. After a 45° rotation, the beam is reflected by a mirror, rotated 45° and reinjected into the TM mode. With this configuration, in which the laser output switches between its two natural polarization modes, symmetric square waves were observed in

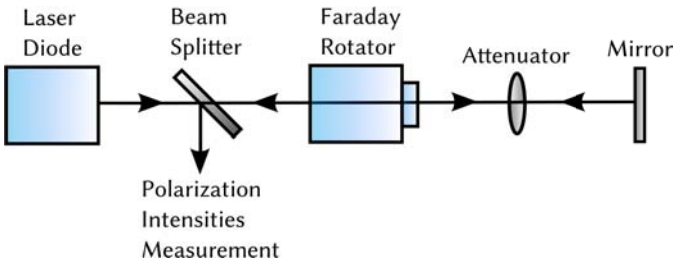


**Figure 1.7:** Polarization-rotated feedback squeme with an EEL and a Faraday rotator.

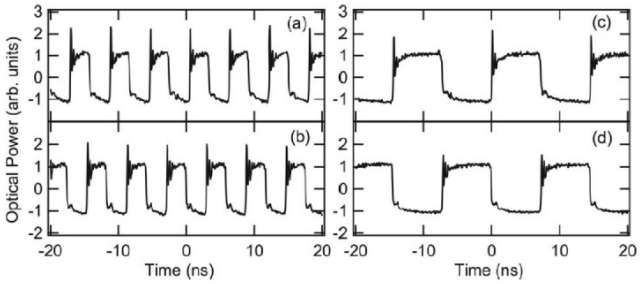


**Figure 1.8:** Experimental time series of square-wave oscillations. Top and bottom, TE and TM mode intensities, respectively. The time delay is $\tau = 2.6\,\text{ns}$ in (a)-(b), and $\tau = 6.92\,\text{ns}$ in (c)-(d). Figure reproduced from [7].

the intensities emitted in each of the polarization directions. As it can be seen in Fig. 1.8, the square waves generated with this setup are in antiphase and have a period close to but larger than twice the delay $\tau$. Besides the frequency $f_D = 2\tau$ induced by the external feedback, these square waves exhibit relaxation oscillations of frequency $f_{\text{RO}} = \sqrt{P/T}/(2\pi) << f_{\text{D}}$, being $P$ the pump power above threshold and $T$ the ratio of carrier to cavity lifetimes [66].

Square-wave switching using PROF has also been reported in mutually coupled EELs, in a scheme where the TE mode of each laser is injected into the TM mode of the other laser [54, 55], and in VCSELs [56, 57, 60].

Square-wave pulsating dynamics also takes place in semiconductor ring lasers [58], although the underlaying mechanism differs from that one in EELs and VCSELs. The origin of square-wave switching in EELs and VCSELs is attributed to a gain difference between the two modes: the gain anisotropy is overcomed with sufficiently strong delayed feedback with crossed polarization, pushing the low-gain mode above laser threshold while turning off the high-gain mode, what in turn gives rise to switching of the laser back to the high-gain mode after one delay. However, in semiconductor ring lasers the two modes are always on due to lineal coupling through a physical process called backscattering. Square-wave switching in semiconductor ring lasers arises from the interaction between the counter- and clockwise modes circulating into the ring laser, provided there exists a certain asymmetry in the lineal coupling between the two modes and the cross-saturation effects [58].

As discussed in more detail in Chapter 3, OEOs are also capable of generating square-wave oscillations. In these sytems, square waves originated with negative feedback have a symmetric duty cycle, namely the duty cycle is half of the period. In contrast, for positive feedback square waves have an asymmetric duty cycle. Generation of stable square waves with symmetric and asymmetric duty cycle in OEOs has been reported in Refs. [61, 62, 63].

## 1.5 Objectives

This thesis has two main objectives.

On the one hand, we aim to study the synchronization of the square waves arising in a system of two mutually coupled OEOs with two different delay times, the coupling delay and the self-feedback delay. More specifically, we aim to investigate the role of the delay-times ratio and that of the sign of the feedback on the synchronization. We will first consider the oscillators to be identical, both subject to positive or negative feedback; and later the possibility of non-identical oscillators and mixed feedback, namely, positive for one oscillator and negative for the other. This system could serve as prototypical to understand the square-wave synchronization in other systems of delay-coupled oscillators.

On the other hand, we aim to contribute to the understanding of SDD dynamics by considering a model for a semiconductor laser with filtered feedback from two cavities with different length and center frequency, with the condition of almost non-overlapping spectra, in such a way that the frequency of the optical field determines which filter is mainly acting at a given time and thus which value takes the delay at that time. We also compare the theoretical and numerical results with experimental results obtained by coworkers. This system is the first controllable photonic implementation of a SDD system and it can be used as a prototype to study the dynamics of other systems with a delay time that is not constant but depends on the state of the system.

Chapter 2

# Tools and methods

2.1

## Introduction

The dynamical systems with delay that we consider in this thesis are nonlinear and thus typically exact analytical time-dependent solutions cannot be found. Furthermore, the study of the stability of fixed points in systems with delay involves transcendental equations which cannot be solved exactly. However, approximate solutions can be obtained with numerical and analytical techniques. In this chapter, we highlight some methods applied in this work, such as linear stability analysis and numerical methods for integration of DDEs, and a few tools to study the stability of periodic solutions. Other methods, such as asymptotic techniques for systems with large delay, will be introduced through the course of this thesis. The following tables list the main methods and tools used in this thesis and indicate the sections in which they can be found.

| **Analytical method or tool** | Section where it is introduced | Other sections where it is used |
|---|---|---|
| *Determination of xed points* | 2.2.4 | 3.2.5, 4.2, 8.5 |
| *Linear stability analysis* | 2.2.1 | 3.2.6, 4.3.1, 5.2, 6.2, 7.2 |
| *Asymptotic methods for large delay* | 5.3 | 5.4, 6.4 |
| Maps for square-wave amplitude | 5.3 | |
| Maps for instabilities of square waves | 5.4 | |
| Maps for square waves with asymmetric duty cycle | 6.4 | |

**Table 2.1:** Analytical methods and tools used in this thesis.

| **Numerical method or tool** | Section where it is introduced | Other sections where it is used |
|---|---|---|
| *Integration of DDEs* | 2.3 | 3.2.8, 3.2.9, 5.5-5.7, 6.3, 6.5-6.7, 7.3-7.6, 8.6-8.8 |
| Euler algorithm | 2.3.1 | 3.2.9 |
| Predictor-corrector algorithm | 2.3.2 | 3.2.8, 3.2.9, 5.5-5.7, 6.3, 6.5-6.7, 7.3-7.6, 8.6-8.8 |
| Data storage schemes | 2.3.2 | 3.2.8, 3.2.9, 5.5-5.7, 6.3, 6.5-6.7, 7.3-7.6, 8.6-8.8 |
| *Bifurcation diagrams* | 2.2.9 | 5.5, 6.5 |
| *Continuation techniques* | 2.2.10 | 6.5 |
| *Projection of phase-space trajectories* | 8.6 | 8.7 |
| *Stability of periodic solutions* | 2.2.5 | 2.2.2 |
| Poincaré section technique | 2.2.5 | 3.2.9, 5.7, 6.7 |
| Hénon's method | 2.2.7 | 3.2.9 |
| Floquet analysis | 2.2.6 | 3.2.9 |
| *Lyapunov exponents* | 2.2.8 | 3.2.9 |
| *Characterization tools of SDD dynamics* | 8.2 | 8.3.2, 8.6, 8.7, 8.9 |
| Computation of optical spectra | 8.6 | |
| Contrast function | 8.2.2 | 8.3.2, 8.6, 8.7 |
| Residence times | 8.2.3 | 8.9 |

**Table 2.2:** Numerical methods and tools used in this thesis.

## 2.2 Stability

The qualitative structure of a flow or a map can change as parameter values are varied. These qualitative changes correspond to bifurcation points. In this section, we introduce several tools to study the local stability of equilibrium points, periodic and quasiperiodic solutions. First, we introduce the linear stability analysis technique and the variational equation governing the temporal evolution of small perturbations. After that, we sketch some codimension-1 local bifurcations of fixed points, which take place as a single parameter is varied. Then, we focus on stability tools for periodic solutions, such as the Poincaré map and the Floquet multipliers. The section ends introducing the Lyapunov analysis, a stability tool not only for periodic solutions but also for quasiperiodic solutions, as well as a tool for characterizing chaotic solutions.

### 2.2.1 Linear stability analysis

The use of linear stability analysis as a tool to investigate the stability in differential equations was pioneered by J.C. Maxwell in 1868 [67] in the context of the industrial revolution and the need to develop automatic control systems. His technique consisted of linearizing the differential equations of motion around a fixed point to find the characteristic equation, which determines the growth rate of perturbations allowing one to find out the stability of the system. Maxwell showed that the system is stable if the real part of the roots of the characteristic equation are all negative. As an example, at the end of the subsection 2.2.4, linear stability analysis is applied to an equilibrium point to find the bifurcation points towards periodic solutions. Linear stability analysis can also be applied to study the stability of periodic and quasiperiodic solutions; in this case the local stability of the solution can be determined by solving the variational equation. In the subsection 2.2.2, we introduce the variational equation for an autonomous dynamical system without delay. The generalization of the variational equation for delay differential equations can be found in [68].

### 2.2.2 The variational equation

Consider an $N$-dimensional continuous-time autonomous dynamical system[1],

$$\mathbf{x}(t) = \mathbf{f}(\mathbf{x}(t)), \quad \mathbf{x}(0) = \mathbf{x}_0. \tag{2.1}$$

The local stability of a solution $\mathbf{x}^*(t)$ of (2.1) can be investigated by following the temporal evolution of the perturbation vector $\delta\mathbf{x}(t) = \mathbf{x}(t) - \mathbf{x}^*(t)$, which is $N$-dimensional[2]. Linearization of the dynamical system (2.1) around $\mathbf{x}^*(t)$ leads to

$$\delta\mathbf{x}(t) = \mathbf{Df}(\mathbf{x}^*(t))\delta\mathbf{x}(t), \tag{2.2}$$

where $\mathbf{Df}(\mathbf{x}^*(t))$ is the $N \quad N$ Jacobian matrix $[\ f_i/\ x_j]$ evaluated at $(\mathbf{x}^*(t))$.

### 2.2.3 Fundamental matrix formalism

A solution of (2.2) can be written as

$$\delta\mathbf{x}(t) = \mathbf{\Phi}(t)\delta\mathbf{x}(0), \tag{2.3}$$

where $\delta\mathbf{x}(0)$ is the initial perturbation vector and $\mathbf{\Phi}$ is the $N \quad N$ *fundamental matrix*. The columns of $\mathbf{\Phi}$ are $N$ independent perturbation vectors.

The fundamental matrix determines the evolution of the perturbations. It can be obtained by integrating simultaneously the dynamical system with the *variational equation*,

$$\mathbf{\Phi}(t) = \mathbf{Df}(\mathbf{x}^*(t))\mathbf{\Phi}(t), \quad \mathbf{\Phi}(0) = I, \tag{2.4}$$

[1] A non-autonomous dynamical system can be converted to an autonomous one by introducing a new variable representing the time.

[2] For the $N$-dimensional system considered here, without delay times, $\delta x(t)$ is $N$-dimensional. For a continuous-time system with delay times, which is infinite-dimensional, $\delta x(t)$ is also infinite-dimensional; in practice, however, $\delta x(t)$ is approximated by a discrete vector with a dimension that depends on the discretization of the time and the numerical integration method.

where $I$ is the $N \quad N$ identity matrix. The eigenvalues of the fundamental matrix $\mathbf{\Phi}$ evaluated at an appropriate moment of time determine the stability of the solution $\mathbf{x}^*(t)$ [69]. For a periodic solution, the eigenvalues of the fundamental matrix evaluated after one period determine the stability of $\mathbf{x}^*(t)$, as discussed later in this chapter.

### 2.2.4 Local stability of xed points of ows

Fixed point solutions $x^*$ of the dynamical system (2.1) fullfill $f(x^*) = 0$. In this case, the solution does not depend on time and $\mathbf{Df}(\mathbf{x}^*)$ is the Jacobian evaluated at the fixed point. Then, the local stability of $x^*$ is determined by the eigenvalues of $\mathbf{Df}(\mathbf{x}^*)$. Perturbations of the fixed point along any eigenvector associated with an eigenvalue with negative real part are exponentially damped. Conversely, perturbations along an eigenvevector associated with an eigenvalue with positive real part grow exponentially. Thus, the fixed point is stable if the real part of all eigenvalues is negative, unstable if the real part of all eigenvalues is positive, and a saddle if there is an eigenvalue with positive real part and another one with negative real part.

In this subsection, we briefly introduce some elementary bifurcations, namely those that affect a local region in phase space and that can be typically encountered by changing only one parameter (usually called local codimension-1 bifurcations): the saddle-node, the transcritical, the pitchfork and the Hopf bifurcations. Saddle-node, transcritical, and pitchfork bifurcations occur in dynamical systems with one or more dimensions ($N \quad 1$) when a real eigenvalue changes sign, whereas the Hopf bifurcation takes place in dynamical systems with $N \quad 2$ when a complex pair of eigenvalues crosses the imaginary axis. We finally introduce an example of Hopf bifurcation arising in a dynamical system with delay.

#### Saddle-node bifurcation

The saddle-node bifurcation, also known as fold bifurcation or turning-point bifurcation, is the basic mechanism for creation and destruction of fixed points. In this bifurcation, two fixed points (one stable and one unstable) are created or annihilated as a control parameter is varied [70].

Consider the prototypical system

$$x(t) = \quad + x^2(t), \tag{2.5}$$

where is a control parameter. Fig. 2.1 shows the bifurcation diagram of this system. For $< 0$, this system has two fixed points ($x^* = - \quad \overline{\quad - \quad}$, stable; and $x^* = \quad \overline{\quad - \quad}$, unstable). At the bifurcation point, $= 0$, the two fixed points collide into a single half-stable fixed point, and for $> 0$ there are no fixed points. Eq. (2.5) is the normal form of the saddle-node bifurcation, namely it is the simplest dynamical system that exhibits a saddle-node bifurcation.

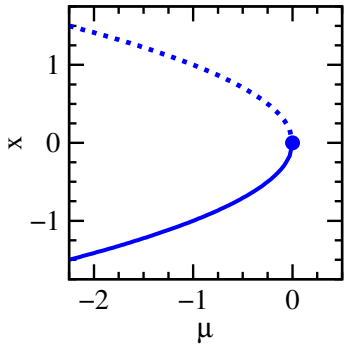


**Figure 2.1: Saddle-node bifurcation**. Bifurcation diagram of Eq. (2.5). Stable and unstable branches emerging from the bifurcation point ($x = 0, \quad = 0$) are plotted in continuous and dashed lines, respectively.

### Transcritical bifurcation

There are certain situations in which a fixed point exists for any value of a control parameter . For instance, in the logistic equation for the population growth of a given species, there is a fixed point of zero population for any value of the growth rate. However, this fixed point exchanges its stability with another fixed point as the parameter is varied. The transcritical bifurcation is the standard mechanism in situations in which two fixed points interchange their stability.

Consider the normal form of the transcritical bifurcation [70],

$$x(t) = \quad x(t) - x^2(t), \tag{2.6}$$

in which the fixed point $x^* = 0$ exists for any value of . The bifurcation diagram of this system is shown in Fig. 2.2. For $< 0$, the fixed point $x^* = 0$ is stable and there is also an unstable fixed point $x^* =$ . At $= 0$, these two fixed points collide; and for $> 0$, the fixed point $x^* = 0$ is unstable and $x^* =$ is a stable fixed point.

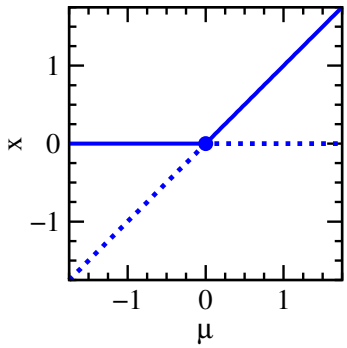


**Figure 2.2: Transcritical bifurcation**. Bifurcation diagram of Eq. (2.6). Stable and unstable branches emerging from the bifurcation point ($x = 0, \quad = 0$) are plotted in continuous and dashed lines, respectively.

### Pitchfork bifurcation

There are two different types of pitchfork bifurcation: subcritical and supercritical. The normal form of the **supercritical pitchfork bifurcation** is [70]

$$x(t) = \quad x(t) - x^3(t). \tag{2.7}$$

The bifurcation diagram of Eq. (2.7) is shown in Fig. 2.3(a). For $\quad < 0$, there is a stable fixed point at the origin, $x^* = 0$. For $\quad > 0$, the fixed point $x^* = 0$ becomes unstable and two stable fixed points appear on both sides of the origin, symmetrically located at $x = \quad \overline{\quad}$.

The cubic term in a supercritical pitchfork bifurcation stabilizes the system; in contrast, in a **subcritical pitchfork bifurcation** it has a destabilizing effect as in [70]

$$x(t) = \quad x(t) + x^3(t). \tag{2.8}$$

The bifurcation diagram of Eq. (2.8) is shown in Fig. 2.3(b). For $\quad < 0$, there is a stable fixed point at the origin, $x^* = 0$, and two unstable fixed points at $x = \quad \overline{\quad}$. For $\quad > 0$, the fixed point $x^* = 0$ becomes unstable. As a result, there are no physical solutions for $\quad > 0$. In real physical systems, however, the presence of high-order terms usually gives rise to stable branches for $\quad > 0$. An example of such a system is

$$x(t) = \quad x(t) + x^3(t) - x^5(t). \tag{2.9}$$

The bifurcation diagram of Eq. (2.9) is sketched in Fig. 2.3(c).

The pitchfork bifurcation is common in systems that have a symmetry [70]. Note that Eqs. (2.7), (2.8) and (2.9) have spatial left-right symmetry, namely are invariant under the change of variables $x \quad -x$.

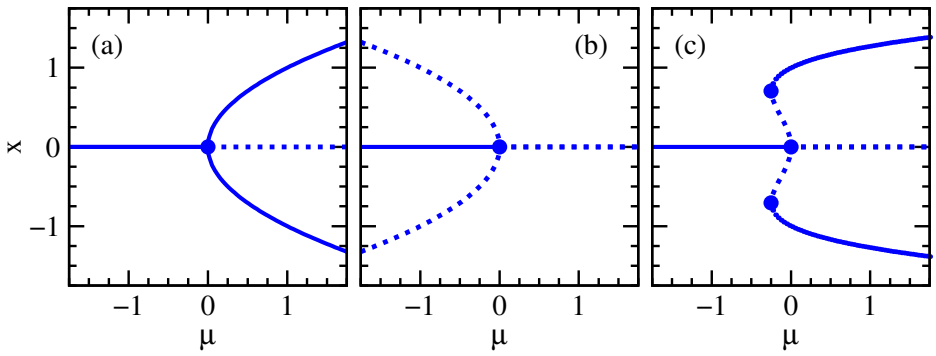


**Figure 2.3: Pitchfork bifurcation**. Bifurcation diagram of (a) Eq. (2.7) (supercritical pitchfork), (b) Eq. (2.8) (subcritical pitchfork) and (c) Eq. (2.9) (subcritical pitchfork with a stabilizing nonlinearity). In (a) and (b) there is a single bifurcation point, ($x \quad = 0, \quad = 0$), whereas in (c) there are three bifurcation points: a subcritical pitchfork at ($x \quad = 0, \quad = 0$), and two saddle-nodes at ($x \quad = 1/\quad \overline{2}, \quad = -0.25$) and ($x \quad = -1/\quad \overline{2}, \quad = -0.25$). Stable and unstable branches are plotted in continuous and dashed lines, respectively.

### Hopf bifurcation

The Hopf bifurcation, also known as Poincaré-Anderson-Hopf bifurcation, is the simplest bifurcation not just involving fixed points. It consists of the birth or death of a periodic solution in the neighborhood of a steady state that changes its stability due to the crossing of a conjugate pair of eigenvalues over the imaginary axis. Therefore, it can only occur in systems with two or more dimensions. This bifurcation was first studied by Poincaré in 1892 and by Anderson and co-workers around 1930. Hopf's main contribution was the extension from two to higher dimensions in 1942 [71].

Like the pitchfork bifurcation, the Hopf bifurcation can take place supercritically or subcritically. In the supercritical Hopf, the periodic solution that is born is stable and it coexists with an unstable fixed point. In the subcritical case, the periodic solution is unstable and coexists with a stable fixed point.

As an example of **supercritical Hopf bifurcation** in two dimensions, consider the following system in polar coordinates,

$$\dot{r}(t) = \quad r(t) - r^3(t), \tag{2.10}$$

$$\dot{\theta}(t) = \omega + \quad r^2(t), \tag{2.11}$$

which has two fixed points, ($r^* = 0$, $\theta^* = \quad _0$) and ($r^* = \quad ^-$, $\theta^* = \quad _0$), being $\quad _0$ a constant. The parameter $\quad$ determines the stability of the fixed point at the origin, $\omega$ gives the frequency of an infinitesimal oscillation, and $\quad$ accounts for the dependence of the frequency on the amplitude for larger-amplitude oscillations. The bifurcation diagram of the coordinate $r$ (2.10) is shown in Fig. 2.4(a).

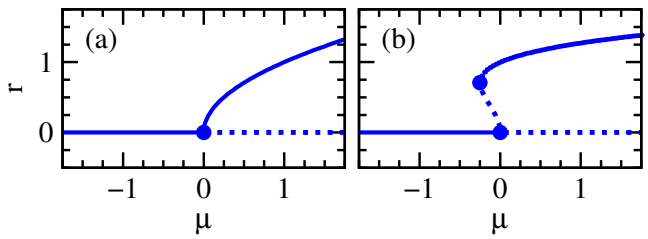


**Figure 2.4: Hopf bifurcation**. Bifurcation diagram of the coordinate $r$ for (a) Eq. (2.10) (supercritical Hopf), and (b) Eq. (2.15) (subcritical Hopf). In (a), there is a single bifurcation point: ($r \quad = 0$, $\quad = 0$). In (b), there are two bifurcation points: ($r \quad = 0$, $\quad = 0$) and ($r \quad = 1/\quad \overline{2}$, $\quad = -0.25$). Stable and unstable branches are respectively plotted in continuous and dashed lines.

To obtain the eigenvalues, we write system (2.10) in cartesian coordinates,

$$\dot{x}(t) = \quad -(x^2+y^2)\ x(t) - \quad \omega + \quad (x^2+y^2)\ y(t), \tag{2.12}$$

$$\dot{y}(t) = \quad \omega + \quad (x^2+y^2)\ x(t) + \quad -(x^2+y^2)\ y(t), \tag{2.13}$$

The jacobian of (2.12) evaluated at the origin is

$$J = \begin{matrix} & -\omega \\ \omega & \end{matrix} \quad . \tag{2.14}$$

The eigenvalues of (2.14) are $= i\omega$. As expected, the eigenvalues cross the imaginary axis at $= 0$. For $< 0$, the fixed point at the origin is a stable spiral. For $> 0$, the spiral is unstable and there is a stable limit cycle of amplitude $^{-}$ and frequency $\omega = -$ .

An example of **subcritical Hopf bifurcation** is given by the two-dimensional system

$$r(t) = r(t) + r^3(t) - r^5(t), \tag{2.15}$$

$$(t) = \omega + r^2(t). \tag{2.16}$$

In contrast to the supercritical case, here the cubic term is destabilizing. The bifurcation diagram of system (2.15) for the coordinate $r$ is shown in Fig. 2.4(b). For $< -0.25$, there is a stable fixed point at the origin; for $-0.25 < < 0$, there is a stable fixed point at the origin, an unstable limit cycle of amplitude $[\ 1-(1+4\ )^{1\ 2}\ /2]^{1\ 2}$ and frequency $\omega = -\ (1-(1+4\ )^{1\ 2})/2$, and a stable limit cycle of amplitude $[\ 1+(1+4\ )^{1\ 2}\ /2]^{1\ 2}$ and frequency $\omega = -\ (1+(1+4\ )^{1\ 2})/2$; and for $> 0$, the fixed point at the origin is unstable and coexists with the stable limit cycle.

So far we have introduced examples of local bifurcations in finite-dimensional systems. The four kinds of bifurcation introduced before have their counterparts in dynamical systems with delay, which are infinite-dimensional. We now introduce an example of **delayed system with multiple Hopf bifurcations**. We will obtain the Hopf bifurcations of the steady state $x = 0$ of Eq. (1.2) with $\alpha > 0$. Following the classical linear stability analysis of the steady state, we introduce exponential perturbations $\delta x = A\exp\ t$ in Eq. (1.2). Since Eq. (1.2) is linear, the perturbations follow the same equation than $x$,

$$A\exp(\ ) = -\alpha A\exp\ (t-\tau). \tag{2.17}$$

Therefore, fulfills the transcendental characteristic equation

$$+\alpha\exp(-\ \tau) = 0, \tag{2.18}$$

which admits multiple roots $_k$. Substituting $_k = r_k + i\omega_k$ into Eq. (2.18) and separating real and imaginary parts leads to two equations for $r_k$ and $\omega_k$:

$$r_k + \alpha\exp(-r_k\tau)\cos(\omega_k\tau) = 0, \tag{2.19}$$

$$\omega_k - \alpha\exp(-r_k\tau)\sin(\omega_k\tau) = 0. \tag{2.20}$$

At the Hopf points $\alpha_k$, the roots of the characteristic equation are purely imaginary, $_k = i\omega_k$. As a result, Eqs. (2.19)-(2.20) can be written as (1.8)-(1.9) and periodic solutions with frequencies given by (1.10) are born at critical values $\alpha_k$ given by (1.11). The solutions of Eqs. (2.19)-(2.20) for $\tau = 1$ and $\alpha > 0$ are plotted in Fig. 2.5. The solutions with real are plotted in red, whereas the solutions with complex are plotted in black ($k = 0$), orange ($k = 1$) and green ($k = 2$). In this figure, it can be seen that $r$ $-$ as $\alpha$ 0. By increasing $\alpha$, the zero solution becomes unstable with the first crossing of a conjugate pair of complex roots through the imaginary axis into the right half plane, namely when the real part $r$ of two conjugate complex eigenvalues $_k$ becomes positive, giving rise to a periodic solution. For $\alpha < 0$, the real eigenvalue is positive and thus the system is unstable as discussed in Sec. 1.2.

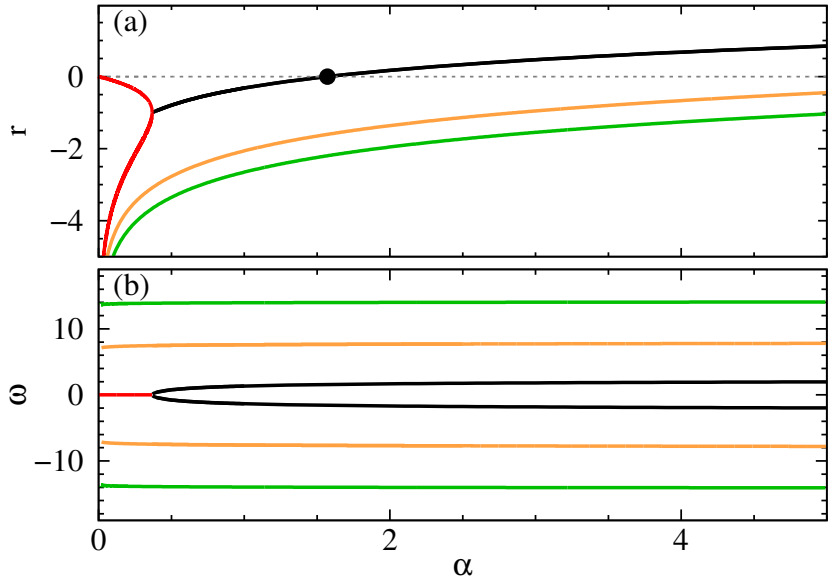


**Figure 2.5:** Solutions of the characteristic equation (2.18) with $\tau = 1$. The red lines correspond to real. The other lines correspond to complex with $k = 0$ (black), $k = 1$ (orange), and $k = 2$ (green). The zero solution is stable in the interval $0 < \alpha < \pi/2$, in which all the $r_k$ are negative. The dot indicates the Hopf point $\alpha = \pi/2$, where $r$ changes sign and a periodic solution (with $\omega \neq 0$) is born.

### 2.2.5 Poincaré map

The solutions of the continuous-time dynamical system (2.1) can be represented by curves or trajectories in the $N$-dimensional phase space. We will now define a $(N-1)$-dimensional surface of section $\Sigma$, where $\Sigma$ is required to be transverse to the flow, what means that all trajectories starting on it intersect it and are not parallel to it. The surface of section can be defined by an equation

$$S(\mathbf{x}) = 0. \tag{2.21}$$

The Poincaré map, $P$, is a mapping from $\Sigma$ to itself, defined by the values of the variables spanning the surface of section at successive intersections $x_k$ $\Sigma$ of the trajectories with $\Sigma$ in a given direction [70]:

$$\mathbf{x}_{k+1} = P(\mathbf{x}_k). \tag{2.22}$$

A fixed point of $P$ is a limit cycle of the original system given by Eq. (2.1), namely a trajectory which starts at $\mathbf{x}^*$ and returns to $\mathbf{x}^*$ after some time $T$ [70].

The number of iterations of the map, namely of crossings through $\Sigma$, required to close the orbit determines the periodicity of a limit cycle. A limit cycle is defined as period $n$ if it returns for the first time to $\mathbf{x}^*$ after $n$ crossings through $\Sigma$, in such a way that $n$ is the smallest natural number satisfying $\mathbf{x}_{k+n} = P^n(\mathbf{x}_k) = \mathbf{x}^*$; for instance, the trajectory in Fig. 2.6 is period 3 because it returns to $\mathbf{x}^*$ after three crossings through $\Sigma$ and thus satisfies $\mathbf{x}_{k+3} = P^3(x_k) = \mathbf{x}^*$.

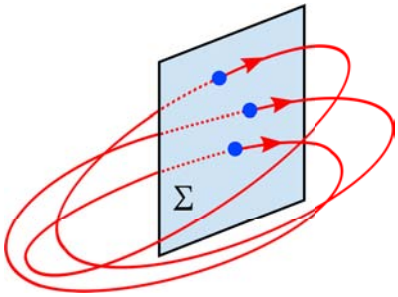


**Figure 2.6:** A period-3 periodic orbit intersects the Poincaré section Σ at three different points.

The local stability of a limit cycle can be determined by analyzing the behavior of $P$ in the vicinity of the fixed point to which the cycle corresponds, as explained in the subsection 2.2.6.

In this thesis, the time intervals $t_k$ between successive intersections through Σ are referred as the Poincaré section return times or simply Poincaré return times. A fine computation of the Poincaré section return times to analyze the periodicity of multiple coexisting periodic solutions can be found in sections 5.7 and 6.7. The recording of the Poincaré section return times can also be used to determine the transient time required to reach a stationary state of the map in a numerical simulation. In this thesis, the transient time for periodic solutions is obtained as the time interval after which the difference between successive return times is zero or it is similar to the numerical precision, in such a way that the return time reaches an horizontal asymptote in a plot of the return time as a function of time.

### 2.2.6 Local stability of periodic orbits

Consider an isolated periodic solution (limit cycle) $\mathbf{x}^P$ of the $N$-dimensional continuous-time dynamical system (2.1), corresponding to a fixed point $\mathbf{x}^*$ of a $(N-1)$-dimensional Poincaré map $P$. The local stability of $\mathbf{x}^*$ is determined by linearizing the map $P$ around $\mathbf{x}^*$,

$$\delta\mathbf{x}_{k+1} = DP(\mathbf{x}^*)\delta\mathbf{x}_k. \tag{2.23}$$

Defining $\delta\mathbf{x}_k = \delta\mathbf{x}(0)$ as the initial perturbation vector, and $\delta\mathbf{x}_{k+1} = \delta\mathbf{x}$ as the perturbation vector after one period $T$, $DP(\mathbf{x}^*)$ is the fundamental matrix after one period, $\mathbf{\Phi}_T(\mathbf{x}^*)$, known as the *monodromy matrix*.

To obtain the monodromy matrix, the dynamical system must be integrated simultaneously with the variational equation (2.4) during one period. Then, the local stability of $\mathbf{x}^*$ is determined by the eigenvalues of the monodromy matrix. More precisely, the characteristic or Floquet multipliers of the periodic solution $\mathbf{x}^P$ determine the local stability of $\mathbf{x}^*$, and thus the stability of $\mathbf{x}^P$. The periodic solution $\mathbf{x}^P$ is stable if all the Floquet multipliers lie inside the unit circle in the complex plane, namely if all Floquet multipliers have modulus smaller than 1 [69], as shown in Fig. 2.7.

In non-autonomous systems, the characteristic multipliers are equal to the eigenvalues of $\mathbf{\Phi}_T(\mathbf{x}^*)$. For autonomous systems, $\mathbf{\Phi}_T(\mathbf{x}^*)$ has always an eivenvalue 1 in the direc-

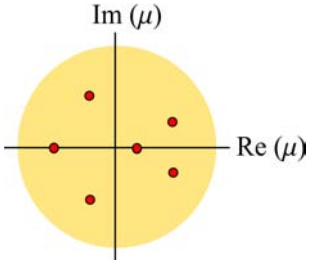


**Figure 2.7:** Floquet multipliers inside the unit circle (yellow area) demonstrating the stability of a periodic solution.

tion of the flow, and the remaining eigenvalues are the Floquet multipliers, namely the eigenvalues of $\mathbf{\Phi}_T(\mathbf{x}^*)$ are $_1, .. \ _N \ _1, 1$ [69].

If one Floquet multiplier leaves the unit circle, the limit cycle undergoes a bifurcation. There are three types of codimension-1 bifurcations of limit cycles: fold, flip, and Neimark-Sacker [72]. Illustrative diagrams of the Floquet multipliers in those bifurcations are shown in Fig. 2.8.

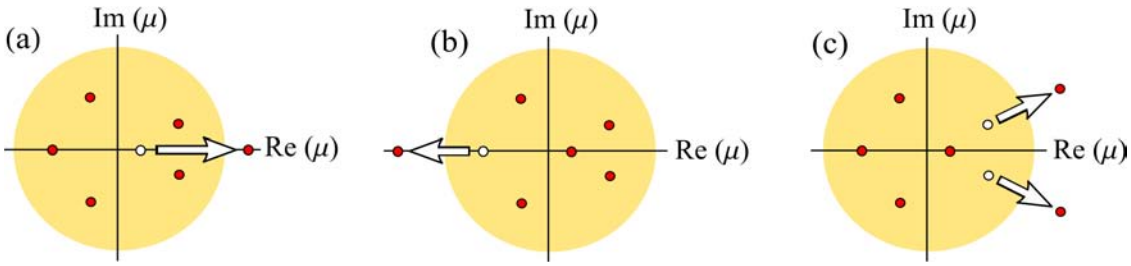


**Figure 2.8:** Floquet multipliers for codimension-1 bifurcations of limit cycles. (a) In a fold bifurcation, a simple positive eigenvalue crosses the unit circle taking the value $= 1$ at the bifurcation point. (b) In a flip bifurcation, a simple negative Floquet multiplier crosses the unit circle taking the value $= -1$ at the bifurcation point. (c) In a Neimark-Sacker, two simple and complex eigenvalues cross the unit circle taking values $= \exp( \ i \ )$ at the bifurcation point.

**Fold bifurcation of cycles**

If a simple real and positive Floquet multiplier crosses the unit circle as illustrated in Fig. 2.8(a), a fold or tangent bifurcation takes place. At this bifurcation, two limit cycles (stable and saddle) collide and disappear. The fold bifurcation is also known as limit point, saddle-node or turning point bifurcation for maps [72].

**Flip bifurcation of cycles**

If a simple and real negative Floquet multiplier crosses the unit circle as illustrated in Fig. 2.8(b) a flip or period-doubling bifurcation occurs. A cycle of period two appears for the map, whereas the fixed point changes its stability [72].

**Neimark-Sacker bifurcation of cycles**

The last codimension-1 bifurcation for cycles corresponds to the case when two complex and simple multipliers cross the unit circle as shown in Fig. 2.8(c). This bifurcation is known as Neimark-Sacker or Hopf bifurcation of cycles [72].

In this thesis, the computation of the largest Floquet multipliers to determine the stability of periodic solutions is addressed in Sec. 3.2.9. The determination of the Floquet multipliers requires a fine computation of the period of the periodic solution. In the subsection 2.2.7, we address the problem of the numerical computation of the period of a periodic solution.

### 2.2.7 The Hénon s trick

In most cases, the Poincaré map cannot be obtained analytically and it has to be computed numerically. The major problem in the numerical computation of the Poincaré section is that the Poincaré return time typically is not a multiple of the integration time step. The reduction of the integration time step reduces the error in the computation of the surface of section, but it also increases the computation time.

One way to obtain an approximation to the Poincaré map is to integrate the dynamical equations and evaluate $S(\mathbf{x})$ at each time until a change of sign is detected, namely until the surface of section is crossed, and applying interpolation between the points located before and after the Poincaré section. Averaging over a large number of crossings through the surface of section, or using high-order interpolation formulae also help to reduce the error.

A convenient trick to facilitate the numerical computation of the Poincaré map was proposed by M. Hénon in 1982 [73]. It consists of rearranging the dynamical system in such a way that one integration point lies exactly on the surface of section. The only requirement for using this trick is that each time step does not depend on previous steps. Consider the simplest case where the surface of section is

$$x_N - a = 0.$$

Hénon proposed to rearrange the dynamical system in such a way that $x_N$ becomes the independent variable and time becomes a dependent variable. This can be done by dividing the first $(N-1)$ equations of the dynamical system by the last one, and inverting the last equation,

$$\begin{aligned} x_i &= \frac{f_i}{f_N}, \qquad i = 1, N-1, \\ t &= \frac{1}{f_N}, \end{aligned} \tag{2.24}$$

where dot means derivative with respect to $x_N$.

The practical procedure has two steps: 1) integrating the original dynamical system until a change of sign is detected in $S(x)$ ($S(x) = x_N - a$ in the case considered here); 2) shifting to system (2.24) and integrating for one step of size $\Delta x_N = -S$ to end up exactly on the surface of section, with an error given by the integration error for a single integration step.

### 2.2.8 Lyapunov exponents

Lyapunov exponents are a generalization of the characteristic multipliers. They are useful to determine the stability of periodic and quasiperiodic solutions. Furthermore, they can be used to characterize a chaotic solution.

Consider an initial condition $\mathbf{x}^*$. Lyapunov exponents measure the average rate of contraction or expansion of infinitesimal perturbations near $\mathbf{x}^*$ on a logarithmic scale. Let $^{i}$, with $i = 1, p$, be the eigenvalues of the fundamental matrix after a finite time $T$, $\mathbf{\Phi}_T(\mathbf{x}^*)$. The Lyapunov exponents of $\mathbf{x}^*$ are defined in the limit as $T$ ,

$$\lambda_i = \lim_{T} \frac{1}{T} ln \quad _i \ , \quad i = 1, ..., p \tag{2.25}$$

whenever the limit exists [69] (pp. 67).

For a periodic solution, $T$ is the period of the solution. After $k$ periods, $\mathbf{\Phi}_{kT}(\mathbf{x}^*) = \mathbf{\Phi}_T(\mathbf{x}^*)^k$ and thus $^{k}_{i}$ are eigenvalues of $\mathbf{\Phi}_{kT}(\mathbf{x}^*)$. Therefore, the Lyapunov exponents of a periodic solution $\mathbf{x}^P$ are

$$\lambda_i = \lim_{k} \frac{1}{kT} ln \quad ^{k}_{i} \quad = \frac{1}{T} ln \quad _i \ . \tag{2.26}$$

For autonomous systems, one eigenvalue of $\mathbf{\Phi}_T(\mathbf{x}^*)$ is always 1 and, therefore, one Lyapunov exponent is always 0. In fact, in any limit set except an equilibrium point it is guaranteed that one Lyapunov exponent vanishes.

In non-chaotic asymptotically stable limit sets (equilibrium points, limit cycles and quasiperiodic solutions), no Lyapunov exponent is positive, and the number of zero Lyapunov exponents coincides with the number of incommensurable frequencies: an equilibrium point has all the Lyapunov exponents negative; an asymptotically stable limit cycle has one zero Lyapunov exponent and the rest negative; a $K$-torus (quasiperiodic solution with $K$ incommensurable frequencies) has $K$ Lyapunov exponents zero and the rest negative. Chaotic attractors differ from non-chaotic attractors in the existence of at least one positive Lyapunov exponent [69] (pp. 70-71).

In the subsection 3.2.9, the Lyapunov exponents are computed for periodic and non-periodic solutions by using an algorithm based on a modified Gram-Schmidt orthonormalization. A detailed explanation of this algorithm can be found in [69] (pp. 78-81).

### 2.2.9 Bifurcation diagrams

DDEs generally admit multiple solutions for fixed values of the parameters. The solution obtained numerically depends on the initial condition and the specific values of the parameters. Furthermore, for each dynamical variable $x_i$, DDEs with multiple parameters $\alpha_j$ exhibit multidimensional bifurcation diagrams, which are typically plotted separately as functions $x_i(\alpha_j)$ or on 3D plots $x_i(\alpha_j, \alpha_{k\ k \neq j})$. For this reason, before starting the numerical integration of a DDE, it is convenient to obtain its fixed points and to perform the linear stability analysis of the fixed points to determine the bifurcation points.

Once this is done, bifurcation diagrams can be obtained from the continuous dynamical system, as in the examples shown above in this section, or from a map.

Examples of methods for construction of maps to draw bifurcation diagrams are given in Chapters 5 and 6. When the dynamical system cannot be solved analytically, the numerical integration of the DDE is useful to draw stable branches leaving from bifurcation points.

### 2.2.10 Continuation techniques

For the numerical integration of DDEs, the initial condition must be selected depending on the analytical results and the branch of solutions that is going to be investigated. For instance, in order to continue a bifurcation diagram from a fixed point $x = x_0$, it is convenient to start with this initial condition for a set of parameter values for which the solution $x = x_0$ is stable, and to follow the solution $x = x_0$ while changing the values of the parameters. In contrast, when dealing with the continuation of a specific branch of periodic orbits coexisting with other branches of solutions, the convergence to the desired solution can be achieved starting with parameter values for which the desired solution is stable and with an initial condition being an approximation to the desired periodic solution, and modifying slowly the parameters.

Sophisticated tools such as DDE-BIFTOOL [74, 75, 76, 77] have been developed for the continuation of unstable periodic solutions. In Part II of this thesis, DDE-BIFTOOL will be used to obtain unstable branches of periodic solutions.

## 2.3 Numerical integration of DDEs

We now introduce some algorithms used in this thesis to integrate DDEs. For simplicity, we consider a one-dimensional dynamical system with one delay, $\tau$,

$$x(t) = f(x(t), x(t-\tau)), \tag{2.27}$$

$$x(t) = f^0(t), \quad t \quad [-\tau, 0], \tag{2.28}$$

where the initial condition is defined as a function of time. The case of multiple delays is discussed in the subsection 2.3.4.

### 2.3.1 Discretization of the time

Numerical integration of a DDE system requires the discretization of the time in small intervals of size $h$, which is a submultiple of $\tau$, namely

$$h = \frac{\tau}{M}, \tag{2.29}$$

where $M$ is an integer. For explicit integration methods, the integration step size $h$ must be smaller than the shorter time scale of the system. We typically take $h$ about 10 times

smaller than the fastest time scale of the system and we check that the result practically does not depend on $h$.

DDEs with very different timescales, as for instance the DDEs for mutually coupled optoelectronic systems that are derived and studied later in this thesis, for which the fastest time scale is of the order of picoseconds whereas the slowest time scale is of the order of microseconds, are examples of stiff problems. The accurate determination of the long time behavior of such systems requires many integration steps.

The discretization of the time results in the transformation of the continuous dynamical system (flow) into a map. Considering Eq. (2.29) and $x(t) = x_i$, it follows that $x(t-\tau) = x_{i\ \ M}$. The simplest map corresponding to the flow (2.31) is given by the Euler method,

$$x_{i+1} = x_i + hf(x_i, x_{i\ \ M}), \tag{2.30}$$

$$x_i = f_i^0, \quad i = -M, 0. \tag{2.31}$$

The Euler method is of first order, which means that the local error (per step) is of order $h^2$ and the global error (after a large number of time steps) is of order $h$.

### 2.3.2 Predictor-corrector algorithm

To find approximate numerical solutions of DDEs, in this thesis we generally use a fourth-order predictor-corrector [69] algorithm, which needs the derivatives at three previous times[3]. The predictor is the four-step Adams-Bashforth method,

$$\begin{aligned} x_{i+1}^P = x_i + \frac{h}{24}[&55f(x_i, x_{i\ \ M}) - 59f(x_{i\ \ 1}, x_{i\ \ M\ \ 1}) \\ &+37f(x_{i\ \ 2}, x_{i\ \ M\ \ 2}) - 9f(x_{i\ \ 3}, x_{i\ \ M\ \ 3})], \end{aligned} \tag{2.32}$$

whereas the corrector is the three-step Adams-Moulton,

$$\begin{aligned} x_{i+1} = x_i + \frac{h}{24}[&9f(x_{i+1}^P, x_{i\ \ M+1}) + 19f(x_i, x_{i\ \ M}) \\ &-5f(x_{i\ \ 1}, x_{i\ \ M\ \ 1}) + f(x_{i\ \ 2}, x_{i\ \ M\ \ 2})]. \end{aligned} \tag{2.33}$$

The reason of choice of a predictor-corrector algorithm for numerical integration of DDEs instead of a fourth-order Runge-Kutta algorithm, which is commonly used for numerical integration of ODEs, is that the predictor-corrector does not need interpolation and, as a result, all the points required to predict the evolution of the variable $x$ at time $t+h$ are real points computed from the integration of the system. Furthermore, at each time step only two evaluations of the function $f$ are required, $f(x_i, x_{i\ \ M})$ and $f(x_{i+1}^P, x_{i\ \ M+1})$; the other values of $f$ can be reused by updating the derivatives at each step,

$$f(x_i, x_{i\ \ M}) \quad f(x_{i\ \ 1}, x_{i\ \ M\ \ 1}), \tag{2.34}$$

$$f(x_{i\ \ 1}, x_{i\ \ M\ \ 1}) \quad f(x_{i\ \ 2}, x_{i\ \ M\ \ 2}), \tag{2.35}$$

$$f(x_{i\ \ 2}, x_{i\ \ M\ \ 2}) \quad f(x_{i\ \ 3}, x_{i\ \ M\ \ 3}). \tag{2.36}$$

[3]The predictor-corrector algorithm is not suitable for methods requiring adaptative time steps. For instance, it is not appropriate for implementing the Hénon s trick, in which the integration scheme is changed, as well as when applying any other method in which the integration step size changes.

To initiate the predictor-corrector algorithm, the first previous derivatives [$f(x_{i\ 1}, x_{i\ M\ 1})$, $f(x_{i\ 2}, x_{i\ M\ 2})$ and $f(x_{i\ 3}, x_{i\ M\ 3})$] can be obtained from the integration of the equations with the Euler method. Since the Euler method is of first order while the predictor-corrector is of fourth order, the initialization with the Euler method requires a smaller integration step. In this thesis, each of the three first derivatives is obtained from integration with the Euler method for 10 steps with a step size $h/10$,

$$x_{i+(k+1)\ 10} = x_{i+k\ 10} + \frac{h}{10} f(x_{i+k\ 10}, x_{i\ M}), \tag{2.37}$$

for $k$ $[0, 9]$ and $i$ $[1, 3]$.

### 2.3.3 Data storage schemes for DDEs

To integrate numerically a DDE, we need to store in an array the values of the dynamical variable at the $M$ previous time steps. In this subsection, we describe some procedures that have been used through this thesis to store the data. Here, for simplicity, we consider the integration of a DDE such as (2.31), with a single scalar variable $x$ and one delay $\tau$, using the predictor-corrector method. The case of multiple delays will be discussed in the subsection 2.3.4.

We will use an array `xr=(xr(1),....x(R))`, with $R$ $M$, to store the delayed values of the variable, and an index, `i`, for the integration time step. We will assume that the first $M$ elements of `xr` are initialized to the historical values of $x$ over one delay time, namely, `xr(1)`$= x(t_0 - \tau)$, `xr(2)`$= x(t_0 - \tau + h)$, ... , `xr(M)`$= x(t_0 - h)$, being $t_0$ the initial time. We will also use the scalar `x` to store the value of the dynamical variable $x(t)$ at each time step (which will be updated at the end of the time step), the scalar `xp` to store the value given by the predictor, and three scalars [`f1`, `f2` and `f3`] to store the value of the derivative at the three previous time steps. The scalars `f1`, `f2` and `f3` are updated at the end of each time step, and we will assume that these values have been initially obtained as described before so that the predictor-corrector can readily start.

The explanation of each method includes selected pieces of FORTRAN code as well as an illustrative diagram. In the code, we assume that the subroutine `derivada` evaluates the right hand side of (2.31) by using the scalar `alpha`, the values of the variable at the time step and at the delayed time, and returns the scalar `f` with the value of the derivative. In the diagram, the elements of the vector `xr` that at time step `i` are already filled are plotted in a box which is filled in green. The elements that are used at a given step to compute the evolution are plotted with a green border, and the elements that are being updated or computed for first time are plotted with a red border.

#### i) Continuous updating with a double loop structure

This method assumes we want to integrate the system for a total time which is $N$ times the delay time. The method uses an array `xr`, which has the minimum length, $R = M$, and will be updated at each time step. The updating takes place through an inner loop where the whole vector `xr` is updated in $M$ time steps. This is repeated $N$ times by using an outer loop.

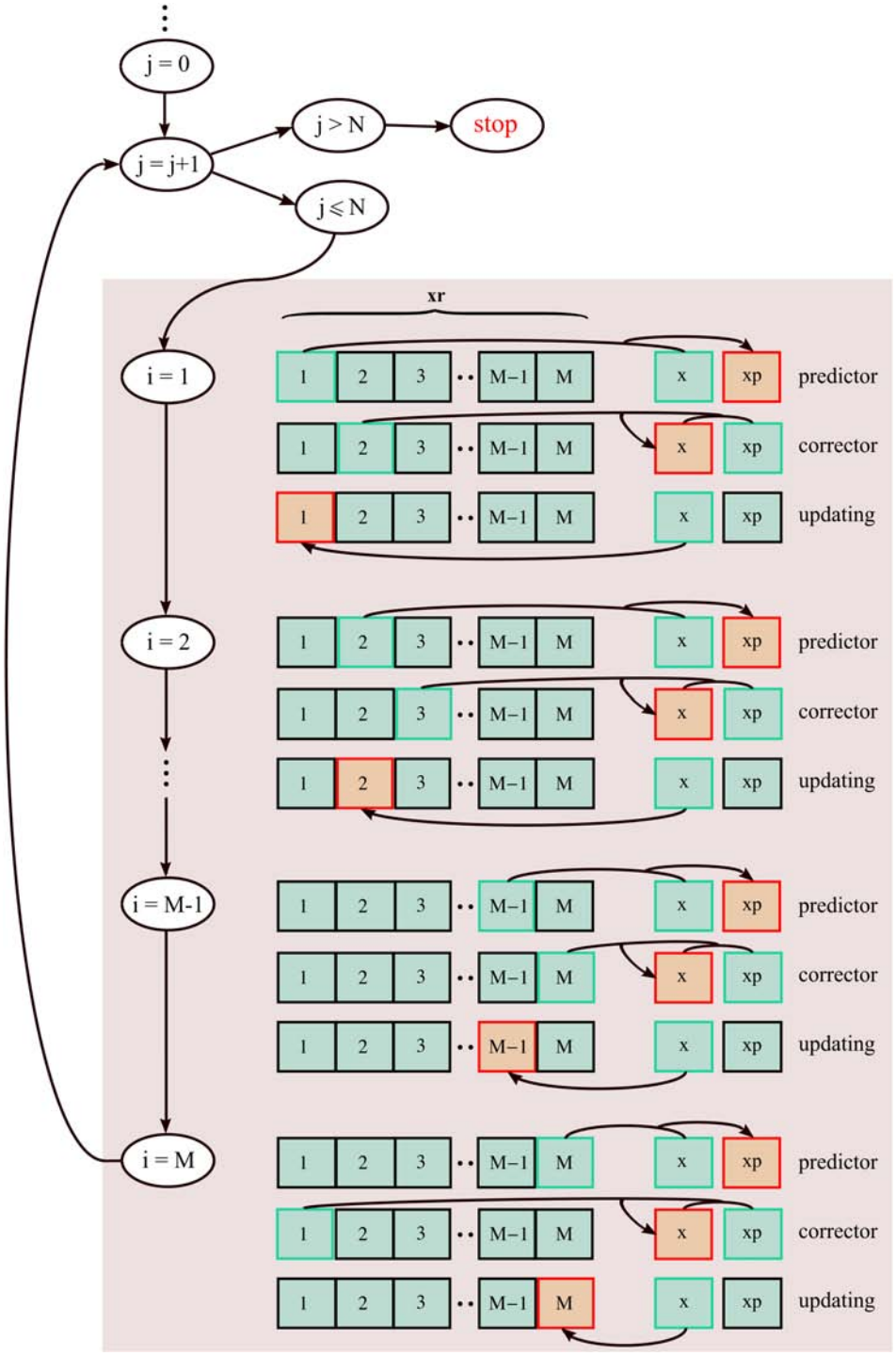


**Figure 2.9:** Double-loop predictor-corrector algorithm for integration of a DDE with a single variable, a single delay, and a single parameter, with an array of minimum dimension, $M = \tau/h$.

The method can be implemented as illustrated in Fig. 2.9 and indicated in the following FORTRAN code.

```
N=NINT(tf/delay) !'N' is the number of delays during time 'tf'
M=NINT(delay/h) ! 'M' is the number of steps of duration 'h' in a single delay
ALLOCATE (xr(M)) ! Dimension of xr: M
! ... Initialization
DO j=0,ndelay-1  !Repetition of the internal loop 'ndelays' times
   DO i=1,M !Integration during a single delay
      ! Predictor
      CALL derivada (alpha, x, xr(i), f)
      xp=x+p1*f-p2*f1+p3*f2-p4*f3
      ! Corrector
      co=i+1
      IF (co.GT.M) co=1
      CALL derivada (alpha, xp, xr(co), fn)
      x=x+p4*fn+p5*f-p6*f1+paux*f2
      xr(i)=x ! Updating of xr
      f3=f2 ! Update the derivatives with the most recent values
      f2=f1
      f1=f
   ENDDO
ENDDO
```

At step `i`, the predictor uses `x` and `xr(i)`, as well as `f1`, `f2` and `f3`, to evaluate the intermediate value `xp`. Similarly, the corrector uses `xp`, `x` and `xr(i+1)` to obtain the value at the next step, except when `i=M`, where `xp`, `x` and `xr(1)` are used. The corrector updates `x` with the new value of the variable $x$. The delay array `xr` is also updated by storing the new value at `xr(i)`. Finally, the derivatives `f1`, `f2` and `f3` are updated.

### ii) Continuous updating with a single loop structure

The previous method can be modified to allow for an arbitrary number of time steps or to integrate until a given condition is reached. This is illustrated in Fig. 2.10 and in the following FORTRAN code, in which the integration is iterated until the variable $x$ crosses the Poincaré section $s = 0$ going from a negative to a positive value.

```
M=NINT(delay/h) ! Discretization of the delay in steps of length h
ALLOCATE(xr(M)) ! Allocation of memory for array xr
! ... Initialization
s=1.D0
i=1
DO WHILE (s.GT.0.D0) ! Repeat until s is 0 or negative
   ! Predictor:
   CALL derivada (alpha, x, xr(i), f)
   xp=x+p1*f-p2*f1+p3*f2-p4*f3
   ! Corrector:
   co=i+1
   IF (co.GT.M) co=1
   CALL derivada (alpha, xp, xr(co), fn)
   xc=x+p4*fn+p5*f-p6*f1+paux*f2
   IF ((x.LT.0.D0).AND.(xc.GT.0.D0)) s=0.D0
   x=xc  ! Update x and xr
   xr(i)=xc
   f3=f2 ! Update the derivatives with the most recent values
   f2=f1
   f1=f
   IF (i.EQ.M) THEN ! Update i
      i=1
   ELSE
      i=i+1
   ENDIF
ENDDO
```

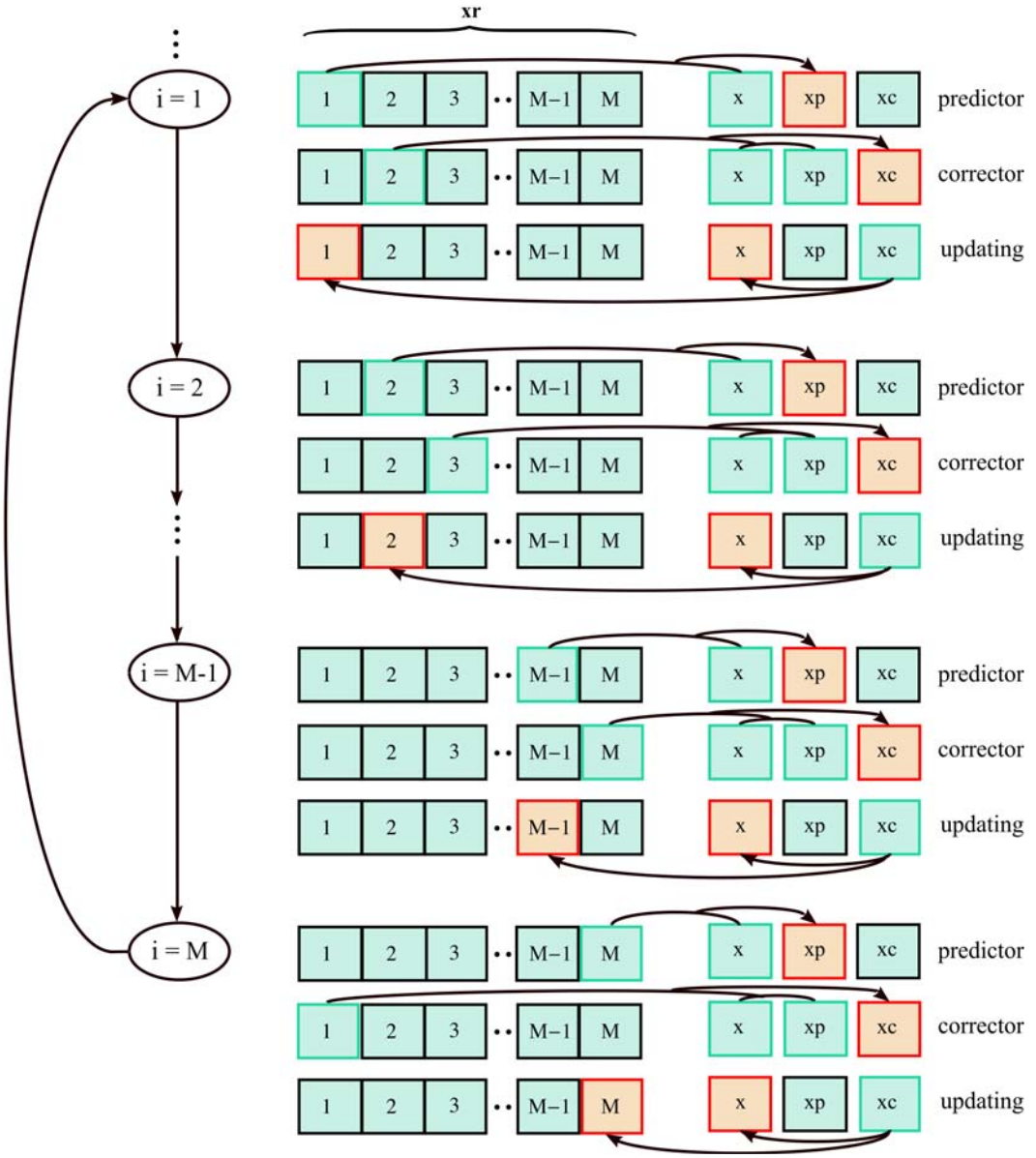


**Figure 2.10:** Single-loop predictor-corrector algorithm for integration of a DDE with a single variable, a single delay, and a single parameter, with an array of minimum dimension $R = M$.

The counter `i` is increased by 1 at each integration time step until it reaches $M$, in which case is reset to 1. This conditional allows to get rid of the inner loop that was present in the procedure i).

### iii) Block updating with a double loop structure

In the two previous methods, the delay array `xr` is updated continuously, one element at each time step. This allows one the use of an array `xr` with the minimal length. We now consider the use of an array `xr` with a much larger length, $R \quad M$. This allows one to integrate over a large number of time steps before updating is required. Once `xr` is filled, we perform a block updating by copying the last part of `xr` at the beginning of the array. An outer loop is used to repeat this procedure as many times as required. This is illustrated in Fig. 2.11 and in the following FORTRAN code.

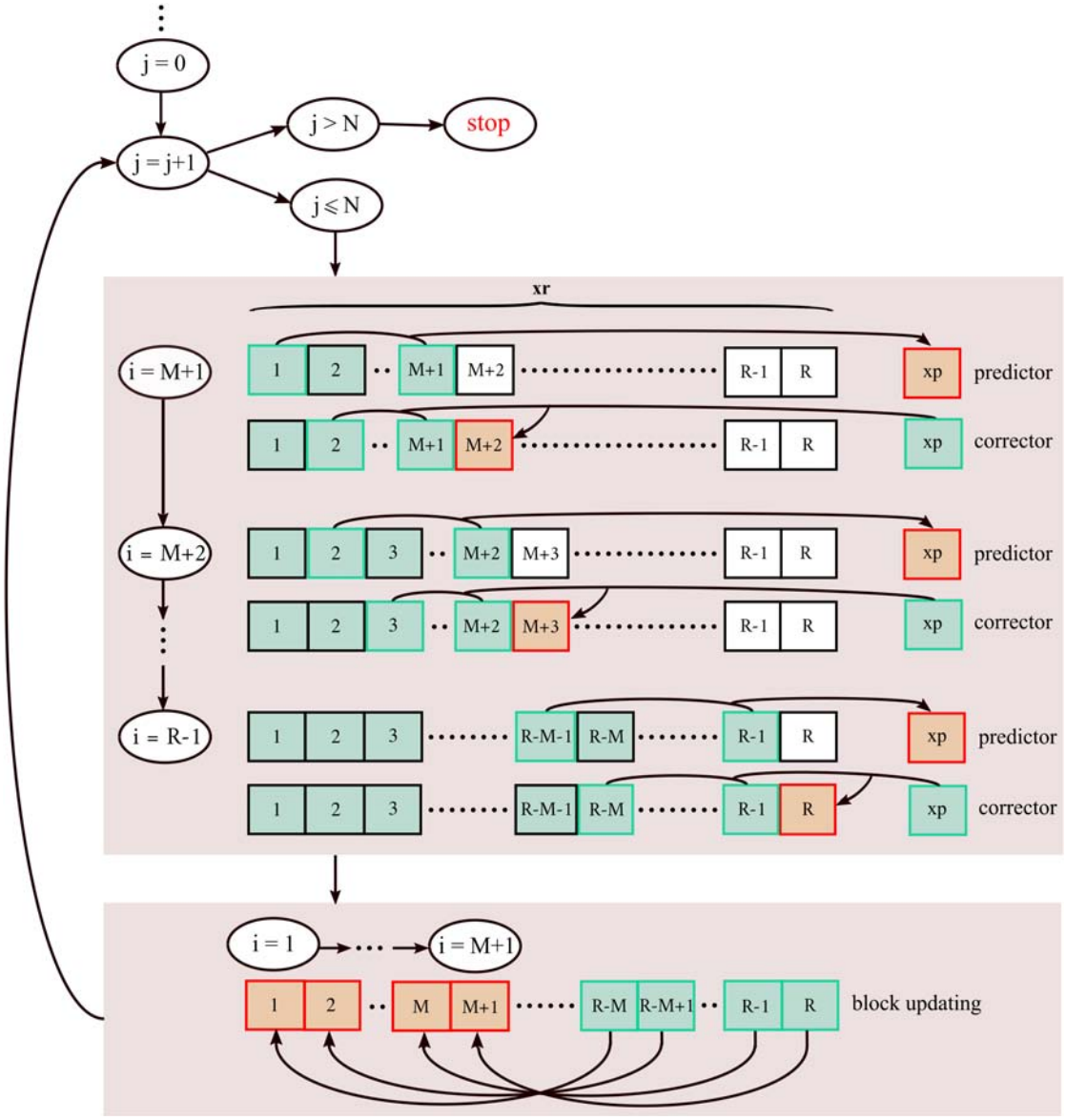


**Figure 2.11:** Multiple-loop predictor-corrector algorithm for integration of a DDE with a single variable, a single delay, and a single parameter, with an array of dimension $R \quad M$.

```
M=NINT(delay/h) ! 'M' is the number of steps of duration 'h' in a single delay
N=NINT(tf/((R-M-1)*h)) ! 'N' is the total number of integration steps of duration 'h'
ALLOCATE (xr(R)) ! Allocation of the array xr with dimension R
! ... Initialization
DO j=1,N
   DO i=M+1,R-1 ! Predictor-corrector algorithm
      ! Predictor:
      CALL derivada (alpha, xr(i), xr(i-M), f)
      xp=xr(i)+p1*f-p2*f1+p3*f2-p4*f3
      ! Corrector:
      CALL derivada(alpha, xp, xr(i+1-M), fn)
      xr(i+1)=xr(i)+p4*fn+p5*f-p6*f1+paux*f2
      f3=f2 ! Update the derivatives
      f2=f1
      f1=f
   ENDDO
   DO i=1,M+1  ! Update in block
      xr(i)=xr(R-M-1+i)
   ENDDO
ENDDO
```

Now, we do not use the scalar `x` to keep the last value of $x(t)$. Instead, historical and present values are all stored in `xr`. We assume that the first $M$ elements of `xr` are initialized as before and that the element `xr(M+1)` contains initially the value of $x(t_0)$.

Within the first inner loop, at each time step `i` ($M+1 \quad i \quad R-M-1$) the predictor uses `xr(i)` and `xr(i-M)` to evaluate the intermediate value `xp`. The corrector uses `xp`, `xr(i)` and `xr(i-M+1)` to obtain the value at the next time step, which is stored in `xr(i+1)`. Finally, as in previous methods, the derivatives `f1`, `f2` and `f3` are updated.

The first inner loop evaluates $R-M-1$ time steps and fills the array `xr`. Then, a second inner loop performs a block updating in which the last $M+1$ elements of `xr` are copied into the first $M+1$ elements. This double inner loop procedure is repeated $N$ times using an outer loop.

With this procedure, the DDE can be easily integrated over any time interval which is a multiple of $(R-M-1)h$. Since $R$ can be chosen arbitrarily (provided it is larger than $M-1$), the total integration time does not need to be a multiple of the delay time. We note that, in order to avoid frequent block updatings, it is convenient to take $R$ so that $R-M-1$ is much larger than $M$.

### iv) Block updating with a single loop structure

Method iii) can be modified to allow for an arbitrary number of time steps or to integrate until a given condition is reached, in a similar way we modified method i) to obtain ii). The new method is illustrated in Fig. 2.12 and in the following FORTRAN code, where integration is performed during `ns` time steps.

```
M=NINT(delay/h) ! Discretization of the time in steps of length h
R=M*3.D0 ! Dimension of the array xr
ALLOCATE(xr(R)) ! Allocation of memory for array xr
! ... Initialization
i=M+1 ! Index of the array xr after initialization with the Euler method
DO steps=1,ns ! Integration during ns steps.
   ! Predictor
   CALL derivada (alpha, xr(i), xr(i-M), f) ! Call to the subroutine "derivada"
   xp=xr(i)+p1*f-p2*f1+p3*f2-p4*f3  ! Value of x predicted by the predictor
   ! Corrector
   CALL derivada (alpha, xp, xr(i+1-M), fn) ! Call to the subroutine "derivada"
   xr(i+1)=xr(i)+p4*fn+p5*f-p6*f1+paux*f2 !
   f3=f2 ! Update the derivatives
   f2=f1
   f1=f
   IF (i.eq.R-1) THEN ! When i+1 it reaches the limit value i=R ...
      DO j=1,M+1 ! Update in block the first M+1 elements of the array xr
         xr(j)=xr(R-(M+1)+j)
      ENDDO
      i=M+1 ! Restore i
   ELSE
      i=i+1 ! Update i
   ENDIF
ENDDO
```

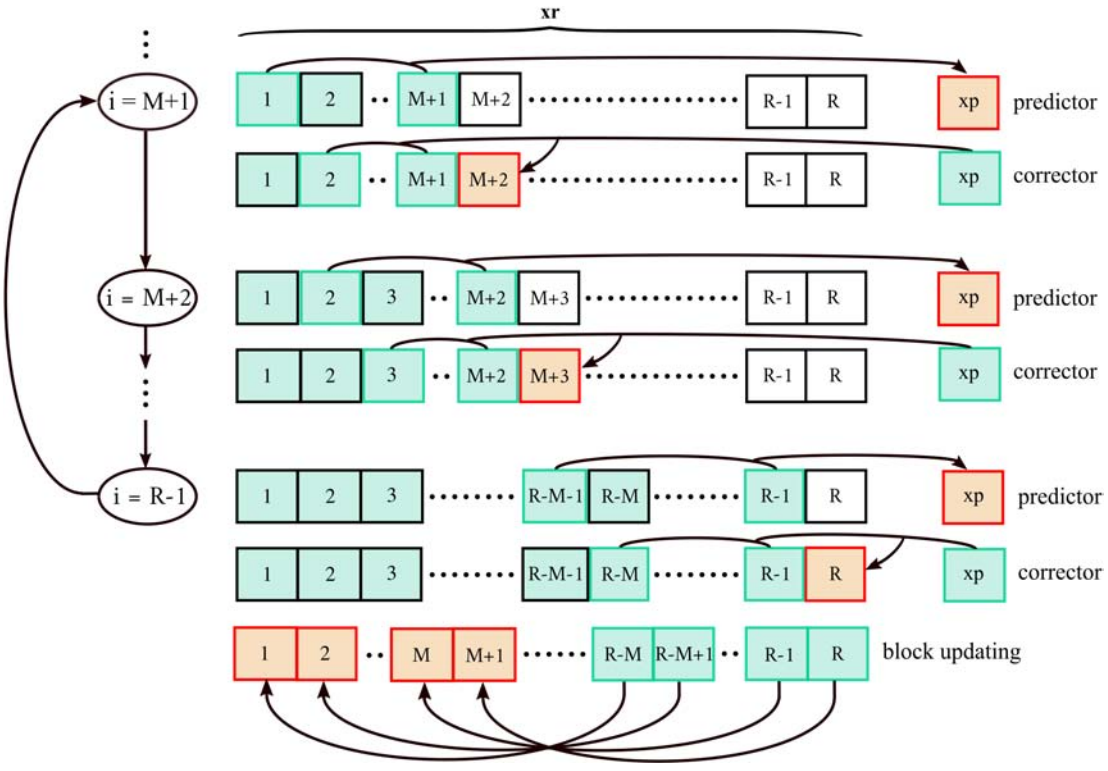


**Figure 2.12:** Single-loop predictor-corrector algorithm for integration of a DDE with a single variable, a single delay, and a single parameter, with an array of dimension $R$.

The counter `i` is increased by 1 at each time step until it reaches $R-1$, in which case is reset to 1 and a block updating is performed. The conditional allows to get rid of the first inner loop of procedure iii).

### 2.3.4 Multiple delays

In case of multiple delays, $h$ should be a submultiple of all of them, namely

$$h = \frac{\tau_1}{M_1} = ... = \frac{\tau_n}{M_n}, \tag{2.38}$$

being $M_i$ integers and $n$ the number of delays.

Consider a scalar DDE so that the delayed values of the variable can be stored in an array `xr=(xr(1),....x(R))`. Then, we have to take $R$ has to be at least as large as the largest $M_i$, in order to store all the past values needed to compute the evolution. The previous procedures can be readily adapted by considering that now $M$ should be taken as the largest $M_i$ and the subroutine `derivada` depends on several delayed values which have to be passed to it.

We illustrate the modifications of method iii) for a scalar DDE that depends on a parameter $\alpha$ and has two time delays, $\tau_1$ and $\tau_2$:

```
M_1=NINT(delay1/h) !Number of time steps associated to delay 1
M_2=NINT(delay2/h) !Number of time steps associated to delay 2
M=MAX (M_1,M_2)
ALLOCATE (xr(R)) ! Allocate the array xr with dimension R
DO j=1,N
   DO i=M+1,R-M-1
     ! Predictor
     call derivada (alpha, xr(i), xr(i-M1),xr(i-M2), f)
      xp= xr(i) + p1*f-p2*f1+p3*f2-p4*f3
      ! Corrector
      call derivada (alpha,xp, xr(i+1-M1),xr(i+1-M2),fn)
      xr(i+1)=xr(i)+p4*fn+p5*f+p6*f1+paux*f2
      f3=f2  ! Update the derivatives
      f2=f1
      f1=f
   ENDDO
   DO i=1,M+1
      xr(i)=xr(R-M-1+i)
   ENDDO
ENDDO
```

We also illustrate the modifications of method ii):

```
M_1=delay1/h ! Discretization of delay1
M_2=delay2/h ! Discretization of delay2
M=MAX(M_1,M_2)
ALLOCATE(xr(M)) ! Dimension of xr: M
! ... Initialization
i=1
DO steps =1,ns ! Repeat during ns steps
   pr1=i+M-M_1
   pr2=i+M-M_2
   co1=pr1+1
   co2=pr2+1
   IF (pr1.gt.M) pr1=pr1-M
   IF (pr2.gt.M) pr2=pr2-M
   IF (co1.gt.M) co1=pr1-M
   IF (co2.gt.M) co2=pr2-M
   ! Predictor:
   CALL derivada (alpha, x, xr(pr1), xr(pr2), f)
   xp=x+p1*f-p2*fx1+p3*f2-p4*f3
   ! Corrector:
   CALL derivada (alpha, xp, xr(co1), xr(co2), fn)
```

```
   x=x+p4*fn+p5*f-p6*f1+paux*f2
   xr(i)=x  ! Update the position i of xr
   IF (j.EQ.M) THEN  !  Update i
      i=1
   ELSE
      i=i+1
   ENDIF
   f3=f2  ! Update the derivatives
   f2=f1
   f1=f
ENDDO
```

The first inner loop could be slightly simplified if one knows beforehand which is the largest delay. For instance, if `M_1` is always the largest delay, then the index `pr1` is always identical to `i` and the lines `pr1=i+M-M_1` and `IF(pr1.gt.M) pr1=pr1-M` are not needed. Nevertheless, the evaluation of the indexes `pr2`, `co1` and `co2` is required to access the delayed elements.

### 2.3.5 Transient dynamics

The number of steps $h$ that a numerical integration algorithm takes from a given initial condition to reach a stationary solution can be large, specially if the system has stiff time scales and thus $h$ is very small compared to the largest time scale of the system. The study of the transient dynamics is interesting in some applications, for instance in reservoir computing. In this thesis, we are mainly interested in stationary dynamical regimes, therefore we ensure that the transient has already elapsed, namely that the essential properties of the dynamics do not change with time.

When dealing with steady states or periodic solutions, to test when the transient has elapsed can be done with the Poincaré Section technique, as it is explained in the subsection 2.2.5. For chaotic solutions, one could check that the statistical properties of the trajectory do not change by integrating over a longer period.

Chapter 3

# Photonic systems with delayed feedback

## 3.1 Introduction

This thesis deals with two different photonic systems with delayed feedback associated to multiple delays. Part II focuses on delay-coupled optoelectronic oscillators, whereas Part III is dedicated to semiconductor laser systems with filtered optical feedback. The main purpose of this chapter is to describe the dynamics of simpler systems with a single delay in which the systems studied in this thesis are based. To this aim, in Sec. 3.2 we focus on the nonlinear dynamics of a single system with a Mach-Zhender Interferometer (MZI) with optoelectronic delayed feedback, referred to as an optoelectronic oscillator; and in Sec. 3.3 we describe the dynamics of a semiconductor laser system with a single optical delayed feedback loop. In doing so, we introduce the fundamental physical principles and modeling equations, describe the different dynamical regimes that can be obtained, and briefly review some experiments and applications.

## 3.2 Nonlinear dynamics of an optoelectronic oscillator

An optoelectronic oscillator (OEO) exhibits nonlinear dynamics, typically due to the presence of a modulator with electro-optical feedback and exhibiting the electro-optic effect, which consists of a change of the refractive index by means of an applied electric field. In order to understand the fundamental physical principle responsible for the nonlinearity induced by such a modulator, in the next subsections we introduce the field of nonlinear optics, the electro-optic effect and its application to build optical modulators or switches.

### 3.2.1 Introduction to nonlinear optics

Nonlinear optics is the field that deals with phenomena that result from the modification of the optical properties of a material system by the presence of light. The term nonlinear refers to the fact that the response of a material system to an incident optical field depends in a nonlinear manner upon the strength of the optical field [78].

The interaction between light and matter in the presence of an electric field $E$ was succesfully described for many years assuming a linear response of the material to an applied electric field,

$$\mathbf{P} = \varepsilon_0 \ ^{(1)}\mathbf{E}, \tag{3.1}$$

where $\mathbf{P}$ is the polarization density of the medium (i.e. the dipole moment per unit volume), $^{(1)}$ is the linear electric susceptibility of the medium, and $\varepsilon_0$ is the permittivity of free space.

Equation (3.1) represented a good approximation for so long because the strength of the fields that researchers were able to achieve was small enough compared to that of the fields inside the atoms and molecules, which is typically $10^5 - 10^8$ V/m. When the intensity of the applied field reaches non negligible values compared to that of the interatomic fields, the relation between $\mathbf{P}$ and $\mathbf{E}$ becomes nonlinear. The polarization can be expanded as a Taylor series in $E$,

$$\mathbf{P} = \ _0( \ ^{(1)}\mathbf{E} + \ ^{(2)}\mathbf{E}^2 + \ ^{(3)}\mathbf{E}^3 ...). \tag{3.2}$$

For an anisotropic medium, each component of the polarization $\mathbf{P} = (P_1, P_2, P_3)$ is in general a function of the three components of the electric field $\mathbf{E} = (E_1, E_2, E_3)$, in such a way that the first, second, and third-order susceptibilities are tensors of second, third and fourth order, respectively [78].

The first nonlinear optical effect was observed in 1877 by John Kerr at the Free Church Training College in Glasgow. Kerr showed that certain solids and liquids under a strong DC field exhibit a small change in the refractive index [79, 80]. In 1893, Friedrich Pockels at the University of Göttingen discovered the so called Pockels effect in certain crystals. The field of nonlinear optics underwent a second birth with the discovery of the second harmonic generation (SHG) by Franken et al. in 1961 [81], shortly after the invention of the first working laser by Maiman in 1960 [82]. Whereas SHG is a purely optical nonlinear effect, the Kerr and the Pockels effects are electro-optic effects in the sense that they take place in the presence of an external electric field and an optical field.

### 3.2.2 Electro-optic e ects

Electro-optic effects consist of variations in the refractive index of a material induced by the presence of an external steady or low-frequency electric field $E$, which distorts the positions, orientations or shapes of the molecules, giving rise to a modulation of the optical properties of the material. Such an electric external field can be for instance applied through two electrodes placed on opposite facets of the crystal and connected to a battery. The frequency of the applied electric field has to be small compared to the

time scale associated to the response of the medium, as well as to the time required for light to cross the material, in such a way that the field can be considered static [78].

We consider the refractive index of an electro-optic medium to be a function $n(E)$ of an applied steady or slowly varying electric field. Since the function $n(E)$ changes only slightly with $E$, it can be expanded as a Taylor series in $E$:

$$n(E) = n_0 + a_1 E + \frac{1}{2} a_2 E^2 + ... \tag{3.3}$$

The second- and third-order terms are typically many orders of magnitude smaller than $n_0$. Higher-order terms are generally very small and thus can be neglected. The change in the refractive index due to the first-order term with $a_1 \neq 0$, linear with the external electric field,

$$\Delta n(E) = a_1 E, \tag{3.4}$$

is called the Pockels effect. The variation in the refractive index due to the second-order term with $a_2 \neq 0$, quadratic with the electric field,

$$\Delta n(E) = a_2 E^2, \tag{3.5}$$

is known as the Kerr effect. It is convenient to write (3.3) in terms of the electro-optic coefficients $r = -2a_1/n_0^3$ and $s = -2a_2/n_0^3$,

$$n(E) = n_0 - \frac{1}{2} r n_0^3 E - \frac{1}{2} s n_0^3 E^2 + ... \tag{3.6}$$

Changes in the refractive index induced by electric fields under Kerr or Pockels effects are very small. Nevertheless, after propagating a sufficiently large distance, a small change in the refractive index can induce a significant modification in the phase of an optical field [78].

### The Pockels e ect

For many materials, the first-order correction to the refraction index is many orders of magnitude higher than the other terms, and thus the refractive index can be approximated by (3.4). Then, the refractive index can be approximated by

$$n(E) = n_0 - \frac{1}{2} r n_0^3 E, \tag{3.7}$$

where $r$ is the Pockels coefficient.

Changes in the refractive index induced by electric fields under the Pockels effect are indeed very small. For instance, for $E = 10^6$ V/m (10 kV applied across a cell of thicknes 1 cm), $\Delta n$ $[10^{-6} - 10^{-4}]$ [83].

The linear electro-optic effect only takes place in non-centrosymmetric crystals such as GaAs or $LiNbO_3$. According to (3.4), if the change in $n$ increases with $E$, it must decrease with $-E$. Only structures with some asymmetry can respond differently to $E$ and $-E$ and thus exhibit the Pockels effect. In non-crystalline materials such as glasses and

liquids, the Pockels coefficient is zero because all the directions have the same dielectric properties and thus the change in the refractive index is the same for $E$ than for $-E$. Similarly, for a crystal with a center of symmetry such as NaCl, the properties of the medium are the same under the transformation $\mathbf{r} \quad -\mathbf{r}$ and thus $a_1 = 0$.

The Pockels effect is a second-order nonlinear optical process. This can be seen considering a nonlinear polarization being quadratic with the electric field,

$$P_{NL} = \ _0 \ ^{(2)} E^2, \tag{3.8}$$

and the electric field $E$ to be composed of an harmonic component at an optical frequency $\omega$, $E(\omega)$, and a steady component (at $\omega = 0$), $E(0)$,

$$E(t) = E(0) + Re \ \ E(\omega) \exp(i\omega t) \ . \tag{3.9}$$

Introducing (3.9) into (3.8), we obtain three components of the polarization at the frequencies 0, $\omega$ and $2\omega$. If the amplitude of the optical field is much smaller than $E(0)$, the second-harmonic polarization, $P_{NL}(2\omega)$, can be neglected compared to the other components, $P_{NL}(0)$ and $P_{NL}(\omega)$. $P_{NL}(\omega)$ is responsible for the Pockels effect and is given by

$$P_{NL}(\omega) = 2 \ _0 \ ^{(2)} E(0)E(\omega) = \ _0\Delta \ \ E(\omega), \tag{3.10}$$

where $\Delta \ = \ ^{(2)} E(0)$ represents the change in the susceptibility proportional to $E(0)$. The corresponding change in the refractive index can be obtained by differentiating the expression $n^2 = 1 + \ $, which gives rise to $2n\Delta n = \Delta \ $. Then, we obtain

$$\Delta n = \frac{^{(2)}}{n} E(0) \tag{3.11}$$

Comparing (3.11) with the change in refractive index given by (3.7), $\Delta n = -\frac{1}{2} r n^3 E(0)$, we conclude that the Pockels coefficient $r$ is related to the second-order nonlinear susceptibility $^{(2)}$ [78].

The Pockels effect given by (3.4) is an oversimplification. In fact, the Pockels coefficient is an element of a tensor and the Pockels effect depends on the polarization and the direction of light, the direction of the applied field and the crystal structure. As an example, we consider light crossing a $LiNbO_3$ crystal in the $z$-direction, and an electric field $E$ applied in the direction parallel to a principal $y$-axes of the crystal. Without the external field $E$, the refractive index in the $x$- and $y$-directions are both equal to the ordinary refractive index $n_0$. The applied field induces a birefringence in the crystal, so that the crystal exhibits two refractive indices,

$$n_1(E) \quad n_0 + \frac{1}{2} r_{22} n_0^3 E, \tag{3.12}$$

$$n_2(E) \quad n_0 - \frac{1}{2} r_{22} n_0^3 E, \tag{3.13}$$

where $r_{22}$ is the element of the Pockels tensor that represents the optical response of the crystal to an applied electric field along a given direction with respect to the principal axes [84].

### The Kerr e ect

The quadratic electro-optic effect or Kerr effect can only be appreciated in centrosymmetric materials such as gases, liquids, and certain crystals, for which the refractive index is an even symmetric funcion of the electric field, invariant to the symmetry $E \quad -E$, and thus the linear coefficient $a_1$ is zero and the first non-zero correction to the refractive index is of second order [84],

$$n(E) = n_0 - \frac{1}{2} s n_0^3 E^2, \tag{3.14}$$

where $s = -a_2/n_0^3$ is the Kerr coefficient.

Changes in the refractive index induced by electric fields under the Kerr effect are small in crystals, and very small in liquids. For instance, for $E = 10^6$ V/m (10 kV applied across a cell of thicknes 1 cm), $\frac{1}{2} s n^3 E^2$ is in the range $[10^{-6} - 10^{-2}]$ in crystals and $[10^{-10} - 10^{-7}]$ in liquids [78].

The Kerr effect is a third-order nonlinear process. In a similar way than for the Pockels effect, considering a monochromatic optical field $E(\omega)$ incident on a medium under the presence of a steady electric field $E(0)$, with $E(\omega)^2 \quad E(0)^2$, it can be shown that the Kerr coefficient is related to the third-order nonlinear susceptibility $^{(3)}$ [78].

We note that (3.14) is an oversimplification of the Kerr effect. In a similar way than for the Pockels effect, $s$ is a tensor and the Kerr effect depends on the crystal structure and the direction of the applied field.

### 3.2.3 Electro-optic modulators

Nonlinear crystals exhibiting the Pockels effect are used as a substrate to produce electrically driven optical devices in many applications such as optical communications or optical signal processing. Electro-optical modulators are made on a substrate of a ferroelectric material such as lithium niobate ($LiNbO_3$) or lithium tantalate ($LiTaO_3$).

$LiNbO_3$ is one of the most important electro-optic materials because it is highly optically transparent in the near infrared wavelengths used in telecommunications, birefringent, and has very low loss and large modulation bandwidth. Together with $LiTaO_3$, it belongs to a relatively modern class of electro-optic materials, which have larger electro-optic coefficients and smaller voltage requirements compared to relatively older electro-optic materials such as ammonium dihydrogen phospate ($NH_4H_2PO_4$), potassium dihydrogen phosphate ($KH_2PO_4$) and potassium didiuterium phosphate ($KD_2PO_4$) [83].

As regards the spectral range over which electro-optic materials are transmissive, most of the electro-optic materials can be used in the visible and near-infrared regions of the electromagnetic spectrum, but cadmium telluride (CdTe) can be used to construct $CO_2$ lasers in the long-wavelength infrared.

We consider a Pockels cell of length $L$ under an electric field $E$. Light crossing the cell experiences a phase shift

$$\phi = \frac{2\pi n(E) L}{\lambda_0}, \tag{3.15}$$

where $\lambda_0$ is the free-space wavelength. Introducing (3.7) in (3.15) and taking into account that an electric field $E = V/d$ is obtained by applying a voltage $V$ across two faces of the cell separated a distance $d$, the phase modulation can be written as

$$\phi = \phi_0 - \pi \frac{V}{V_\pi}, \tag{3.16}$$

where $\phi_0 = \frac{2\pi n_0 L}{\lambda_0}$ is the phase shift of the cell with $E = 0$, and

$$V_\pi = \frac{d\lambda_0}{2Lrn_0^3} \tag{3.17}$$

is the so called half-wave voltage, the voltage required to obtain a phase modulation of $\pi$. $V_\pi$ depends on the material properties, $n_0$ and $r$, the wavelength, and the dimensions $d$ and $L$.

Electro-optic modulators can be longitudinal or transversal. In longitudinal modulators the electric field is applied parallel to the direction of light propagation, whereas in transverse modulators the field is applied perpendicularly to the direction of light propagation.

Consider, for instance, a transverse phase modulator of length $L$ made of $LiNbO_3$. A field $E = V/d$ applied along the $y$ axis, perpendicularly to the direction $z$ of light propagation, induces birefringence in the crystal, in such a way that the components $E_x$ and $E_y$ experience different refractive index, $n_1$ and $n_2$, given by (3.12) and (3.13). The phase change between the two components $E_x$ and $E_y$ induced by the Pockels effect in this case is [84]

$$\phi = \frac{2\pi}{\lambda_0} n_0^3 r_{22} \frac{L}{d} V. \tag{3.18}$$

### The Mach-Zehnder interferometer

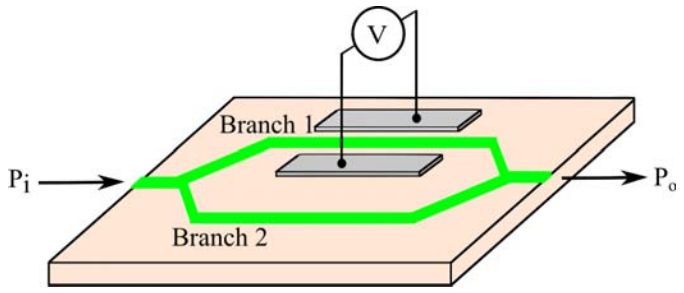


**Figure 3.1:** Mach-Zehnder Interferometer with transverse Pockels effect in one of the arms.

Electro-optic phase modulation can be converted into amplitude modulation by using an interferometer. Consider for instance the Mach-Zehnder interferometer (MZI) illustrated in Fig. 3.1, with electro-optic modulation in one of the arms. We assume that the system is illuminated with linearly polarized light and that there isn't any reflection in the optical path, in such a way that the electric field can be considered as a scalar. In the ideal

case in which the input optical field $E_i$ is divided in two equal parts, at the end of the interferometer, where the two beams are recombined, the electric field is

$$E_o = \frac{E_i}{2} \left( e^{i\ \phi_1} + e^{i\ \phi_2} \right) , \tag{3.19}$$

where $\phi_1$ and $\phi_2$ are the phase shifts of light across branches 1 and 2, repectively. Then, the output power, $P_o$, is related to the input intensity, $P_i$, by a nonlinear function of the phase difference $\phi = \phi_1 - \phi_2$ of light between the two branches,

$$P_o = P_i \cos^2 \left( \frac{\phi}{2} \right) . \tag{3.20}$$

Because only branch 1 is modulated, $\phi_2 = \phi_{2_0}$ is a constant phase shift. According to Eq. (3.17), we have $\phi_1 = \phi_{1_0} - \pi V/V_\pi$. Then, $\phi = \phi_0 - \pi V/V_\pi$, where $\phi_0 = \phi_{1_0} - \phi_{2_0}$ depends on the optical path difference between the two branches without modulation. Assuming the two branches to be identical, we have $\phi = -\pi V/V_\pi$.

The applied voltage usually has two components: a constant or DC (direct current) component which fixes the operating point of the device, and a variable or RF (radio-frequency component) $V(t)$, in such a way that the output power can be written as

$$P_o = P_i \cos^2 \left( \frac{\pi V(t)}{2V_{\pi_{RF}}} + \frac{\pi V_B}{2V_{\pi_{DC}}} \right) . \tag{3.21}$$

### 3.2.4 OEO architecture

The OEO is a photonic device able to generate a high speed and low noise oscillatory output, which is suitable for radio-frequency applications such as wireless communications, radar, signal processing, and sensing. The generation of low noise, high repetition rate microwave signals using photonic techniques was pioneered by Neyer and others [85, 86]. However, the invention of the OEO is attributed to Yao and Maleki for their introduction in 1996 of a long optical fiber to generate high spectral purity and low phase noise microwaves [87, 88].

A conventional OEO consists of a light source, a modulator, an optical cavity, a photodetector, and an electronic circuit in which the signal is filtered, amplified and fed back to the modulator to close the loop. The feedback loop generates self-sustained oscillations provided that the overall gain exceeds the loss, and the waves circulating in it end up in phase. Since the loop can support waves travelling once, twice, ... $n$ times, the oscillator is multimode. By adding a filter in the loop, only the modes supported by the bandwidth of the components can survive [88].

An OEO can be configured in a variety of ways by using different optical and electrical components. The light source can be of any suitable type, including a laser or a source of amplified spontaneous emission. Light modulation can be achieved either with a modulator or directly with the current of the laser. The optical cavity can be a long-delay fibre line, a Fabry-Pérot or a whispering gallery mode resonator. The frequency at which the OEO oscillates can either be controlled with a frequency selective element

placed in the electronic part of the loop or tuned in the optical part of the loop by changing the cavity's optical path length or the laser wavelength [88].

The first OEOs were based on a long fiber delay as storing energy element, and frequency filtering in the electronic part of the loop. Since then, several OEO architectures have been considered [89, 90]. Single-loop OEOs have been demonstrated by using different configurations, including OEOs with direct laser modulation [91], those with electro-absorption modulation [92], OEOs based on photonic filters which use atomic transitions [93], and chip-scale OEOs based on whispering gallery modes [94, 95, 96]. Multi-loop OEOs have been implemented by using different coupling schemes, including the dual-loop OEO in which a short loop fixes the frequency range and a long loop determines the mode spacing [97], two nonlinearly coupled OEOs in which the output of one loop modulates the other in order to improve phase noise performance [98], and OEOs based on homogeneous and heterogeneous multicore fibres [99].

### 3.2.5 Modelization of a delay-line OEO

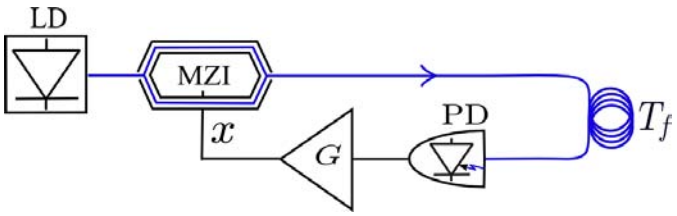


**Figure 3.2:** OEO composed of a laser diode (LD), a Mach -Zehnder Interferometer (MZI), a fiber delay line of delay time $T_f$, a photodiode (PD) and an amplifier ($G$).

Following [100], the OEOs considered in this thesis are composed of a laser source feeding a MZI with optoelectronic feedback. A scheme of such an OEO is illustrated in Fig. 3.2, where a continuous wave (CV) semiconductor laser with optical power $P$ feeds a Mach-Zehnder Interferometer (MZI) with electro-optic modulation in only one of the arms[1]. The electro-optic effect is achieved by applying RF and DC voltages $V(t)$ and $V_B$ to the RF and DC electrodes, respectively. The RF and DC half-wave voltages are respectively $V_{\pi_{RF}}$ and $V_{\pi_{DC}}$. The two beams are recombined at the end of the MZI. The resulting light enters an optoelectronic loop composed of a monomode optical fiber delay line with delay time $T_f$, a photodiode with sensitivity $S$ to detect the optical signal and convert it into an electrical signal, and a RF band-pass amplifier with a gain $G$.

[1]This configuration is sometimes referred to as a semiconductor laser system with electro-optical feedback [101]. We prefer the terminology *optoelectronic oscillator* instead of *semiconductor laser system with electro-optical feedback* because in this system the feedback loop is not closed onto the laser but onto the Mack-Zehnder Interferometer. We note that the term *electro-optic* is typically used to refer to optical devices whose dynamics is modified by the influence of an external electric field, such as lasers and electro-optic modulators. In contrast, the term *optoelectronic* typically refers to electronic devices with optical input or output, such as solar cells, liquid crystal displays or light emmitting diodes [78]. In this thesis, we use the term *optoelectronic* instead of *electro-optic* to refer to such oscillators for two reasons: first, because the dynamical variable of this system is not optic but electronic; and second, because the feedback loop starts optical and ends electronic.

The dynamics of this system can be described in terms of a variable, $x(t)$, which is proportional to the electrical signal $V(t)$ that modulates one of the arms of the MZI closing the optoelectronic loop,

$$x(t) = \frac{\pi V(t)}{2V_{\pi_{RF}}}. \tag{3.22}$$

The nonlinear dynamics generated after the MZI is band-pass filtered by the electrical circuit. Finally, the overall attenuation of the feedback loop is represented by the attenuation parameter 1. Considering that the low and high cut-off frequencies $f_L$ and $f_H$ of the band-pass filter are separated enough ($f_L$ $f_H$), the band-pass filter can be approximated by a cascade of two first-order linear filters, a low-pass filter and a high-pass filter, in such a way that the dynamical variable obeys the following integro-differential delay equation [100, 102],

$$x(t) + \tau\frac{d}{dt}x(t) + \frac{1}{-}\int_{t_0}^{t} x(t')dt' = \cos^2[x(t - T_f) + \Phi], \tag{3.23}$$

where

$$\tau = \frac{1}{2\pi f_H} \tag{3.24}$$

and

$$= \frac{1}{2\pi f_L} \tag{3.25}$$

are the filter characteristic times,

$$= \frac{GSP\pi}{2V_{\pi_{RF}}} \tag{3.26}$$

is the normalized feedback strength, and

$$\Phi = \frac{\pi V_B}{2V_{\pi_{DC}}} \tag{3.27}$$

is the normalized bias offset. The steps to derive Eq. (3.23) are detailed in [102].

Typically, $T_f$ is of the order of tens of nanoseconds, of the order of several microseconds and $\tau$ of the order of a few tens of picoseconds, so that we can consider the term $1 + \tau_i \ _i{}^1$ 1. The integral term plays a relevant role in the dynamics since it is responsible for the zero mean value of $V$, which is achieved after a slow transient characteristic of the bandpass dynamics that removes any DC component; indeed, large transient dynamics of the order of the slowest time are observed [103].

The integral term in (3.23) can be rewritten in terms of the intermediate variable $y(t) = \int_{t_0}^{t} x(t')dt'$, giving rise to a system of two DDEs,

$$\begin{aligned} y(t) &= x(t) \\ \tau\dot{x}(t) &= -x(t) - \frac{1}{-}y(t) + \cos^2[x(t - T_f) + \Phi], \end{aligned} \tag{3.28}$$

where overdot means differentiation with respect to time $t$.

The steady-state solution of (3.28) is given by

$$x_{st} = 0, \quad y_{st} = \quad \cos^2 \Phi. \tag{3.29}$$

Introducing $Y(t) = [y(t) - y_{st}]/T_f$ and $s = t/T_f$, (3.28) reads

$$\begin{aligned} Y'(s) &= x(s), \\ \varepsilon x'(s) &= -x(s) - \delta Y(s) + \quad \cos^2[x(s-1) + \Phi] - \cos^2 \Phi \quad , \end{aligned} \tag{3.30}$$

where prime stands for derivative with respect to the dimensionless time $s$ and

$$\varepsilon = \tau/T_f, \quad \delta = T_f/ \ . \tag{3.31}$$

Taking into account the typical time scales of the system, $\varepsilon$ is of order $10^{\ 4}$ and $\delta$ of order $10^{\ 3}$.

The dynamics of a single OEO has been analyzed in detail in [101, 104, 62, 63] both experimentally and theoretically for different values of the feedback strength and the offset phase $\Phi$. It has been found that system (3.30) admits multiple periodic solutions which are born sinusoidal from Hopf bifurcations of the steady state. In the subsection 3.2.6, we analyse these Hopf bifurcations leading to different periodic solutions. We note that a similar analysis of these Hopf bifurcations was already reported in [101]. However, we introduce in this section a different definition of the intermediate variable $y$ and the adimensional parameters, in order to be consistent with the analysis to be developed in Part II.

### 3.2.6 Periodic solutions in a delay-line OEO

In this subsection, we first focus on the onset of periodic solutions in a delay-line OEO. Considering small perturbations around the zero solution, $U(s) = x(s) - x_{st}$ and $V(s) = Y(s) - Y_{st}$, we can formulate the linearized equations for the perturbations:

$$\begin{aligned} \varepsilon U'(s) &= -U(s) - \quad U(s-1) - \delta V, \\ V'(s) &= U(s), \end{aligned} \tag{3.32}$$

where

$$\sin(2\Phi) \tag{3.33}$$

plays the role of an effective bifurcation parameter. Taking into account that is positive, following Eq. (3.33), takes the same sign than $\Phi$. According to Eq. (3.32), the feedback is negative for $> 0$ ($\Phi \quad [0, \pi/2]$) and positive for $< 0$ ($\Phi \quad [-\pi/2, 0]$).

Equations (3.32) admit solutions of exponential form, $U(s) = u \exp[(\lambda + i\omega)s]$, and, since $V$ is the integral of $U$, $V(s) = u \exp[(\lambda + i\omega)s]/(\lambda + i\omega)$. Replacing $U$ and $V$ in Eq. (3.32) leads to

$$0 = 1 + \varepsilon(\lambda + i\omega) + \delta(\lambda + i\omega) \ ^{1} + \frac{}{2} e^{\ (\lambda + i\ )}. \tag{3.34}$$

At the Hopf bifurcation, $\lambda = 0$ so that

$$0 = 1 + i\varepsilon\omega - i\frac{\delta}{\omega} + \quad \exp(-i\omega). \tag{3.35}$$

Splitting (3.35) into real and imaginary part leads to two equations for and $\omega$,

$$\cos(\omega) = -1, \tag{3.36}$$

$$\sin(\omega) = \varepsilon\omega - \frac{\delta}{\omega}. \tag{3.37}$$

From Eq. (3.36), the oscillation threshold is

$$= -\frac{1}{\cos(\omega)}, \tag{3.38}$$

whereas dividing (3.37) by (3.36) we obtain an equation for $\omega$,

$$\tan\omega = \frac{\delta}{\omega} - \varepsilon\omega. \tag{3.39}$$

Because $\delta$ and $\varepsilon$ are small, the frequency of the oscillations is close to a multiple of $\pi$,

$$\omega_n = n\pi + \alpha_n(\varepsilon, \delta), \tag{3.40}$$

where $\alpha_n$ is a correction of order $O(\varepsilon, \delta)$. Introducing Eq. (3.40) into Eq. (3.39) and expanding the tangent as a Taylor series up to second order in $\alpha_n$, we obtain a closed equation for $\alpha_n$,

$$\alpha_n^2(1+\varepsilon) + \alpha_n n\pi(1+2\varepsilon) + \varepsilon(n\pi)^2 - \delta = 0. \tag{3.41}$$

For $n = 0$, $\alpha_n$ determines the frequency. Setting $n = 0$ in Eq. (3.41) leads to

$$\alpha_0^2(1-\varepsilon) - \delta = 0. \tag{3.42}$$

Then,

$$\omega_0 = \alpha_0 = \quad \frac{\overline{\delta}}{1+\varepsilon} \qquad \overline{\delta}. \tag{3.43}$$

With $n = 0$, the period of the solution scaled to $T_f$ is typically in the microsecond regime, much larger than the delay time. Inserting (3.43) into (3.36), we obtain an approximation to the instability threshold for the microsecond solution,

$$_0 \quad -\frac{1}{\overline{\delta}} \quad -1 - \frac{\delta}{2}. \tag{3.44}$$

For $n$ 1, the correction $\alpha_n$ can typically be neglected since it is much smaller than $n\pi$, and the frequency of the solution can be approximated as

$$\omega_n \quad n\pi, \quad n \quad 1. \tag{3.45}$$

Therefore, for $n \quad 1$, the period of the solution scaled to $T_f$ is close to a divisor of twice the delay time, typically in the nanosecond regime. Inserting (3.45) into (3.36), we obtain an approximation to the instability threshold of the square-wave solutions,

$$_n \quad -\frac{1}{\cos(n\pi)} = (-1)^{n+1}, \quad n \quad 1. \tag{3.46}$$

To first order in Eq. (3.41), the correction to the frequency $\alpha_n$ is

$$\alpha_n \quad \frac{\delta - (n\pi)^2\varepsilon}{n\pi(1+2\varepsilon)} \quad \frac{\delta}{n\pi} - n\pi\varepsilon, \quad n \quad 1, \tag{3.47}$$

in such a way that the oscillation frequency is

$$\omega_n \quad n\pi + \frac{\delta}{n\pi} - n\pi\varepsilon, \quad n \quad 1, \tag{3.48}$$

and the instability threshold is

$$_n \quad -\frac{1}{\cos[n\pi(1-\varepsilon) + \delta(n\pi)^{\ 1}]} \quad (-1)^{n+1} + \delta - (n\pi)^2\varepsilon, \quad n \quad 1, \tag{3.49}$$

where we have used a Taylor series expansion of $_n$ about $\omega_n$ given by Eq. (3.48) with $\alpha_n$ small, in which we have kept only terms to first order in $\delta$ and $\varepsilon$.

For negative feedback ($\Phi > 0$), the instability threshold takes place at $_n \quad 1$. According to (3.46), $n$ must be odd, namely $n = 2m+1$, with $m$ being an integer. From (3.45), we have a family of coexisting solutions with different periods $T = 2/(2m+1)$. These solutions are born supercritically with a sinusoidal shape and increasing about $_n$ they soon adquire a square-wave shape with a symmetric duty cycle. Considering the dimensional time units, the fundamental solution has a period $T_0 = 2T_f$ while harmonics have a period $T_m = T_0/(2m+1)$. The coexistence of these square waves is illustrated in Fig. 3.3.

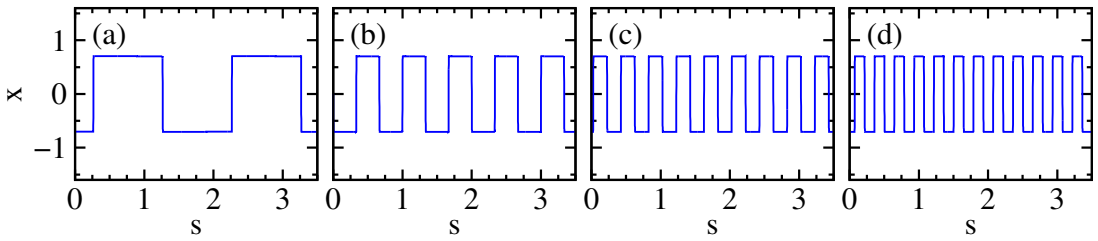


**Figure 3.3:** Symmetric square waves coexisting with $T_f = 30\,\text{ns}$, $= 5$ s, $\tau = 25\,\text{ps}$, $\Phi = 0.2\pi$ and $P = 1.5$. (a) Fundamental solution ($T = 2$), (b) first harmonic ($T = 2/3$), (c) second harmonic ($T = 2/5$), and (d) third harmonic ($T = 2/7$).

For positive feedback ($\Phi < 0$), the instability threshold takes place at $_n \quad -1$. Therefore, from (3.46) and (3.45), we have a family of solutions with $n$ even, namely $n = 2m$. The case $n = m = 0$ corresponds to the microsecond solution with frequency $\omega_0$ given by

(3.43), which arises at $_0$ [see Eq. (3.44)]. Since this solution has a period much larger than the delay time, it never takes a square-wave shape. The other coexisting solutions with $n = 2, 4, ...$ correspond to square waves which, in general, have an asymmetric duty cycle, as illustrated in Fig. 3.4. The asymmetry of the duty cycle depends on the offset phase $\Phi$, being the solutions symmetrical for $\Phi = -\pi/4$ and progressively more asymmetric as $\Phi$ goes away from this value. Square waves with asymmetric duty cycle are born subcritically while microsecond solutions are born supercritically.

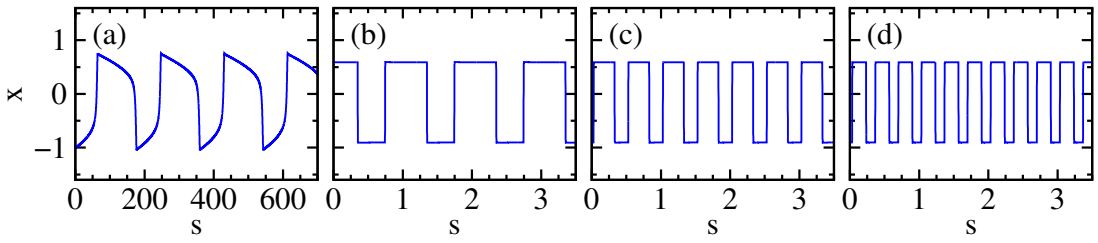


**Figure 3.4:** Solutions with asymmetric duty cycle coexisting for positive feedback. Parameters as in Fig. 3.3 but $\Phi = -0.2\pi$. (a) Microsecond solution, (b) fundamental square wave ($T = 1$), (c) first harmonic ($T = 1/2$), and (d) second harmonic ($T = 1/3$).

### 3.2.7 Experimental results

Experimental evidence of microsecond and square-wave solutions using a setup such as that shown in Fig. 3.2 has been reported in [101] and [62] through time traces similar to the ones shown in Figs. 3.3 and 3.4. However, the coexistence of multiple square waves with this system has never been observed experimentally. Following the original idea of Ikeda and coworkers [48, 49] of recovering the desired harmonic by introducing a suitable periodic perturbation to the system, the coexistence of multiple square waves in a large delay single OEO has recently been demonstrated experimentally [8], in a setup in which a pattern generator is used to recover several harmonics; this system is modeled with an equation similar to Eq. (3.30) but with $\tanh[x(s-1)]$ instead of $x(s-1)$.

Experimental time traces of coexisting square waves obtained with negative feedback are shown in Fig. 3.5. As expected for negative feedback, the square waves of Fig. 3.5 exhibit a period close to an odd divisor of twice the delay.

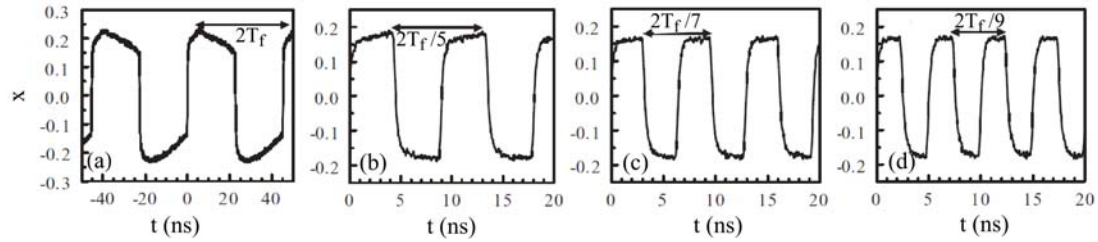


**Figure 3.5:** Experimental time traces of coexisting square waves for negative feedback with $\phi = 0.21\pi$, $\varepsilon = 0.0157$, $\delta = 0.2042$, $T_f = 22\,\text{ns}$, and $= 1.94$. (a) Fundamental square wave, (b) second harmonic, (c) third harmonic, and (d) fourth harmonic. Modified from [8].

Figure 3.6 shows experimental time traces of microsecond solutions (a) and square waves [(b)-(d)] obtained for positive feedback. In agreement with the theoretical results for positive feedback, the period of the square waves shown in Fig. 3.6 [(b)-(d)] is close to a divisor of the delay. In Figs. 3.6(a) and 3.6(b) the solution is slightly asymmetric because the offset phase $\phi = -0.27\pi$ is very close to the symmetric offset phase $\phi = -0.25\pi$, whereas in Figs. 3.6(c) and 3.6(d) the solutions are symmetric because the offset phase is $\phi = -0.25\pi$.

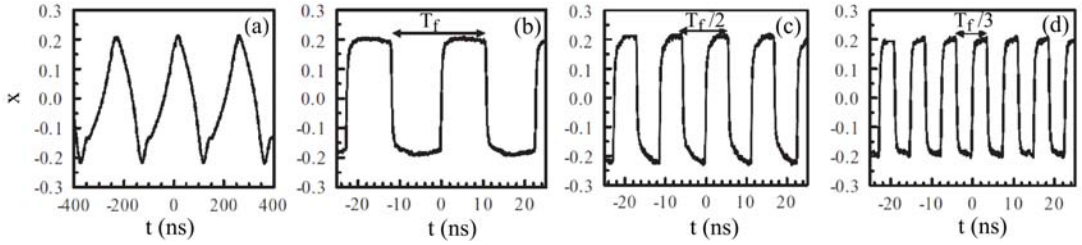


**Figure 3.6:** Experimental time traces of microsecond and square-wave solutions obtained with positive feedback with $\varepsilon = 0.0157$, $\delta = 0.2042$, and $T_f = 22\,\text{ns}$. The values of the control parameters are $\phi = -0.27\pi$ and  = 1.94 in [(a)-(b)], and $\phi = -0.25\pi$ and  = 2.2 in [(c)-(d)]. (a) Microsecond solution, (b) fundamental square wave, (c) first harmonic, and (d) second harmonic. Modified from [8].

### 3.2.8 Secondary instabilities and routes to chaos in OEOs

OEOs have been designed with two different and complementary configurations: narrowband and wideband. In the narrowband configuration, the filter is inserted in the electrical part of the loop between the photodiode and the amplifier, and may not be considered as two cascaded first-order filters but as a single resonant bandpass filter. Typically, in the narrowband OEO, $T_f$ is of the order of tens of microseconds,  is lower than a picosecond, and $\tau$ is in the nanosecond range. In this case, a single frequency is allowed for a given set of values of the parameters and thus the system can be modelled using a slowly varying complex envelope equation [102, 101].

In the configuration shown in Fig. 3.2, a broadband filter is used instead, yielding to hiperchaos when the feedback gain is large enough. In this case, in which the single-mode approach is not valid, asymptotic techniques in the limit of large delays can be used to study the dynamics of the system [105]. In this thesis, we mainly work in the wideband configuration.

#### Narrowband OEO

The single-mode microwaves generated with the narrowband OEO undergo a quasiperiodic route to chaos, in which increasing , a steady state evolves to period-1 oscillations, quasiperiodic oscillations (with two frequencies with incommensurable ratio) and chaotic states [101, 106, 102]. In particular, the oscillatory solution undergoes a Neimark-Sacker

bifurcation, that is a bifurcation of a limit cycle to a torus, at $-2.31$. This instability limits the performance of OEOs for ultrapure microwave generation [106].

### Wideband OEO

The larger the bandwidth of the OEO, the larger the set of frequencies competing in the system [107]. As a result, the wideband OEO exhibits a larger variety of complex behaviours than the narrowband OEO. In particular, it can generate chaotic breathers as well as multiple fast square waves coexisting with slower solutions.

The bifurcation diagram for the square-wave solutions of periods $2T_f$ and $T_f$ of the wideband OEO has been obtained in [62] and [63], respectively, both experimentally and numerically. A period doubling route to chaos has been reported in [62] for the $2T_f$ symmetric square waves with $\Phi > 0$ as is increased. The bifurcation diagram of the slow solutions and the asymmetric square waves arising with $\Phi < 0$ has been obtained in the vecinity of the first Hopf bifurcation [63].

The period of the slow solutions arising with $\Phi < 0$ increases with keeping fixed $\Phi$, whereas keeping fixed it changes with $\Phi$ being minimum in the symmetric case with $\Phi = -0.25\pi$ [108].

By increasing , periodic breathers are born, as shown in [61, 101]. The periodic breathers oscillate at the same scale than the coexisting square waves and are surrounded by a microsecond periodic envelope with a period in the microsecond range. By further increasing , the breathers become chaotic. Increasing still further leads to the fully developed chaos.

The periodic breathers reported in [101] for the symmetric case ($\Phi = 0.25\pi$) have identical plateau lengths and exhibit a period $2T_f$, as the coexisting symmetric square waves for the same value of $\Phi$. It has been found that the symmetry of the breathers with respect to $x = 0$ depends on the value of $\Phi$. The condition for symmetric breathing with respect to $x = 0$, namely oscillating with identical amplitudes, is the same than for symmetric square-wave switching: $\Phi = -0.25\pi$. With $\Phi \neq -0.25\pi$, the breathers with $x > 0$ are born with different amplitude than the ones with $x < 0$ [61, 101], and thus could become chaotic at different values of the feedback gain [109].

Figures 3.7 and 3.8 illustrate an example of asymmetric chaotic breathers found with $\Phi = -0.15\pi$. In Fig. 3.7, we can see the birth, evolution and death of the breathers while increasing the feedback strength, whereas Fig. 3.8 is a zoom of Fig. 3.7. As it can be seen in Fig. 3.8(b), the periodic breathers are born with identical plateau lengths and a period $2T_f$; and increasing they become chaotic as shown in Fig. 3.8(c).

For larger values of , it has been found a regime in which three different dynamics are present: a microsecond periodic envelope, a nanosecond square wave and chaotic breathers within the square waves (see Figs. 7 and 10 of [104]). As shown in Fig. 3.8(d) for $\phi < 0$, the nanosecond square-wave periodic envelope surrounding the chaotic breathers has two different plateau lengths and period $T_f$. Increasing further , the nanosecond envelope undergoes a period doubling and exhibits a periodic envelop with a period in the microsecond range, as shown in Figs. 3.8(e) and 3.7(e).

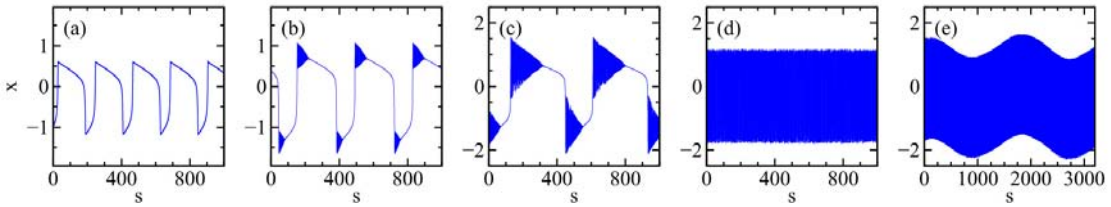


**Figure 3.7:** Birth, evolution and destruction of asymmetric chaotic breathers with a microsecond periodic envelope with $\Phi = -0.15\pi$. (a) = 1.5, (b) = 2, (c) = 2.5, (d) = 3, and (e) = 3.2.

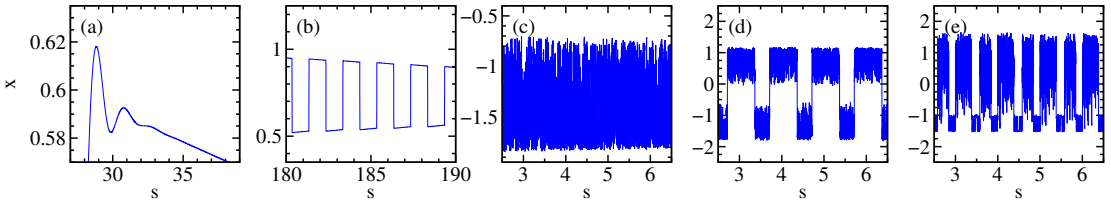


**Figure 3.8:** Inner structure of the breathers. Zoom of panels (a)-(e) of Fig. 3.7: (a) birth of the breathing with = 1.5, (b) $2T_f$ breathers with = 2, (c) chaotic breathers with = 2.5, and chaotic breathers with nanosecond periodic envelope with = 3 (d) and = 3.2 (e).

Similarly to the narrowband OEOs, the wideband OEO also undergoes a quasiperiodic route to chaos when is increased. In the subsection 3.2.9, we show an example of numerical study of the local stability of periodic and quasiperiodic solutions in a wideband OEO.

### 3.2.9 Stability analysis of periodic solutions in wideband OEOs

The study of the local stability of periodic and quasiperiodic solutions in wideband OEOs is a stiff problem, specially when the ratio between the fastest and the slowest time scales is very high. As an example, in this section we show the study of the local stability of the dominant periodic and quasiperiodic solutions of an OEO with delay time $T_f = 3\,\text{ns}$, filter characteristic times = 0.1 s and $\tau = 100\,\text{ps}$, and offset phase $\phi = 0.25$, as the feedback strength is increased. The dominant solution is obtained choosing an initial condition close to the unstable fixed point $(x = 0, Y = 0)$ of the dynamical system (3.30).

In the periodic regime, the dominant solution is the fundamental solution, namely the solution with larger period, which is sinusoidal close the Hopf bifurcation at = 1 and becomes square wave increasing , as shown in Fig. 3.9. Because the offset phase is positive, the feedback is negative, and thus slow pure monochromatic solutions with period in the microsecond range, which would naturally arise as the dominant solutions for positive feedback, are not allowed.

The local stability of the fundamental periodic solution has been computed using the Floquet theory, which requires an accurate computation of the period of the solution. The period of the solution has been determined using two different methods introduced

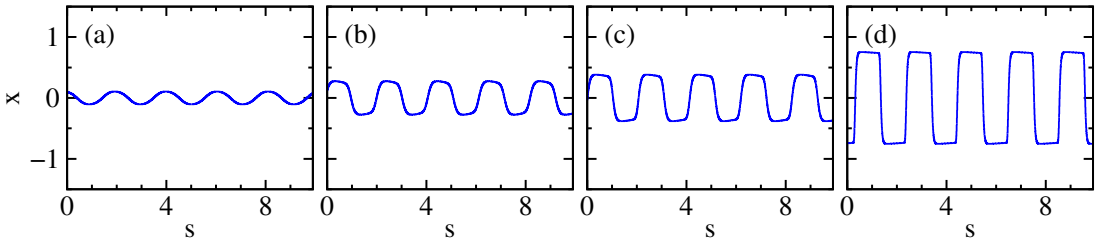


**Figure 3.9:** Dynamics of the fundamental square wave with $T_f = 3\,\text{ns}$, $= 0.1$ s, $\tau = 100\,\text{ps}$, $\phi = 0.25$, $= 1.01$ (a), $= 1.05$ (b), $= 1.1$ (c), and $= 1.5$ (d).

in the subsection 2.2.7: linear interpolation and the Hénon's trick. Whereas the Hénon's trick is applied once, lineal interpolation is applied iteratively until the relative difference between two consecutive results is lower than $10^{-15}$. For numerical integration of the dynamical system and the variational equations, the Euler method has been used for both methods[2], with integration time step $h = 5 \quad 10^{-4}\,\text{ns}$.

The results for the period as a function of are shown in Fig. 3.10. As expected, the pure monochromatic dominant solution has a period close to twice the delay. The correction to the frequency predicted by Eq. 3.47 for $n = 1$, $\delta = 0.03$ and $\varepsilon = 0.0333$, $\alpha_1 = -0.09517$, gives rise to an oscillation frequency $\omega_1$ 3.05, which corresponds to a period $T$ 2.06, very close to the period shown in Fig. 3.10 close to $= 1$. Keeping fixed $\Phi$ and increasing from $= 1$, the dominant periodic solution changes its shape from sinusoidal towards square-wave, as shown in Fig. 3.9; while its period increases until reaching a maximum and then decreases, as shown in Fig. 3.10. Nevertheless, the overall variation of the period over the whole interval for is very small (of the order of 0.5%), so we can assume that square waves have a period which is practically independent of .

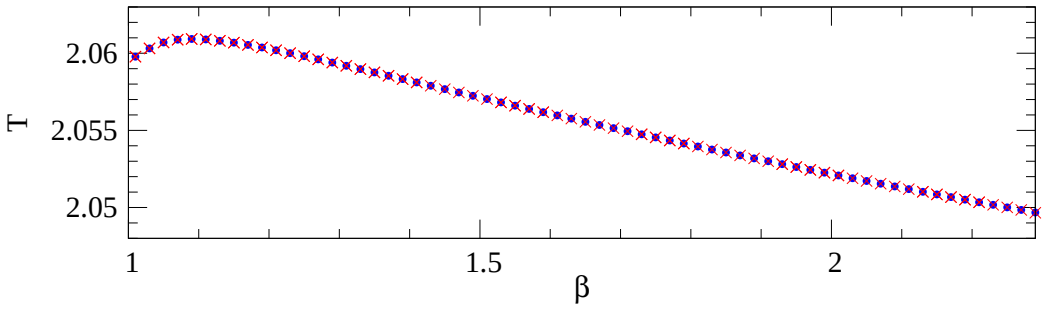


**Figure 3.10:** Period of the fundamental square wave with $T_f = 3\,\text{ns}$, $= 0.1$ s, $\tau = 100\,\text{ps}$ and $\phi = 0.25$ as a function of . Blue dots and red crosses correspond to interpolation and the Hénon's trick, respectively.

[2]The predictor-corrector is not convenient when applying the Hénon s trick, which requires that the prediction at each step does not depend on the derivatives at previous steps.

The difference between the period obtained with interpolation and that one obtained by applying the Hénon's trick is smaller than the integration time step $h$, which is small compared to the variation of the period of the solution induced by changing , which is of order 10 $^{2}$. As a result, there is no appreciable difference between the results obtained with these two methods.

Increasing further and keeping fixed $\Phi$, the square waves undergo a quasiperiodic route to chaos. A Neimark-Sacker bifurcation occurs at 2.29, when a pair of complex Floquet multipliers crosses the unit circle on the right hand-side. The modulus of the dominant eigenvalues (with largest modulus) of the monodromy matrix for the fundamental square wave is plotted in Fig. 3.11 as a function of the feedback strength. Since system (3.30) is autonomous, one eigenvalue of the monodromy matrix is always 1; the other two are the two Floquet multipliers with largest modulus.

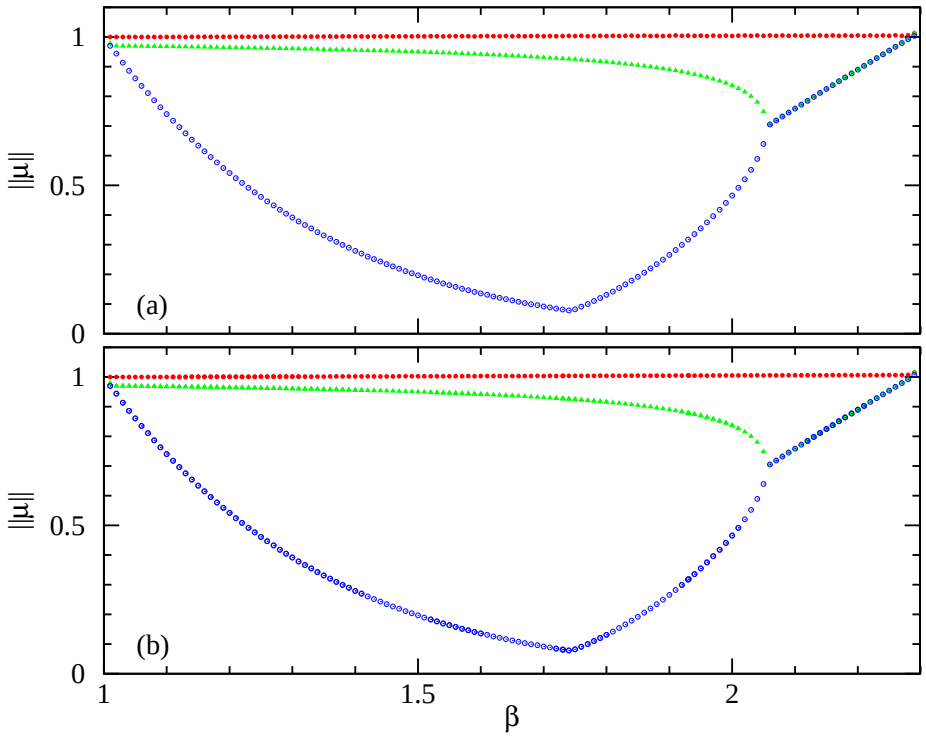


**Figure 3.11:** Modulus of the dominant eigenvalues of the monodromy matrix of the fundamental square wave for the same values of the parameters than in Fig. 3.10. Panels (a) and (b) correspond to interpolation and the Hénon's trick, respectively.

In the quasiperiodic regime, a fast oscillation of period close to twice the delay time is surrounded by a microsecond periodic envelope, as shown in Fig. 3.12, where panels (a)-(e) show the fast oscillation while panels (f)-(j) show the microsecond envelope. In this case, an Adams-Bashforth-Moulton fourth-order predictor-corrector with time step size $h = 5$ 10 $^{4}$ns has been used for the numerical integration of the dynamical and variational equations.

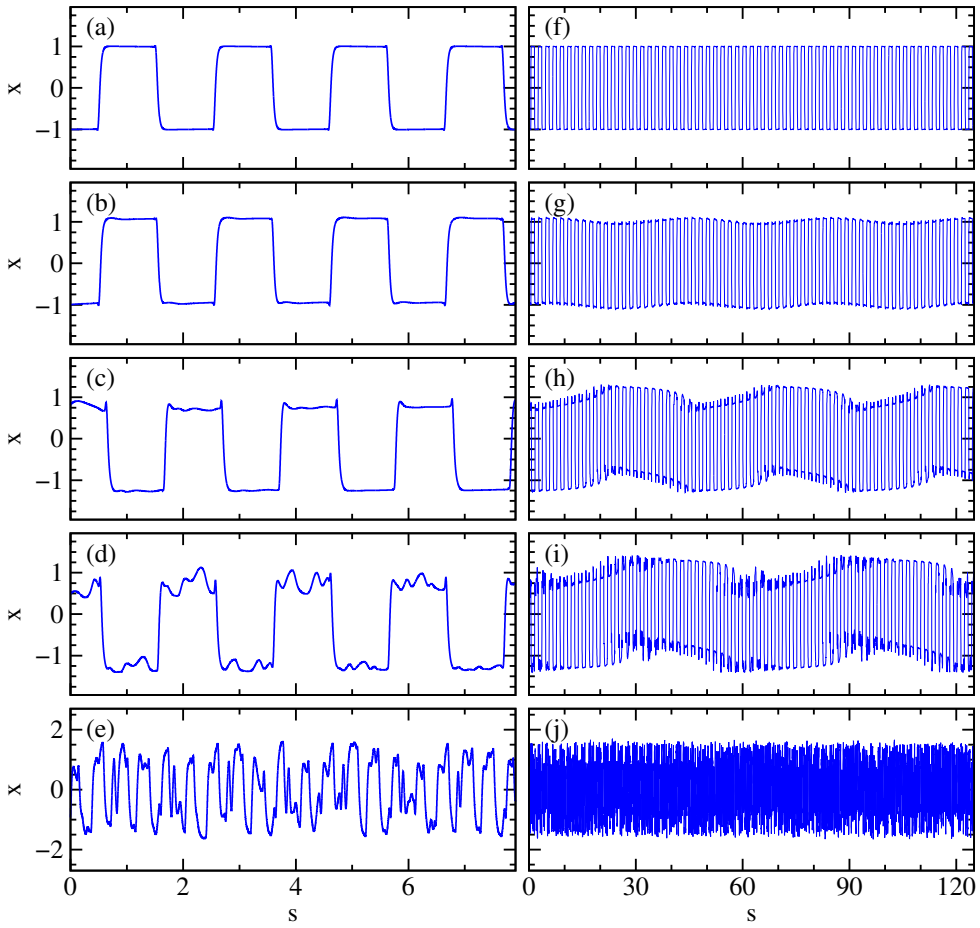


**Figure 3.12:** Fast (a)-(e) and slow (f)-(i) dynamics of system (3.30) for the same values of the parameters than in Fig. 3.10 but = 2.2 [(a), (f)], = 2.3 [(b), (g)], = 2.5 [(c), (h)], = 2.7 [(d), (i)], and = 3.4 [(e), (j)].

In the quasiperiodic regime, the Floquet theory is no longer valid. The study of the local stability of the quasiperiodic solutions of this system has been addressed computing the spectrum of Lyapunov exponents of the fundamental solution. From the spectrum of Lyapunov exponents as a function of plotted in Fig. 3.13, in addition to the periodic region with $1-2.29$ in which one Lyapunov exponent is zero and the rest are negative, we can identify a region with $2.29-2.75$ in which two Lyapunov exponents are zero and the rest are negative, corresponding to stable quasiperiodic solutions.

Increasing further the feedback strength, the dynamics gets chaotic and there is at least one positive Lyapunov exponent. A zoom of Fig. 3.13 showing the spectrum of the Lyapunov exponents when the system becomes chaotic is shown in Fig. 3.14. Increasing further the feedback strength, more and more Lyapunov exponents become positive as the chaoticity of the solution increases. An example of dynamical timetrace with full developed chaos is shown in panels (e) and (j) of Fig. 3.12.

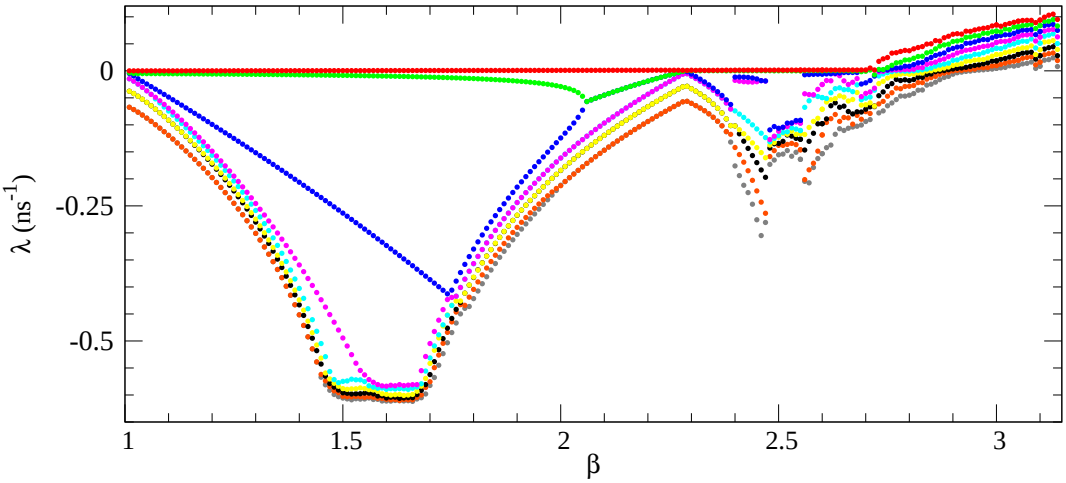


**Figure 3.13:** Nine largest Lyapunov exponents for the same parameters than in Fig. 3.10 as a function of .

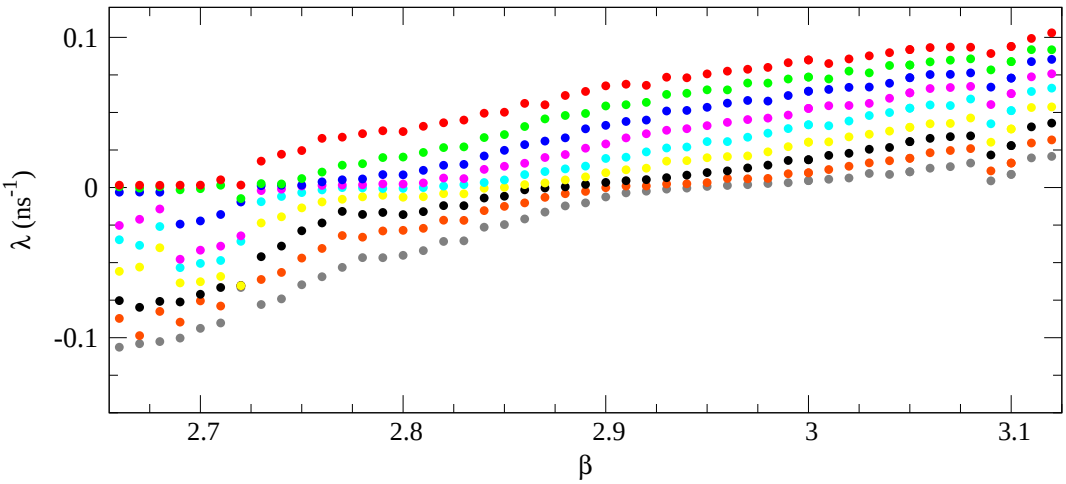


**Figure 3.14:** Zoom of Fig. 3.13.

### 3.2.10 Applications and advantages of OEOs

OEOs exhibit a rich variety of dynamical regimes [101, 61] with different technological applications. Narrowband OEOs in the periodic regime have been proposed and studied to produce efficient ultra-pure microwaves [102, 87, 88, 106] for radar applications. The robustness to noise of the microwaves generated by narrowband OEOs has been studied both theoretically and experimentally [110].

Wideband OEOs in the periodic regime can generate ultra-fast square-wave pulses of controllable period [62, 63, 111, 112, 113], paving the way towards applications such as encoding of information in high-capacity memory devices. In the chaotic regime, wideband OEOs have been used as chaos generators for secure chaos-based communications

[114, 115, 116]. Finally, wideband OEOs operating close to the steady state regime have been implemented in experiments demonstrating optical information processing with a photonic liquid state machine performing a kind of neuromorphic computer [117, 24, 118].

As compared to optical feedback systems and optical injection systems, in which the dynamics depends on the frequency, phase, and amplitude of the field, and for which a frequency detuning of a few hundred of MHz between the two systems can lead to a large degradation of the synchronization, optoelectronic systems are more flexible due to their insensitiveness to optical phase variations. Another advantage of OEOs is that they can be electrically driven [119].

## 3.3 Semiconductor lasers with optical feedback

In this section, we first briefly introduce the fundamental principles and different types of lasers, while reviewing some important contributions related to the laser invention. After that, we focus on semiconductor lasers and introduce the rate equations model for semiconductor lasers with optical feedback. Finally, we briefly review the different dynamical regimes of semiconductor lasers with delayed optical feedback.

### 3.3.1 Introductory remarks on lasers

Laser is the acronym for Light Amplification by Stimulated Emission of Radiation. Lasing action typically takes place for radiation undergoing stimulated emission, a process in which a photon stimulates an electron of an atom to make a transition to a lower energy state by emitting another photon with identical frequency, polarization, phase and direction of propagation. The first photon that allows for stimulated emission is provided by spontaneous emission, a process in which an excited atom transitions to a lower energy state by emitting a photon with the transition energy.

The concepts of spontaneous and stimulated emission were introduced by Albert Einstein in 1917 in a paper entitled On the quantum theory of radiation [120]. In his theory of radiation, Einstein proposed that radiation of frequency can induce a molecule in a state $Z_m$ with energy $E_m$ to make a transition to another state $Z_n$ with energy $E_n < E_m$ by emitting the radiative energy of the transition $E_m - E_n = h$ , with a probability in time $dt$ proportional to the radiation density $\rho$, $dW = \rho B_{mn} dt$, being $B_{mn}$ a constant to be determined. Einstein named this process stimulated emission. He proposed a similar argument for (stimulated) absorption, the inverse process of stimulated emission in which radiation of frequency induces an atom to transition from the state $Z_n$ to the state $Z_m$ by absorbing the energy of the transition, $E_m - E_n = h$ , with a probability in time $dt$ given by $dW = \rho B_{nm} dt$. He also asserted that the probability for spontaneous emission of an excited atom to undergo a transition to a lower energy state without the influence of radiation (spontaneous emission) in time $t$ is $dW = A_{mn} dt$.

For an atom or a molecule in thermal equilibrium, the probability of stimulated absorption is higher than that of stimulated emission because the ground state is more populated

than the excited states. For stimulated emission to take place, a population inversion between two states must occur, so that there are more atoms in the excited state than in the lowest energy state. Population inversion requires more energy than that of the system in equilibrium. Pumping an excited state can be achieved with another laser, an electrical discharge, chemical reactions, etc.

With the purpose to better determine the frequency of a molecular transition, in 1947 Willis E. Lamb and Robert C. Retherford were able to amplify, by stimulated emission, the radiation emitted by hydrogen molecules [121]. The well known Lamb shift represented the first experimental result on light-matter interaction satisfying the condition of population inversion necessary for lasing action to occur.

The idea to use a resonant cavity as feedback loop to amplify radiation by stimulated emission is due to Charles Hard Townes. In 1954, Townes and coworkers working at Columbia University in New York demonstrated the first coherent optical oscillator based on Einstein's predictions, which was called MASER because it amplified microwave radiation [122]. The generation of coherent light in the microwave range was mainly motivated by radar applications after the second World War, but also by the interest of scientists in revealing molecular structure. In 1958, Townes and A. L. Schawlow showed theoretically that masers could be built to operate in the optical and infrared regions of the electromagnetic spectrum [123]. However, the invention of the laser is attributed to Theodore Maiman for the demonstration in 1960 of the first working laser producing visible light [82].

As the field propagates through the excited medium, radiation at the frequency corresponding to the energy level difference is exponentially amplified. For lasing action to take place, two conditions must be satisfied: i) the gain per pass through the medium must exceed the loss, and ii) the phase shift of light in a round-trip within the resonator must be a multiple of $2\pi$.

The laser invented by Maiman was a solid state laser made with a ruby crystal. Today, there exists a wide variety of lasers with different active media, including solids (crystals, glasses, fibers, powders), gases (atoms, ions, molecules, excimers), liquids (organic dye solutions), plasma and other more exotic active media such as the energy levels of an electron in a magnetic field in free-electron lasers.

Two mirrors are typically used to provide an optical cavity as the feedback mechanism for light amplification [124]. However, laser action can also be achieved without the need of a resonator, provided that the system produces enough gain per pass through the medium to generate significant output [125]. The generation of superluminiscent coherent light taking place via amplified spontaneous emission (ASE), a noise driven amplifying process, was studied for the first time for gases by R. H. Dicke [126] seven years before the invention of the laser. Superluminiscence has been achieved for different systems, including gas lasers, dye lasers, semiconductor lasers with multiquantum-well structures, and solid state lasers [125]. In free-electron lasers, for instance, coherent radiation is produced via self-amplified spontaneous emission (SASE) of radiation by free electrons, a process in which free electrons are accelerated to relativistic speeds in the presence of a spatially periodic transverse magnetic field to produce synchrotron radiation, which is exponentially amplified by noise (photons emitted by spontaneous

emission) [127, 128]. Based on the SASE principle, ultraviolet (UV) and X-ray free-electron lasers allow the generation of coherent ultrashort (typically 10-100fs) pulses with very high peak brilliance[3]. In particular, free-electron X-ray sources provide the required brilliance and wavelength to access to atomic motion information, typically in the sub-picosecond scale.

### 3.3.2 Semiconductor lasers

Semiconductor lasers have been so far the most technologically important type of lasers. The possibility to use a semiconductor material to emit coherent light was proposed for the first time by John von Neumann in 1953 [129]. The first working semiconductor lasers were developed in 1962 by four independent american research groups (Hall *et al* [130], Holonyak and Bevacqua [131], Nathan *et al* [132], and Quist *et al* [133].

One of the advantages of semiconductor lasers with respect to other types of laser is their size. Apart from being smaller than other lasers, they are reliable, efficient, and relatively low-cost. Furthermore, semiconductor lasers can cover a large range of frequencies, from the ultraviolet to the infrared regions of the electromagnetic spectrum, some are tunable, and can be built with a large variety of structures.

These special characteristics have made semiconductor lasers an enabling technology for applications extended in diverse areas such as optical fiber and free-space communication, data storage, scanning, combustion ignition, metrology, spectroscopy, material processing, laser printers, sensing, pumping of other types of lasers, holography, tracking, illumination, optical trapping of small particles, laser surgery, photodynamic therapy, etc. They are everywhere in our diary life, for instance in bar-code readers, DVDs and blue-rays.

The simplest architecture of semiconductor laser is a laser diode, also known as injection laser, which consists of a forward-biased $p-n$ junction with its parallel cleaved surfaces acting as reflectors. The $p-n$ junction is formed by a $p-$type (with many holes) and an $n-$type (with many electrons) semiconductor in contact with each other. The forward-biasing is obtained by applying an external voltage, which makes possible the diffusion of electrons and holes across the junction. The diffused electrons and holes can recombine either radiatively by emitting the excess of energy in the form of photons, or non-radiatively by releasing the energy in the form of lattice vibrations (phonons) and ultimately as heat in the crystal lattice. Photons of energy close to the energy gap between the two bands are emitted by radiative recombination. In a stimulated emission event, a photon stimulates the recombination (annihilation) of an electron-hole pair by emitting another photon identical to the incoming photon. However, the reverse process of stimulated absorption generates a new electron-hole pair. Beyond a certain threshold of external voltage, a population inversion situation is reached, with more electrons in the conduction band than in the valence band. In this situation stimulated emission prevails [134].

[3]Brilliance is defined as a function of frequency given by the number of photons emitted by the source per unit time, per unit solid angle, per unit surface of the source, and per unit bandwidth of frequencies around the given one.

Semiconductor lasers are grouped in two categories, which are illustrated in Fig. 3.15: surface-emitting, in which radiation emerges from a surface in the plane of the recombination layer as in (a); and edge-emitting, in which light emerges from a surface on an edge of the crystal as in (b), namely, from an area of the crystal face perpendicular to the active layer [84].

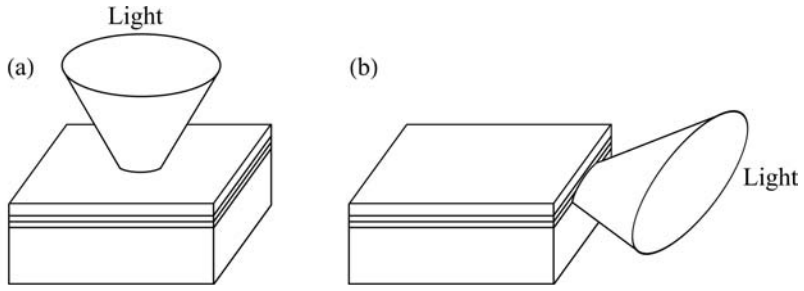


**Figure 3.15:** (a) Surface-emitting laser and (b) edge-emitting laser.

Modeling lasers accurately requires a full quantum description of light and its interaction with matter. However, a semi-classical approach where matter is quantized but not light, and even a classical model, can provide good qualitative agreement between theory and experiments [105]. It can be in fact demonstrated that the quantum equations for the light-matter interaction reduce to the classical equations proposed by Lorentz before the advent of quantum mechanics, within a factor called the oscillator strength, in the limit of small intensities [135]. For semiconductor lasers in particular, good quantitative agreement between experiments and theory using rate equations models is possible but it requires a sofisticated description of the active media [105]. In the subsection 3.3.3, the well-known Lang Kobayashi rate equations model for semiconductor lasers with optical feedback is introduced. Before introducing the Lang Kobayashi rate equations model, we emphasize three important features of semiconductor lasers: their high sensitivity to feedback, fast dynamics, and linewidth enhancement factor.

### High sensitivity to feedback

The ideal case of a semiconductor laser without external feedback belongs to the lasers class B. The dynamics of class B lasers can be described in terms of the electric field and the population inversion [136]. Under constant pump, class B lasers's output is constant or periodic. Nevertheless, semiconductor lasers can be destabilized and show chaotic behaviour introducing external perturbations such as optical or optoelectronic feedback [134]. In fact, semiconductor lasers are extremely sensitive to noise due to their particular geometries and small size, and naturally show instabilities due to optical feedback of a small fraction of the laser output.

On the one hand, uncontrolled instabilities in semiconductor lasers can produce damage to the laser. To avoid uncontrolled optical feedback, optical isolators and Faraday rotators are often used in semiconductor laser experimental setups. Stabilization of the laser output of semiconductor lasers was one of the first problems in the study of the nonlinear dynamics of semiconductor lasers subject to external optical feedback [1].

On the other hand, powerful applications such as chaos-based secure communications, random number generation or remote sensing have been achieved by exploiting the chaotic output of semiconductor lasers with external optical feedback. Furthermore, from the point of view of dynamical systems, because semiconductor lasers subject to optical feedback show a rich variety of dynamical regimes, they can be used as test-beds to explore nonlinear dynamical phenomena taking place in photonics and other research fields. An example of interesting dynamics that can be studied with semiconductor lasers with optical feedback is state-dependent delay dynamics, which is the central topic of Part III of this thesis.

#### Fast dynamics

The dynamics of semiconductor lasers is experimentally difficult to investigate due to their fast intrinsic time scales, which are of the order of picoseconds or even smaller. As a result, there is a trade-off between temporal resolution and length in time series adquisition of the intensity of a diode laser: a high resolution camera can be used to resolve the dynamics of the intensity of the laser for a short interval of time, whereas long time series can only be analyzed with poor temporal resolution.

Fourier analysis is a typical method to investigate experimentally the dynamics of semiconductor lasers. On the one hand, radiofrequency power spectrum analyzers are typically used to measure the spectrum of the laser intensity, that is the squared modulus of the Fourier transform of the intensity of the electrical field. On the other hand, the optical spectrum of the laser is typically obtained with an optical spectrum analyzer containing a diffraction grating.

#### Linewidth enhancement factor

A remarkable feature of semiconductor lasers is the effect of the carrier density on both the optical gain and the refractive index of the active region, which results in amplitude-phase coupling with a dramatic impact on many laser characteristics [137]. One of the well-known effects of such amplitude-phase coupling is the broadening of the laser linewidth by a factor of $1 + \alpha^2$, where $\alpha$ is referred to as the linewidth enhancement or Henry factor [138], defined as the ratio of the real and imaginary parts of the pump-induced susceptibility $\chi_p$,

$$\alpha = -\frac{Re(\chi_p)}{Im(\chi_p)}. \tag{3.50}$$

### 3.3.3 Rate equations model for semiconductor lasers with external cavity feedback

The first model describing the dynamics of a semiconductor laser subject to external optical feedback was introduced by Lang and Kobayashi in 1980 [139]. In this model, the strength of the feedback is assumed to be moderate so that multiple reflections can be disregarded, and the laser is assumed to be single-mode [134]. The Lang and Kobayashi

model consists of two ordinary delay differential equations for the slowly varying complex amplitude of the electrical field with respect to the laser frequency, $E(t)$, and the number of excited carriers in the active medium, $N(t)$:

$$\begin{aligned} E(t) &= \frac{1+i\alpha}{2}[G(N,E)-\gamma]E(t) + \quad e^{i} \; E(t-\tau), \\ N(t) &= \frac{I}{e} - \gamma_n N(t) - G(N,E) \; E(t)^{\;2}. \end{aligned} \tag{3.51}$$

In Eqs. (3.51), the dot stands for time derivative, $\alpha \quad 2-5$ is the linewidth enhancement factor defined above, $\gamma \quad 0.2-0.5\,\mathrm{ps}^{\;1}$ is the photon decay rate, $\gamma_n \quad 0.5-1\,\mathrm{ns}^{\;1}$ is the decay rate for the carriers, $I$ is the injection current, $e$ is the electron charge, and the feedback term contains the external cavity round trip time $\tau$, the feedback strength and the feedback phase .

In the original work by Lang and Kobayashi, the gain $G(N(t)E(t))$ was assumed to be linear with $N$. Nevertheless, the gain saturates at large values of the intensity of emission. This effect is usually taken into account considering a nonlinear function for the gain,

$$G(N,E) = g\frac{N(t)-N_0}{1+s\;E(t)^{\;2}},$$

where $g \quad 1.5 \;\; 10^{\;8}\,\mathrm{ps}^{\;1}$ is the differential gain coefficient, $N_0 \quad 1.8 \;\; 10^8$ the carrier number at transparency[4] and $s \quad 10^{\;7}$ the gain saturation coefficient.

In the absence of feedback ( $= 0$), two different steady state solutions are obtained setting $E(t)=0$ and $N(t)=0$: the off solution

$$E_{st} = 0,$$

$$N_{st} = \frac{I}{e\gamma_n},$$

and the lasing solution given by $G(N,E)=\gamma$, in which

$$E_{st} \;=\; \sqrt{\frac{g\frac{I}{e} - g\gamma_n N_0 - \gamma\gamma_n}{\gamma(\gamma_n s + g)}}$$

and

$$N_{st} = N_0 + \frac{1+s\;E_{st}^{\;2}}{g}.$$

The threshold condition of the solitary laser (without feedback) is

$$I_{th} = e\gamma_n\left(N_0 + \gamma/g\right).$$

The feedback term can decrease significantly this threshold [105].

Such a simple rate equations model turns out to be a good formulation for numerical analysis of semiconductor lasers with delayed feedback. It also allows for analysis of

[4]Transparency refers to the situation below threshold in which there is a balance between the gain and the absorption within the active medium so that $G(N_0)=0$ [84].

dynamics and stability [140]. Furthermore, it can be easily extended to include modulation and noise [141, 142] and it gives good qualitative understanding of lasing for different dynamical regimes, including mode hopping [143, 144], low-frequency fluctuations [145, 146, 147], coherence collapse [143, 148], coexisting periodic solutions, and square-wave switching [58]. However, it does not explain multimode phenomena such as carrier sharing, spatial hole burning and mutual field injection, for which a full rate equations model of multi-mode semiconductor lasers should be considered [141, 148].

### Semiconductor lasers subject to ltered optical feedback

Originally, Lang and Kobayashi considered the feedback from an external mirror. If a frequency selective grating is used instead of a mirror, the Lang Kobayashi model (3.51) can be extended introducing an additional equation for the field that is fed back to the laser after spectral filtering. If a lorentzian filter is considered, the frequency dependent transmission function of the filter is [149, 150]

$$H(\omega) = \frac{}{+ i( \quad - \omega)}, \tag{3.52}$$

where is the filter half-width at half-maximum and is the frequency detuning between the solitary laser and the filter. Introducing this Lorentzian filter in the external cavity of the laser with delay time $T$ leads to the filtered field

$$F(\omega) = H(\omega) e^{i( \quad T)} E(\omega), \tag{3.53}$$

in such a way that in the time domain $F(t)$ obeys the delay differential equation

$$F(t) = \quad E(t-T)e^{i \quad} + (i \quad - \quad) F(t), \tag{3.54}$$

being $\varphi$ a constant phase induced by the filter. Summarizing the previous steps, the Lang-Kobayashi equations for filtered feedback read

$$\begin{aligned} E(t) &= \frac{1+i\alpha}{2}[G(N,E) - \gamma]E(t) + \quad F(t), \\ N(t) &= \frac{I}{e} - \gamma_n N(t) - G(N,E)\ E(t)\ ^2, \\ F(t) &= \quad E(t-T)e^{i \quad} + (i \quad - \quad) F(t). \end{aligned} \tag{3.55}$$

Filtered optical feedback offers the possibility to tune the frequency of the system by selecting specific values of the filter width and the frequency detuning between the laser and the filter [151, 152]. In particular, it turns to be practical for applications requiring stable single-mode operation or selection of a specific frequency [153]. In Part III of this thesis, we introduce a model of a semiconductor laser with multiple filtered optical feedback and explore a particular case with two filters displaying state-dependent delay dynamics characterized as erratic jumps between the states corresponding to two different delay time values.

### 3.3.4 External cavity modes, low frequency uctuations, coherence collapse and bridges

The Lang Kobayashi equations (3.55) admit periodic solutions of constant frequency $\omega_{st}$, field amplitude $\mathcal{E}_{\rm st}$ and carrier number $N_{\rm st}$,

$$\begin{aligned} E(t) &= \mathcal{E}_{\rm st} e^{i \ {\rm st} t}, \\ N(t) &= N_{\rm st}, \end{aligned} \tag{3.56}$$

which are known as external cavity modes (ECMs) and result from the interference between the electrical field at time $t$, $E(t)$, and the delayed electrical field coming back to the laser, $E(t-\tau)$. For a semiconductor laser with filtered optical feedback, the dynamics of which is given by Eqs. (3.55), the ECMs are given by Eqs. (3.56) and

$$F(t) = \mathcal{F}_{\rm st} e^{i( \ {\rm st} t + \ st)}, \tag{3.57}$$

where $\mathcal{F}_{\rm st}$ and $\phi_{st}$ are real positive constants. In the limit of low feedback ( 0) there is a single ECM, and this can be practical for imaging techniques [105, 154]. Increasing the feedback, successive ECM are born by pairs mode-antimode through saddle-node bifurcations [146]. The number of ECMs scales with because the feedback reduces the effective losses in the external cavity [105].

The ECMs are typically represented on a tilted ellipse in the $\omega_{st} - n$ plane, with $n = (N - N_0)g/\gamma - 1$, in which the points on the upper and lower half are called antimodes and modes, respectively. The tilting of this ellipse scales with $\alpha$. Destructive interference gives rise to saddle solutions or antimodes [146], which are unstable upon their birth, whereas the node solutions or modes appear at constructive interference conditions and can be stable [147]. The mode with maximum gain, corresponding to the lowest value of $N$, is always stable [155]. As an example, Fig. 3.16 shows the ECMs in the $\omega - n$ plane for a semiconductor laser with $\alpha = 5$, $g = 1.5 \ \ 10^{\ 8}\,{\rm ps}^{\ 1}$, and $N_0 = 1.5 \ \ 10^8$, without filtering (a) and with lorentzian filtering with $T = 1\,{\rm ns}$, $\ = 25\,{\rm ns}^{\ 1}$, $\ /2\pi = -8$ GHz, $\varphi = 0$ and different filter bandwidths. The ECMs constitute a backbone around which the dynamics is organized. We will come back to this topic in Part III of this thesis, where we address the study of the dynamics of a semiconductor laser with filtered feedback from multiple filters.

An interesting dynamical regime of semiconductor lasers with delayed optical feedback is low-frequency fluctuations (LFFs), which takes place under the conditions of low injection current and moderate feedback strength. The LFF regime, also known as intermittent chaos, is characterized by sudden dropouts of the laser output intensity [154], as shown in Fig. 1.2. These dropouts take place irregularly in time with an average frequency of the order of several MHz to a hundred of MHz, as opposed to the fast relaxation oscillations which occur at the GHz scale [105]. LFFs also exhibit fast inner temporal structures on the subnanosecond scale [20]. In the limit of small feedback rate and large delay, LFFs coexist with a stable emission of the maximum gain mode for a broad range of values of the parameters [156]. Increasing the pump current, the time intervals between dropouts decrease until the LFFs disappear, giving rise to the full developed coherence collapse regime [157] characterized by chaotic itinerancy between the ECMs [158, 159, 20].

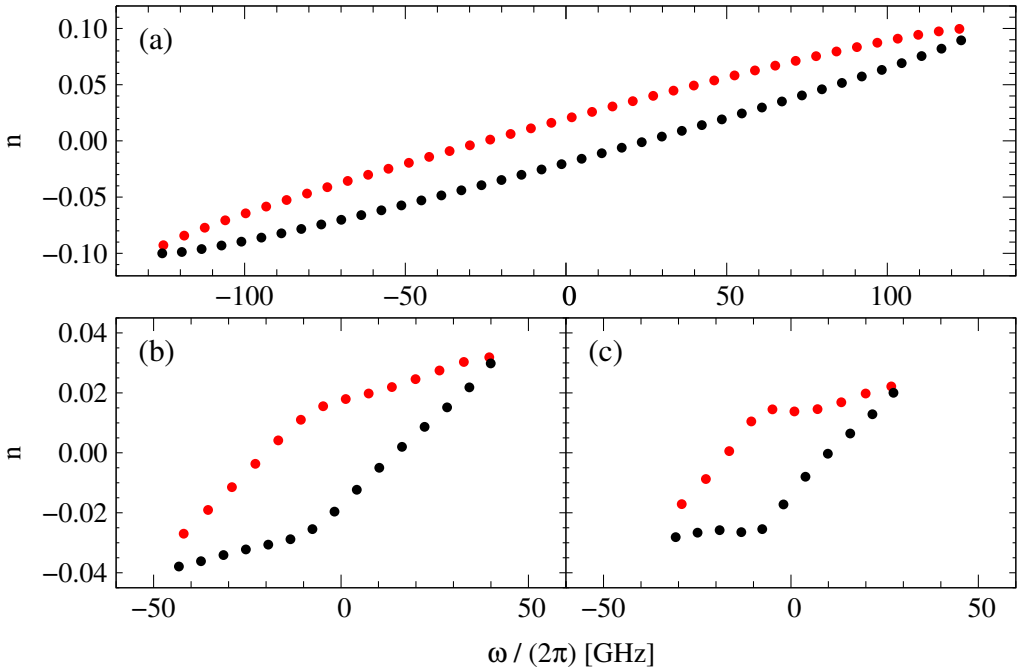


**Figure 3.16:** ECMs in the $\omega_{st} - n$ plane for a semiconductor laser with $\alpha = 5$, $g$ 1.5 10 $^{8}$ ps $^{1}$, and $N_0 = 1.5$ $10^8$, (a) without filtering and (b)-(c) with lorentzian filtering with $T = 1\,\text{ns}$, $= 25\,\text{ns}$ $^{1}$, $/2\pi = -8\,\text{GHz}$, $\varphi = 0$ and (b) $/(2\pi) = 8\,\text{GHz}$ (c) $/(2\pi) = 16\,\text{GHz}$. Black and red dots represent modes and antimodes, respectively.

The origin of LFFs is attributed to successive Hopf bifurcations of the ECMs [160]. In 1994, Petermann and Tager [161] discovered that semiconductor lasers with delayed feedback could exhibit fast oscillations with frequencies of several tens of GHz, induced by the mode-antimode beating between two ECMs of the external cavity with the same carrier number. They found that these high-frequency oscillations occur under the conditions of short delay time and high feedback rate. These solutions are known as bridges and have also been analyzed in [162, 163, 164]. In particular, Pieroux et al. found that the ECMs are interconnected through bridges via a Hopf bifurcation mechanism [162]. The period of these fast oscillations is inversely proportional to the frequency difference between the two modes, $P = 2\pi$ $_1 -$ $_2$ $^{1}$ [105]. Such fast oscillations could be interesting for signal processing applications.

# Part II

# Synchronization in mutually delay-coupled optoelectronic oscillators

Chapter 4

# Introduction, model, and onset of periodic solutions with identical OEOs

## 4.1 Introduction

We study in the next three chapters the synchronization phenomenon in two coupled OEOs. Each oscillator is subject to the influence of its delayed feedback loop (self-feedback), as well as to the delayed output of the other oscillator (cross-feedback).

In systems with multiple delays, the ratio between different delay times plays a crucial role in the synchronization, as it has recently been shown for mutually coupled chaotic systems [165]. Here, we focus on the tunability of multiple stable periodic solutions generated by the mutually coupled OEOs rather than on their synchronization efficiency in the chaotic regime. We will show that the interplay between the intrinsic and coupling delay times leads to interesting dynamical regimes.

We will consider the limit of large delay times, in which delays are large compared to the intrinsic time scales, and we will mainly consider parameter values for which periodic square waves are stable. In particular, we will focus on the existence and stability of synchronized square-wave solutions.

From a theoretical point of view, the OEO systems considered here have the advantage that, despite showing a rich variety of dynamical behaviours, they are described by relatively simple equations. On the one hand, this enables to evaluate the Hopf bifurcations of the steady state allowing to predict the different families of oscillatory solutions that arise as the pump power is increased. On the other hand, this allows one to develop asymptotic methods for large delays which are useful to determine the amplitude and shape of the oscillatory solutions. We expect that this combined methodology can be applied to other systems with two delay times and lead to similar results.

As we will see in Chapter 5, two mutually coupled identical OEOs with negative feedback can generate stable in-phase and out-of-phase[1] synchronized square waves with symmet-

[1] In this thesis, by out-of-phase, we will refer to synchronized periodic solutions that are dephased by half of the period, also referred as antiphase solutions in the literature.

ric duty cycle when the ratio between the delay times fulfills suitable conditions [111]. For positive feedback, as we will show in Chapter 6, in- and out-of-phase synchronization is also obtained but in this case the duty cycle is not symmetric [112].

Synchronization of square waves has also been obtained with EELs subject to polarization rotated feedback (PROF) [57], in vertical-cavity surface-emitting lasers (VCSELs) [56, 57, 60] and semiconductor ring lasers [58]. The square waves generated with mutually EELs under PROF were always in anti-phase.

An advantage of using mutually coupled OEOs with respect to mutually coupled EELs is that OEOs can produce both synchronized in-phase and out-of phase square waves. Furthermore, we will show that two mutually coupled OEOs can generate symmetric and asymmetric square-wave switching even when they are identically coupled, in contrast with ring lasers which need to have asymmetric couplings to produce asymmetric square waves.

Moreover, in Chapter 7, we show that two mutually coupled non-identical OEOs, besides in-phase and out-of-phase, can generate square waves synchronized at a quarter of the period ($T/4$) [113]. The key point to obtain such $T/4$ solutions is that the two OEOs operate with different offset phases, in such a way that the feedback is negative in one and positive in the other, namely the feedback is mixed.

### 4.1.1 Outline

The outline of this part of the thesis is the following. In this chapter, in Sec. 4.2 we describe the system of two mutually coupled OEOs which is studied in the next three chapters for square-wave pulse generation, in Sec. 4.3 we particularize this system for the case of identical OEOs, and in Sec. 4.4 we show the emergence of square-wave solutions from the linear stability analysis of the zero solution in the limit of large delays and the ideal case of identical OEOs. The results obtained in Secs. 4.3 and 4.4 are relevant for Chapter 5 and Chapter 6, in which identical delay-coupled OEOs are considered. In Chapter 5, we study the generation of symmetric square-wave pulses in a model for two mutually delay-coupled OEOs with offset phases in the range for negative feedback [111]. In Chapter 6, we study the emergence of stable asymmetric square waves in the same model but in the case where the offset phases are in the range for positive feedback [112]. The general case of non-identical delay-coupled OEOs is addressed in Chapter 7 [113].

## 4.2 System description

We consider two OEOs similar to those of [166], mutually coupled with delay, both fed by a cw semiconductor laser (LD) emitting with intensity $P$ as illustrated in Fig. 4.1. Each OEO consists of a Mach-Zehnder interferometer (MZI), an optical delay line, a photodiode (PD) with sensitivity $S$ and an amplifier. The variables related to loop $i$ are identified with subindex $i$, $i = 1, 2$. The optical power after $\mathrm{MZI}_i$ is split into two

parts. A fraction $\alpha_{ii}$ is delayed $T_{ii}$ within $\text{OEO}_i$ (self-feedback) and a fraction $\alpha_{ij}$ with $j \neq i$ couples $\text{OEO}_i$ with $\text{OEO}_j$ with a delay time $T_{ij}$ (cross-feedback). A photodiode (PD) detects the intensity resulting from the combination of the self- and cross-feedback optical beams and produces an electrical signal, which is amplified, band-pass filtered, and finally used to drive the Mach-Zehnder AC electrode. For each loop, the dynamics results from a combination of the nonlinear effect due to the MZI plus a linear filtering process associated to the electrical circuit [100, 166].

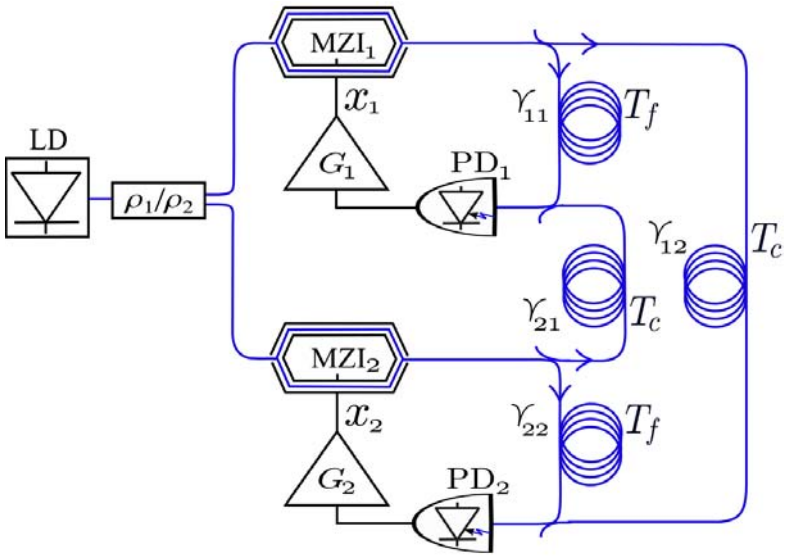


**Figure 4.1:** Schematic diagram of the system we are modeling consisting of two mutually coupled OEOs. Each OEO consists of Mach-Zehnder Interferometer labeled as MZI, a fiber delay loop with a delay time $T_f = T_{ii}$, a photodiode labeled as PD, and a RF amplifier labeled as $G$. The output of the amplifier modulates one of the arms of the Mach-Zehnder. The OEOs are fed by a laser diode, labeled as LD, the power output of which is split in two parts by a $\rho_1/\rho_2$ fiber splitter. The two OEO are mutually coupled with a cross-feedback delay time $T_c = T_{ij,j\neq i}$.

The dynamics of the coupled OEOs can be described as follows. As in [166], we assume there isn't any reflection in the optical path so that the optical electric field can be described as a scalar $E$. Each arm of the MZI can be considered as a Pockels cell exhibiting a linear dependence of the refractive index $n$ on $E$,

$$n(E) = n_0 + \left.\frac{dn}{dE}\right|_{E=0} E, \tag{4.1}$$

where $n_0$ is the intrinsic refractive index of the material (without electric field). Light with wavelength $\lambda_0$ crossing the Pockels medium changes its phase depending on the refractive index as well as on the length $L$ of the arm:

$$\Delta\varphi = \frac{2\pi}{\lambda_0} n(E) L. \tag{4.2}$$

When a voltage $V$ is applied across an arm of transversal size $d$, the corresponding electric field is given by $E = V/d$, and thus the phase change along that arm can be

written as

$$\Delta\varphi = \Delta\varphi_0 + \pi\frac{V}{V_\pi}, \tag{4.3}$$

where $\Delta\varphi_0 = 2\pi n_0/\lambda_0$ and $V_\pi$ is the voltage required for a modulation of $\pi$ in the phase,

$$V_\pi = \frac{\lambda_0 d}{2L}\left.\frac{dn}{dE}\right|_{E=0}^{-1}. \tag{4.4}$$

Considering that the optical field at the input of MZI$_i$ is $\sqrt{P\rho_i}e^{i}$ and that the voltage $V_i$ applied to MZI$_i$ has a DC and a RF component, $V_{B_i}$ and $V_{RF_i}(t)$ respectively, and introducing the normalized voltages $x_i(t) = \pi V_{RF_i}(t)/2V_{\pi_i}$ and $\Phi_i = \pi V_{B_i}/2V_{\pi_i}$, the electric field at the output of MZI$_i$ is given by

$$E_{\mathrm{MZI}_i}(t) = \sqrt{P\rho_i}e^{i} \left[1 + e^{i[2x_i(t)+2]}\right], \tag{4.5}$$

where $\phi_{0_i} = \Delta\varphi_{0_i} + \varphi_i$. Without losing generality and for simplicity, we take $\phi_{0_1} = 0$ and define $\Phi_0 = \phi_{0_2}$. The optical field arriving at photodiode PD$_i$ is given by

$$E_{\mathrm{PD_i}}(t) = \alpha_{ii}E_{\mathrm{MZI_i}}(t - T_{ii}) + \alpha_{ji}E_{\mathrm{MZI_j}}(t - T_{ji}). \tag{4.6}$$

The output of photodiode PD$_i$ with sensitivity $S_i$ is

$$V_{\mathrm{PD_i}}(t) = S_i \left|E_{\mathrm{PD_i}}(t)\right|^2. \tag{4.7}$$

Finally, the voltage $V_{\mathrm{PD}_i}(t)$ is amplified and filtered by the linear band-pass amplifier with effective gain $G_i$ and low and high cut-off characteristic times $_i$ and $\tau_i$, respectively. The normalized voltage at the output of the amplifier, $x_i(t)$, (which is used to modulate MZI$_i$) is given by

$$\left(1 + \frac{\tau_i}{i}\right)\left[\dot{x}_i + \tau_i x_i + \frac{1}{i}\int_{t_0}^{t} x_i(s)ds\right] = G_i V_{\mathrm{PD_i}}, \tag{4.8}$$

where the dot stands for time derivative. In this thesis, we will consider $_i = 5$ s and $\tau_i = 25$ ps for the most part of the work, so that we can consider the term $1 + \tau_i\,{}_i^{-1} \approx 1$. As in the subsection 3.2.5, the integral term plays a relevant role in the dynamics since it is responsible for the zero mean value of $V$, which is achieved after a slow transient, of the order of the slowest time , characteristic of the bandpass dynamics that removes any DC component [103]. Combining Eqs. (4.5)-(4.8), one gets that the dynamics of the system is ruled by two delay integro-differential equations. Introducing two additional variables, $y_i(t) = \int_{t_0}^{t} x_i(t')dt'$, leads to a system of four delay differential equations,

$$\begin{aligned}\tau_i\dot{x}_i(t) = -x_i(t) - {}_i^{-1}y_i(t) + P\,\Big[&\gamma_{ii}^2\cos^2\left[x_i(t - T_{ii}) + \Phi_i\right] + \gamma_{ji}^2\cos^2\left[x_j(t - T_{ji}) + \Phi_j\right] \\ &+ 2\gamma_{ii}\gamma_{ji}\cos\left[x_j(t - T_{ji}) + \Phi_j\right]\cos\left[x_i(t - T_{ii}) + \Phi_i\right] \\ &\cos\left[x_i(t - T_{ii}) - x_j(t - T_{ji}) + \Phi_i - \Phi_j + (-1)^i\Phi_0\right], \\ \dot{y}_i(t) = x_i(t),\end{aligned} \tag{4.9}$$

where $i, j = 1, 2$, $j \neq i$, and $\gamma_{ij} = \sqrt{G_j S_j}\sqrt{\rho_i\rho_j}\alpha_{ij}$ are effective coupling strengths.

For simplicity, now we take the two systems identical as concerns and $\tau$ and consider only two different delays, $T_f = T_{ii}$ and $T_c = (T_{12} + T_{21})/2$. Then, the system (4.9) has a fix point solution,

$$\begin{aligned} x_i(t) &= x_{i_{st}} = 0, \\ y_i(t) &= y_{i_{st}} = \ P\ \gamma_{ii}^2 \cos^2\Phi_i + \gamma_{ji}^2 \cos^2\Phi_j + 2\gamma_{ii}\gamma_{ji}\cos\Phi_j \cos\Phi_i \cos\left[\Phi_1 - \Phi_2 - \Phi_0\right] \ , \end{aligned} \tag{4.10}$$

where as before $i, j = 1, 2$ and $j \neq i$. This is the only fixed point solution of the system. Introducing $Y_i(t) = \left[y_i(t) - y_{i_{st}}\right]/T_c$ and scaling the time with $T_c$, $s = t/T_c$, we get

$$\begin{aligned} \varepsilon x_i'(s) = -x_i(s) - \delta Y_i(s) + P\ \gamma_{ii}^2\ \ &\cos^2\left[x_i(s-s_0) + \Phi_i\right] - \cos^2\Phi_i \\ &+ \gamma_{ji}^2\ \ \cos^2\left[x_j(s-1) + \Phi_j\right] - \cos^2\Phi_j \\ &+ 2\gamma_{ii}\gamma_{ji}\ \ \cos\left[x_i(s-s_0) + \Phi_i\right]\cos\left[x_j(s-1) + \Phi_j\right] \\ &\quad \cos[x_i(s-s_0) - x_j(s-1) + \Phi_i - \Phi_j + (-1)^i\Phi_0] \\ &- \cos\Phi_i \cos\Phi_j \cos(\Phi_1 - \Phi_2 - \Phi_0) \quad , \\ Y_i'(s) = x_i(s), & \end{aligned} \tag{4.11}$$

where prime means differentiation with respect to time and

$$s_0 = T_f/T_c, \quad \varepsilon = \tau T_c\ ^{1}, \quad \delta = T_c\ \ ^{1}. \tag{4.12}$$

In this notation, the fixed point is $(x_{st} = 0, Y_{st} = 0)$; in what follows, we refer to it as the zero solution.

We consider that the delay time $T_c$ has a value of the order of tens of nanoseconds. Therefore, $\varepsilon$ is of order $10\ ^{3}$ and $\delta$ of order $10\ ^{2}$. We will consider $T_f$ to be not much larger than $T_c$, so that we focus in the range $0 \quad s_0 \quad 2$.

## 4.3 Identical delay-coupled OEOs

In the next two chapters, we consider that the two Mach-Zhenders are identical, so that $\Phi_0 = 0$, $\Phi_1 = \Phi_2 = \Phi$, and $\gamma_{11} = \gamma_{22} = \gamma_{12} = \gamma_{21} = \gamma$. Making use of the trigonometric identity $\cos(\alpha)\cos(\ ) = \frac{1}{2}\left[\cos(\alpha - \ ) + \cos(\alpha + \ )\right]$, Eqs. (4.11) with $\Phi_0 = 0$ and $\gamma_{11} = \gamma_{22} = \gamma_{12} = \gamma_{21} = \gamma$ can be simplified as

$$\begin{aligned} \varepsilon x_i'(s) = &- x_i(s) - \delta Y_i(s) + P\gamma^2\ \ \cos\left[2x_i(s-s_0) + 2\Phi\right] + \cos\left[2x_j(s-1) + 2\Phi\right] \\ &+ \cos^2\left[x_i(s-s_0) - x_j(s-1)\right] - 1 - 2\cos(2\Phi) \quad , \\ Y_i'(s) = &x_i(s). \end{aligned} \tag{4.13}$$

We note that Eqs. (4.13) are invariant to the symmetry $x_i \quad -x_i$, $\Phi_i \quad -\Phi_i - \frac{\pi}{2}$, provided that

$$x_j(s - s_0) = x_i(s - 1), \tag{4.14}$$

where $i, j = 1, 2$ and $j \neq i$. As discussed in Sec. 5.3, this condition is fulfilled by solutions exhibiting generalized lag synchronization.

Eqs. (4.11) and (4.13) admit time-periodic square-wave solutions. These periodic square-wave solutions arise through Hopf bifurcations of the zero solution. In Sec. 4.4, we determine the Hopf bifurcations of the zero solution for the ideal case of identical oscillators. The analysis of Sec. 4.4 is valid for Chapter 5 and Chapter 6, in which the system (4.13) of identical OEOs is considered. The linear stability analysis of the zero solution with the general model (4.11) for non-identical OEOs is addressed in Chapter 7.

## 4.4 Linear stability analysis of the zero solution for identical OEOs

In this subsection, we concentrate on the Hopf bifurcations of the steady state for identical OEOs. Specifically, we consider small perturbations $U_i(s) = x_i(s) - x_{i_{st}}$ and $V_i(s) = Y_i(s) - Y_{i_{st}}$ around the zero solution, and formulate the linearized equations for the small perturbations $U_i$ and $V_i$. Using $\cos[2U_i + 2\Phi] = \cos(2\Phi) - \sin(2\Phi)U_i + O(U^2)$ and $\cos[U_i + U_j] = 1 + O(U_i^2, U_j^2)$, we obtain

$$\begin{aligned} \varepsilon U_i'(s) &= -U_i(s) - \frac{}{2}\left[U_i(s - s_0) + U_j(s-1)\right] - \delta V_i, \\ v_i'(s) &= U_i(s), \end{aligned} \tag{4.15}$$

where

$$4P\gamma^2 \sin(2\Phi) \tag{4.16}$$

is an effective bifurcation parameter as seen below. According to Eqs. (4.15), the feedback is negative for $\quad > 0$ ($\Phi \quad [0, \pi/2]$) and positive for $\quad < 0$ ($\Phi \quad [-\pi/2, 0]$).

Equations (4.15) admit solutions of exponential form, $U_i(s) = u_i \exp\left[(\lambda + i\omega)s\right]$ and, since $V_i$ is the integral of $U_i$, $V_i(s) = u_i \exp\left[(\lambda + i\omega)s\right]/(\lambda + i\omega)$. Replacing $U_i$ and $V_i$ in Eqs. (4.15) leads to a homogeneous system of two linear algebraic equations for $u_1$ and $u_2$:

$$\begin{aligned} 0 =& u_1 \;\; 1 + \varepsilon(\lambda + i\omega) + \delta(\lambda + i\omega) \;\; ^{1} + \frac{}{2} e \;\; ^{(\lambda + i \;\; )s_0} \;\; + u_2 \frac{}{2} e \;\; ^{(\lambda + i \;\; )}, \\ 0 =& u_1 \frac{}{2} e \;\; ^{(\lambda + i \;\; )} + u_2 \;\; 1 + \varepsilon(\lambda + i\omega) + \delta(\lambda + i\omega) \;\; ^{1} + \frac{}{2} e \;\; ^{(\lambda + i \;\; )s_0} \;\; . \end{aligned} \tag{4.17}$$

At the Hopf bifurcation, $\lambda = 0$ and the linearized problem reduces to

$$\begin{aligned} 0 =& u_1 \;\; 1 + i\omega\varepsilon - i\frac{\delta}{\omega} + \frac{}{2} e \;\; ^{i \;\; s_0} \;\; + u_2 \frac{}{2} e \;\; ^{i \;\; }, \\ 0 =& u_1 \frac{}{2} e \;\; ^{i \;\; } + u_2 \;\; 1 + i\omega\varepsilon - i\frac{\delta}{\omega} + \frac{}{2} e \;\; ^{i \;\; s_0} \;\; . \end{aligned} \tag{4.18}$$

The condition of a non-trivial solution leads to the characteristic equation

$$1 + i\omega\varepsilon - i\frac{\delta}{\omega} + \frac{}{2} e \;\; ^{i \;\; s_0} = \;\; \frac{}{2} e \;\; ^{i \;\; } \;\; . \tag{4.19}$$

Replacing Eq. (4.19) into Eq. (4.18), we obtain $u_1 =$ $u_2$. Therefore, there are two different families of Hopf bifurcations. The + sign leads to in-phase oscillations of $x_1$ and $x_2$, while for the − sign the oscillations are out-of-phase.

Splitting Eq. (4.19) into real and imaginary part gives rise to two equations for and $\omega$:

$$1 + \frac{}{2}\left[\cos(\omega s_0) \quad \cos(\omega)\right] = 0, \tag{4.20}$$

$$\omega\varepsilon - \frac{\delta}{\omega} - \frac{}{2}\left[\sin(\omega s_0) \quad \sin(\omega)\right] = 0. \tag{4.21}$$

### 4.4.1 In-phase oscillations

For in-phase oscillations, Eqs. (4.20) and (4.21) can be written as

$$\cos \quad \omega\frac{s_0+1}{2} \quad \cos \quad \omega\frac{s_0-1}{2} \quad = -1, \tag{4.22}$$

$$\sin \quad \omega\frac{s_0+1}{2} \quad \cos \quad \omega\frac{s_0-1}{2} \quad = \omega\varepsilon - \frac{\delta}{\omega}. \tag{4.23}$$

Dividing Eq. (4.23) by Eq. (4.22) leads to an implicit equation for $\omega$ which does not depend on ,

$$\tan \quad \omega\frac{s_0+1}{2} \quad = \frac{\delta}{\omega} - \omega\varepsilon. \tag{4.24}$$

Since $\delta$ and $\varepsilon$ are small, the argument of the tangent must be close to a multiple of $\pi$. Therefore, the frequency of the in-phase oscillations is given by

$$\omega_n^{\text{in}} = \frac{2n\pi}{s_0+1} + \alpha_n^{\text{in}}(\varepsilon,\delta), \tag{4.25}$$

where $\alpha_n^{\text{in}}$ is a correction of order $O(\varepsilon,\delta)$.

The correction $\alpha_n^{\text{in}}$ can be obtained replacing Eq. (4.25) in Eq. (4.24) and expanding the tangent. Doing so, we obtain a quadratic equation for $\alpha_n^{\text{in}}$,

$$(s_0+1)^2(s_0+1+2\varepsilon){\alpha_n^{\text{in}}}^2 + 2n\pi(s_0+1)(s_0+1+4\varepsilon)\alpha_n^{\text{in}} - 2\delta(s_0+1)^2 + 4n\pi\varepsilon = 0. \tag{4.26}$$

For $n = 0$, $\alpha_0^{\text{in}}$ is the only contribution to the frequency. From Eq. (4.26), we obtain

$$\omega_0^{\text{in}} \qquad \overline{\frac{2\delta}{s_0+1+2\varepsilon}} \qquad \overline{\frac{2\delta}{s_0+1}}. \tag{4.27}$$

These are in-phase oscillations at a low frequency that is determined mainly by $\delta$. For typical parameter values, the period of these solutions is of the order of hundreds of microseconds. As shown in the subsections 3.2.6 and 3.2.8, the slow oscillations, which in this thesis are also referred to as microsecond solutions, are also found in a single OEO with positive feedback [61, 104] and can be used for pure microwave generation [87, 88, 106, 101]. The period of the microsecond oscillations can be much larger than

the delay times present in the system and, therefore, they do not take the shape of square waves, as illustrated in Sec. 6.3. For this reason here we will be mainly interested in the case $n \quad 1$.

For $n \quad 1$, $\alpha_n^{\text{in}}$ can be neglected for the values of $s_0$ considered here since it is of order $\varepsilon$ and $\delta$, which are typically of order $10^{-3}$ and $10^{-2}$ respectively, and therefore it is much smaller than $\frac{2n\pi}{s_0+1}$. To zero order in $\alpha_n^{\text{in}}$ we obtain

$$\omega_n^{\text{in}} \quad \frac{2n\pi}{s_0+1}, \quad n \quad 1. \tag{4.28}$$

Considering only the terms at first order in $\alpha_n^{\text{in}}$ in Eq. (4.26), we get

$$\alpha_n^{\text{in}} \quad \frac{\delta(s_0+1)^2-(2n\pi)^2\varepsilon}{n\pi(s_0+1)(s_0+1+4\varepsilon)} \quad \frac{\delta(s_0+1)^2-(2n\pi)^2\varepsilon}{n\pi(s_0+1)^2} = \frac{\delta}{n\pi} - \frac{4n\pi\varepsilon}{(s_0+1)^2}, \quad n \quad 1. \tag{4.29}$$

We now determine the threshold for the onset of in-phase oscillations. From (4.22), we obtain

$$\overset{\text{in}}{n} = -\frac{1}{\cos \ \omega_n \frac{s_0+1}{2} \ \cos \ \omega_n \frac{s_0 \ 1}{2}}. \tag{4.30}$$

For in-phase microsecond oscillations ($n = 0$), replacing Eq. (4.27) into Eq. (4.30) leads to

$$\overset{\text{in}}{0} = -\frac{1}{\cos \ \sqrt{\frac{(s_0+1)}{2}} \ \cos \ (s_0-1) \ \sqrt{2(s_0+1)}} \quad -1-\frac{\delta}{2}\frac{s_0^2+1}{s_0+1}. \tag{4.31}$$

Thus, the Hopf bifurcation associated to microsecond oscillations can only take place for positive feedback. As for fast in-phase oscillations ($n \quad 1$), at zero order, replacing Eq. (4.28) into Eq. (4.22) leads to

$$\overset{\text{in}}{n} \quad -\frac{1}{\cos(\omega_n^{\text{in}})}, \quad n \quad 1. \tag{4.32}$$

Therefore, fast in-phase oscillations can appear both for positive and negative feedback provided $\quad 1$.

### 4.4.2 Out-of-phase oscillations

For out-of-phase oscillations, Eqs. (4.20) and (4.21) can be written as

$$\sin \ \omega\frac{s_0+1}{2} \ \sin \ \omega\frac{s_0-1}{2} \ = 1, \tag{4.33}$$

$$\cos \ \omega\frac{s_0+1}{2} \ \sin \ \omega\frac{s_0-1}{2} \ = \omega\varepsilon - \frac{\delta}{\omega}. \tag{4.34}$$

Dividing Eq. (4.34) by Eq. (4.33) leads to

$$\cot \ \omega\frac{s_0+1}{2} \ = \omega\varepsilon - \frac{\delta}{\omega}. \tag{4.35}$$

In the limit of small $\delta$ and $\varepsilon$, the argument of the cotangent must be closer to $n\pi + \pi/2$. Thus, out-of-phase oscillations have a frequency given by

$$\omega_n^{\text{out}} = \frac{(2n+1)\pi}{s_0+1} + \alpha_n^{\text{out}}(\varepsilon, \delta), \tag{4.36}$$

where $\alpha_n^{\text{out}}$ is a correction of order $O(\varepsilon, \delta)$, which is much smaller than $\frac{(2n+1)\pi}{s_0+1}$ for any $n$, including $n = 0$, for the values of $s_0$ considered here. Thus there are no low frequency solutions synchronized out of phase for low values of $s_0$. To zero order in $\alpha_n^{\text{out}}$, we get

$$\omega_n^{\text{out}} \quad \frac{(2n+1)\pi}{s_0+1}, \quad n \quad 0. \tag{4.37}$$

The correction $\alpha_n^{\text{out}}$ can be obtained replacing Eq. (4.36) in Eq. (4.35) and expanding the cotangent. Doing so leads to a quadratic equation for $\alpha_n^{\text{out}}$,

$$(s_0+1)^2 \alpha_n^{\text{out}\,2} + (2n+1)\pi(\ \ + \varepsilon)(s_0+1)\alpha_n^{\text{out}} - \delta(s_0+1)^2 + (2n+1)^2\pi^2\varepsilon, \tag{4.38}$$

where $\ = \frac{s_0+1}{2} + \varepsilon$. Considering only the terms at first order in $\alpha_n^{\text{out}}$, we get the following equation for the correction $\alpha_n^{\text{out}}$,

$$\alpha_n^{\text{out}} \quad \frac{2\delta(s_0+1)^2 - 2(2n+1)^2\pi^2\varepsilon}{(2n+1)\pi(s_0+1)\left[(s_0+1)+4\varepsilon\right]} \quad \frac{2\delta}{(2n+1)\pi} - \frac{2(2n+1)\pi\varepsilon}{(s_0+1)^2}. \tag{4.39}$$

Finally, we obtain the threshold for out-of-phase oscillations. From (4.33), we get

$$\begin{matrix}\text{out}\\ n\end{matrix} = \frac{1}{\sin\ \ \omega_n \frac{s_0+1}{2}\ \ \sin\ \ \omega_n \frac{s_0\ \ 1}{2}}. \tag{4.40}$$

Replacing Eq. (4.37) into Eq. (4.33) and using that $\sin(a + \pi/2) = \cos(a)$, we obtain, at zero order,

$$\begin{matrix}\text{out}\\ n\end{matrix} \quad \frac{1}{\cos(\omega_n^{\text{out}})}, \quad n \quad 0. \tag{4.41}$$

Therefore, fast out-of-phase oscillations can appear both for positive and negative feedback provided 1.

Chapter 5

# Identical delay-coupled OEOs with negative feedback

5.1

## Introduction

In this chapter, we consider the system of two identical delay-coupled OEOs described in Sec. 4.2 under negative delayed feedback as prototypical to study the conditions for synchronization of square-wave oscillations with symmetric duty cycle, namely with a duty cycle that is half of the period.

This chapter is organized as follows. We first determine parameter conditions for which synchronized square-wave periodic solutions appear, on the basis of the results for the Hopf bifurcations obtained in Sec. 4.4. Second, we develop a map approximation to obtain a theoretical prediction for the amplitude of the periodic oscillations, as well as to determine the secondary instabilities of the periodic square-wave oscillations. Then, the theoretical predictions are compared with numerical simulations of the full dynamical model. After that, we analyze the effect of a small mismatch in the delay times on the degradation of the square waves. Finally, we summarize our results.

5.2

## Hopf bifurcations of the steady state

In Sec. 4.4, it was shown that, for negative feedback ($\Phi \quad [0, \pi/2]$), fast in-phase and out-of-phase oscillations can appear provided $\quad 1$. We now aim to obtain the dependence of the period of the oscillations on the ratio $s_0$ between the two delays. To do so, we consider $s_0$ as a control parameter and plan to determine the Hopf bifurcation points in terms of $\ _n$.

There is a family of in-phase Hopf bifurcation curves $\ ^{\text{in}}_n(s_0)$, which can be obtained solving numerically Eqs. (4.24) and (4.30). The bifurcation curves with $n \quad 9$ with $0 \quad \ _n \quad 2$ and $s_0 \quad [0, 2]$ for the in-phase solutions are shown in Fig. 5.1(a).

Similarly, there is a family of out-of-phase Hopf bifurcation lines $^{\text{out}}_{n}(s_0)$, which can be obtained from Eqs. (4.35) and (4.40). The out-of-phase Hopf bifurcation curves with $n$ 9, 0 $_n$ 2 and $s_0$ [0, 2] are plotted in Fig. 5.1(b). All the curves exhibit a minimum at $_n = 1$ and close to the minimum have a parabolic shape.

From a physical point of view, we are particularly interested in determining the possible Hopf bifurcations that appear exactly at $_n = 1$ for specific values of $s_0$, since these correspond to the first Hopf bifurcations that are encountered when increasing $_n$, proportional to the LD power $P$, in a system with given delay times. This situation corresponds to $\cos(\omega_n) = -1$ in Eq. (4.32) or $\cos(\omega_n) = 1$ in Eq. (4.41).

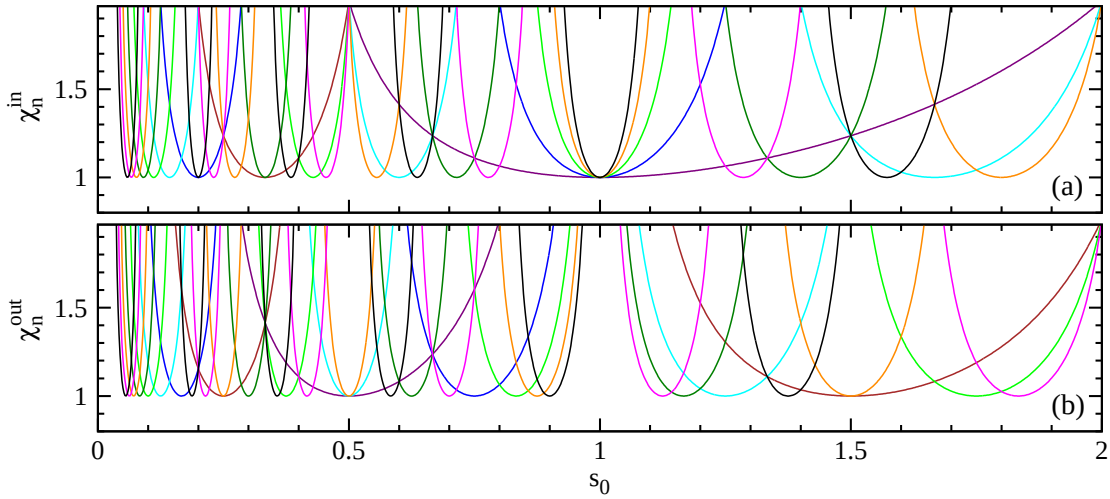


**Figure 5.1:** Hopf bifurcation curves with $_n > 0$ for the in-phase (a) and out-of-phase (b) solutions with $n = 1$ (purple line), $n = 2$ (brown line), $n = 3$ (dark cyan line), $n = 4$ (cyan line), $n = 5$ (green-yellow line), $n = 6$ (dark green line), $n = 7$ (orange line), $n = 8$ (magenta line), and $n = 9$ (black line).

### 5.2.1 In-phase oscillations

For in-phase oscillations, the condition $\cos(\omega_n) = -1$ implies $\omega_n = (2m + 1)\pi$, where $m$ $Z$. Then, from Eq. (4.28), we obtain the following values of $s_0$:

$$s_0^{\text{in}} = \frac{2(n - m) - 1}{2m + 1} = \frac{2l + 1}{2m + 1}, \tag{5.1}$$

where

$$l \quad n - m - 1. \tag{5.2}$$

The condition $s_0^{\text{in}} > 0$ restricts the value of $m$ to the range 0 $m < (2n - 1)/2$, thus $l$ 0. The period of the Hopf bifurcation oscillations is determined using Eq. (4.28) and is given by

$$T^{\text{in}} = \frac{2}{2m + 1}. \tag{5.3}$$

From Eq. (5.1), one has

$$1 - s_0^{\text{in}} = \frac{2(m-l)}{2m+1}, \tag{5.4}$$

namely, for in-phase periodic solutions, the dimensionless time difference $(T_c - T_f)/T_c = 1 - s_0$ has to be an even/odd rational number. Using Eq. (5.4), the period can also be written as

$$T^{\text{in}} = \frac{1 - s_0^{\text{in}}}{m-l}. \tag{5.5}$$

### 5.2.2 Out-of-phase oscillations

For out-of-phase oscillations, the condition $\cos(\omega_n) = 1$ implies $\omega_n = 2m\pi$ where $m \quad Z$. Then, from Eq. (4.37), we determine the following values of $s_0$:

$$s_0^{\text{out}} = \frac{1 + 2(n-m)}{2m} = \frac{2k+1}{2m}, \tag{5.6}$$

where

$$k \quad n - m. \tag{5.7}$$

The condition $s_0^{\text{out}} > 0$ now restricts the value of $m$ to the range $0 < m < (1+2n)/2$, thus $k \quad 0$. The period of the Hopf bifurcation oscillations is found using Eq. (4.37) and is

$$T^{\text{out}} = \frac{1}{m}. \tag{5.8}$$

From (5.6) one has

$$1 - s_0^{\text{out}} = \frac{2(m-k)-1}{2m}, \tag{5.9}$$

that is, the dimensionless time difference $1 - s_0$ has to be an odd/even rational number. From Eq. (5.6) and Eq. (5.9), the period can be written as

$$T^{\text{out}} = \frac{2(1 - s_0^{\text{out}})}{2(m-k)-1}. \tag{5.10}$$

### 5.2.3 Remarks on the onset of in- and out-of-phase solutions

A few observations are worth pointing out. First, in-phase and out-of-phase Hopf bifurcation points never appear for the same $s_0$. This can be verified by equating Eq. (5.1) with $n_1 > 0$ and $m_1 \quad 0$, and Eq. (5.6) with $n_2 \quad 0$ and $m_2 > 0$. After simplifying, we find $4m_2n_1 = (2m_1+1)(1+2n_2)$, which implies that an even number should be equal to an odd number.

Second, several in-phase Hopf bifurcations or several out-of-phase solutions with different periods may appear for the same value of $s_0$. This means that the Hopf bifurcation at $_n = 1$ can be multiple. This degeneracy is not eliminated if we consider $\varepsilon \neq 0$. For example, if $s_0 = 1$, Hopf bifurcations to in-phase solutions appear if $m = (n-1)/2$ ($n > 0$, $m \quad 0$). From the conditions for a Hopf bifurcation with $\varepsilon \neq 0$, we find $_n = \quad \overline{1+\varepsilon^2}$ and all the frequencies satisfying $\tan(\omega_n) = -\varepsilon$ ($\omega_n \quad n\pi - \varepsilon$).

These two observations are illustrated in Fig. 5.2, where the period of Hopf bifurcation points emerging from $_n = 1$ is plotted as a function of $s_0$. In Fig. 5.2, points with the same $m$ are located in horizontal lines; and in linear scale [Fig. 5.2(a)], points with the same $l$ or the same $k$ are located in straight lines of positive slope starting from the origin $(s_0 = 0, T = 0)$, whereas points with the same $m - l$ or the same $m - k$ are located in straight lines that start at $(s_0 = 1, T = 0)$.

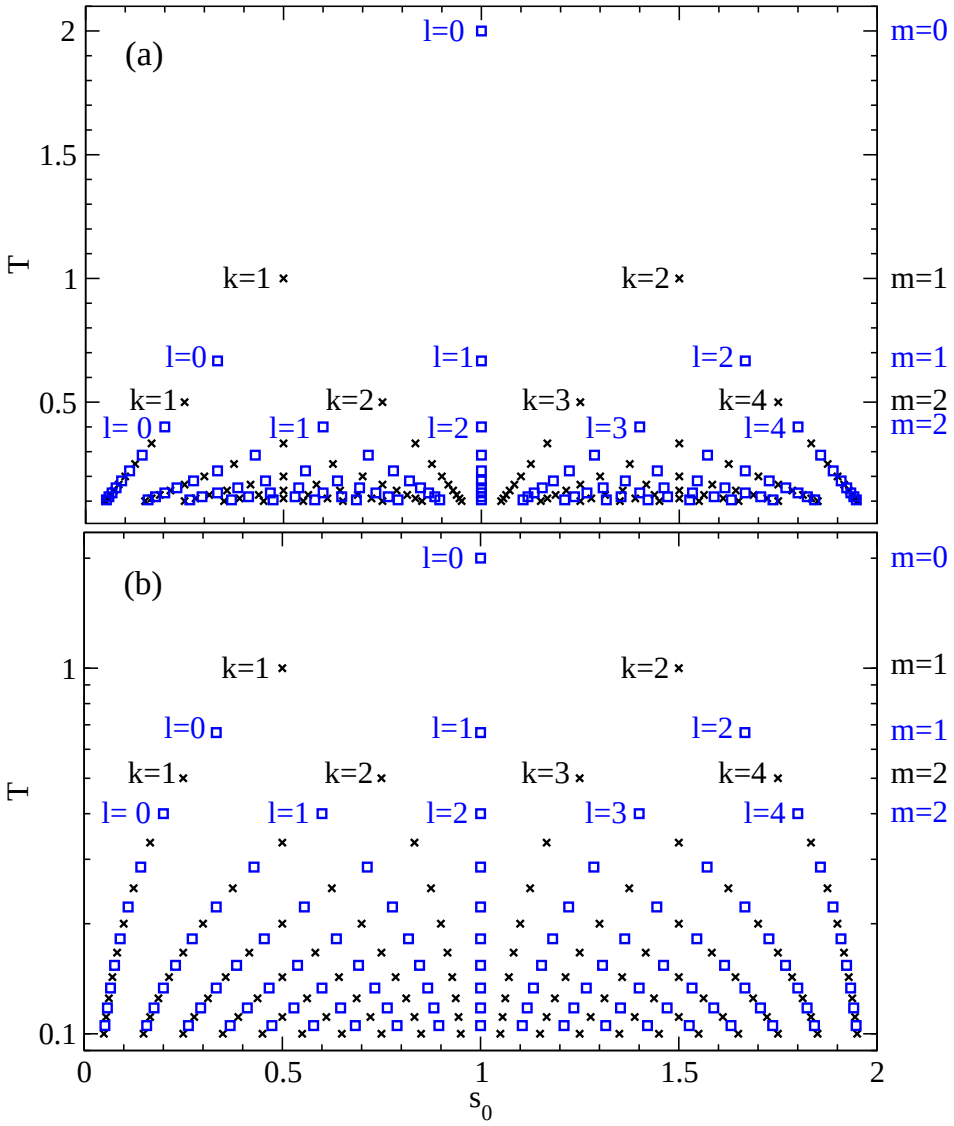


**Figure 5.2:** Hopf bifurcation points appearing at $_n = 1$ as a function of $s_0$ leading to oscillatory solutions with different periods $T$. Squares and crosses correspond to in- and out-of-phase Hopf bifurcations, respectively. Panel (a) shows the period $T$ in linear scale while panel (b) in logarithmic scale. As $T$ approaches zero, the number of Hopf bifurcations increases dramatically (only the bifurcations verifying $T$ 0.1 are shown).

Finally, we note that, according to Eqs. (5.1) and (5.6), in- and out-of-phase periodic solutions appear when the ratio between the self- and cross-feedback delays is odd/odd and odd/even, respectively. Each OEO can be seen as having two delay times, $\tau_1 = T_f$ and $\tau_2 = 2T_c$. Therefore in- and out-of-phase solutions exist when the ratio $\tau_2/\tau_1$ is even/odd. This is in agreement with the conditions for synchronization found for coupled chaotic lasers [165].

### 5.2.4 Coexistence of oscillatory solutions

We now discuss in more detail the coexisting solutions for a given value of $s_0$. We note that, once $s_0$ is fixed, not all the values of $l$ and $m$ are possible. For instance, for an in-phase solution with $s_0 = 5/7$, the smaller possible values for $l$ and $m$ are $l_0 = 2$ and $m_0 = 3$, so the fundamental solution has a period $T_0^{\text{in}} = 2/7$. The first harmonic is associated with values of $l$ and $m$ that can be obtained multiplying both the numerator and denominator of $s_0 = 5/7$ by 3, namely 15/21, so that $l_1 = 7$ and $m_1 = 10$, and the period is $T_1^{\text{in}} = T_0^{\text{in}}/3 = 2/21$. Notice that multiplying by an even number will lead to a ratio of two even numbers which does not fulfill the condition (5.1).

For a given $s_0$, the fundamental in-phase solution is given by the minima $l$ and $m$ that fulfill Eq. (5.1). Higher harmonics are obtained by multiplying numerator and denominator of Eq. (5.1) by an odd number. Therefore, the values allowed for $m$ and $l$ are given by

$$\begin{aligned} m_j^{\text{in}} &= (2j+1)m_0^{\text{in}} + j, \\ l_j^{\text{in}} &= (2j+1)l_0^{\text{in}} + j, \end{aligned} \tag{5.11}$$

where $j$ stands for the order of the harmonic, in such a way that $j = 0$ corresponds to the fundamental solution. The period of the harmonic is

$$T_j^{\text{in}} = \frac{T_0^{\text{in}}}{2j+1} = \frac{1 - s_0}{(m_0^{\text{in}} - l_0^{\text{in}})(2j+1)}, \tag{5.12}$$

where we have used Eq. (5.5).

For out-of-phase solutions, a similar argument applies. For a given $s_0$, the fundamental solution is given by the minima $k$ and $m$ that fulfill Eq. (5.6), while the harmonic of order $j$ can be obtained by multiplying numerator and denominator of (5.6) by $(2j+1)$; therefore the values allowed for $m$ and $k$ are given by

$$\begin{aligned} m_j^{\text{out}} &= (2j+1)m_0^{\text{out}}, \\ k_j^{\text{out}} &= (2j+1)k_0^{\text{out}} + j, \end{aligned} \tag{5.13}$$

and the period is

$$T_j^{\text{out}} = \frac{T_0^{\text{out}}}{2j+1} = \frac{2(1 - s_0)}{[2(m_0^{\text{out}} - k_0^{\text{out}}) - 1](2j+1)}, \tag{5.14}$$

where we have used Eq. (5.10).

Combining Eqs. (5.11) with Eq. (5.2), and Eqs. (5.13) with Eq. (5.7), we obtain

$$n_j^{\text{in}} = (2j+1)n_0^{\text{in}}, \tag{5.15}$$
$$n_j^{\text{out}} = (2j+1)n_0^{\text{out}} + j, \tag{5.16}$$

where

$$n_0^{\text{in}} = m_0^{\text{in}} + l_0^{\text{in}} + 1, \tag{5.17}$$
$$n_0^{\text{out}} = m_0^{\text{out}} + k_0^{\text{out}}. \tag{5.18}$$

Writing the ratio between the delay times as an irreducible rational number,

$$s_0^{\text{in}} = \frac{2l_0^{\text{in}}+1}{2m_0^{\text{in}}+1} = \frac{q'}{\tilde{q}}, \tag{5.19}$$
$$s_0^{\text{out}} = \frac{2k_0^{\text{in}}+1}{2m_0^{\text{out}}} = \frac{q'}{\tilde{q}}, \tag{5.20}$$

leads to

$$n_0^{\text{in}} = \frac{q'+\tilde{q}}{2}, \tag{5.21}$$
$$n_0^{\text{out}} = \frac{q'+\tilde{q}-1}{2}. \tag{5.22}$$

## 5.3 Nonlinear maps for primary periodic square-wave oscillations

Following the understanding gained in the previous section on the period of the solutions arising when the zero state becomes unstable, we now develop a map to determine the amplitude of these solutions. To this end, we plan to formulate equations for a map relating $x_1(s)$ to $x_1(s-T/2)$, where $T$ is the period, taking advantage of the small value of $\varepsilon$. Note that we need to take into account the effect of $\delta$ to ensure that $x(t)$ has a zero time average in the stationary regime.

We first consider the case of the in-phase oscillations. With the condition $x_2(s) = x_1(s)$ $x(s)$ and $Y(s)$ $Y_1(s) = Y_2(s + T^{\text{in}}/2)$, Eqs. (4.13) with $\varepsilon = 0$ reduce to

$$\begin{aligned} x(s) =& P\gamma^2 \cos 2x(s - s_0^{\text{in}}) + 2\Phi + \cos[2x(s-1) + 2\Phi] - 1 - 2\cos 2\Phi \\ &+ \cos^2 x(s - s_0^{\text{in}}) - x(s-1) - \delta Y(s), \end{aligned} \tag{5.23}$$
$$Y'(s) = x(s). \tag{5.24}$$

The period $T^{\text{in}}$ of the in-phase Hopf bifurcation was defined by Eq. (5.3). Starting with Eq. (5.1) and using Eq. (5.3), we may relate $s_0^{\text{in}}$ to $T^{\text{in}}$,

$$s_0^{\text{in}} = \frac{2l}{2m+1} + \frac{1}{2m+1} = lT^{\text{in}} + \frac{T^{\text{in}}}{2}. \tag{5.25}$$

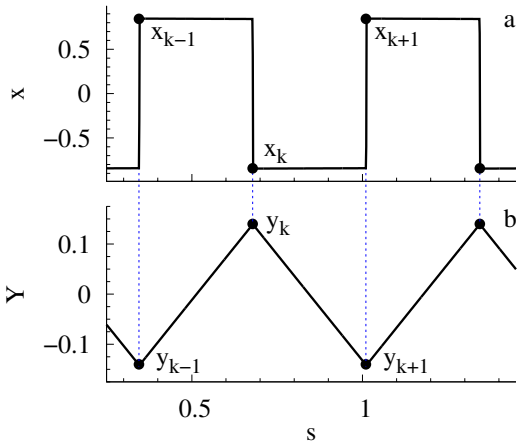


**Figure 5.3:** Numerical solution of the full dynamical model (4.9) for $\Phi = \pi/4$, $\gamma = 0.5$, $P = 1.7$, $T_f = 30\,\text{ns}$ and $T_c = 90\,\text{ns}$, so that $s_0 = 1/3$, $\varepsilon = 2.78 \quad 10^{-4}$ and $\delta = 0.018$.

Furthermore, a second useful equation is obtained by relating 1 to $T^{\text{in}}$ as

$$1 = \frac{2m+1}{2m+1} = mT^{\text{in}} + \frac{T^{\text{in}}}{2}, \tag{5.26}$$

where we again used Eq. (5.3). Using Eqs. (5.25) and (5.26), Eq. (5.23) simplifies as

$$x(s) = 2P\gamma^2 \quad \cos \quad 2x(s - T^{\text{in}}/2) + 2\Phi \quad - \cos 2\Phi \quad - \delta Y(s). \tag{5.27}$$

Eq. (5.27) is a first equation for a map relating $x(s)$ and $x(s - T^{\text{in}}/2)$. To obtain a second equation relating $Y(s)$ and $Y(s - T^{\text{in}}/2)$, we integrate Eq. (5.24) from $s - T^{\text{in}}/2$ to $s$. As illustrated in Fig. 5.3, we consider square-wave solutions in which $x(s)$ remains practically constant over half of the period. Introducing now the notations $x_k = x(s)$, $x_{k \ 1} = x(s - \frac{T^{\text{in}}}{2})$, $Y_k = Y(s)$, and $Y_{k \ 1} = Y(s - \frac{T^{\text{in}}}{2})$, with $x_k$ located at the beginning of the semiperiod (see Fig. 5.3), we have

$$x_k = 2P\gamma^2 \left[\cos(2x_{k \ 1} + 2\Phi) - \cos(2\Phi)\right] - \delta Y_k, \tag{5.28}$$

$$Y_k = Y_{k \ 1} + x_{k \ 1} \frac{T^{\text{in}}}{2}. \tag{5.29}$$

Subtraction of Eq. (5.28) evaluated at $x_k$ and at $x_{k \ 1}$ gives

$$x_k - x_{k \ 1} = 2P\gamma^2 \left[\cos(2x_{k \ 1} + 2\Phi) - \cos(2x_{k \ 2} + 2\Phi)\right] - \delta \left(Y_k - Y_{k \ 1}\right). \tag{5.30}$$

Then,

$$x_k = \quad 1 - \delta \frac{T^{\text{in}}}{2} \quad x_{k \ 1} + 2P\gamma^2 \left[\cos(2x_{k \ 1} + 2\Phi) - \cos(2x_{k \ 2} + 2\Phi)\right]. \tag{5.31}$$

For the out-of-phase solution, we assume that $x_1(s)$ and $x_2(s)$ are $T^{\text{out}}-$periodic solutions, where $T^{\text{out}}$ is given by Eq. (5.8). Using the fact that $x(s) \quad x_1(s) = x_2(s + T^{\text{out}}/2)$

and $Y(s)$ $Y_1(s) = Y_2(s+T^{\rm out}/2)$, from Eqs. (4.13) with $\varepsilon = 0$, we obtain the following equations for $x(s)$ and $Y(s)$:

$$x(s) = P\gamma^2 \ \cos\ 2x(s-s_0^{\rm out}) + 2\Phi \ + \cos\ 2x(s-T^{\rm out}/2-1) + 2\Phi \ - 1 - 2\cos 2\Phi$$
$$+ \cos^2\ x(s-s_0^{\rm out}) - x(s-T^{\rm out}/2-1) \ - \delta Y(s), \tag{5.32}$$
$$Y'(s) = x(s). \tag{5.33}$$

As for the in-phase solutions, we now use Eqs. (5.6) and (5.8) and determine useful relations between $s_0^{\rm out}$ and $T^{\rm out}$, and $T^{\rm out}$ and 1. Specifically, we find

$$s_0^{\rm out} = kT^{\rm out} + \frac{1}{2m} = kT^{\rm out} + \frac{T^{\rm out}}{2}, \tag{5.34}$$
$$1 = \frac{m}{m} = mT^{\rm out}. \tag{5.35}$$

Using Eqs. (5.34) and (5.35), Eq. (5.32) simplifies as

$$x(s) = 4P\gamma^2\ \cos^2\ x(s-T^{\rm out}/2) + \Phi \ - \cos^2\Phi \ - \delta Y(s), \tag{5.36}$$

which is the same equation as (5.27) replacing $T^{\rm in}$ by $T^{\rm out}$. Introducing $x_k = x(s)$, $x_{k\ 1} = x(s-T^{\rm out}/2)$, $Y_k = Y(s)$, and $Y_{k\ 1} = Y(s-T^{\rm out}/2)$, with $x_s$ located at the beginning of the semiperiod, one obtains exactly the same map as for in-phase solutions, namely, Eq. (5.31).

## 5.4 Nonlinear maps for square-wave oscillations generated by secondary bifurcations

We now consider a generalization of the map obtained in the previous section in order to describe the instabilities of the primary periodic square-wave solutions seen in the numerical simulations described in the next section. In fact, the map (5.31) can be extended to a more general class of lagged solutions of the form

$$x_2(s-1+s_0) = x_1(s) \quad x(s). \tag{5.37}$$

The lag time $1-s_0$ corresponds physically to the difference $T_c - T_f$ normalized to $T_c$. In- and out-of-phase solutions are particular cases. For the in-phase solution, $1-s_0$ is a multiple of $T^{\rm in}$ [see Eq. (5.5)] and, therefore, $x_2(s) = x_1(s)$. For out-of-phase solutions, from Eq. (5.10) $s_0 - 1 = (k-m)T^{\rm out} + T^{\rm out}/2$ and, therefore, $x_2(s+T^{\rm out}/2) = x_1(s)$.

Substituting Eq. (5.37) in the set (4.13), with $\cos[2x_2(s-1)+2\Phi] = \cos[2x_1(s-s_0)+2\Phi]$ and $\cos^2[x_1(s-s_0) - x_2(s-1)] = 1$, we obtain

$$\varepsilon x'(s) = -\,x(s) - \delta Y(s) + 2P\gamma^2\ \cos[2x(s-s_0)+2\Phi] - \cos 2\Phi \ , \tag{5.38}$$
$$Y'(s) = x(s). \tag{5.39}$$

## 5.4. NONLINEAR MAPS FOR SQUARE-WAVE OSCILLATIONS GENERATED BY SECONDARY BIFURCATIONS

We consider square-wave solutions in which $x(s)$ remains practically constant over a plateau of duration $s_p$. For consistency, we require $qs_p = s_0$, $q$ being an integer. Then, we can introduce $x_k = x(s)$, $x_{k-1} = x(s - s_p)$, $Y_k = Y(s)$, and $Y_{k-1} = Y(s - s_p)$ and choose $x_k$ located at the beginning of the plateau. Considering $\varepsilon = 0$, from Eqs. (5.38) and (5.39), one has

$$x_k = 2P\gamma^2 \left[\cos(2x_{k-q} + 2\Phi) - \cos(2\Phi)\right] - \delta Y_k, \tag{5.40}$$

$$Y_k = Y_{k-1} + x_{k-1} s_p. \tag{5.41}$$

Subtracting Eq. (5.40) evaluated at $k-1$ from the same equation evaluated at $k$, one obtains

$$x_k = (1 - \delta s_p)\, x_{k-1} + 2P\gamma^2 \left[\cos(2x_{k-q} + 2\Phi) - \cos(2x_{k-q-1} + 2\Phi)\right]. \tag{5.42}$$

We now make a few remarks about this map. First, notice that to obtain this map we have not imposed that the solutions are periodic. Therefore, the map is, in principle, useful to determine the secondary instabilities of the primary periodic square waves.

Second, for a given set of parameter values, namely, for a fixed value of $s_0$, one has several coexisting solutions with plateaus of length $s_p = s_0/q$. The amplitude of all these solutions is given by the map with the corresponding value of $q$.

Third, for the primary in-phase square-wave periodic solutions discussed in the previous section, $s_p = T^{\text{in}}/2$; as a consequence, from Eq. (5.25), it follows that $s_0 = (2l+1)s_p$, so $q = 2l + 1$. Similarly, for the primary out-of-phase square-wave periodic solutions, $s_p = T^{\text{in}}/2$; and from (5.34), it follows that $s_0 = (2k+1)s_p$, so that $q = 2k + 1$.

Fourth, for solutions with a period that is twice the length of the plateau, as is the case of primary square waves, $x_{k-2l-1} = x_{k-1}$. This is why the maps obtained in the previous section, where we explicitly considered the periodicity of the solution, correspond to $q = 1$.

Fifth, the map for the primary square waves can in fact be further simplified considering that the square wave is centered at zero and defining $x^* = x_k = x_{k-2} = -x_{k-1}$. Then, one has

$$x^* = \frac{}{2} \sin 2x^*. \tag{5.43}$$

Namely, the amplitude of all coexisting primary in-phase periodic solutions is the same and it is given by the fixed points of the sinus map (5.43), and similarly for all coexisting out-of-phase periodic solutions with different periods.

Figure 5.4(a) shows the bifurcation diagram of Eq. (5.42) for $q = 1$ as function of , where is changed by increasing $P\gamma^2$ while the offset phase is kept constant at $\Phi = \pi/4$. For small values of , the only stationary solution of the map is the fixed point $x^* = 0$, which corresponds to the zero solution in Eq. (4.13). Increasing , the zero solution becomes unstable and, at = 1, as expected from the linear stability analysis, one encounters a periodic solution for which the amplitude $x^*$ can be obtained from Eq. (5.43). Close to the bifurcation point = 1, the amplitude grows as $x^*$ $( - _c)^{1/2}$. Increasing , the map (5.42) shows a period doubling; and for larger values of $P\gamma^2$, one has chaotic behavior. For the offset phase $\Phi = \pi/4$, the map is always symmetric around $x = 0$.

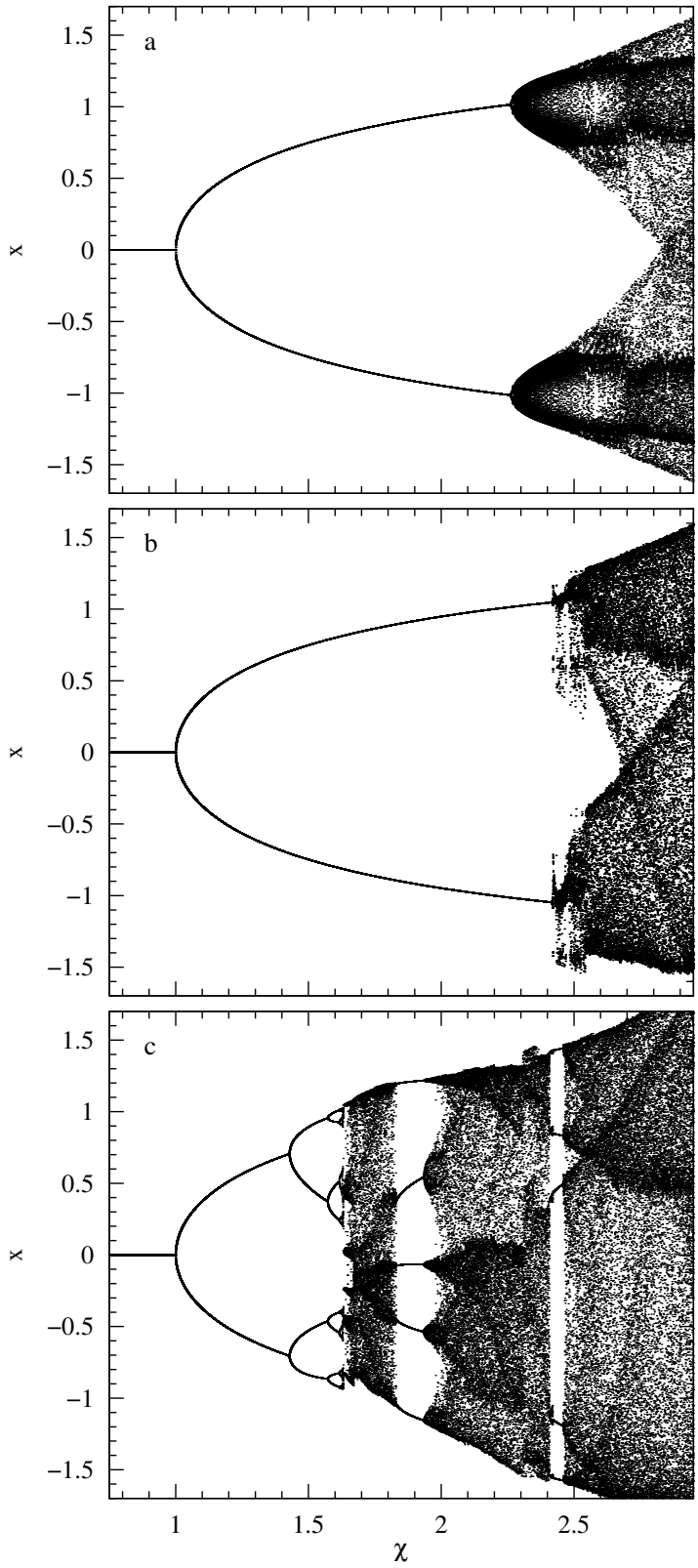


**Figure 5.4:** Bifurcation diagram of the map (5.42) for $q = 1$ and offset phases (a) $\Phi = \pi/4$, (b) $\Phi = 0.3\pi$, and (c) $\Phi = 0.35\pi$.

The effect of the offset phase is illustrated in Figs. 5.4(b) and 5.4(c), which show the equivalent bifurcation diagram for offset phases $\Phi = 0.3\pi$ and $\Phi = 0.35\pi$, respectively. Again, for small , the system goes to the zero solution, which becomes unstable at = 1. Above that value, one encounters in- or out-of-phase periodic solutions with amplitude $x^*$ given by same sinus map (5.43). Then, these solutions become unstable and periodic solutions of higher order appear. The point where the simple periodic solution becomes unstable depends on the offset phase. The higher-order periodic solutions that appear beyond this point have an asymmetric amplitude, as discussed in Sec. 5.5. Finally, the map becomes chaotic.

## 5.5 Numerical simulations of periodic solutions

We have performed numerical simulations of the dynamical model (4.11). We encounter that the zero solution becomes unstable at = 1 for any value of $s_0$ leading to an oscillatory solution.

In Fig. 5.5, we show the in-phase oscillatory solution arising when increasing for $s_0 = 1/3$. The periodic solution is born sinusoidal, as shown in Figs. 5.5(a) and 5.5(b). Already for = 1.01, the shape of the oscillation resembles a square wave, although the plateaus are slightly tilted [see Figs. 5.5(c) and 5.5(d)]. As shown in [62] and [63] for a single OEO, the tilting of the plateau is an effect of $\delta$. The square-wave form becomes even more clear as increases, as shown in Figs. 5.5(e) and 5.5(f). Nevertheless, the period of the periodic solution remains practically constant, as discussed for a single OEO in the subsection 3.2.9.

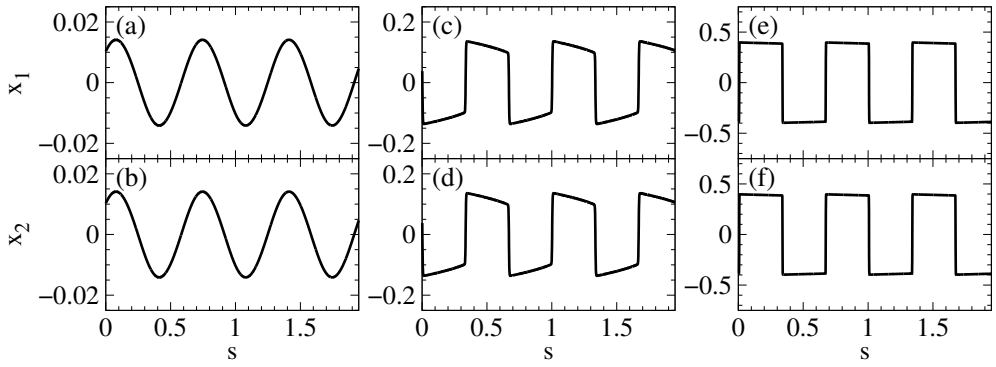


**Figure 5.5:** In-phase periodic oscillations after the Hopf bifurcation with $\Phi = \pi/4$, $\gamma = 0.5$, $T_f = 30\,\text{ns}$ and $T_c = 90\,\text{ns}$, so that $s_0 = 1/3$, $\varepsilon = 2.78$ 10 $^4$ and $\delta = 0.018$. In [(a) and (b)] we consider $P = 1.0001$ so that = 1.0001, in [(c) and (d)] $P = 1.01$ ( = 1.01), and in [(e) and (f)] $P = 1.11$ ( = 1.11).

Similarly, Fig. 5.6 displays the shape of the out-of-phase periodic solution obtained when considering $s_0 = 3/4$. In both cases, the period of the oscillations coincides with the predicted one within order $\varepsilon$, as expected.

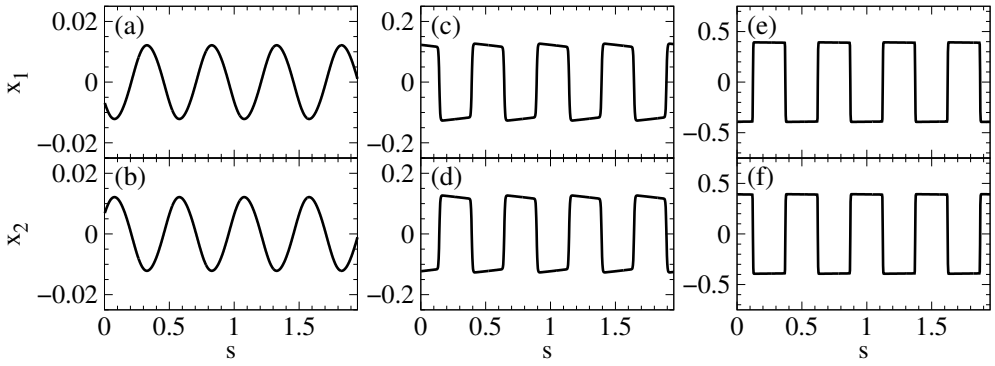


**Figure 5.6:** Out-of-phase periodic oscillations after the Hopf bifurcation with $\Phi = \pi/4$, $\gamma = 0.5$, $T_f = 30\,\text{ns}$ and $T_c = 40\,\text{ns}$, so that $s_0 = 3/4$, $\varepsilon = 6.25$ 10 $^{4}$ and $\delta = 0.008$. In [(a) and (b)] we consider $P = 1.0001$ so that = 1.0001, in [(c) and (d)] $P = 1.01$ ( = 1.01), and in [(e) and (f)] $P = 1.11$ ( = 1.11).

Comparing Fig. 5.5 with Fig. 5.6, one sees that, for a given value of , the amplitude of both the in- and out-of-phase oscillations is the same. This is in agreement with the fact that the amplitude of both in- and out-of-phase oscillations is given by Eq. (5.43). We further illustrate this result in Fig. 5.7, where the solid line shows the amplitude given by the fixed point of the map (5.43) for $P = 1.11$ and $\gamma = 0.5$ as function of the offset phase $\Phi$, while the symbols show the numerical results obtained for several values of $s_0$ leading to different in- and out-of-phase solutions. As it can be seen from Fig. 5.7, the theoretical prediction for the oscillation amplitude is in excellent agreement with the numerical simulations of the full dynamical model.

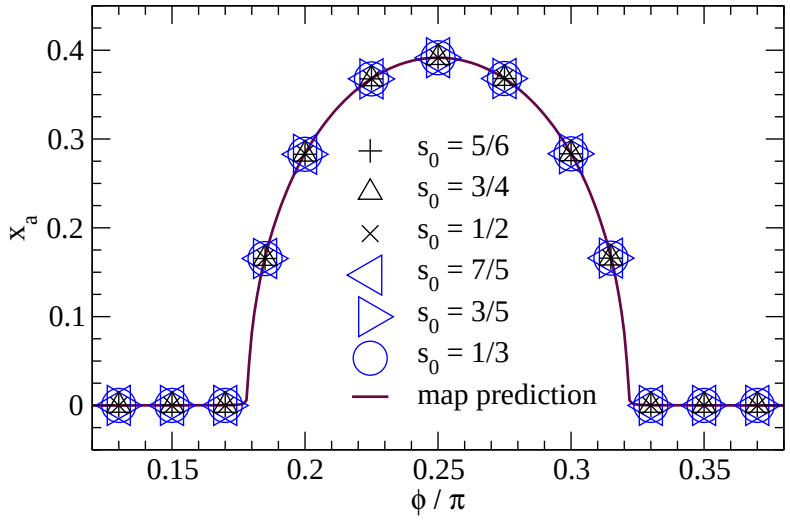


**Figure 5.7:** Amplitude of square-wave periodic oscillations as a function of the offset phase $\Phi$ with $P = 1.11$ and $\gamma = 0.5$, = 5 s, and $\tau = 25\,\text{ps}$. The solid line corresponds to the theoretical prediction. Symbols correspond to the numerical integration of the full dynamical model with $T_c = 50\,\text{ns}$ and $T_f = 60\,\text{ns}$ (+); $T_c = 30\,\text{ns}$ and $T_f = 40\,\text{ns}$ ( ); $T_c = 30\,\text{ns}$ and $T_f = 60\,\text{ns}$ ( ); $T_c = 70\,\text{ns}$ and $T_f = 50\,\text{ns}$ ◁; $T_c = 30\,\text{ns}$ and $T_f = 50\,\text{ns}$ ▷; and $T_c = 30\,\text{ns}$ and $T_f = 90\,\text{ns}$ .

As discussed in Sec. 5.4, with increasing $P\gamma^2$ the in- and out-of-phase solutions become unstable, leading to higher-order periodic solutions. Figure 5.8 shows the bifurcation diagram of the map (5.42) for $q = 1$, $\gamma = 0.5$ and $P = 1.8$ as a function of the feedback phase $\Phi$. There is a central region around $\Phi = \pi/4$ in which the system has periodic solutions such as the in-phase solution shown in Figs. 5.9(c) and 5.9(d) for $\Phi = 0.18\pi$. Further away from the center, the system has a period doubling bifurcation in which it shows lagged synchronization [see Figs. 5.9(a) and 5.9(b)]. The values of the plateaus for these period-2 solutions are not symmetrically located around $x = 0$. This is also noticeable in the bifurcation diagram shown in Fig. 5.8, which is not symmetrical around the axis $x = 0$. Instead, it is symmetrical around the point $x = 0$, $\Phi = \pi/4$. The

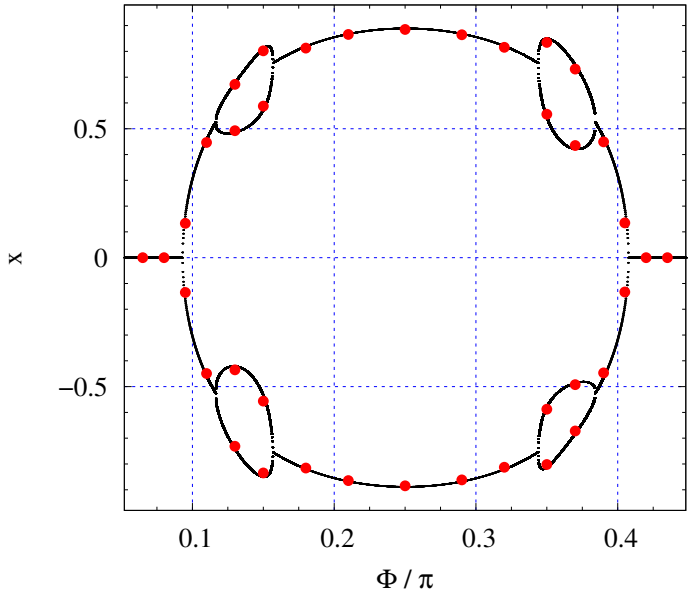


**Figure 5.8:** Amplitude of square-wave oscillations as a function of the offset phase $\Phi$ with $P = 1.8$ and $\gamma = 0.5$. The solid line corresponds to the theoretical prediction (5.42) with $q = 1$. Symbols correspond to the numerical integration of the full dynamical model with $T_f = 30\,\text{ns}$ and $T_c = 90\,\text{ns}$.

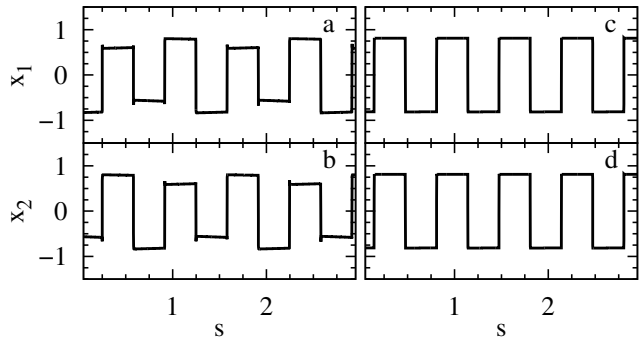


**Figure 5.9:** Time traces of the square-wave oscillations obtained for $P = 1.8$, $\gamma = 0.5$, $T_f = 30$ ns and $T_c = 90\,\text{ns}$ for [(a) and (b)] $\Phi = 0.15\pi$ and [(c) and (d)] $\Phi = 0.18\pi$.

map (5.42) predicts quite accurately the amplitude of these lag synchronized solutions obtained numerically, as shown by the solid line.

We now address the coexistence of multiple periodic solutions for fixed values of the parameters. As shown in Fig. 5.2 and discussed in Sec. 5.2, for a given value of $s_0$, that is for a given value for the delay times $T_f$ and $T_c$, there are several Hopf bifurcations leading to oscillations with different period $T$, all of them taking place at $= 1$. Thus, the linear stability analysis of the zero solution indicates that multiple periodic solutions with different periods can exist for $= 1$, although it does not give information about the stability of these solutions. It turns out that indeed there are several stable periodic square-wave solutions coexisting for fixed values of the parameters, as illustrated in Fig. 5.10. The different square-wave solutions are obtained integrating numerically the dynamical equations (4.11) starting from different initial conditions. More precisely, as initial condition for $x_1(s)$ within the interval $-\max(1, s_0) < s < 0$, we take a square wave with amplitude given by the the fixed point $x^*$ of map (5.28) and with a period $T$. For in-phase solutions, the initial condition for $x_2$ is given by $x_2(s) = x_1(s)$; while for out-of-phase solutions, we take $x_2(s) = -x_1(s)$. Regarding the initial condition for $Y_i$, we take $Y_1(0) = x^*T/4$ and $Y_2(0) = x^*T/4$.

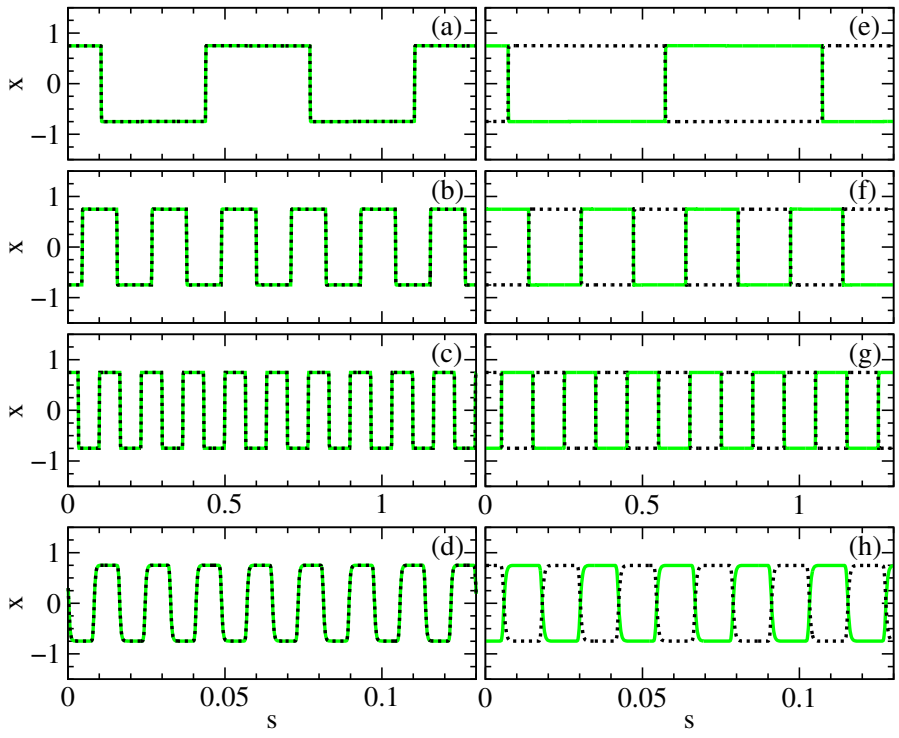


**Figure 5.10:** Time trace of the square-wave periodic solutions with $P = 1.5$, $\gamma = 0.5$, $\Phi = 0.25\pi$ and $T_f = 30\,\text{ns}$. (a)-(d) Coexisting in-phase solutions for $T_c = 90\,\text{ns}$ ($s_0 = 1/3$, $\varepsilon = 2.78$ $10^{-4}$, and $\delta = 0.018$) obtained with suitable initial conditions as indicated in the text. (e)-(h) Coexisting out-phase solutions for $T_c = 60\,\text{ns}$ ($s_0 = 1/2$, $\varepsilon = 4.167$ $10^{-4}$, and $\delta = 0.012$). Shown are (a) and (e) the fundamental solution $j = 0$, (b) and (f) the first harmonic $j = 1$, (c) and (g) the second harmonic $j = 2$, and (d) and (h) the twentieth harmonic $j = 20$. Notice that the time scale used in (d) and (h) is 10 times smaller than in the other panels.

Figures 5.10(a)-5.10(d) illustrate the coexistence of several in-phase solutions obtained considering $P = 1.5$, $\gamma = 0.5$, $\Phi = \pi/4$, $T_f = 30\,\text{ns}$ and $T_f = 90\,\text{ns}$ so that $s_0 = 1/3$ and $= 1.5$. For $s_0 = 1/3$, the fundamental solution corresponds to $l_f = 0$ and $m_f = 1$, as given by Eq. (5.1); its period is given by $T_f^{\text{in}} = 2/3$, while the period of the higher harmonics is given by Eq. (5.12). Fig. 5.10(a) shows the fundamental solution, $x_1(s)$ in continuous green and $x_2(s)$ in dashed black. Similarly, panels (b)-(c) show $x_1(s)$ for the first and second harmonics, which have periods $T_1^{\text{in}} = T_f^{\text{in}}/3 = 2/9$ and $T_2^{\text{in}} = T_f^{\text{in}}/5 = 2/15$. Higher-order harmonics are also found. As an example, Fig. 5.10(d) shows the $20^{\text{th}}$ harmonic, which has a period $T_{20}^{\text{in}} = T_f^{\text{in}}/41 = 2/123$ (notice that we have used a different scale on the time axis).

Figures 5.10(e)-5.10(h) illustrate the coexistence of several out-of-phase solutions obtained with the same parameters but $T_f = 60\,\text{ns}$ so that $s_0 = 1/2$. The fundamental solution corresponds to $k_f = 0$ and $m_f = 1$ as given by Eq. (5.6), and has a period $T_f^{\text{out}} = 1$. The period of the higher harmonics is given by Eq. (5.14). Fig. 5.10(e) shows the fundamental solution, while Figs. 5.10(f) and 5.10(g) show the first and the second harmonic. Finally, Fig. 5.10(h) displays the twentieth harmonic.

For high harmonic solutions, the raising and falling edges are not symmetric, as it can be seen in Fig. 5.11 for the fundamental and twentieth harmonic out-of-phase square waves of Figs. 5.10(e) and 5.10(h), respectively.

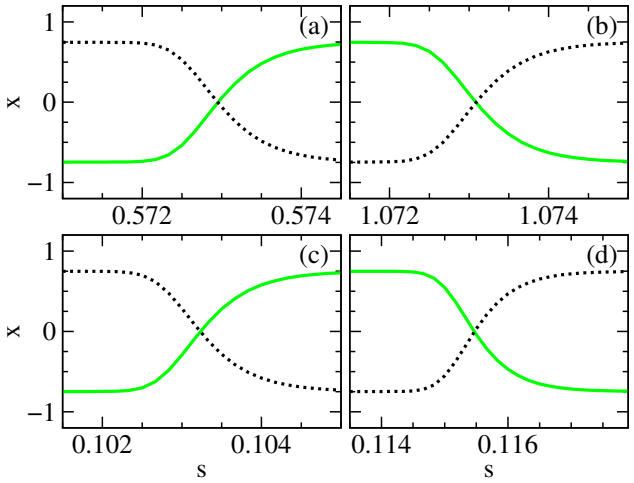


**Figure 5.11:** Zoom of raising [(a) and (c)] and falling [(b) and (d)] edges of the fundamental solution [(a) and (b)] and the twentieth harmonic [(c) and (d)] shown in Figs. 5.10(e) and 5.10(h), respectively.

All these solutions are stable against small numerical perturbations. For $\varepsilon = 0$, one could have an infinite number of such square-wave periodic orbits. In practice, in the full model, the transition between the plateaus of the square waves takes a time of order $\varepsilon$ and this limits the minimal period for square-wave periodic solutions. Nevertheless, as shown in Fig. 5.10, it is perfectly feasible in this system to have tens of coexisting square-wave periodic solutions. The fundamental solution is the one with a larger basin of attraction; therefore, starting from arbitrary initial conditions, one usually ends up in

the fundamental solution. However, by setting appropriately the initial condition, one can make the system operate in any of the other higher-order square-wave solutions.

## 5.6 E ect of mismatch in the delay-times ratio

Here we analyse the dynamics when the ratio between the delay times is not exactly a simple rational ratio but it is close to it. To do so, we have performed numerical simulations of the dynamical system (4.11) for filter characteristic times = 5 s and $\tau = 25\,\text{ps}$, low feedback and coupling rates ($P = 1.5$, $\gamma = 0.5$), offset phases $\Phi = \pi/4$ and $\Phi_0 = 0$, varying the self-feedback delay $T_f$ and keeping fixed the coupling delay $T_c$. As initial condition, we use an in-phase or out-of-phase periodic solution, as described in Sec. 5.5.

The dynamics of periodic solutions in which $x_1$ and $x_2$ are in-phase is shown in Fig. 5.12 for the fundamental square-wave solution and the first harmonic [Figs. 5.12(b), 5.12(d), 5.12(f), and 5.12(h)]. We consider $T_c = 90\,\text{ns}$, while $T_f$ is changed from $T_f = 30.0\,\text{ns}$ to $29.2\,\text{ns}$. [Figs. 5.12(a), 5.12(c), 5.12(e), and 5.12(g)],

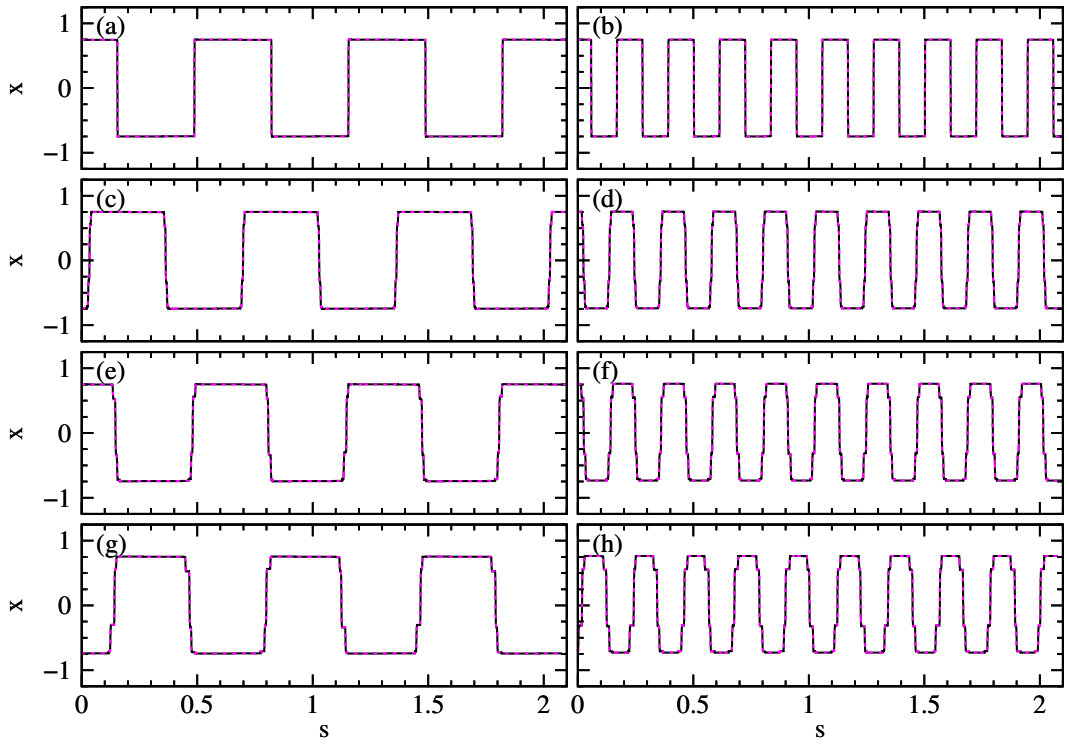


**Figure 5.12:** Dynamics of in-phase periodic solutions with $T_c = 90\,\text{ns}$ and different values of $T_f$: (a) and (b) $T_f = 30.0\,\text{ns}$, (c) and (d) $T_f = 29.6\,\text{ns}$, (e) and (f) $T_f = 29.4\,\text{ns}$, and (g) and (h) $T_f = 29.2\,\text{ns}$.

For $T_f = 30\,\text{ns}$, one has a perfect matching condition for in-phase solutions, $s_0 = 1/3$. The fundamental solution has a period $T_f^{\text{in}} = 2/3$, while the period of the first harmonic is $T_f^{\text{in}}/3 = 2/9$. In this case, one observes periodic square waves as discussed before [see Figs. 5.12(a) and 5.12(b)].

When a small mismatch is introduced, the square-wave form is maintained, but the transition layer becomes progressively wider, as illustrated in Figs. 5.12(c) and 5.12(d). For a larger mismatch, of the order of 2% in $T_f^{\text{in}}$, the square-wave form starts to degrade and small intermediate plateaus appear. These small plateaus are not symmetrically located around $x = 0$. In the case illustrated in the figure, the jump from the main plateau to the intermediate one at $x > 0$ is smaller than the equivalent jump at $x < 0$. We note that, despite the degradation in the shape of the square wave, the amplitude of the solution does not change. Higher-order harmonics are more sensitive to the mismatch since they have shorter periods and, therefore, will be more affected by widening and progressive degradation of the transition layer. Nevertheless, one can conclude that the square-wave solutions are robust to a mismatch in the delay times of the order of a few percent and that several stable in-phase solutions can coexist, even in presence of mismatch. Similar results are found for out-of-phase periodic solutions, as shown in Fig. 5.13.

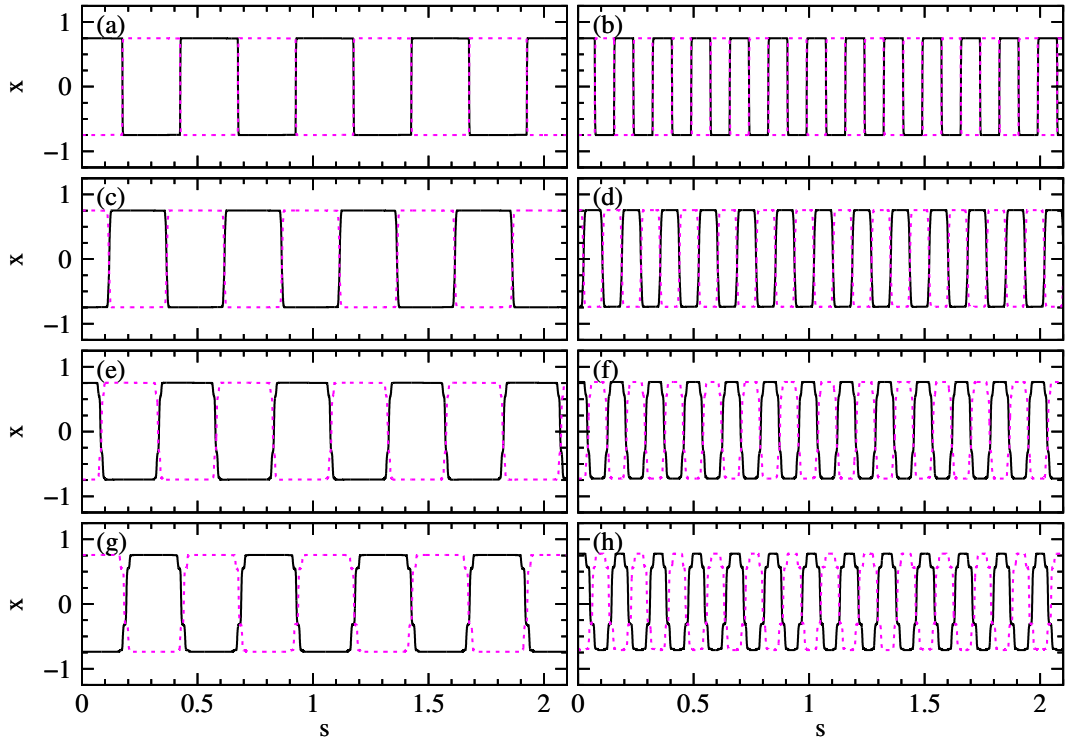


**Figure 5.13:** Dynamics of out-of-phase periodic solutions with $T_c = 40\,\text{ns}$ and different values of $T_f$: (a) and (b) $T_f = 30.0\,\text{ns}$, (c) and (d) $T_f = 29.8\,\text{ns}$, (e) and (f) $T_f = 29.6\,\text{ns}$, and (g) and (h) $T_f = 29.4\,\text{ns}$.

## 5.7 Detailed analysis of the period of the solutions

In this section, we investigate in detail the effect of a mismatch in the delay-times ratio on the period of the square waves from numerical simulations of the full dynamical model (4.11). Specifically, we compute the Poincaré return times with a Poincaré section at $x_1 = 0$ when $x_1$ becomes positive. We observe a nonlinear effect consisting of the temporal splitting in different intervals. Here we illustrate this effect first in in-phase solutions and later in out-of-phase solutions. More examples of this splitting are found in Appendix A.

### 5.7.1 Temporal splitting of in-phase solutions

To illustrate the temporal splitting of in-phase solutions, here we consider the ratio $s_0 = T_f/T_c$ to be close to $s_0 = 1/3$.

### 5.7.2 $s_0$ near $s_0 = 1/3$ ($n_0 = 2$)

For $s_0 = 1/3$, according to (5.17), $n_0 = l_0 + m_0 + 1 = 2$ because the minimum values of $l$ and $m$ that satisfy Eq. (5.1) are $l_0 = 2$ and $m_0 = 1$; alternatively, according to (5.19) and (5.21), $n_0 = (q' + \tilde{q})/2 = (1 + 3)/2 = 2$.

In Fig. 5.14, the Poincaré return times are plotted for $T_c = 90\,\text{ns}$, $\varepsilon = 2.78\ 10^{-4}$, $\delta = 1.8\ 10^{-2}$ and different values of $T_f$ near $T_f = 30\,\text{ns}$. Panels [(a)-(d)] correspond to the fundamental square wave, whereas panels [(e)-(h)] and [(i)-(l)] correspond to the first and second harmonics, respectively; red dots correspond to numerical simulations, orange dashed lines to the numerical value of the mean period, and black dashed lines to the prediction for the period given by Eqs. (4.25) and (4.29). In panels (a), (e) and (i) $T_f = 30\,\text{ns}$, so that $s_0 = 1/3$, whereas in the other panels there is a small mismatch in $s_0$ with respect to the ideal ratio.

At the ideal ratio $s_0 = 1/3$ [Fig. 5.14(a)], the fundamental solution has a period $T_0^{\text{in}} = 0.6669$, in good agreement with the prediction given by Eq. (4.25), $T_2^{\text{in}} = 0.6667$, taking into account the correction $\alpha_2^{\text{in}}$ of order $\varepsilon$ and $\delta$ given by Eq. (4.29) for $n = 2$. With a 1% mismatch with respect to the ideal ratio [Figs. 5.14(b) and 5.14(c)], the period of the fundamental solution is also in agreement with the prediction given by Eq. (4.25). With a 2% mismatch [panel (d)], there is splitting in $n_0 = 2$ different Poincaré return times, although the mean value of the two different intervals is similar to the prediction given by Eq. (4.25).

The harmonic of order $j$ has a small splitting in $2j + 1$ different intervals, as shown in Figs. 5.14(e) and 5.14(i) for the first ($j = 1$) and second ($j = 2$) harmonics, respectively. Notice that this splitting is present even for the case of perfect delay-time matching ($s_0 = 1/3$). Curiously enough, the splitting is not unique but depends on the initial condition, as shown in Fig. 5.15 for same values of the parameters but slightly different initial conditions for the first harmonic.

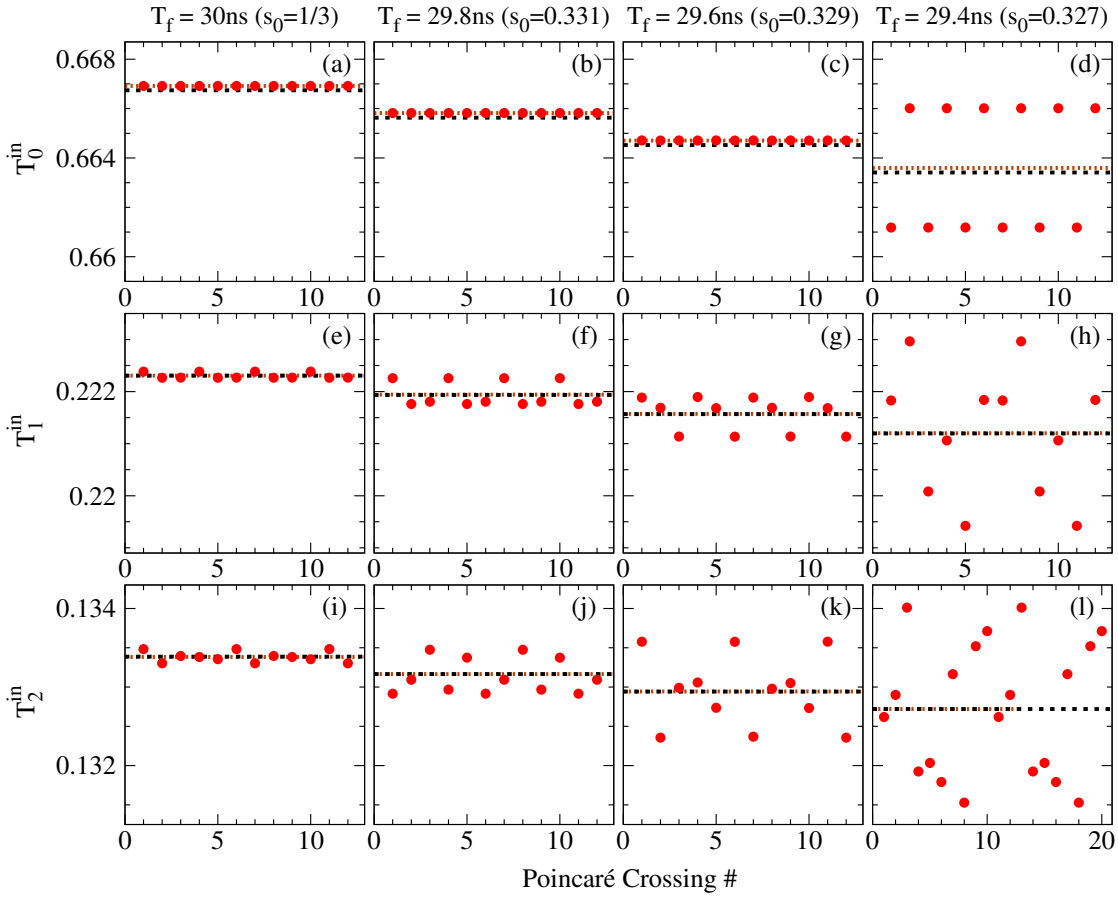


**Figure 5.14:** Poincaré return times for in-phase square waves with $\phi = 0.25\pi$, $P = 1.5$, $\gamma = 0.5$, $T_c = 90\,\text{ns}$, $\varepsilon = 2.78\ \ 10^{\ -4}$, $\delta = 1.8\ \ 10^{\ -2}$ and different values of $T_f$: 30 ns ($s_0 = 1/3$) in (a), (e) and (i); 29.8 ns ($s_0 = 0.331$) in (b), (f) and (j); 29.6 ns ($s_0 = 0.329$) in (c), (g) and (k); and 29.4 ns ($s_0 = 0.327$) in (d), (h) and (l).

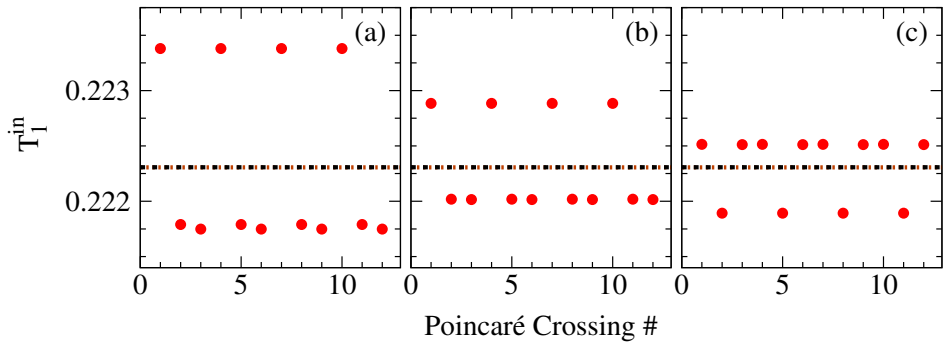


**Figure 5.15:** Poincaré return times for in-phase square waves with identical values of the parameters than in Fig. 5.14(e) but different initial conditions.

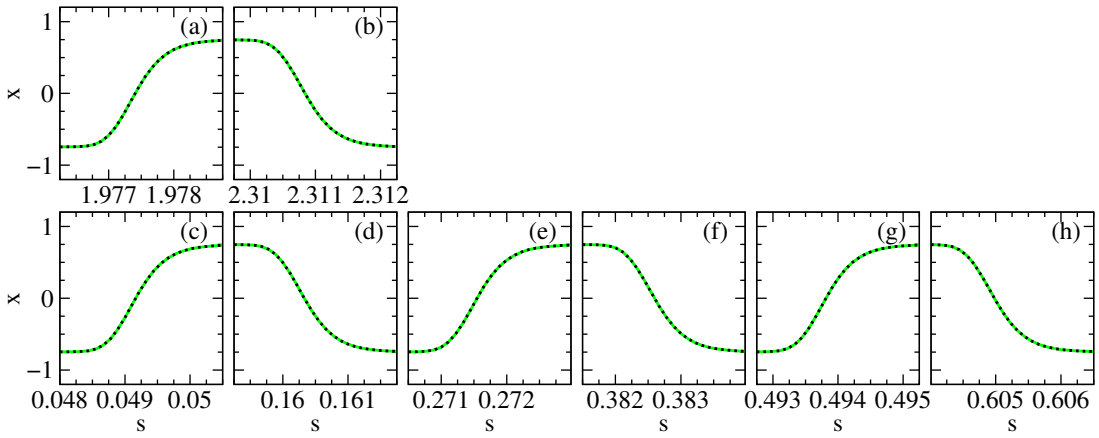


**Figure 5.16:** Raising [(a), (c), (e), and (g)] and falling [(b), (d), (f), and (h)]] edges of the fundamental solution [(a) and (b)] and the first harmonic [(c)-(h)]. Panels (a) and (b) correspond to Fig. 5.14(a), whereas panels (c)-(h) show three consecutive oscillations corresponding to the splitting shown in Fig. 5.14(e).

This splitting is a nonlinear effect that may be related to the temporal asymmetry between the positive and negative jumps of the square wave. This asymmetry is shown in Fig. 5.16 for the fundamental solution [(a) and (b)] and the first harmonic [(c)-(h)], where panels (a) and (b) correspond to Fig. 5.14(a) and panels (c)-(h) to Fig. 5.14(e).

Based on that, since the rising and falling interval times of the square wave increase with the mismatch in the delay-times ratio, as we will see next, we expect the splitting to be enhanced with a mismatch with repect to the ideal ratio. Introducing mismatch, the splitting increases indeed, as it can be seen in Figs. 5.14(f) and 5.14(g) for the first harmonic, and in Figs. 5.14(j) and 5.14(k) for the second harmonic. With a 2% mismatch, the harmonic of order $j$ has a splitting in $n_j = (2j+1)n_0 = 4j+2$ values, namely 6 and 10 different intervals for $j = 1$ [Fig. 5.14(h)] and $j = 2$ [Fig. 5.14(l)], respectively.

The mean value of all the different intervals is very similar to the prediction given by Eq. (4.25) for $n = 6$ and $n = 10$, for the first and second harmonics, respectively.

The effect of a small mismatch with respect to the ideal ratio $s_0 = 1/3$ on the transition layers between the plateaus of the square wave is shown in Figs. 5.17 and 5.18 for the fundamental and first harmonic solutions of Fig. 5.14, respectively. With a 1% mismatch, panels on the first and second rows of Figs. 5.17 and 5.18, corresponding to panels [(b)-(c)] and [(f)-(g)] of Fig. 5.14, respectively, show that the transition time increases up to a factor of 10 [compare for instance Fig. 5.17(e) with Fig. 5.16(a)] and secondary plateaus appear in the transition layers. As shown in panels (g) and (h) of Fig. 5.17, which are zooms of panels (e) and (f) of the same figure, these secondary plateaus are not symmetric. With a 2% mismatch, the transition layers become more asymmetric and double in number. For the fundamental solution, panels (i)-(l) of Fig. 5.17 show the four transition layers corresponding to Fig. 5.14(d), whereas for the first harmonic panels (m)-(x) of Fig. 5.18 show the twelve transition layers corresponding to Fig. 5.14(h).

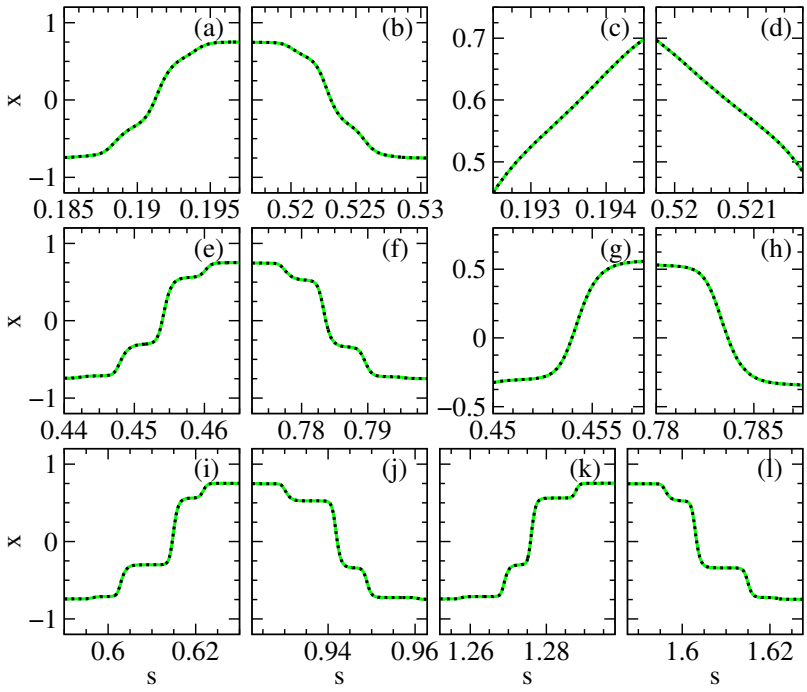


**Figure 5.17:** Raising [(a), (e), (i), and (k)] and falling [(b), (f), (j), and (l)] edges of the fundamental solution with increasing the delay-times ratio mismatch, corresponding to Figs. 5.14(b) [(a) and (b)], 5.14(c) [(e) and (f)] and 5.14(d) [(i), (j), (k) and (l)]. Panels (c), (d), (g), and (h) are zooms of panels (a), (b), (e), and (f), respectively.

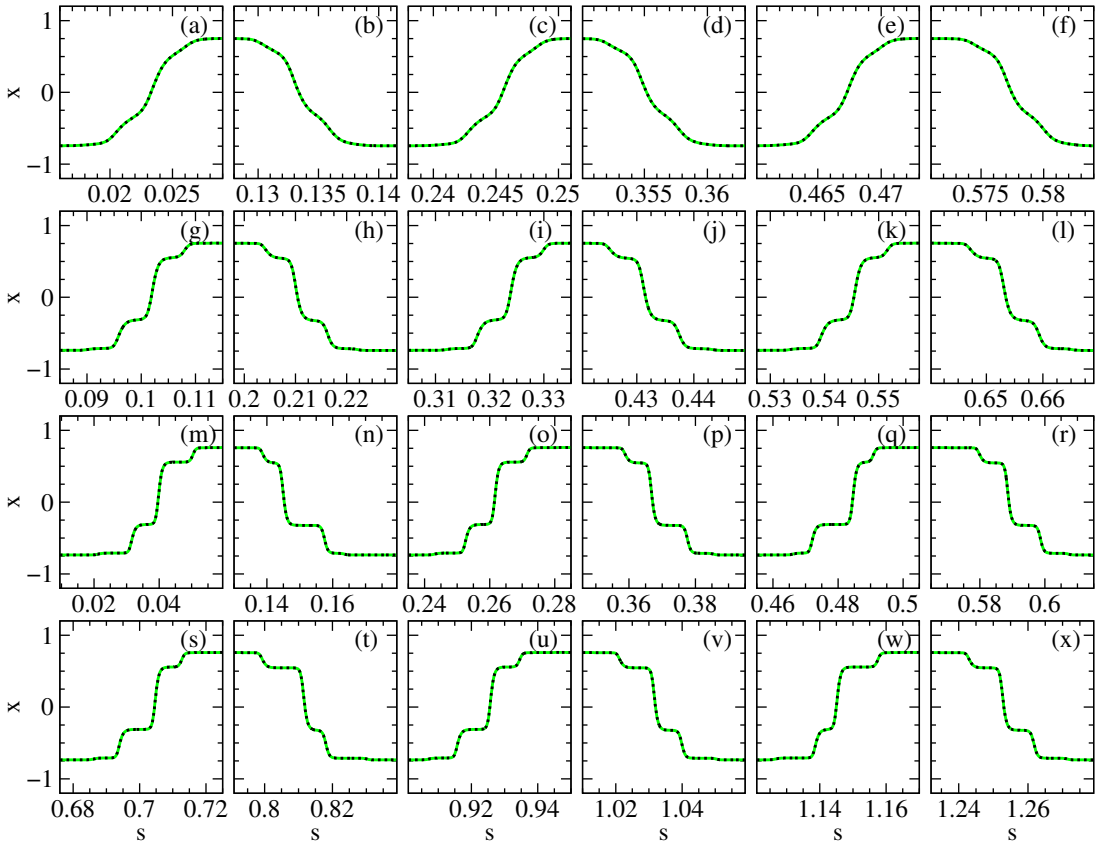


**Figure 5.18:** Raising and falling edges of the first harmonic with increasing the delay-times ratio mismatch, corresponding to Figs. 5.14(f) [(a), (b), (c), (d), (e), and (f)], 5.14(g) [(g), (h), (i), (j), (k), and (l)], and 5.14(h) [(m), (n), (o), (p), (q), (r), (s), (t), (u), (v), (w) and (x)].

#### Main result for in-phase solutions

As also shown in Appendix A for in-phase square-wave solutions arising with other values of $s_0$, the period of the fundamental solution undergoes a splitting in $n_0^{\text{in}}$ values as the delay-time mismatch is increased, whereas the period of higher-order harmonics shows a splitting in $(2j+1)$ values in the matching case and undergoes a secondary splitting in $(2j+1)n_0^{\text{in}}$ values with increasing the mismatch.

### 5.7.3 Temporal splitting of out-of-phase solutions

We now show that a similar splitting occurs for out-of-phase solutions. To illustrate this, we consider the ratio $s_0 = T_f/T_c$ to be close to $s_0 = 3/4$.

### 5.7.4 $s_0$ near $s_0 = 3/4$ ($n_0 = 3$)

For $s_0 = 3/4$, according to (5.18), $n_0 = k_0 + m_0 = 3$ because the minimum values of $k$ and $m$ that satisfy Eq. (5.6) are $k_0 = 1$ and $m_0 = 2$; alternatively, according to (5.20) and (5.22), $n_0 = (q' + \tilde{q} - 1)/2 = (3 + 4 - 1)/2 = 3$.

The fundamental solution for the ideal ratio $s_0 = 3/4$ [Fig. 5.19(a)] has a period $T_0^{\rm in} = 0.500328$, in good agreement with the prediction given by Eq. (4.36), $T_4^{\rm in} = 0.5003157755$, taking into account the correction $\alpha_3^{\rm out}$ of order $\varepsilon$ and $\delta$ given by Eq. (4.39) for $n = 3$. With a mismatch of the order of 1% with respect to the ideal ratio [Figs. 5.19(b) and 5.19(c)], the period of the fundamental solution is also in agreement with the prediction given by Eq. (4.36). With a 2% mismatch [Fig. 5.19(d)], there is splitting in $2n_0 + 1 = 7$ different Poincaré return times, although the mean value of the three different intervals is in good agreement with the prediction given by Eq. (4.36).

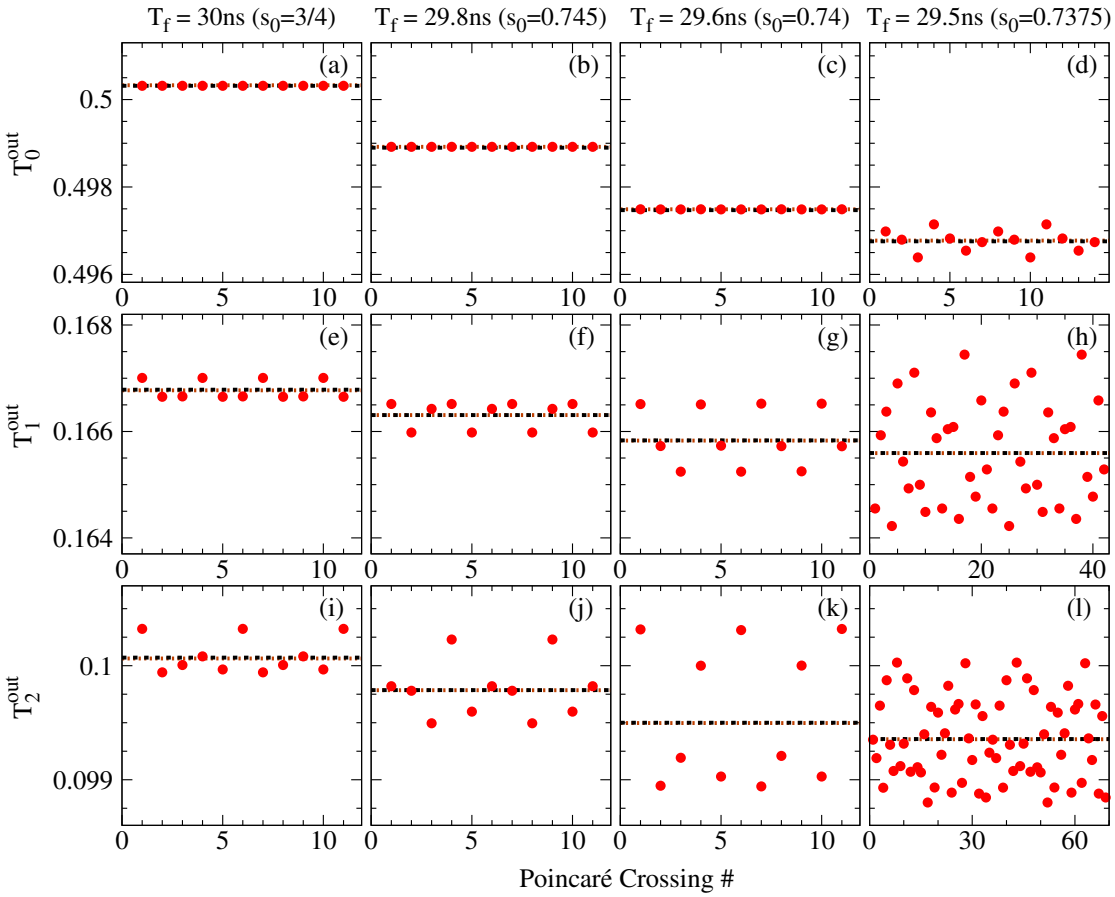


**Figure 5.19:** Poincaré return times for out-of-phase square waves with $\phi = 0.25\pi$, $P = 1.5$, $\gamma = 0.5$, $T_c = 40\,$ns, $\varepsilon = 6.25\ \ 10^{\ -4}$, $\delta = 8\ \ 10^{\ -3}$ and different values of $T_f$: 30 ns ($s_0 = 3/4$) in (a), (e) and (i); 29.8 ns ($s_0 = 0.745$) in (b), (f) and (j); 29.6 ns ($s_0 = 0.74$) in (c), (g) and (k); and 29.5 ns ($s_0 = 0.7375$) in (d), (h) and (l).

The harmonic of order $j$ for $s_0 = 3/4$ has a small splitting in $(2j+1)$ different intervals, as shown in panels (e) and (i) of Fig. 5.19 for the first ($j = 1$) and second ($j = 2$) harmonics. Introducing a mismatch of the order of 1% with respect to the ideal ratio, this splitting increases, as it can be seen in panels (f)-(g) and (j)-(k) of Fig. 5.19 for the first and second harmonics, respectively. With a 2% mismatch, the harmonic of order $j$ has already a splitting in $2n_j + 1 = (2j+1)(2n_0+1) = 14j + 7$ values, namely 21 and 35 different intervals for $j = 1$ [Fig. 5.19(h)] and $j = 2$ [Fig. 5.19(l)], respectively. The mean value of all the different intervals is very similar to the prediction given by Eq. (4.36) for $n = 21$ and $n = 35$, for the first and second harmonics, respectively.

#### Main result for out-of-phase solutions

As also shown in Appendix A for out-of-phase square-wave solutions arising with other values of $s_0$, the period of the fundamental out-of-phase square wave undergoes a splitting in $2n_0^{\text{out}}+1$ values as the mismatch in the delay times is increased, whereas the period of the higher-order harmonics shows a splitting in $2j+1$ values in the matching case and undergoes a secondary splitting in $(2j+1)n_0^{\text{out}}$ values with increasing the mismatch.

## 5.8 Summary

We have studied the synchronization conditions in the delay times for in- and out-of-phase periodic square-wave solutions in a system with two identical delay-coupled optoelectronic delay loops with negative feedback. We have demonstrated that in- or out-of-phase synchronization is possible if the ratio between the self- and cross-delay times satisfies a rational relationship. In particular, the synchronization is in-phase if the ratio involves two odd numbers, while it is out-of-phase for ratios involving an odd and an even number. We have derived analytical expressions for the period of the solutions and an approximate map for the amplitude of the square-wave oscillations. Remarkably, the map turns out to be the same for in-phase and out-of-phase solutions. We have also given an extension of this map that allows us to predict the secondary instabilities of the periodic square-wave solutions. The theoretical predictions are confirmed with numerical simulations of the full dynamical model.

We have also analyzed the effect of a small mismatch in the delay times, showing that in- and out-of-phase synchronized square waves are robust to small mismatches (up to a few percent). For a larger mismatch, the square waves develop secondary plateaus. Finally, we have demonstrated that a detailed analysis of the period of the solution using Poincaré sections shows a splitting in the duration of the periods. The fundamental solution undergoes splitting only if there is a sufficiently large mismatch. The higher harmonics show temporal splitting even in the case of perfect matching although the differences in the duration of the periods are enhanced by mismatch in the delay times. For a sufficiently large mismatch, higher harmonics undergo a secondary splitting.

Chapter 6

# Identical delay-coupled OEOs with positive feedback

## 6.1 Introduction

In this chapter, we consider the system of two identical delay-coupled OEOs described in Sec. 4.2 under positive delayed feedback as prototypical to study the conditions for synchronization of square-wave oscillations with an asymmetric duty cycle. We show that the scenario arising for positive feedback is much richer than with negative feedback.

Square-wave pulses with asymmetric duty cycle and a period close to but longer than twice the delay time have been obtained in mutually coupled EELs subject to PROF [57, 58], in ring lasers [58] and in a single OEO [62, 63]. With mutually coupled EELs [57, 58], the TE mode of each laser is rotated and coupled to the TM mode of the other laser. With this scheme, the duty cycle can be changed continuously with the coupling strength and the injection current. The square waves generated with mutually EELs under PROF were always in anti-phase.

An advantage of using mutually coupled OEOs with respect to mutually coupled EELs is that OEOs can produce square waves with asymmetric duty cycle synchronized in-phase or out-of-phase. Furthermore, we will show that two mutually coupled OEOs can generate asymmetric square-wave switching even when they are identical and they are identically coupled, in contrast with ring lasers which need to have asymmetric couplings to produce asymmetric square waves.

The outline of this chapter is the following. It begins with the study of the Hopf bifurcations of the steady state using the results described in Sec. 4.4. After showing some numerical simulations of periodic square waves with positive feedback, a map approximation is developed to provide theoretical predictions to characterize the shape of the square waves. Then, the analytical results are compared with numerical simulations of the full dynamical model. At last, the effect of a small mismatch in the delay times is studied.

6.2

## Onset of periodic solutions

In Sec. 4.4, it was shown that fast in-phase and out-of phase oscillations can appear for positive feedback ($\Phi \quad [-\pi/2, 0]$) provided $\quad -1$. Taking $s_0$ as a parameter, there is a family of in-phase Hopf bifurcation curves $\quad {}^{\text{in}}_{n}(s_0)$, which can be obtained by solving numerically Eqs. (4.24) and (4.30). Similarly, there is a family of out-of-phase Hopf bifurcation curves $\quad {}^{\text{out}}_{n}(s_0)$ given by Eqs. (4.35) and (4.40). These bifurcation curves are plotted in Fig. 6.1 for $n \quad 9$ in the range $-2.2 \quad {}_{n} \quad 0$. All the curves with $n \quad 1$ have a maximum at $\quad {}_{n} = -1$ and have a parabolic shape close to the maximum. Increasing $n$, the parabolic shape narrows, curves have more maxima, and maxima are located closer.

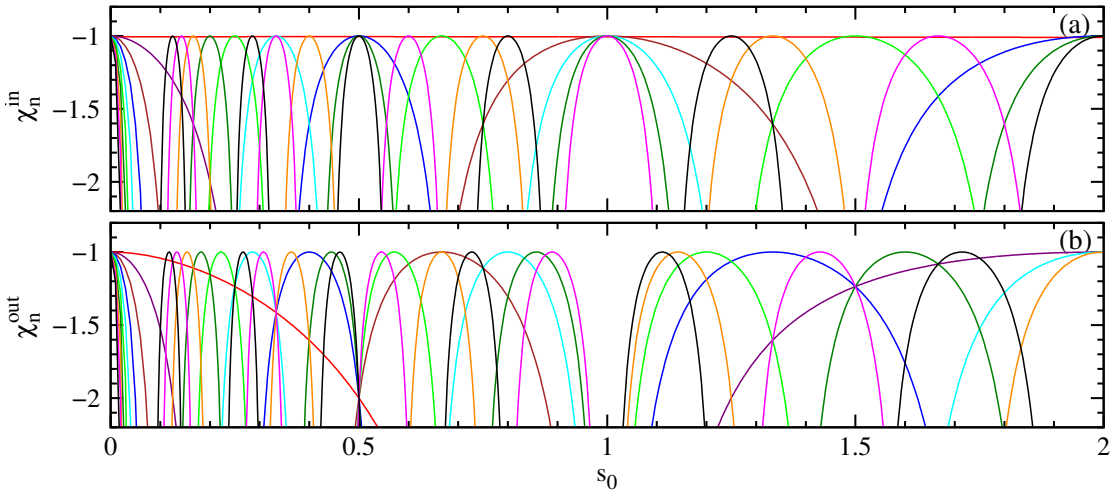


**Figure 6.1:** Hopf bifurcation curves with $\quad {}_{n} < 0$ for the in-phase (a) and antiphase (b) solutions with $n = 0$ (red line), $n = 1$ (purple line), $n = 2$ (brown line), $n = 3$ (dark cyan line), $n = 4$ (cyan line), $n = 5$ (green-yellow line), $n = 6$ (dark green line), $n = 7$ (orange line), $n = 8$ (magenta line), and $n = 9$ (black line). The red line corresponds to microsecond solutions.

The Hopf bifurcations appearing at $\quad {}_{n} = -1$ for a given value of $s_0$ are particularly relevant from the physical point of view since these are the first instabilities that appear increasing the LD power in a system with given delay times. Setting $\quad {}_{n} = -1$ in Eqs. (4.32) and (4.41), we have $\omega_n^{\text{in}} = 2m\pi$ $(m = 1, 2, ...)$ and $\omega_n^{\text{out}} = (2m + 1)\pi$ $(m = 0, 1, 2...)$, respectively, for in and out-of-phase fast oscillations. Therefore, the period is given by

$$T^{\text{in}} = \frac{1}{m}, \tag{6.1}$$

$$T^{\text{out}} = \frac{2}{2m+1}. \tag{6.2}$$

From Eqs. (4.28) and (4.37), we then determine the following values of $s_0$:

$$s_0^{\text{in}} = \frac{n-m}{m} = \frac{k}{m}, \tag{6.3}$$

$$s_0^{\text{out}} = \frac{2(n-m)}{2m+1} = \frac{2k}{2m+1}, \tag{6.4}$$

where

$$k \quad n-m. \tag{6.5}$$

The condition $s_0 > 0$ implies $k \quad 1$ and restricts the value of $m$ to the range $0 < m < n$ and $0 \quad m < n$, for in- and out-of-phase solutions, respectively.

From Eqs. (6.1)-(6.4), we have

$$s_0^{\text{in}} = kT^{\text{in}}, \tag{6.6}$$

$$1 - s_0^{\text{in}} = \frac{m-k}{m} = (m-k)T^{\text{in}}, \tag{6.7}$$

$$s_0^{\text{out}} = kT^{\text{out}}, \tag{6.8}$$

$$1 - s_0^{\text{out}} = \frac{2(m-k)+1}{2m+1} = \quad m-k+\frac{1}{2} \quad T^{\text{out}}. \tag{6.9}$$

Thus, the dimensionless time difference $(T_c - T_f)/T_c = 1 - s_0$ can be any rational number for in-phase periodic solutions, whereas it has to be an odd/odd rational number for out-of-phase solutions.

### 6.2.1 Remarks on the onset of periodic solutions

A few observations are worth pointing out. First, all the values of $s_0$ satisfying Eq. (6.4), and thus allowing for out-of-phase solutions, also satisfy Eq. (6.3); therefore, out-of-phase solutions always coexist with in-phase solutions. The coexistence of in- and out-of-phase Hopf bifurcation points for the same $s_0$ that appears with positive feedback ( $_n < 0$) is not allowed with negative feedback ( $_n > 0$), as shown in Chapter 5.

Second, several in-phase Hopf bifurcations or several out-of phase solutions may appear for the same value of $s_0$ with different periods. This means that the Hopf bifurcation at $_n = -1$ can be multiple.

These two observations are illustrated in Fig. 6.2, where the period of Hopf bifurcation points emerging from $_n = -1$ is plotted as a function of $s_0$. In this figure, points with the same $m$ are located in horizontal lines; and in linear scale [Fig. 6.2(a)], points with the same $k$ are located in straight lines of slope $1/k$ starting from the origin ($s_0 = 0, T = 0$), whereas points with the same $m-k$ are located in straight lines that start at $(s_0 = 1, T = 0)$.

### 6.2.2 Coexistence of oscillatory solutions

Regarding coexistence of solutions, we note that, once $s_0$ is fixed, only certain values of $k$ and $m$ are possible. For a given $s_0$, the fundamental in-phase nanosecond solution is the

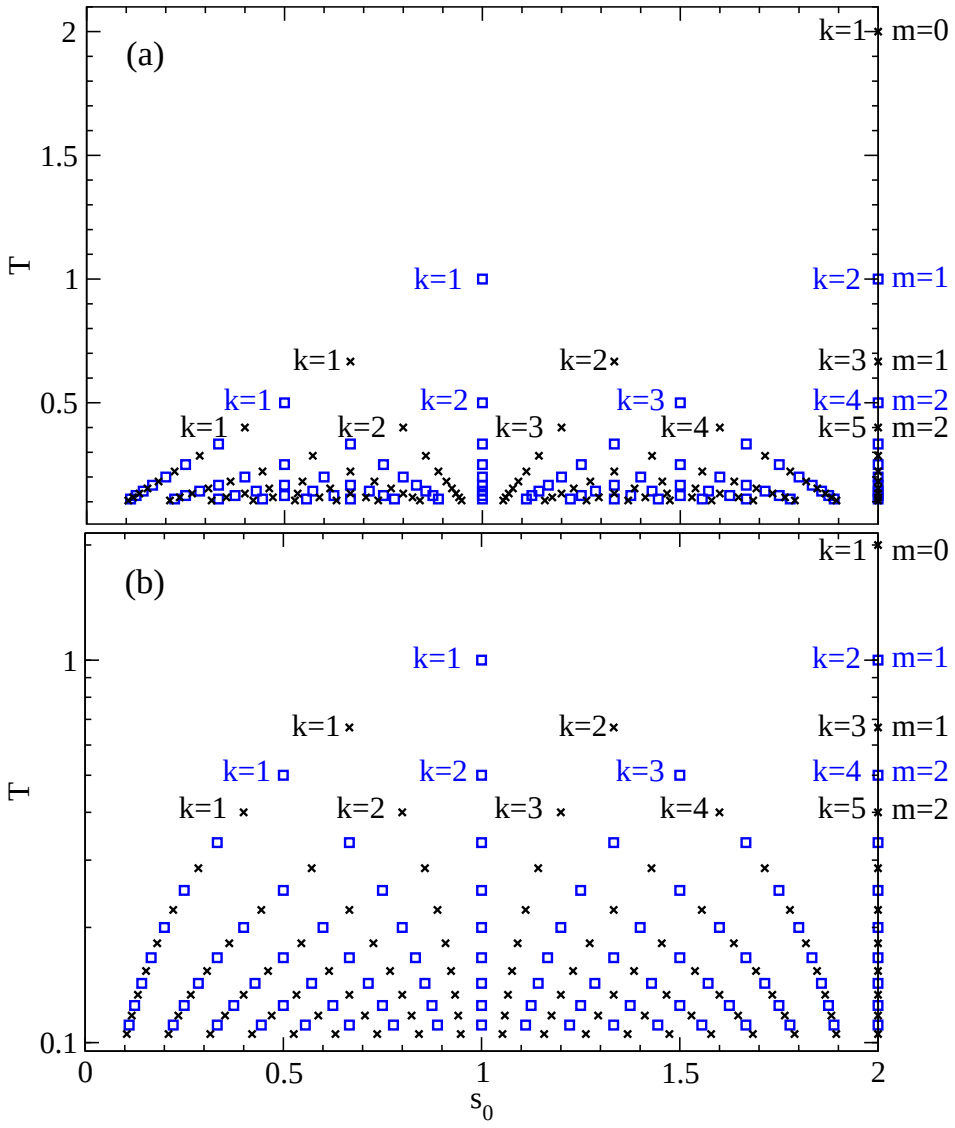


**Figure 6.2:** Hopf bifurcation points appearing at $_n = -1$ as a function of $s_0$ leading to fast oscillatory solutions with different periods $T$. Squares and crosses correspond to in- and out-of-phase Hopf bifurcations, respectively. Panel (a) shows the period $T$ in linear scale while panel (b) in logarithmic scale. As $T$ approaches zero, the number of Hopf bifurcations increases dramatically (only the bifurcations verifying $T$ 0.1 are shown).

one with frequency $\omega_1^{\text{in}}$ and corresponds to the minimum values of $k$ and $m$ that fulfill Eq. (6.3), which we label as $k_1^{\text{in}}$ and $m_1^{\text{in}}$. Higher harmonics are obtained by multiplying numerator and denominator of Eq. (6.3) by any positive integer number. This is in contrast with the system with negative feedback, for which only odd multipliers were allowed [111]. The values of $m$ and $k$ for the in-phase harmonic of order $j-1$ are given by

$$m_j^{\text{in}} = jm_1^{\text{in}},\ k_j^{\text{in}} = jk_1^{\text{in}},\ j = 1, 2, ... \tag{6.10}$$

and the period by

$$T_j^{\text{in}} = \frac{T_1^{\text{in}}}{j} = \frac{s_0^{\text{in}}}{jk_1^{\text{in}}}. \tag{6.11}$$

Note that here $j = 1$ corresponds to the fundamental in-phase nanosecond solution, $j = 2$ to the first harmonic, and so on. This is because $j = 0$ corresponds, in fact, to the slow solution at microsecond time scale. Combining Eq. (6.5) with Eqs. (6.10), we obtain

$$n_j^{\text{in}} = jn_1^{\text{in}},\ j = 1, 2, ... \tag{6.12}$$

where

$$n_1^{\text{in}} = k_1^{\text{in}} + m_1^{\text{in}}. \tag{6.13}$$

Writing the ratio between the delay times as an irreductible rational number,

$$s_0^{\text{in}} = \frac{k_1^{\text{in}}}{m_1^{\text{in}}} = \frac{q'}{\tilde{q}}, \tag{6.14}$$

leads to

$$n_1^{\text{in}} = q' + \tilde{q}. \tag{6.15}$$

The out-of-phase fundamental solution corresponds to the mimimum values of $k$ and $m$ that fulfill Eq. (6.4), which we label as $k_0^{\text{out}}$ and $m_0^{\text{out}}$. Multiplication of numerator and denominator by an even number leads to a ratio that does not fulfill Eq. (6.4). Therefore, similarly to what encountered for negative feedback [111], only odd multipliers are allowed. The harmonic of order $j$ is obtained by multiplying numerator and denominator of Eq. (6.4) by $(2j + 1)$. Therefore, the values allowed for $m$ and $k$ are given by

$$m_j^{\text{out}} = (2j + 1)m_0^{\text{out}} + j,\ k_j^{\text{out}} = (2j + 1)k_0^{\text{out}},\ j = 0, 1, 2, ... \tag{6.16}$$

The period of harmonic $j$ is

$$T_j^{\text{out}} = \frac{T_0^{\text{out}}}{2j + 1} = \frac{s_0^{\text{out}}}{(2j + 1)k_0^{\text{out}}}. \tag{6.17}$$

Here, as in Chapter 5, $j = 0$ corresponds to the fundamental nanosecond solution. Combining Eq. (6.5) with Eqs. (6.16), we obtain

$$n_j^{\text{out}} = (2j + 1)n_0^{\text{out}} + j,\ j = 0, 1, 2, ..., \tag{6.18}$$

where

$$n_0^{\text{out}} = k_0^{\text{out}} + m_0^{\text{out}}. \tag{6.19}$$

Writing the ratio between the delay times as an irreducible rational number,

$$s_0^{\text{out}} = \frac{2k_0^{\text{out}}}{2m_0^{\text{out}} + 1} = \frac{q'}{\tilde{q}}, \tag{6.20}$$

leads to

$$n_0^{\text{out}} = \frac{q' + \tilde{q} - 1}{2}. \tag{6.21}$$

## 6.3 Numerical simulations of periodic solutions with positive feedback

We encounter that the zero solution becomes unstable at $= -1$ for any value of $s_0$, leading to multiple fast oscillatory solutions, the fundamental and the harmonics, with a fundamental period of the order of tens of nanoseconds.

### 6.3.1 Fundamental nanosecond solution

We first focus on the fundamental in-phase nanosecond solution $\omega_1^{\text{in}}$. Just after the bifurcation at $= -1$, the nanosecond periodic solution is sinusoidal, as shown in Fig. 6.3(a) for $= -1.0001$. The sinusoidal shape is soon degraded [see Fig. 6.3(b) for $= 1.001$] and already for $= 1.01$ [Fig. 6.3(c)] the solution is almost a square wave with two tilted plateaus and sharp transition layers. Increasing further, the transition layers become sharper and the plateaus become practically horizontal, as shown in Fig. 6.3(d) for $= 1.1$. In Fig. 6.3, we have only plotted $x_1$ for clarity; for the values of the delays used in Fig. 6.3, $x_2$ is synchronized in phase with $x_1$. For $\Phi = -0.25\pi$, the nanosecond oscillatory solution appears supercritically. For other values of the offset phase, the solutions can appear subcritically.

### 6.3.2 Microsecond solution

Another bifurcation takes place at $^{\text{in}}_0(s_0)$ towards in-phase periodic solutions with period of the order of microseconds, corresponding to $\omega_0^{\text{in}}$. Microsecond solutions are born unstable, as discussed below; however, by increasing they soon become stable. Figure 6.3(e) shows the stable microsecond solutions found for $= -1.0104$. For values of close to -1, microsecond solutions have a sinusoidal shape. By increasing , the sinusoidal shape is degraded, as can be seen in Figs. 6.3(f), 6.3(g) and 6.3(h) with $= -1.03$, $= -1.106$, and $= -1.3$, respectively. The shape of the microsecond solutions shown in Fig. 6.3 is not square-wave because the period of the solutions is large compared to the delay times present in the system.

As reflected in Figs. 6.3(e) and 6.3(f), the period of the microsecond solutions shows a strong dependence with , contrary to the fast oscillations for which the period remains practically constant as increases. More quantitatively, Fig. 6.4 shows how the period of microsecond solutions increases with the pump close to $= -1$. The empty symbols correspond to the Hopf instability $^{\text{in}}_0(s_0)$. The filled symbols correspond to stable microsecond solutions obtained from numerical simulations. The prediction of the period close to the Hopf is excellent. Further away, the period continues to increase with a nonlinear dependence with $P$.

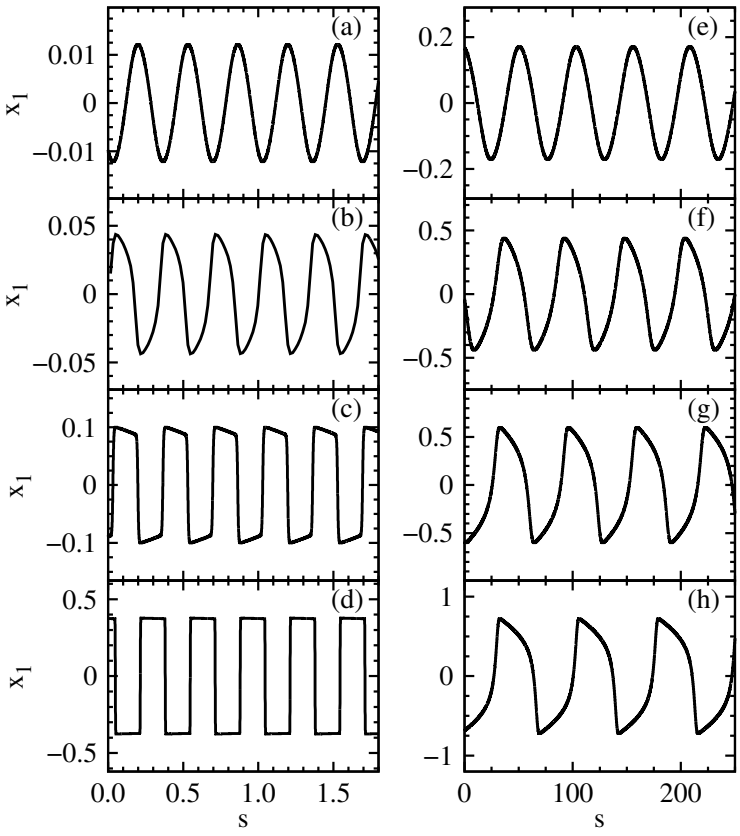


**Figure 6.3:** Periodic solutions with $\gamma = 0.5$, $\Phi = -0.25\pi$, $T_f = 40\,\text{ns}$ and $T_c = 60\,\text{ns}$, so that $s_0 = 2/3$, $\varepsilon = 4.17 \quad 10^{-4}$ and $\delta = 0.012$. The panels on the left depict nanosecond periodic solutions with $\quad = -1.0001$ (a), $\quad = -1.001$ (b), $\quad = -1.01$ (c), and $\quad = -1.1$ (d). The panels on the right depict microsecond periodic solutions with $\quad = -1.0104$ (e), $\quad = -1.03$ (f), $\quad = -1.106$ (g), and $\quad = -1.3$ (h).

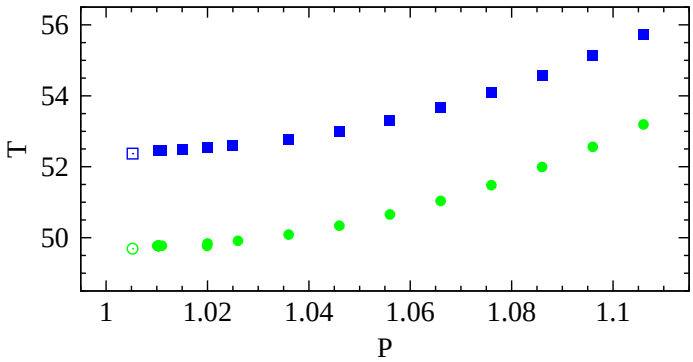


**Figure 6.4:** Period of microsecond solutions with $\gamma = 0.5$ and $\Phi = -0.25\pi$ as a function of the laser power. Blue filled squares and green filled circles correspond to numerical simulations with $s_0 = 2/3$ ($T_f = 40\,\text{ns}$ and $T_c = 60\,\text{ns}$) and $s_0 = 1/2$ ($T_f = 30\,\text{ns}$ and $T_c = 60\,\text{ns}$), respectively. Empty symbols depict the Hopf bifurcation point to microsecond solutions $\overset{\text{in}}{0}(s_0)$.

As stated before, microsecond solutions are born unstable. Thus, approaching $\overset{\text{in}}{_0}(s_0)$ from above, they become unstable slightly before reaching the threshold value. For delay-times ratios allowing for out-of-phase oscillations, microsecond solutions acquire an out-of-phase modulation with period $T_0^{\text{out}}$. For instance, for $T_f = 40\,\text{ns}$ and $T_c = 60$ ns ($s_0 = 2/3$), the microsecond becomes unstable at $= -1.01036$, before reaching the threshold $\overset{\text{in}}{_0} = -1.0052$, as shown in Fig. 6.5. Figs. 6.5(a), 6.5(b), 6.5(c) and 6.5(d) show the onset of the instability. This is a long transient, obtained after time 2 $10^5 T_c$. The final state is the fundamental out-of-phase square wave shown in Figs. 6.5(e) and 6.5(f). For delay-times ratios allowing only for in-phase oscillations, such as $T_f = 30$ ns and $T_c = 60\,\text{ns}$ ($s_0 = 1/2$), the microsecond solution has a slightly larger range of stability, up to $= -1.00992$. Nevertheless, it finally destabilizes before reaching the threshold value $\overset{\text{in}}{_0} = -1.005$. In this case, the instability originates as an in-phase modulation with period $T_1^{\text{in}}$ and leads to the fundamental in-phase square wave.

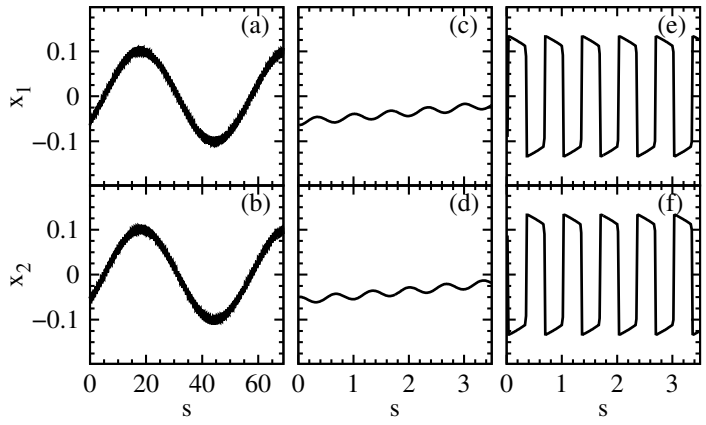


**Figure 6.5:** Numerical solutions with $P = 1.01036$, $\gamma = 0.5$, $\Phi = -0.25\pi$, $T_f = 40\,\text{ns}$ and $T_c = 60\,\text{ns}$, so that $s_0 = 2/3$, $\varepsilon = 4.17$ $10^{-4}$ and $\delta = 0.012$, starting from a microsecond oscillation as initial condition. Panels (a) and (b), with a zoom in (c) and (d), show the onset of the fast out-of-phase instability. Panels (e) and (f) show the final nanosecond periodic solutions after a long transient.

Figure 6.6 shows the microsecond periodic solution obtained with different values of $\Phi < 0$ for a larger pump ($P = 1.5$). In this figure, $x_1$ and $x_2$ are plotted in black and pink dots, respectively. The zooms plotted in the right column show that microsecond solutions are always perfectly in-phase, as predicted theoretically. Microsecond solutions are symmetric only for $\Phi = -\pi/4$. The period shows a strong dependence with the offset phase, being minimum for the symmetric solution [Fig. 6.6(e)] and increasing while the shape becomes more and more asymmetric as $\Phi$ is moved away from $\Phi = -\pi/4$. This is discussed in more detail in Sec. 6.5. Notice that, since in-phase microwaves satisfy (4.14), there is a symmetry $x_i$ $-x_i$, $\Phi_i$ $-\Phi_i - \frac{\pi}{2}$ in the time traces shown in Fig. 6.6.

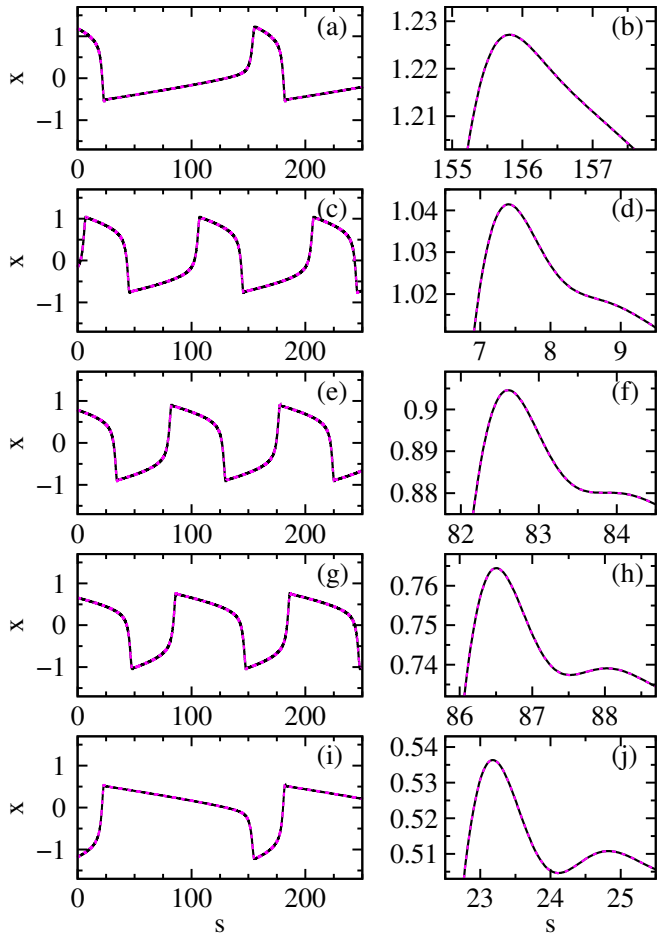


**Figure 6.6:** Microsecond oscillations with $\gamma = 0.5$, $P = 1.5$, $T_f = 40\,\text{ns}$ and $T_c = 60\,\text{ns}$ , so that $s_0 = 2/3$, $\varepsilon = 4.17 \quad 10^{-4}$ and $\delta = 0.012$. We consider $\Phi = -0.3795\pi$ in (a) and (b), $\Phi = -0.3\pi$ in (c) and (d), $\Phi = -0.25\pi$ in (e) and (f), $\Phi = -0.2\pi$ in (g) and (h), and $\Phi = -0.1205\pi$ in (i) and (j). Panels on the left column show a zoom close to a maximum of the oscillation.

### 6.3.3 Coexistence of multiple solutions

We now focus on the fast square-wave solutions. For even/odd ratio between self- and cross-delay, in- and out-of-phase square waves coexist, as predicted in Sec. 6.2. To illustrate this situation, Figs. 6.7 and 6.8 show, respectively, the in-phase and the out-of-phase fundamental square waves, both coexisting for $s_0 = 2/3$, $P = 1.5$, $\gamma = 0.5$, and different offset phases $\Phi$. As it can be seen in these figures, the periodic square waves are symmetric for $\Phi = -\pi/4$; namely, they reach a plateau value $-x^*$ for half of the period and a value $x^*$ for the other half. For other offset phases, the shape is asymmetric with a duty cycle that depends on the offset phase. This is in contrast with the negative feedback case, in which square waves are always symmetric [111]. For both in- and out-of-phase square waves, the period coincides with the predicted one within order $\varepsilon$. For $s_0 = 2/3$, the in-phase fundamental square wave corresponds to $k_1 = 2$ and $m_1 = 3$; thus, $T_1^{\text{in}} = 1/3$; while the fundamental out-of-phase oscillation corresponds to

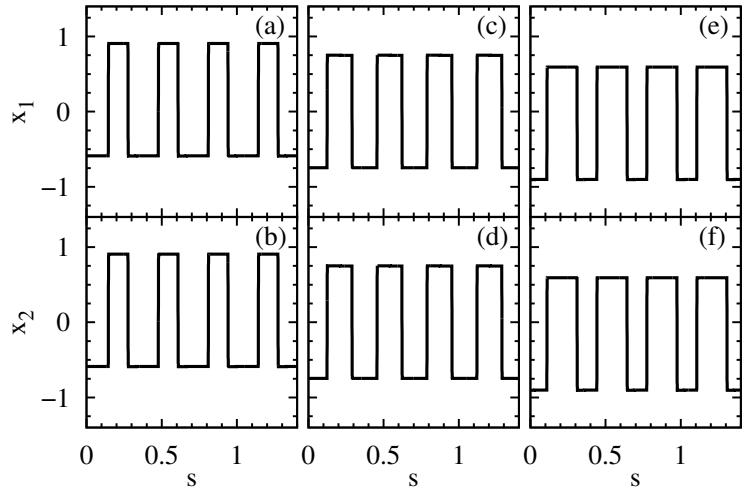


**Figure 6.7:** In-phase fundamental square wave for $\gamma = 0.5$, $P = 1.5$, $T_f = 40\,\text{ns}$ and $T_c = 60$ ns, so that $s_0 = 2/3$, $\varepsilon = 4.17 \quad 10^{-4}$ and $\delta = 0.012$. We consider $\Phi = -0.3\pi$ in (a) and (b), $\Phi = -0.25\pi$ in (c) and (d), and $\Phi = -0.2\pi$ in (e) and (f). The period of these solutions is $T_1^{\text{in}} = 1/3$.

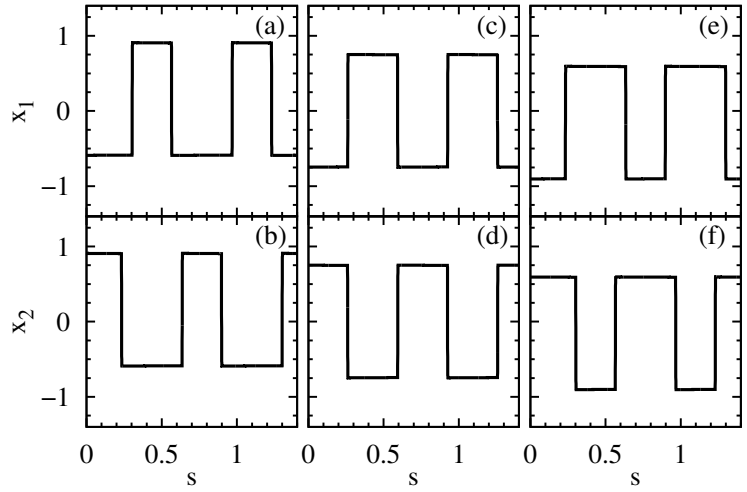


**Figure 6.8:** Out-of-phase fundamental square wave for the same parameter values as Fig. 6.7. The period of these solutions is $T_0^{\text{out}} = 2/3$.

$k_0 = 1$ and $m_0 = 2$; thus, $T_0^{\text{out}} = 2/3$. We finally note that the period does not depend on the offset phase $\Phi$; thus, varying the offset phase allows one to tune the asymmetry of the square waves without changing the period.

We now analyze the coexistence of multiple harmonics. As discussed in Sec. 6.2, the linear stability analysis predicts the emergence of multiple coexisting harmonics at $=$ $-1$ but it does not assess the stability of these solutions. Indeed, several stable harmonics coexist for given parameter values, as illustrated in Fig. 6.9. The different harmonics are obtained from numerical integration of the dynamical equations (4.13) starting from different initial conditions. More precisely, as initial condition for $x_1(s)$ within the

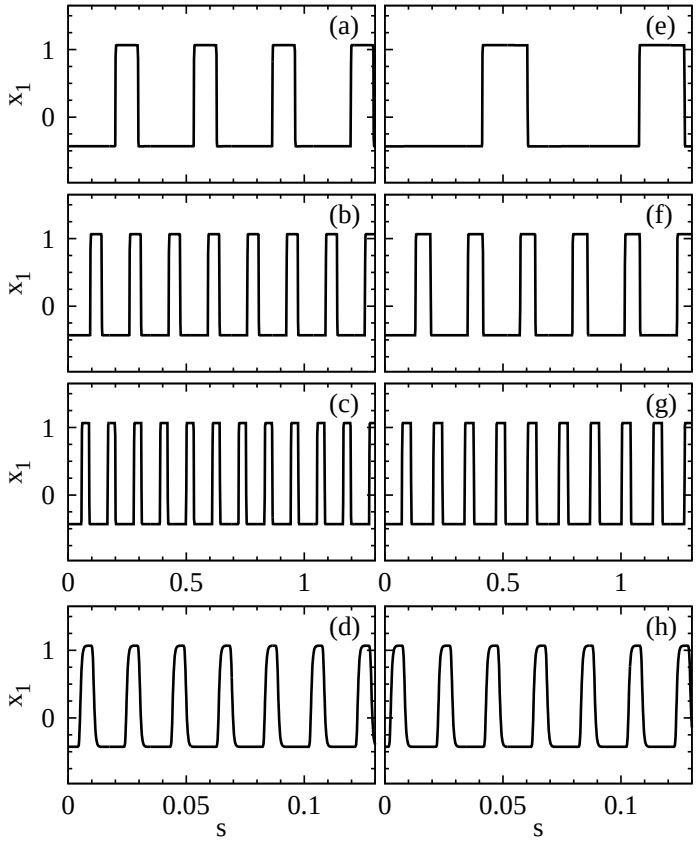


**Figure 6.9:** Time trace of square-wave periodic solutions for the same parameter values as Fig. 6.7 but $\Phi = -0.35\pi$. The panels (a)-(b)-(c)-(d) display coexisting in-phase solutions obtained starting with suitable initial conditions as indicated in the text. The panels (e)-(f)-(g)-(h) display coexisting out-of-phase solutions. The top row shows the fundamental solution (a)-(e). The second row shows the first harmonic [(b)-(f)]. The third row shows the second harmonic [(c)-(g)]. The bottom row shows the seventieth harmonic [(d)-(h)]. Notice that the time scale used in panels (d) and (h) is 10 times smaller than in the other panels.

interval $-\max(1, s_0) < s < 0$, we take a square wave with extrema $x_a$ and $x_b$, plateau lengths $s_a$ and $s_b$, and period $T_j^{\rm in}$ or $T_j^{\rm out}$. An analytic approximation for the values of $x_a$, $x_b$, $s_a$ and $s_b$ is derived in Sec. 6.4. For in-phase solutions, the initial condition for $x_2$ is given by $x_2(s) = x_1(s)$; while for out-of-phase solutions, we take $x_2(s) = x_1(s + T/2)$.

Fig. 6.9(a) shows the fundamental in-phase solution $x_1(s)$ with period $T_1^{\rm in} = 1/3$. The time trace for $x_2(s)$ (not shown) coincides with the one for $x_1(s)$. Figs. 6.9(b) and 6.9(c) show $x_1(s)$ for the 1st and 2nd in-phase harmonics, with periods $T_2^{\rm in} = T_1^{\rm in}/2 = 1/6$ and $T_3^{\rm in} = T_1^{\rm in}/3 = 1/9$, respectively. Higher-order harmonics are also solutions. As an example, Fig. 6.9(d) shows the $17^{\rm th}$ in-phase harmonic which has a period $T_{18}^{\rm in} = T_1^{\rm in}/18 = 1/54$ (notice that we have used a different scale in the time axis). As regards out-of-phase solutions, the fundamental solution with period $T_0^{\rm out} = 2/3$ is shown in Fig. 6.9(e). As in the previous case, we only display the time traces for $x_1(s)$. The time traces for $x_2(s)$ are identical but out of phase with respect to $x_1(s)$, that is $x_2(s) =$

$x_1(s + T^{\text{out}}/2)$. Figures 6.9(f) 6.9(g) show the 1st and 2nd harmonics, with periods $T_1^{\text{out}} = T_0^{\text{out}}/3 = 2/9$ and $T_2^{\text{out}} = T_0^{\text{out}}/9 = 2/27$ respectively. Finally, Fig. 6.9(h) displays the $17^{\text{th}}$ harmonic, which has a period $T_{17}^{\text{out}} = T_0^{\text{out}}/35 = 2/105$.

All these coexisting solutions are stable against small numerical perturbations. In the limit $\varepsilon = 0$, the number of possible square-wave periodic solutions coexisting for the same parameter values is infinite. In practice, however, the number of harmonics is finite because the minimal period of the square-wave periodic solution is limited by the transition time between the plateaus of the square waves, which is of order $\varepsilon$. Nevertheless, as it can be seen from Fig. 6.9, this system can exhibit tens of coexisting square-wave periodic solutions. In addition, for beyond $^{\text{in}}_{0}$, the microsecond periodic in-phase solution also coexists with the multiple fast solutions. For instance, the microsecond periodic solutions shown in Figs. 6.6(c) and 6.6(d) have been obtained with the same parameter values as the square wave shown in Figs. 6.7(a) and 6.7(b). The microsecond periodic solution turns out to have the larger basin of attraction and, starting from arbitrary initial conditions, we usually end up in this solution. However, the system may operate in any fast square-wave solution by setting the proper initial condition.

## 6.4 Map approximation for synchronized square waves with asymmetric duty cycle

In this section, we consider periodic asymmetric square waves with two different plateaus of lengths $s_a$ and $s_b$, and thus period $T = s_a + s_b$, and extrema $x_a > 0$ and $x_b < 0$, as illustrated in Fig. 6.10, and we analyze the form of the solutions in the limit of large delays. More precisely, we extend the procedure of [62, 63] for a single OEO to coupled OEOs in order to determine the extrema of the solutions and the length of each plateau.

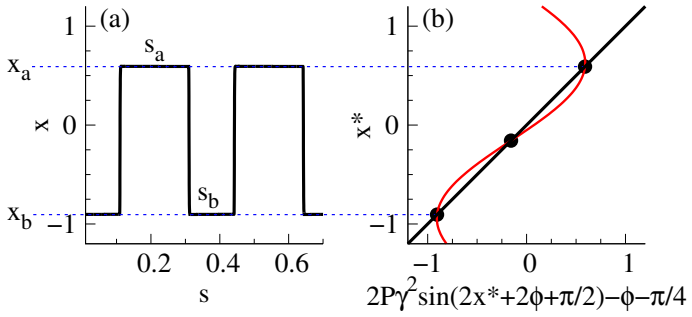


**Figure 6.10:** (a) In-phase numerical solution of the full dynamical model (4.9) for $\Phi = -0.2\pi$, $\gamma = 0.5$, $P = 1.5$, $T_f = 40\,\text{ns}$ and $T_c = 60\,\text{ns}$, so that $s_0 = 2/3$, $\varepsilon = 4.17 \quad 10^{-4}$ and $\delta = 0.012$. (b) Graphical representation of Eq. (6.40). The roots (black dots) are found where the black line [left-hand side of Eq. (6.40)] intersects the red curve [right-hand side of Eq. (6.40)]. The roots $x_a$ and $x_b$ coincide with the extrema of the numerical solution plotted in (a).

To this end, we consider lagged solutions of the form

$$x_2(s-1+s_0) = x_1(s) \quad x(s), \tag{6.22}$$

where the lag time $1-s_0$ corresponds physically to the difference $T_c-T_f$ normalized to $T_c$. In-phase and out-of-phase solutions are particular cases. For the in-phase oscillations, Eq. (6.7) leads to $x_2(s) = x_1(s)$. For the out-of-phase oscillations, from Eq. (6.9) we have $x_2(s-T^{\text{out}}/2) = x_1(s)$, namely out-of-phase periodic solutions are delayed by half of the period.

Substitution of Eq. (6.22) into Eqs. (4.13) leads to

$$\begin{aligned} \varepsilon x'(s) =& - x(s) - \delta Y(s) + 2P\gamma^2 \ \cos\left[2x(s-s_0)+2\Phi\right] - \cos 2\Phi \ , \\ Y'(s) =& x(s). \end{aligned} \tag{6.23}$$

Since for both in- and out-of-phase oscillations $s_0$ is a multiple of the period $T$ [see Eqs.(6.6) and (6.8)], in the limit $\varepsilon \quad 0$ Eqs. (6.23) lead to

$$Y(s) = -\frac{x(s)}{\delta} + \frac{2P\gamma^2}{\delta} \ \cos[2x(s)+2\Phi] - \cos(2\Phi) \ , \tag{6.24}$$

$$Y'(s) = x(s). \tag{6.25}$$

An approximate solution can be obtained taking advantage of the small value of $\delta$. Specifically, we consider the following expansion of the solution:

$$x(s) = x^0(s) + \delta x^1(s) + ..., \tag{6.26}$$

$$Y(s) = \delta \ {}^1Y^0(s) + Y^1(s) + ..., \tag{6.27}$$

where $x^0(s) = x_a$ along the positive plateau $0 < s < s_a$ and $x^0(s) = x_b$ along the negative plateau $s_a < s < T = s_b + s_a$. At order $\delta \ {}^1$, we have

$$Y^0(s) = - x^0(s) + 2P\gamma^2[\cos(2x^0(s)+2\Phi) - \cos(2\Phi)], \tag{6.28}$$

$$Y'^0(s) = 0. \tag{6.29}$$

At order $\delta^0$, we obtain

$$Y^1(s) = - x^1(s) \ \ 1 + 4P\gamma^2 \sin(2x^0(s)+2\Phi) \ , \tag{6.30}$$

$$Y'^1(s) = x^0(s). \tag{6.31}$$

Since, according to (6.29), $Y^0(s)$ is a constant, the continuity of $Y(s)$ implies $Y^1(s_a) = Y^1(s_a^+)$. Then, solving (6.31) with the initial condition $Y^1(0) = 0$ leads to

$$Y^1(s) = x_a s, \quad 0 \quad s \quad s_a, \tag{6.32}$$

$$Y^1(s) = x_a s_a + x_b(s-s_a), \quad s_a < s \quad T. \tag{6.33}$$

Since we are considering periodic solutions with period $T = s_a + s_b$, $Y^1(s_a+s_b) = Y^1(0)$, which leads to an equation relating $s_a$, $s_b$, $x_a$ and $x_b$,

$$x_a s_a + x_b s_b = 0. \tag{6.34}$$

Since $s_a > 0$ and $s_b > 0$, according to Eq. (6.34), $x_a$ and $x_b$ must have different sign. Without losing generality, we consider $x_a > 0$ and $x_b < 0$.

Substituting (6.32) and (6.33) into (6.30), we obtain

$$x^1(s) = -\frac{x_a s}{1 + 4P\gamma^2 \sin(2x_a + 2\Phi)}, \quad 0 \quad s \quad s_a, \tag{6.35}$$

$$x^1(s) = -\frac{x_a s_a + x_b(s - s_a)}{1 + 4P\gamma^2 \sin(2x_b + 2\Phi)}, \quad s_a < s \quad T. \tag{6.36}$$

The continuity condition $x^1(s_a^+) = x^1(s_a)$ implies

$$\cos(x_b + x_a + 2\Phi)\sin(x_b - x_a) = 0. \tag{6.37}$$

Since $x_a \neq x_b$, the solution of (6.37) is $x_a + x_b + 2\Phi = \quad (2n+1)\pi/2$. For $\Phi \quad [-\pi/2, 0]$, as suitable for negative feedback, we obtain the following equation relating $\Phi$ to the extrema $x_a$ and $x_b$:

$$\Phi = -\pi/4 - (x_a + x_b)/2. \tag{6.38}$$

Therefore, the square wave is symmetric ($x_b = -x_a$) for $\Phi = -\pi/4$, asymmetric with $x_a > x_b$ for $\pi/2 \quad \Phi < -\pi/4$, and asymmetric with $x_a < x_b$ if $-\pi/4 < \Phi < 0$. To determine $x_a$ and $x_b$, we need an additional equation relating both. Subtracting Eq. (6.28) with $x^0(s) = x_a$ from the same equation with $x^0(s) = x_b$, we obtain

$$(x_a - x_b) = 4P\gamma^2 \sin(x_a + x_b + 2\Phi)\sin(x_b - x_a). \tag{6.39}$$

Introducing (6.38) into (6.39), we obtain an equation for $x_a$ or $x_b$, which we label as $x^*$,

$$x^* = 2P\gamma^2 \sin(2x^* + 2\Phi + \pi/2) - \Phi - \pi/4. \tag{6.40}$$

Introducing (6.40) into (6.28), we get the value for $Y_0$,

$$Y^0 = \Phi + \pi/4 - 2P\gamma^2 \cos(2\Phi). \tag{6.41}$$

Defining

$$z^* = x^* + \Phi + \pi/4, \tag{6.42}$$

Eq. (6.40) can be written as

$$z^* = 2P\gamma^2 \sin(2z^*). \tag{6.43}$$

Equation (6.43) has always the root $z^* = 0$, which corresponds to $x^* = x_c = -\pi/4 - \Phi$. Substituting this result into (6.38), we get that $x_c = (x_a + x_b)/2$, namely this root corresponds to the average of the two extrema of the square wave. For $P\gamma^2 > 1/4$, there are also two non-zero roots, $z_a$ and $z_b$, with $z_b = -z_a$, which correspond to the extrema $x_a > 0$ and $x_b < 0$ of the square wave. For $\Phi = -\pi/4$, $x^* = z^*$ and $x_b = -x_a$. As the offset phase departs from $\Phi = -\pi/4$, the roots for $x$ are asymmetrically located with respect to 0. The limit value of $\Phi$ for which Eq. (6.40) has solutions with $x_a > 0$ and $x_b < 0$ can be obtained setting $x^* = 0$ and solving the resulting equation,

$$\Phi_m = -\pi/4 - 2P\gamma^2 \cos(2\Phi_m). \tag{6.44}$$

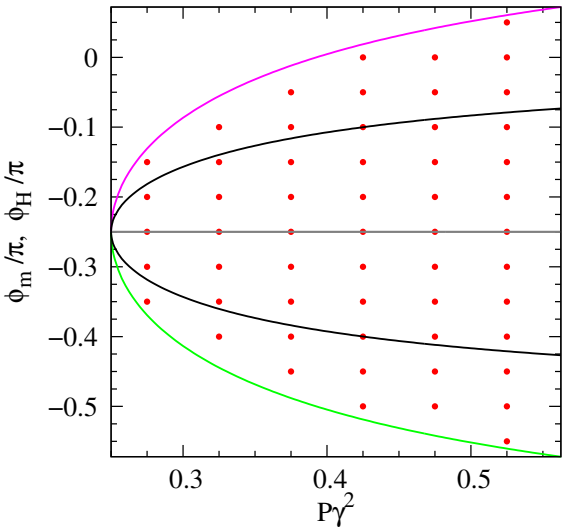


**Figure 6.11:** Red dots show the region of existence of the square-wave solutions. Boundaries are set by the solutions of Eq. (6.44), $\Phi_{m_a}$ [pink line] and $\Phi_{m_b}$ [green line], which correspond to the most asymmetric square waves. Black lines correspond to the Hopf bifurcation. Square waves coexist with the zero solution in the subcritical region between black and color lines.

This equation has a trivial solution, $\Phi_{m_s} = -\pi/4$, and two nontrivial solutions, $\Phi_{m_a}$ and $\Phi_{m_b}$. These solutions are plotted in Fig. 6.11 as a function of $P\gamma^2$. For a given value of $P\gamma^2$, $\Phi_{m_a}$ corresponds to the most asymmetric solution with $x_a = 0$ and $s_a = T$ [pink line], and $\Phi_{m_b}$ to the one with $x_b = 0$ and $s_b = T$ [green line]. In contrast, the symmetric solution, $\Phi_{m_s}$, is given by the horizontal line. Since (6.43) is independent of $\Phi$, using (6.42), it turns out that, for a given $P\gamma$, $x_a$ and $x_b$ have a linear dependence with $\Phi$ with slope $-1$. Then, since the intercept is given by $\Phi_{m_a}$ or $\Phi_{m_b}$, we can write

$$x_a = -\Phi + \Phi_{m_a}, \tag{6.45}$$

$$x_b = -\Phi + \Phi_{m_b}. \tag{6.46}$$

Comparing these equations with (6.38), we have $\Phi_{m_a} + \Phi_{m_b} = -\pi/2$. The range of offset phases $[\Phi_{m_b}, \Phi_{m_a}]$ for which asymmetric periodic square waves are predicted to exist increases with $P\gamma^2$. For comparison, the black lines show the offset phase at the Hopf bifurcation $_n = -1$, which, from Eq. (4.16), is given by

$$\Phi_{\rm H} = \frac{(-1)^k\ 1}{2} \arcsin\ \ \frac{1}{4P\gamma^2}\ \ + k\pi. \tag{6.47}$$

It is clear that, for a given $P\gamma^2$, the range $[\Phi_{m_b}, \Phi_{m_a}]$ extends well beyond the range given by Hopf offset phases. Therefore, according to this theoretical analysis, the Hopf bifurcation leading to square waves is subcritical for offset phases that differ from $-\pi/4$. In fact, for $P\gamma^2 = \pi/8$, asymmetric solutions exist over the whole range of positive feedback with $\Phi$ $[-\pi/2, 0]$, and for larger $P\gamma^2$ they can be found beyond this range. Thus, although asymmetric square waves are born at Hopf bifurcations which can only take place for positive feedback, once they are born, increasing $P\gamma^2$ and changing the feedback phase, we can obtain stable asymmetric square waves with negative feedback.

Finally, taking into account that the total period is $T = s_a + s_b$, the length of the plateaus can be obtained from Eq. (6.34):

$$s_a = -\frac{x_b}{x_a - x_b}T, \tag{6.48}$$

$$s_b = \frac{x_a}{x_a - x_b}T. \tag{6.49}$$

Since $x_a$ and $x_b$ are the roots of (6.40) and, therefore, depend on the offset phase $\Phi$, the duty cycle of the square wave can be tuned with $\Phi$, as seen from numerical simulations in Sec. 6.3 and Sec. 6.5.

## 6.5 Comparison between theoretical results for square waves and numerical simulations

In this section, we compare the theoretical predictions of the previous section with numerical simulations of Eq. (4.13). The first feature to note is that, comparing Fig. 6.7 with Fig. 6.8, it is clear that, for a given value of , both extrema $x_a$ and $x_b$ are the same for in- and out-of-phase oscillations, as predicted by Eq. (6.40) which is the same for in- and out-of-phase oscillations.

A more detailed comparison of the theoretical predictions and numerical results is shown in Fig. 6.12 for $P = 1.5$ and $\gamma = 0.5$ as function of the offset phase $\Phi$. Figure 6.12(a) shows the bifurcation diagram of the extrema $x_a$ and $x_b$. The pink and green solid lines represent, respectively, the theoretical values for $x_a$ and $x_b$ obtained solving Eq. (6.40), while the solid black line shows the stable zero solution. Unstable solutions are plotted as dotted black lines. The unstable branch of periodic solutions that connects the Hopf bifurcation point to the branch of stable periodic square-wave solutions has been obtained using DDE-BIFTOOL [74, 75, 76, 77]. The results of numerical simulations are plotted with symbols. Red points correspond to in- and out-of-phase square waves obtained starting from suitable initial conditions, as explained in Sec. 6.3. Black points represent numerical simulations verifying the stability of the zero solution. Clearly, the theoretical prediction for the square-wave amplitudes is in perfect agreement with the numerical simulations. Following Eqs. (6.45) and (6.46), the amplitudes have a linear dependence with the offset phase. The amplitudes are symmetrical for $\Phi = -\pi/4$ and become progressively more asymmetric as $\Phi$ is moved away from this value. The square-wave solution disappears when one of the amplitudes touches zero. Starting from an offset phase far away from the symmetric case $\Phi = -\pi/4$ and changing $\Phi$ towards the symmetric value, the bifurcation from the zero solution to the square-wave solutions appears subcritically, as predicted theoretically in Sec. 5.3. The width of the subcritical region agrees with the theoretical prediction. We note that, for smaller values of $P\gamma^2$ close to the limit value 0.25, numerically one finds that the subcritical region is smaller than the predicted one because at these power levels nanosecond solutions do not have a square-wave shape.

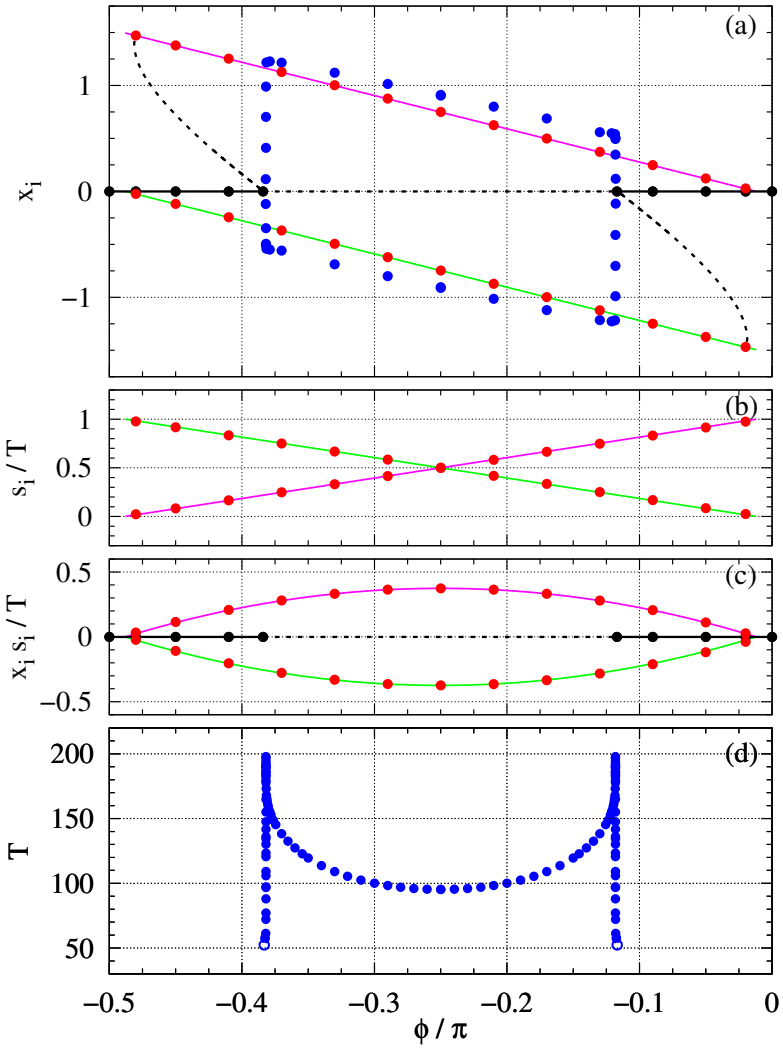


**Figure 6.12:** Bifurcation diagram of the zero solution showing (a) the extrema $x_a$ [pink line] and $x_b$ [green line] of the square waves, (b) the length $s_1$ [pink line] and $s_2$ [green line] of the plateaus scaled to the period $T$, and (c) the scaled products $x_a s_a/T$ and $x_b s_b/T$ as a function of $\Phi$ with $P = 1.5$ and $\gamma = 0.5$. Panel (d) shows the period of microsecond solutions. Lines correspond to the theoretical prediction of stable (solid) and unstable (dashed) solutions (see text). Filled circles correspond to different solutions obtained from the numerical integration of the full dynamical model with $T_f = 40\,\text{ns}$ and $T_c = 60\,\text{ns}$: zero solution (black points), in- or out-of-phase square waves (see text) (red points), and microsecond solutions (blue points). The empty blue circles in (d) show the theoretical threshold for microsecond solutions.

Figure 6.12(b) shows the lengths $s_a$ and $s_b$ of the two plateaus of the asymmetric square waves scaled to the period $T$, while Fig. 6.12(c) shows the scaled products $x_a s_a/T$ and $x_b s_b/T$. Again, the theoretical prediction is in excellent agreement with the numerical simulations.

For comparison, blue points in Fig. 6.12(a) show the amplitude from numerical simulations of the microsecond solution that coexists with the nanosecond square waves.

Microsecond solutions are born supercritically from the zero solution, an indication that they have a nature that differs from that of the fast nanosecond square waves. Furthermore, as indicated when discussing Fig. 6.6, the period of the microsecond solution has a strong dependence with $\Phi$. Quantitative results for this dependence are shown in Fig. 6.12(d). Empty circles in Fig. 6.12(d) correspond to the theoretical prediction for the period at threshold, $T(\ {}^{in}_{0})$. Just after threshold, the stationary amplitudes $x_a$ and $x_b$ and the period increase very fast. The period increases by a factor 4 from $\Phi = -0.3826\pi$ ( $= -1.0090$) to $\Phi = -0.3818\pi$ ( $= -1.0143$), where it takes a maximum. Both amplitudes $x_a$ and $x_b$ keep increasing until $\Phi_{\max} = -0.379\pi$ ( $= -1.0337$), where $x_a$ reaches a maximum. At this point, the amplitudes are larger than those of the square wave for the same parameters. After that, increasing $\Phi$, $x_a$ and $x_b$ decrease practically linearly with $\Phi$ with a slope slightly smaller than that of the square waves. At $\Phi = -0.25\pi$, where the microsecond solution is symmetrical, the period has a relative minimum taking a value which is, nevertheless, about the double than the one at threshold. The value of the period as function of the feedback phase is symmetrical with respect to $\Phi = -0.25\pi$. As for the amplitudes, $x_a$ and $x_b$ keep decreasing linearly up to $\Phi_{\min} = -0.121\pi$ ( $= -1.0337$), where $x_b$ reaches a minimum beyond which $x_a$ and $x_b$ decrease fast to zero.

Increasing $P\gamma^2$, the bifurcation diagram has a similar shape but the range in which oscillatory solutions exist increases. As predicted by (6.44) for periodic square waves, for $P\gamma^2 > \pi/8$ this range includes positive values of $\Phi$ (negative feedback). This theoretical prediction is confirmed by numerical simulations, as illustrated in Fig. 6.13, which displays in-phase square waves with asymmetric duty cycle with zero feedback ( $= 0$) and negative feedback ( $> 0$) obtained from numerical integration of (4.13). In Fig. 6.13, the positive plateau is larger than the negative plateau. In general, for any solution with $\Phi$ $[-\pi/4, \pi/4]$, the positive plateau is longer than the negative one, while for $\Phi$ $[-3\pi/4, -\pi/4]$ is the other way around.

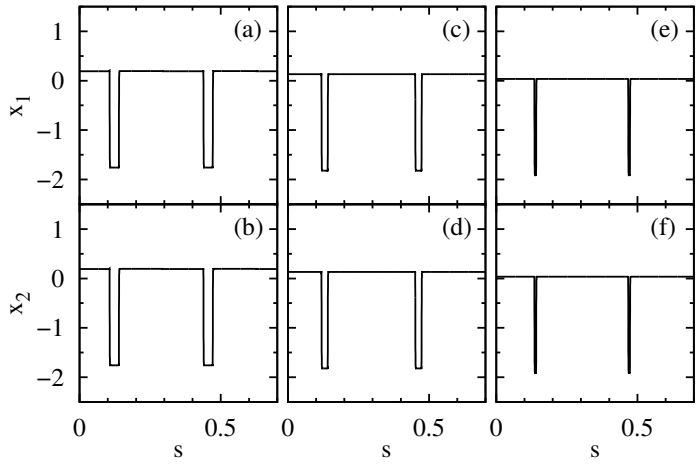


**Figure 6.13:** Periodic square waves with $P = 2.1$, $\gamma = 0.5$, $T_f = 40\,\text{ns}$, $T_c = 60\,\text{ns}$, $= 0$ [(a) and (b)], $= 0.02$ [(c) and (d)], and $= 0.05$ [(e) and (f)].

If the laser power is further increased, the square-wave periodic solutions degrade and finally destabilize. The system becomes chaotic, although $x_1$ and $x_2$ can be still synchronized for moderate values of the laser power, as it can be seen in Figs. 6.14(a) and 6.14(b), 6.14(c) and 6.14(d), and 6.14(e) and 6.14(f). For $P$ 2.9, synchronization is lost; and for larger $P$, the solutions become more and more chaotic, as can be seen in Figs. 6.14(g) and 6.14(h), 6.14(i) and 6.14(j), and 6.14(k) and 6.14(l).

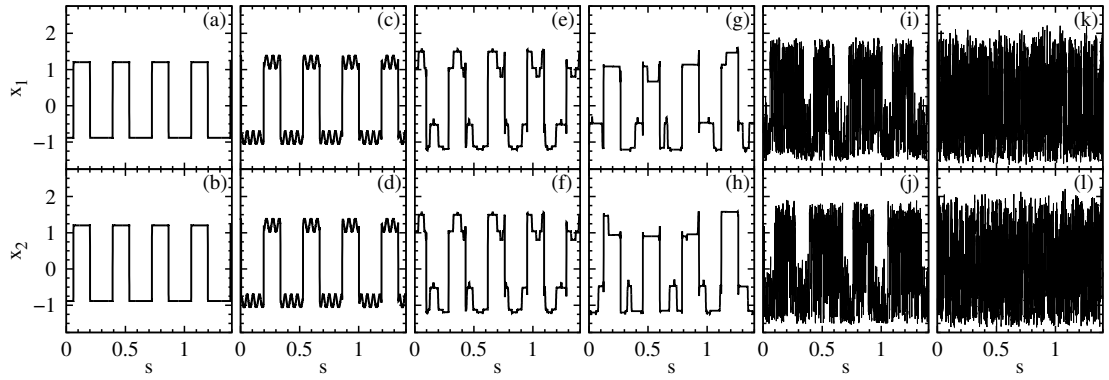


**Figure 6.14:** Numerical simulations with $\gamma = 0.5$, $T_f = 40\,\text{ns}$, $T_c = 60\,\text{ns}$, and $\Phi = -0.3\pi$, where the initial condition is an in-phase periodic solution with period $T^{\text{in}} = 2/3$. We consider $P = 2.4$ in (a) and (b), $P = 2.5$ in (c) and (d), $P = 2.8$ in (e) and (f), $P = 2.9$ in (g) and (h), $P = 3.5$ in (i) and (j), and $P = 4$ in (k) and (l).

## 6.6 Mismatch in the delay-times ratio

The square-wave solutions with asymmetric duty cycle emerging from a Hopf bifurcation with positive feedback are stable to numerical perturbations and robust to changes of the offset phase. Nevertheless, from the experimental point of view, it is important to assess also the robustness in front of an eventual mismatch in the delay-times ratio with respect to the ideal case of being a simple rational fraction. In this section, we analyse this keeping $T_c$ fixed while changing $T_f$. As initial condition for each simulation, we use an in-phase or out-of-phase square-wave ideal solution with amplitudes given by (6.45), (6.46), and (6.44); period predicted by (6.1) or (6.2); and duty cycle given by (6.48) and (6.49).

In Fig. 6.15, we can see the fundamental (a) and first harmonic (b) out-of-phase periodic square waves generated for a perfect matching condition $s_0 = 2$. For a small mismatch in $T_f$, the plateaus become shorter and the transition looses sharpness, as can be seen in panels (c) and (d) for a 1% mismatch in $T_f$, in panels (e) and (f) for a 3% mismatch, and in panels (g) and (h) for a 5% mismatch. The fundamental solution is robust to mismatches larger than 5%, but the first harmonic is more sensible to mismatch because it has a smaller period.

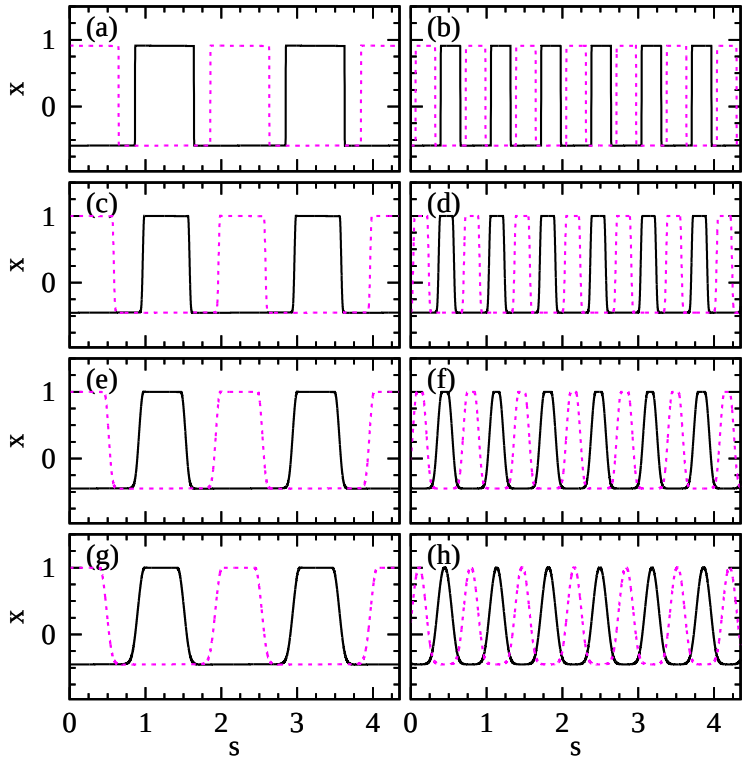


**Figure 6.15:** Out-of-phase periodic solutions with $\Phi = -0.3\pi$, $\gamma = 0.5$, $P = 1.5$ and $T_c = 30$ ns, so that $\varepsilon = 8.33 \quad 10^{-4}$ and $\delta = 0.006$, with perfect matching condition $s_0 = 2$ with $T_f = 60$ ns [(a) and (b)], a 1% mismatch with $T_f = 60.6$ ns [(c) and (d)], a 3% mismatch with $T_f = 61.8$ ns [(e) and (f)], and a 5% mismatch with $T_f = 62.7$ ns [(g) and (h)]. Panels on the left show the fundamental solution ($T_0^{\text{out}} = 2$); panels on the right show the first harmonic ($T_1^{\text{out}} = 2/3$).

The same effect takes place for in-phase solutions, as can be seen from Fig. 6.16, although the first harmonic in this case only survives until a 3% mismatch. For a 5% mismatch, the first harmonic initial condition leads to a stationary solution with a much smaller period ($T = 0.083$) [Fig. 6.16 (h)]. For the same parameter values, out-of-phase solutions are more resilient to delay-time mismatches because they have a larger period, as shown in Fig. 6.2. Another way to increase the robustness to mismatch in the delay times consists of decreasing the asymmetry of the duty cycle, since the mismatch makes the lengths of the plateaus smaller.

As discussed in Sec. 5.6 for symmetric square waves arising in the negative feedback case, for a 2% mismatch the degradation leads to the apparition of small secondary plateaus at intermediate values of $x_1$ and $x_2$. These plateaus are not symmetrically located around $x = 0$ and, thus, their apparition is a way for the system to break the symmetry of the solution. On the contrary, square waves with asymmetric duty cycle show a larger degree of robustness since they don't exhibit secondary plateaus with a small mismatch in the delay times. Their intrinsic asymmetry allows them to flexibly adapt to a small mismatch in the delay time with a minimal deformation in the slope.

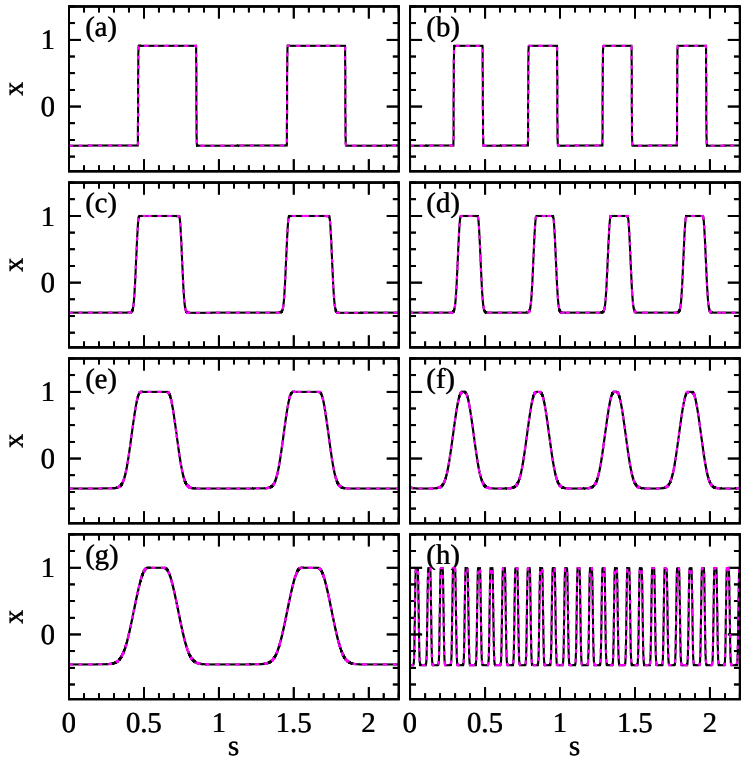


**Figure 6.16:** In-phase periodic solutions for the same parameter values as Fig. 6.15. Panels on the left show the fundamental nanosecond solution ($T_1^{\text{in}} = 1$), while panels on the right show the first harmonic ($T_2^{\text{in}} = 0.5$). Panel (h) shows the stationary solution found with a 5% mismatch when the initial condition is the first harmonic.

## 6.7 Detailed analysis of the period of the solutions

In this section, we investigate in detail the frequency of the square waves with asymmetric duty cycle from numerical simulations of the full dynamical model (4.11). As in Sec. 5.7, we compute the Poincaré return times with a Poincaré section at $x_1 = 0$ when $x_1$ becomes positive. In this case, we also obtain temporal splitting in different intervals, but the scenario is much simpler. The number of intervals is given by the order of the harmonic, $j$,

$$S_j = j, \tag{6.50}$$

and there is no secondary splitting when moving further away from the rational value for $s_0$.

For the harmonics, the mean value of the different $S_j$ intervals is in good agreement with the prediction obtained in Sec. 4.4 from the linear stability analysis of the zero solution taking into account the effects of $\varepsilon$ and $\delta$. We note that the larger the value of $n_j$ the closer the numerical value for the period to the prediction, which suggests the existence of a nonlinear effect which decreases with $n_j$.

In the figures shown in this section, panels [(a)-(d)] correspond to the fundamental square wave, whereas panels [(e)-(h)] and [(i)-(k)] correspond to the first and second harmonics, respectively; red dots correspond to numerical simulations, orange dashed lines to the numerical value of the mean period, and black dashed lines to the prediction for the period given by Eqs. (4.25) and (4.29) or (4.36) and (4.39). We will consider $\Phi = -0.25\pi$, $P = 1.5$, $\gamma = 0.5$, $= 5$ s, $\tau = 25$ ps and different values of $s_0$ near $s_0 = 2$.

### 6.7.1 Temporal splitting in in-phase solutions

As an example for in-phase solutions, in Fig. 6.17 the Poincaré return times are plotted for $T_c = 30$ ns, $\varepsilon = 8.33 \ 10^{-4}$, $\delta = 6 \ 10^{-3}$ and different values of $T_f$ near $T_f = 60$ ns. In panels (a), (e) and (i), $T_f = 60$ ns, so that $s_0 = 2$, whereas in the other panels there is a small mismatch in $s_0$ with respect to the ideal ratio. For $s_0 = 2$, the minimum values of $k$ and $m$ that fulfill Eq. (5.6) are $k_1 = 2$ and $m_1 = 1$; thus, according to Eq. (6.13), $n_1 = k_1 + m_1 = 3$.

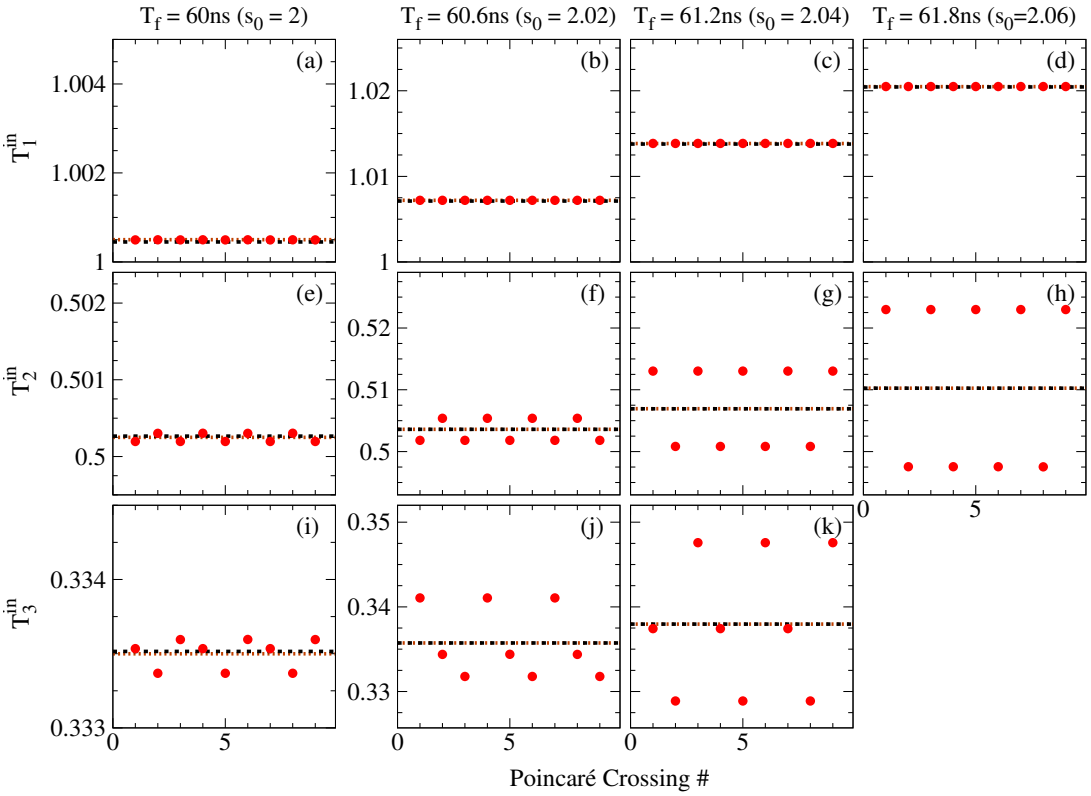


**Figure 6.17:** Poincaré return times for in-phase square waves with $\phi = -0.25\pi$, $P = 1.5$, $\gamma = 0.5$, $T_c = 30$ ns, $\varepsilon = 8.33 \ 10^{-4}$, $\delta = 6 \ 10^{-3}$ and different values of $T_f$: 60 ns ($s_0 = 2$) in (a), (e) and (i); 60.6 ns ($s_0 = 2.02$) in (b), (f) and (j); 61.2 ns ($s_0 = 2.04$) in (c), (g) and (k); and 29.4 ns ($s_0 = 2.06$) in (d) and (h).

At the ideal ratio $s_0 = 2$ [panel (a)], the fundamental solution has a period $T_1^{\rm in} = 1.0005$, in agreement with the prediction given by Eqs. (4.25) and (4.29) for $n = 3$, $T^{\rm in} = 1.00045$. With a small mismatch with respect to the ideal ratio, the period of the fundamental solution is also in agreement with the prediction given by Eqs. (4.25) and (4.29), as shown in panels (b), (c) and (d) for 1%, 2% and 3% mismatches, respectively.

The harmonic of order $j$ for $s_0 = 2$ has a small splitting in $j$ different intervals, as shown in panels (e) and (i) for the first ($j = 1$) and second ($j = 2$) harmonics. The splitting increases with the mismatch, as it can be seen in panels (f)-(h) and (j)-(k). The mean value of all the different intervals is very similar to the prediction given by Eqs. (4.25) and (4.29) for $n = 6$ and $n = 9$, for the first and second harmonics, respectively. With a 3% mismatch, the second harmonic becomes unstable.

### 6.7.2 Temporal splitting in out-of-phase solutions

As an example for out-of-phase solutions, in Fig. 6.18 the Poincaré return times are plotted for $T_c = 30\,$ns, $\varepsilon = 8.33\ \ 10^{\ -4}$, $\delta = 6\ \ 10^{\ -3}$ and different values of $T_f$ near $T_f = 60\,$ns. In panels (a), (e) and (i), $T_f = 60\,$ns, so that $s_0 = 2$, whereas in the other

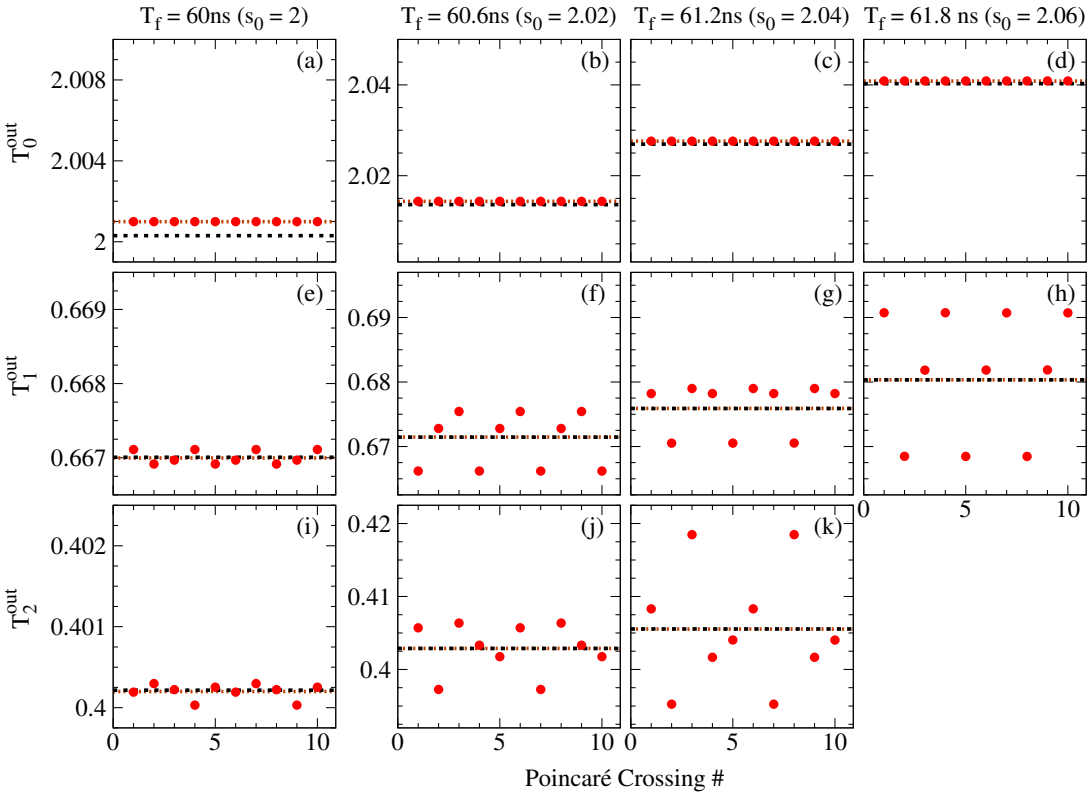


**Figure 6.18:** Poincaré return times for out-of-phase square waves with $\phi = -0.25\pi$, $P = 1.5$, $\gamma = 0.5$, $T_c = 30\,$ns, $\varepsilon = 8.33\ \ 10^{\ -4}$, $\delta = 6\ \ 10^{\ -3}$ and different values of $T_f$: 60 ns ($s_0 = 2$) in (a), (e) and (i); 60.6 ns ($s_0 = 2.02$) in (b), (f) and (j); 61.2 ns ($s_0 = 2.04$) in (c), (g) and (k); and 29.4 ns ($s_0 = 2.06$) in (d) and (h).

panels there is a small mismatch in $s_0$ with respect to the ideal ratio. For $s_0 = 2$, the minimum values of $k$ and $m$ that satisfy Eq. (5.6) are $k_0 = 1$ and $m_0 = 0$; thus, according to (6.20), $n_0 = k_0 + m_0 = 1$.

At the ideal ratio $s_0 = 2$ [panel (a)], the fundamental solution has a period $T_0^{\text{out}} = 2.00099$, whereas the prediction given by Eqs. (4.36) and (4.39) is $T^{\text{out}} = 2.0003$. For larger values of $n$, the difference between the prediction and the numerical value is smaller.

With a small mismatch with respect to the ideal ratio, the period of the fundamental solution is also in agreement with the prediction given by Eqs. (4.36) and (4.39), as shown in panels (b), (c) and (d) for 1%, 2% and 3% mismatches, respectively.

The harmonic of order $j$ for $s_0 = 2$ has a small splitting in $j$ different intervals, as shown in panels (e) and (i) for the first ($j = 1$) and second ($j = 2$) harmonics. Similarly than for the square waves generated with negative feedback, introducing a small mismatch the splitting increases, as it can be seen in panels (f)-(h) and (j)-(k) for the first and second harmonics, respectively. The mean value of all the different intervals is very similar to the prediction given by Eqs. (4.36) and (4.39) for $n_1 = 4$ and $n_2 = 7$, for the first and second harmonics, respectively. With a 3% mismatch, the second harmonic is not stable.

## 6.8 Summary and concluding remarks

In this chapter we have studied analytically and numerically the dynamics of two delay-coupled identical OEOs subject to positive feedback. We have determined the conditions for in- and out-of-phase synchronized periodic solutions and derived analytical expressions for the period of the solutions, as well for the amplitude and the plateau lengths of the square-wave solutions. Our analytical results are in good agreement with numerical simulations of the full dynamical model and bifurcation diagrams obtained from continuation techniques.

In comparison to the negative feedback case, $> 0$, the positive feedback case, $< 0$, shows a much richer scenario. In both cases in- and out-of-phase fast square-wave oscillations are encountered when the feedback and the coupling delay times satisfy appropriate ratios. Also, in both cases the fast square waves are born at Hopf bifurcations from the zero state at $= 1$ and multiple stable periodic solutions with different periods can coexist for the same parameter values. However, the square waves born for negative feedback have always a symmetric duty cycle while for positive feedback have in general an asymmetric one with a degree of asymmetry depending on the offset phase. For positive feedback out-of-phase square waves always coexist with in-phase square waves. This coexistence was not present for solutions born with negative feedback, as shown in Chapter 5. The coexistence of in- and out-of-phase solutions provides a large degree of flexibility for tuning the period of the square waves without changing any parameter, just by selecting a suitable initial condition, making this system a good candidate to be implemented for information encoding as a high-capacity memory device. Besides, the duty cycle of the periodic square waves can be tuned with the offset phase.

Curiously enough, we have also shown that, in fact, for a sufficiently large pump strength, in- and out-of-phase square waves with asymmetric duty cycle can also exist for negative feedback. These square waves are born at a Hopf bifurcation taken place at positive feedback and, therefore, a convenient way to generate them is to start from positive feedback and change the offset phase while increasing the pump level.

Another difference with the negative feedback case is that, for positive feedback, besides the fast square-wave oscillations, which for typical parameter values are at nanosecond time scale, there are in-phase microsecond periodic solutions. For the periodic microsecond solutions, both the period and the duty cycle asymmetry can be tuned with the offset phase.

We have also shown that square waves with asymmetric duty cycle born at positive feedback turn out to be more robust and flexible with respect to changes in the parameter values than the solutions with symmetric duty cycle obtained with negative feedback. In particular, while square waves with symmetric duty cycle for $> 0$ are quite rigid and undergo a period doubling route to chaos changing the feedback phase, square waves with asymmetric duty cycle are able to maintain their period by adapting their shape in response to changes of the offset phase instead of undergoing a period doubling. Furthermore, they are also more robust to mismatches in the delay times with respect to the ideal ratio.

Finally, we have found that a detailed analysis of the period of the solution using Poincaré sections shows that in- and out-of-phase square waves for positive feedback can undergo a splitting in the duration of the period. In this case, the splitting takes place only for the harmonics, while the period of the fundamental solution remains single-valued as delay-time mismatch is increased. Also, at a difference with the negative feedback case, the harmonics do not undergo a secondary splitting.

Chapter 7

# Non-identical delay-coupled OEOs

## 7.1 Introduction

We have seen in the last chapters that two identical delay-line OEOs mutually coupled through delayed cross-feedback as described in Sec. 4.2 can generate multi-stable nanosecond periodic square-wave solutions that arise through Hopf instabilities. In this chapter, we consider the same system but in the general case of non-identical offset phases and coupling strength coefficients. We show that, for suitable ratios between self and cross delay times, the two non-identical OEOs can generate square waves with different amplitude but synchronized in phase, out of phase or with a dephasing of a quarter of the period ($T/4$).

Synchronization at a quarter of the period has been observed in some animal gaits of quadrupeds as walk and jump [167], in the limb coordination in crustacean swimming [168], between the oscillations of pedestrian walking on a bridge and the structural oscillation [169], in predator-prey cycles [9, 170], in human cortical sources [171], neural networks [172] and in solar transverse oscillations [173]. An example of synchronization at a quarter of the period is shown in Fig. 7.1 for a predator-prey system with a single prey type[1]. Nevertheless, in none of the aforementioned studies the oscillations have a square-wave shape.

By exploring the dynamical regimes that can arise in a prototypical model for mutually delay-coupled OEOs, in this chapter we show that stable square-wave pulses synchronized at a quarter of the period do exist in a broad parameter region. We also show that the synchronization is robust to small mismatches in the delay times. The key point to obtain $T/4$ solutions is that the two OEOs operate with different offset phases, in such a way that the feedback is negative in one and positive in the other, namely the feedback is mixed. It should also be emphasized that these $T/4$ solutions are in the nanosecond time scale, orders of magnitude faster than the above systems.

[1] In predator-prey systems, T/4 synchronization arises when a single prey type is dominant, whereas synchronization is out-of-phase in the case of multiple preys [9, 170].

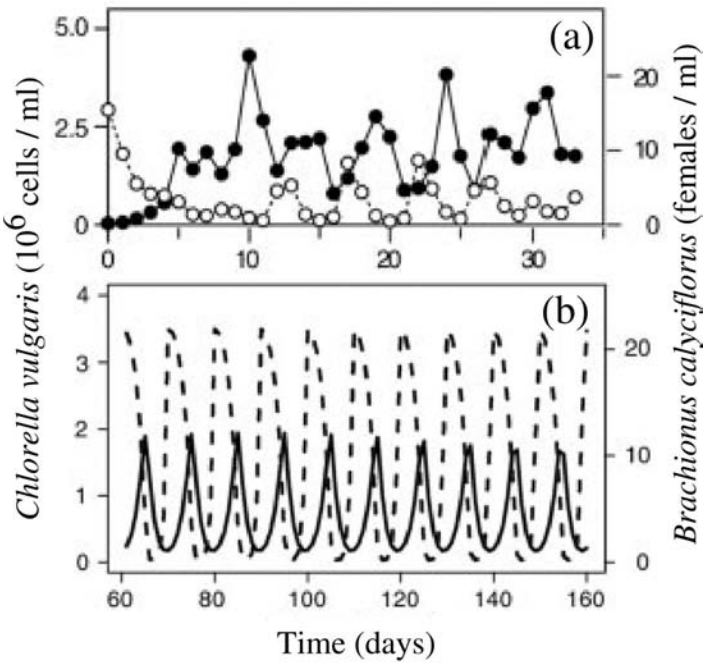


**Figure 7.1:** T/4 synchronization of population cycles in a predator-prey system with a single prey type. (a) Experimental results showing the population cycles of a rotifer alga system. Filled and open circles correspond to predator (*B. calyci orus*) and prey (*C. vulgaris*), respectively. (b) Cycles predicted by a single-prey model. Solid and dashed lines correspond to predator (*B. calyci orus*) and prey (*C. vulgaris*), respectively. Figure reproduced from [9].

The outline of this chapter is the following. In Sec. 7.2, we study the Hopf bifurcations of the steady state; in Sec. 7.3, we analyze the onset of in- and out-of-phase square waves with symmetric duty-cycle typically occurring when both non-identical OEOs have negative feedback; in Sec. 7.4, we analyze the periodic solutions with asymmetric duty cycle arising when both OEOs have positive feedback; in Sec. 7.5, we study the square waves synchronized at a quarter of the period; in Sec. 7.6, we study the effect of a small mismatch in the delay times on the degradation of the $T/4$ square waves; and Sec. 7.7 concludes the chapter.

## 7.2 Oscillatory instabilities of the steady state

In the limit of large delays, Eqs. (4.11) admit periodic square-wave solutions, which are born sinusoidal from Hopf bifurcations of the steady state $x_i^{\rm st} = Y_i^{\rm st} = 0$, which take place increasing $P$. We first analyze the steady state stability by considering the linearized equations for the small perturbations, $U_i(s) = x_i(s) - x_i^{\rm st}$ and $V_i(s) = Y_i(s) - Y_i^{\rm st}$,

$$\begin{aligned} \varepsilon U_i'(s) &= -U_i(s) - \delta V_i - P\left[F_i U_i(s-s_0) + K_i U_j(s-1)\right] \\ V_i'(s) &= U_i(s), \end{aligned} \tag{7.1}$$

where the effective self-feedback and coupling coefficients are given by

$$F_i = \gamma_{ii}^2 \sin 2\Phi_i + 2\gamma_{ii}\gamma_{ji}\cos\Phi_j \sin\ 2\Phi_i - \Phi_j + (-1)^i\Phi_0\ ,$$
$$K_i = \gamma_{ji}^2 \sin 2\Phi_j + 2\gamma_{ii}\gamma_{ji}\cos\Phi_i \sin\ 2\Phi_j - \Phi_i - (-1)^i\Phi_0\ . \tag{7.2}$$

Equations (7.1) admit solutions of exponential form, $U_i(s) = u_i \exp[(\lambda + i\omega)s]$, and, since $V_i$ is the integral of $U_i$, $V_i(s) = u_i \exp[(\lambda + i\omega)s]/(\lambda + i\omega)$. Replacing $U_i$ and $V_i$ in Eqs. (7.1) leads to

$$0 = 1 + \varepsilon(\lambda + i\omega) + \delta(\lambda + i\omega)\ ^{1} + PF_1 e^{\ (\lambda+i\ )s_0}\ u_1 + PK_1 e^{\ (\lambda+i\ )}u_2,$$
$$0 = 1 + \varepsilon(\lambda + i\omega) + \delta(\lambda + i\omega)\ ^{1} + PF_2 e^{\ (\lambda+i\ )s_0}\ u_2 + PK_2 e^{\ (\lambda+i\ )}u_1. \tag{7.3}$$

The condition for the existence of non-trivial solutions is that the determinant vanishes, namely

$$0 = 1 + \varepsilon(\lambda + i\omega) + \delta(\lambda + i\omega)\ ^{1} + PF_1 e^{\ (\lambda+i\ )s_0}$$
$$1 + \varepsilon(\lambda + i\omega) + \delta(\lambda + i\omega)\ ^{1} + PF_2 e^{\ (\lambda+i\ )s_0}\ - P^2K_1K_2 e^{\ 2(\lambda+i\ )}. \tag{7.4}$$

The steady state becomes unstable at the bifurcation point $P = P_c$, where $\lambda = 0$. Splitting Eq. (7.4) into real and imaginary parts, for $\lambda = 0$ we obtain:

$$0 = 1 + P_{\rm c}(F_1 + F_2)\ \cos(\omega s_0) + \ \varepsilon\omega - \delta\omega\ ^{1}\ \sin(\omega s_0)$$
$$+ P_{\rm c}^2\left[F_1F_2\cos(2\omega s_0) - K_1K_2\cos(2\omega)\right] - \ \varepsilon\omega - \delta\omega\ ^{1\ \ 2}, \tag{7.5}$$
$$0 = P_{\rm c}(F_1 + F_2)\quad \varepsilon\omega - \delta\omega\ ^{1}\ \cos(\omega s_0) - \sin(\omega s_0)$$
$$- P_{\rm c}^2\left[F_1F_2\sin(2\omega s_0) - K_1K_2\sin(2\omega)\right] + 2(\varepsilon\omega - \delta\omega\ ^{1}). \tag{7.6}$$

The solutions of Eq. (7.5) are the zeros of a second-order polynomial for $P_{\rm c}$ with coefficients depending on the system parameters and the perturbation frequency $\omega$. We first consider the case $\varepsilon = \delta = 0$. The value of the polynomial is 1 for $P_{\rm c} = 0$; thus, for small $P_{\rm c}$, Eq. (7.5) has no solutions, meaning that the steady state is stable. For given $F_i$, $K_i$ and $s_0$, the first instabilities are those such that the linear coefficient of the polynomial, $(F_1 + F_2)\cos(\omega s_0)$, takes the lowest negative value, namely

$$\omega s_0 = k'\pi, \tag{7.7}$$

being $k'$ an integer, odd for $F_1 + F_2 > 0$ and even for $F_1 + F_2 < 0$. Then, Eq. (7.6) leads to $K_1K_2\sin(2\omega) = 0$, namely

$$\omega = \tilde{k}\pi/2, \tag{7.8}$$

where $\tilde{k}$ is an integer. For Eqs. (7.8) and (7.7) to be mutually compatible, it is required that

$$s_0 = \frac{2k'}{\tilde{k}}. \tag{7.9}$$

Thus, the instabilities with lower threshold take place for rational $s_0$. The period of the emerging oscillatory solutions is given by

$$T = \frac{2(1-s_0)}{2\tilde{k}-k'} = \frac{2s_0}{k'} = \frac{4}{\tilde{k}}. \tag{7.10}$$

The Hopf instability threshold, $P_c$, can be obtained substituting Eqs. (7.8) and (7.7) in Eq. (7.5):

$$1 + P_c(F_1+F_2)(-1)^{k'} + P_c^2(F_1F_2 - K_1K_2(-1)^k) = 0. \tag{7.11}$$

If $F_1F_2 = K_1K_2(-1)^k$, then

$$P_c = -\frac{(-1)^{k'}}{F_1+F_2}, \tag{7.12}$$

else the smaller positive solution for $P_c$ is

$$P_c = \frac{-(F_1+F_2)(-1)^{k'} - \sqrt{(F_1-F_2)^2 + 4K_1K_2(-1)^k}}{2[F_1F_2 - K_1K_2(-1)^k]}. \tag{7.13}$$

In order for Eq. (7.13) to be real, it is required that $(F_1-F_2)^2+4K_1K_2(-1)^k > 0$. Since $P_c$ depends only on the parity of $k'$ and $\tilde{k}$, many bifurcations have the same threshold.

Introducing Eqs. (7.8) and (7.7) in Eq. (7.5) leads to a ratio for the perturbation amplitudes:

$$u_2 = Qu_1, \quad Q = -(i)^k \frac{1 + P_cF_1(-1)^{k'}}{P_cK_1}. \tag{7.14}$$

For even $\tilde{k}$, $Q$ is real and there are two kinds of solutions depending on the sign of $Q$. For $Q > 0$, $u_1$ and $u_2$ have the same sign and the instability leads to oscillatory solutions in which $x_1$ and $x_2$ are in phase (although the amplitude may not be the same), while for $Q < 0$ the instability leads to out-of-phase oscillations. For odd $\tilde{k}$, $Q$ is a purely imaginary number. Considering $x_i = U_i + c.c.$ leads to $x_1$ and $x_2$ being dephased by $T/4$.

In Fig. 7.2, we plot $P_c$ obtained from Eqs. (7.12) and (7.13) for $\gamma_{ij} = \gamma = 0.5$ and different parities of $\tilde{k}$ and $k'$. Provided that $\gamma_{ij}$ are identical, the same results are obtained for other values of $\gamma$ rescaling $P_c$ with $\gamma^2$. Pink regions correspond to offset phases for which $P_c > 5$, while white and grey regions correspond to unphysical solutions for $P_c$ (negative or complex values, respectively). For $\Phi_1 \quad \Phi_2$, along the diagonal, only instabilities associated to even $\tilde{k}$ can take place [panels (a) and (b)]. Thus, as pump is increased, the steady state becomes unstable to either in-phase or out-of-phase oscillations. On the contrary, for $\Phi_1 = -\Phi_2$, along the anti-diagonal, the only possible instabilities are those with odd $\tilde{k}$ [panels (c) and (d)] leading to periodic oscillations dephased by $T/4$. In fact, there is a broad parameter region where the lower threshold corresponds to $\tilde{k}$-odd instabilities leading to $T/4$ dephased oscillations.

As illustrated in Fig. 7.3 for non-identical $\gamma_{ij}$, the regions in the $(\Phi_1, \Phi_2)$ parameter space get distorted. Nevertheless, there are regions where $\tilde{k}$-even instabilities dominate, such as $\Phi_1 \quad \Phi_2$, leading to in-phase and out-of-phase solutions, and regions where $\tilde{k}$-odd instabilities leading to $T/4$ dephased solutions are the first to take place increasing the

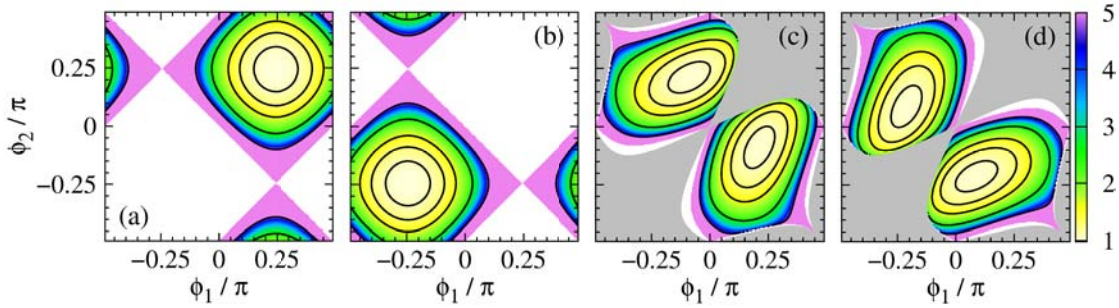


**Figure 7.2:** $P_c$ as given by Eqs. (7.12)-(7.13) for $\gamma_{ij} = 0.5$ and $\Phi_0 = 0$. (a) odd $k'$ and even $\tilde{k}$, (b) even $k'$ and even $\tilde{k}$, (c) odd $k'$ and odd $\tilde{k}$, (d) even $k'$ and odd $\tilde{k}$. Parameter regions in which $P_c$ is negative or imaginary are plotted in white and grey, respectively.

pump. In general, physical solutions for $P_c$ with odd $k'$ and even $\tilde{k}$ [panel (a) in Figs. 7.2 and 7.3] exist for offset phases such that $F_1 + F_2 > 0$ (negative feedback), solutions with even $k'$ and odd $\tilde{k}$ [panel (b)] exist for offset phases such that $F_1 + F_2 < 0$ (positive feedback), and solutions with odd $\tilde{k}$ [panels (c) and (d)] exist for offset phases such that $K_1 K_2 < 0$ (mixed feedback).

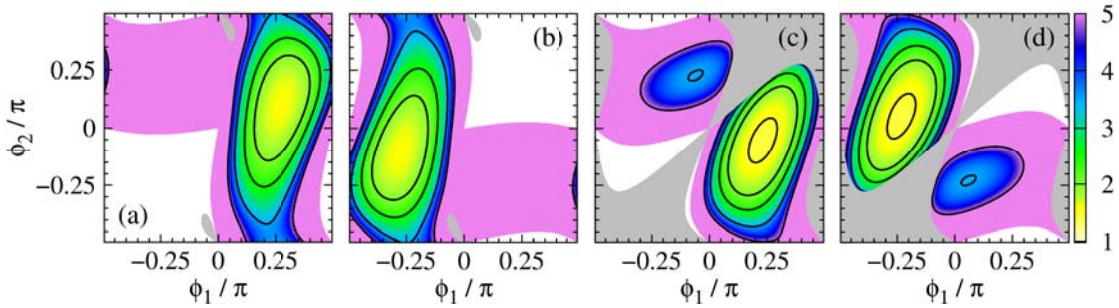


**Figure 7.3:** Value of $P_c$ as in Fig. 7.2 for $\gamma_{11} = 0.5$, $\gamma_{22} = 0.3$, $\gamma_{12} = 0.2$ and $\gamma_{21} = 0.4$.

In Fig. 7.4, we plot in $(\Phi_1, \Phi_2)$ parameter space the dominant parities of $\tilde{k}$ and $k'$, for which the instabilities with lower pump threshold $P_c$ take place. The different colors correspond to: odd $k'$ and even $\tilde{k}$ (white), even $k'$ and even $\tilde{k}$ (green), odd $k'$ and odd $\tilde{k}$ (blue), and even $k'$ and odd $\tilde{k}$ (orange). In panels (a) and (b), the parameter values are the same than in Figs. 7.2 and 7.3, respectively.

We note that for $\Phi_0 = 0$, changing the sign of $\Phi_1$ and $\Phi_2$ changes the sign of $F_i$ and $K_i$ so that Eqs. (7.12) and (7.13) are the same replacing $k'$ by $k' + 1$. As a consequence, the instabilities associated to odd $k'$ occur for offset phases that are the specular image of those for even $k'$ [compare panel (a) with (b) and (c) with (d) in Figs. 7.2 and 7.3]. This symmetry is broken for $\Phi_0 \neq 0$.

In the general case of $\varepsilon \neq 0$, $\delta \neq 0$ and arbitrary $s_0$, we can determine $P_c$ and $\omega$ by solving numerically Eqs. (7.5) and (7.6). From Eq. (7.3), we can also obtain a theoretical

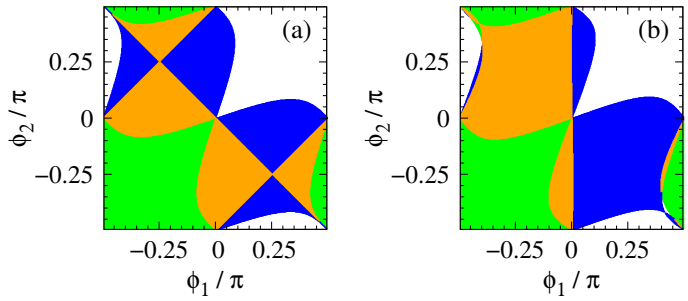


**Figure 7.4:** Dominant parities of $k'$ and $\tilde{k}$. White corresponds to odd $k'$ and even $\tilde{k}$, green to even $k'$ and even $\tilde{k}$, blue to odd $k'$ and odd $\tilde{k}$ and orange to even $k'$ and odd $\tilde{k}$. In panels (a) and (b), the parameters are the same than in Figs. 7.2 and 7.3, respectively.

prediction for $Q = u_2/u_1$, which is a complex number; its modulus,

$$Q = \frac{1 + \varepsilon\omega - \delta\omega^{-1}{}^2 + P_c^2 F_1^2 + 2P_c F_1[\cos(\omega s_0) - \varepsilon\omega - \delta\omega^{-1} \sin(\omega s_0)]^{1/2}}{P_c K_1}, \quad (7.15)$$

gives the ratio between the oscillation amplitudes, and its phase gives the phase difference between $x_1$ and $x_2$,

$$\varphi_2 - \varphi_1 = \arctan \frac{\sin(\omega) + \varepsilon\omega - \delta\omega^{-1} \cos(\omega) + P_c F_1 \sin[\omega(1 - s_0)]}{\cos(\omega) - (\varepsilon\omega - \delta\omega^{-1}) \sin(\omega) + P_c F_1 \cos[\omega(1 - s_0)]}. \quad (7.16)$$

In the next sections we analyze the in- and out-of-phase solutions arising for negative and positive feedback, and the $T/4$ dephased solutions taking place for mixed feedback.

## 7.3 Onset of periodic square waves for negative feedback

As discussed in Chapter 5, for identical $\gamma_{ij}$, $\Phi_0 = 0$ and $\Phi_1 = \Phi_2 = \Phi \quad [0, \pi/2]$, increasing the pump, the steady state becomes unstable to in-phase or out-of-phase periodic oscillations. The instability is supercritical and, as the pump is further increased, the oscillations soon become square-shape with a duty cycle half of the period. Due to parameter symmetry, the oscillations in $x_1$ and $x_2$ have the same amplitude. Here we show that square waves with symmetric duty cycle can also be found for non-identical $\gamma_{ij}$ or offset phases (although $x_1$ and $x_2$ have different amplitudes) in a broad parameter region associated to negative feedback in both OEOs. More precisely, they arise for parameter values such that the steady state instabilities associated to odd $k'$ and even $\tilde{k}$ dominate [compare panel (a) in Figs. 7.2 or 7.3 with the other panels or, alternatively, look at the white region of Fig. 7.4].

### 7.3.1 Hopf bifurcations

To illustrate this, we consider $\Phi_1 = 0.2\pi$, $\Phi_2 = 0.3\pi$ and $\gamma_{ij} = 0.5$. Fig. 7.5 shows all the Hopf bifurcations in the range $\omega < 10\pi$ and $0 < P_c < 2$ obtained solving numerically Eqs. (7.5) and (7.6). For these parameter values, Eq. (7.13) has physical solutions only for odd $k'$ and even $\tilde{k}$ (see Fig. 7.2). Thus, the bifurcations with lower threshold occur at $s_0 = 2k'/\tilde{k} = k'/n$ (integer $n = \tilde{k}/2$), namely at irreducible rational fractions $s_0 = q'/\tilde{q}$ with odd numerator. At these values of $s_0$, multiple bifurcation lines with $k' = jq'$ and $\tilde{k} = 2j\tilde{q}$ (odd $j$) are born simultaneously [Fig. 7.5(a)]. $j = 1$ corresponds to the fundamental solution with $\omega = \tilde{q}\pi$, while $j = 3, 5, ...$ correspond to harmonics with $\omega = j\tilde{q}\pi$. Moving away from $s_0 = q'/\tilde{q}$, the degeneracy is broken and $P_c$ has a parabolic dependence with $s_0 - q'/\tilde{q}$, the parabola being narrower for higher harmonics.

For odd $\tilde{q}$, $\tilde{k} = 2j\tilde{q}$ is even but not multiple of 4 (singly even) and $Q > 0$, so that all the harmonics are in phase (plotted in red in Fig. 7.5). In the notation of Chapter 5, $\tilde{q}$ corresponds to $2m_0 + 1$ and the index $j$ to $2j + 1$, so that the fundamental solution $j = 1$ corresponds to $j = 0$.

Conversely, for even $\tilde{q}$, $\tilde{k} = 2j\tilde{q}$ is multiple of 4 (doubly even) and $Q < 0$, which leads to out-of-phase oscillations (black lines in Fig. 7.5). In the notation of Chapter 5, $\tilde{q}$ corresponds to $2m_0$ and the index $j$ to $2j + 1$, so that the fundamental solution $j = 1$ corresponds to $j = 0$.

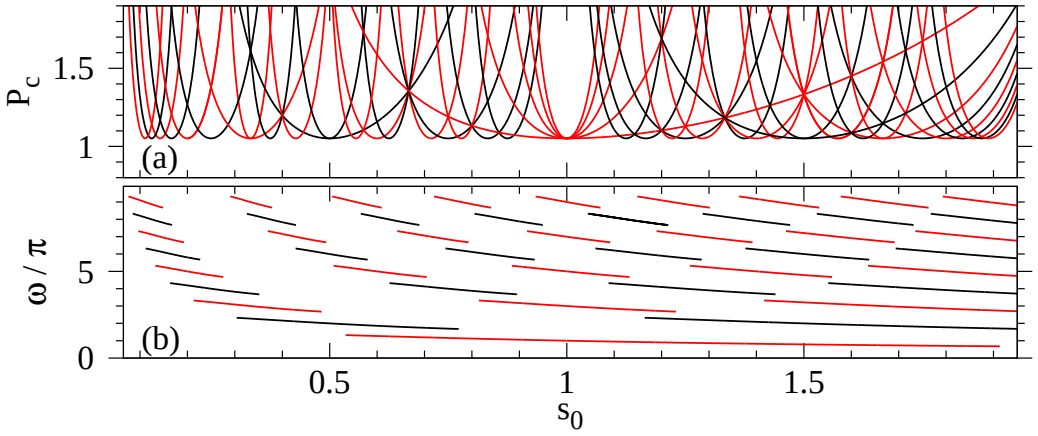


**Figure 7.5:** Hopf bifurcations with $\omega < 10\pi$ for $\Phi_1 = 0.2\pi$, $\Phi_2 = 0.3\pi$, $\Phi_0 = 0$, $\gamma_{ij} = 0.5$, $\varepsilon = 4.17 \quad 10^{-4}$ and $\delta = 1.2 \quad 10^{-2}$. In (b), lines are plotted only in the range where $P_c < 2$. Red and black lines correspond to in- and out-of-phase oscillations, respectively.

### 7.3.2 Numerical results

The previous results have been obtained from the linear stability analysis of the steady state. To analyze to which extent this results are valid far away from the bifurcation point, we numerically integrate the full nonlinear dynamical equations (4.11). Figure 7.6 shows the fundamental out-of-phase solution for $\Phi_1 = 0.2\pi$, $\Phi_2 = 0.25\pi$ and $s_0 = 3/4$, so that $k' = 3$ and $\tilde{k} = 8$. For the parameters of the figure, the steady state becomes unsta-

ble at $P_c = 2.1167$, giving rise to out-of-phase quasi-sinusoidal oscillations [Fig. 7.6(a)] with a period $T = 1/2$ (20 ns) as predicted by Eq. (7.10). While the two OEOs are synchronized in frequency, their amplitudes differ because each oscillator receives a different feedback strength. The ratio $Q$ between the amplitudes of the oscillations in $x_1$ and $x_2$ obtained from the numerical integration of (4.11), $Q = -0.2529$, is in good agreement with the prediction of the linear stability analysis (7.15), $Q = -0.2521$, and also with the approximation (7.14), $Q = -0.2519$. Increasing the pump, the shape of the solution becomes less and less sinusoidal, approaching a square-wave [Figs. 7.6(b) and (c)]. Nevertheless, the solutions remain synchronized out of phase, and the period and the ratio $Q$ between the amplitudes remain practically constant. Similar good agreements are found for in-phase solutions arising at delay times fulfilling the ratio $s_0 = q'/\tilde{q}$ with odd $q'$ and $\tilde{q}$.

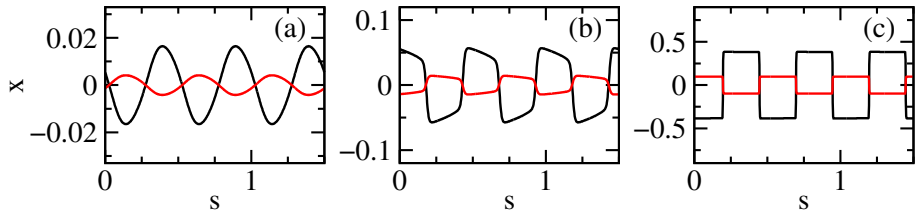


**Figure 7.6:** Out-of-phase oscillations with symmetric duty cycle for $\Phi_1 = 0.2\pi$, $\Phi_2 = 0.25\pi$, $\Phi_0 = 0$, $\gamma_{11} = 0.5$, $\gamma_{22} = 0.3$, $\gamma_{12} = 0.2$, $\gamma_{21} = 0.4$, $T_f = 30$ ns, $T_c = 40$ ns, $\varepsilon = 6.25 \quad 10^{-4}$, $\delta = 8 \quad 10^{-3}$, $P = 2.117$ (a), $P = 2.12$ (b), and $P = 2.3$ (c). Black and red lines correspond respectively to $x_1$ and $x_2$.

## 7.4 Onset of periodic oscillations for positive feedback

For $\Phi_0 = 0$ and $\Phi_1 = \Phi_2 = \Phi \quad [-\pi/2, 0]$, the square waves typically have an asymmetric duty cycle and are born subcritically, as discussed in Chapter 6. The degree of asymmetry depends on the offset phase, so that the duty cycle is symmetric (and square waves are supercritical) for $\Phi = -\pi/4$ and becomes progressively more asymmetric as the offset phase is changed away form $-\pi/4$. For delay times with an irreducible rational ratio $s_0 = q'/\tilde{q}$, for odd $q'$ the system displays in-phase square waves while for even $q'$ both in-phase and out-of-phase asymmetric square waves coexist. The system can also display periodic oscillations with a period much longer than the delay times, typically in the microsecond regime. These oscillations are always in phase, born supercritically and do not have a square-wave shape. Here we show that a similar scenario occurs for non-identical offset phases and parameter values for which instabilities associated to both even $k'$ and $\tilde{k}$ dominate [see green region in Fig. 7.4].

### 7.4.1 Hopf bifurcations

To illustrate this, we consider $\Phi_1 = -0.2\pi$, $\Phi_2 = -0.3\pi$ and $\gamma_{ij} = 0.5$. Figure 7.7 shows all the Hopf bifurcations in the range $\omega < 10\pi$ and $0 < P_c < 1.15$ obtained solving numerically Eqs. (7.5) and (7.6). For these parameter values, Eq. (7.13) has physical solutions only for odd $k'$ and even $\tilde{k}$ (See Fig. 7.2). Multiple Hopf bifurcation lines are born simultaneously at irreducible rational values $s_0 = q'/\tilde{q}$. Different Hopf lines correspond to different values of $k' = jq'$ and $\tilde{k} = 2j\tilde{q}$.

For odd $q'$, $j$ must be even, thus $\tilde{k}$ is doubly even and $Q > 0$, which leads to in-phase oscillations in a similar way as described in Chapter 6 for $s_0$ fullfilling (6.3) but not (6.4).

For even $q'$, any $j$ is allowed ($q'/\tilde{q}$ irreducibility requires odd $\tilde{q}$, which is not restrictive since $\tilde{k} = 2j\tilde{q}$ is always even). This case corresponds to the case in Chapter 6 where $s_0$ fullfills (6.4), for which (6.3) is also satisfied and thus in- and out-of-phase square waves coexist. The fundamental solution $j = 1$ and the odd harmonics have a singly even $\tilde{k}$ and $Q < 0$ and thus are out of phase, while the even harmonics are in phase. As before, the degeneracy is broken for $s_0$ different from $q'/\tilde{q}$ and the Hopf lines have a parabolic shape which is narrower for higher harmonics.

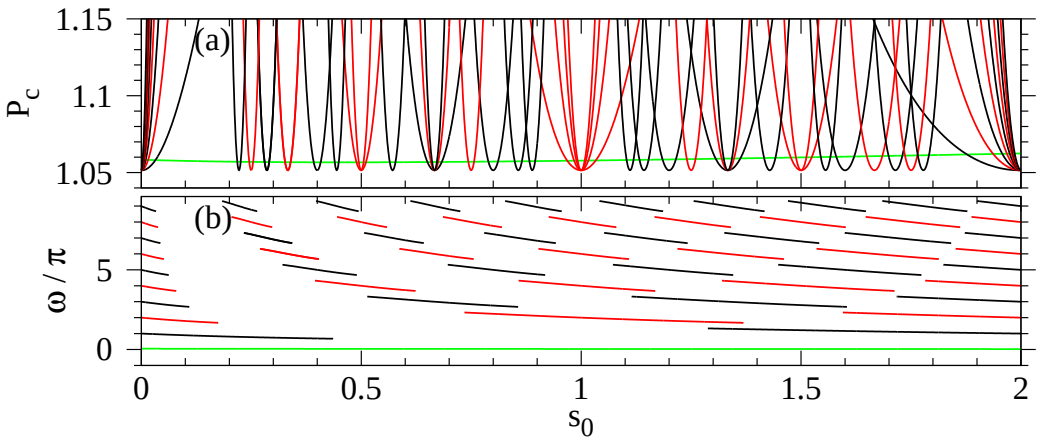


**Figure 7.7:** Hopf bifurcations for $\Phi_1 = -0.2\pi$ and $\Phi_2 = -0.3\pi$. Other parameters as in Fig. 7.5. The green line corresponds to microsecond oscillations.

### 7.4.2 Numerical results for square waves

For identical $\gamma_{ij}$ and $\Phi_0 = 0$, the square waves have a symmetric duty cycle and arise supercritically if $\Phi_1 + \Phi_2 = -\pi/2$, as the fundamental out-of-phase solution for $T_f = 40$ ns and $T_c = 60$ ns ($s_0 = 2/3$) shown in Fig. 7.8. Here $k' = 2$, $\tilde{k} = 6$ and the solution has a period $T = 2/3$ (40 ns). For other offset phases, oscillations are born subcritically and have an asymmetric duty cycle, as shown in Fig. 7.9 for the same delay times but with non-identical $\gamma_{ij}$, $\Phi_1 = -0.25\pi$, and $\Phi_2 = -0.15\pi$. For the parameter values of Fig. 7.9, $P_c = 1.6334$. As pump is increased above this threshold, the periodic solution becomes more square-wave shaped while the duty cycle asymmetry decreases [Figs. 7.9(c) and

(d)]. Below this threshold, decreasing pump, the duty cycle asymmetry increases until the length of the shorter plateau vanishes. In Fig. 7.9(a), the width of the pulse is only $0.044T$. The duty cycle asymmetry also increases moving the offset phases away from $\Phi_1 + \Phi_2 = -\pi/2$. The minimum duty cycle is set by the transition time between the square-wave plateaus, which is determined by $\tau$; thus, it is of order $\varepsilon$ in dimensionless time. Other than that, the duty cycle can be conveniently tuned over the whole period, while keeping the period constant, by changing the pump or the DC voltages applied to the MZIs, as shown in Chapter 6 for $\Phi_1 = \Phi_2$.

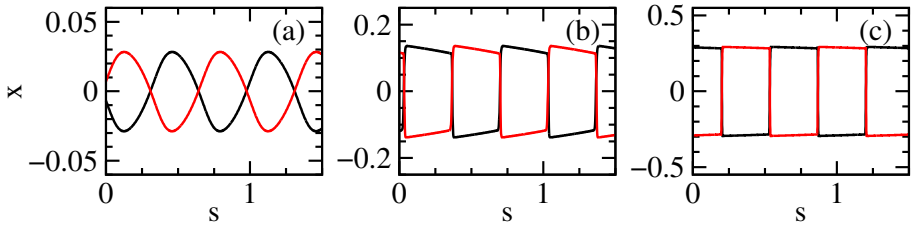


**Figure 7.8:** Fundamental out-of-phase solution for $\Phi_1 = -0.1\pi$, $\Phi_2 = -0.4\pi$, $\Phi_0 = 0$, $\gamma_{ii} = 0.5$, $T_f = 40\,\text{ns}$, $T_c = 60\,\text{ns}$, $\varepsilon = 4.17 \quad 10^{-4}$, $\delta = 1.2 \quad 10^{-2}$, $P = 1.702$ (a), $P = 1.72$ (b), and $P = 1.8$ (c). $P_c = 1.7013$.

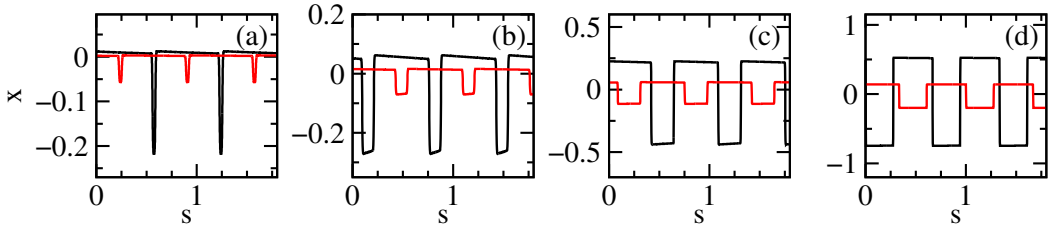


**Figure 7.9:** Fundamental out-of-phase solution for $\Phi_1 = -0.25\pi$, $\Phi_2 = -0.15\pi$, $T_f = 40\,\text{ns}$, $T_c = 60\,\text{ns}$, $\varepsilon = 4.17 \quad 10^{-4}$, $\delta = 1.2 \quad 10^{-2}$, $P = 1.616$ (a), $P = 1.6271$ (just below threshold) (b), $P = 1.7$ (c), and $P = 2$ (d). Other parameters as in Fig. 7.6.

So far in this section we have considered mostly that self- and cross-feedback strength coefficients are all identical, $\gamma_{ij} = \gamma$. We now discuss the effect of non-identical $\gamma_{ij}$. As an example, in Fig. 7.10 we show the fundamental and first harmonic in-phase square waves arising for $\gamma_{11} = \gamma_{12} = 0.5$ and the increasing values of $\gamma_{21}$ while keeping constant $\gamma_{22} + \gamma_{21} = 1$. It is clear that square waves remain stable with the same shape and period but the amplitude of $x_1$ and $x_2$ now differs. For $\gamma_{21} < 0.5$, the strength of the cross-feedback arriving at OEO 2 ($\gamma_{12}$) is larger than the one arriving at OEO 1 ($\gamma_{21}$) and, at the same time, the strength of the self-feedback in OEO 2 is larger than the self-feedback in OEO 1 ($\gamma_{22} > \gamma_{11} = 0.5$). Altogether OEO 2 has a stronger feedback than OEO 1 and, as a consequence, the amplitude of $x_2$ is larger. On the contrary, for $\gamma_{21} > 0.5$, the strength of the cross-feedback arriving at OEO 2 is smaller than the one at OEO 1 ($\gamma_{21} > \gamma_{12}$) and the self-feedback in OEO 2 is also weaker than in OEO 1, so $x_2$ has a smaller amplitude than $x_1$. Similar results can be obtained for the out-of-phase square-wave solutions, as shown in Fig. 7.11.

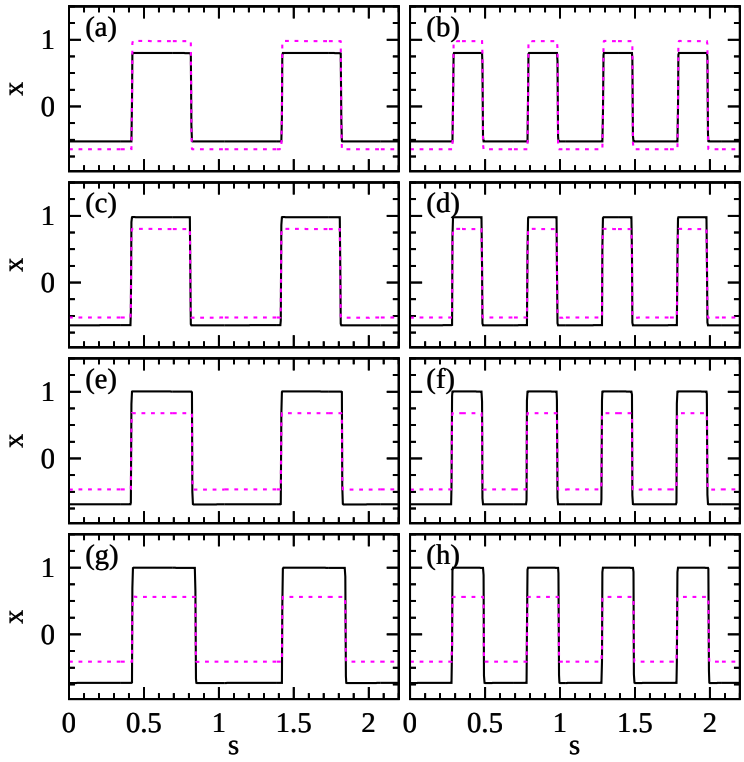


**Figure 7.10:** In-phase periodic solutions with $\Phi = -0.3\pi$, $P = 1.5$, $T_f = 60\,\text{ns}$ and $T_c = 30\,\text{ns}$, so $s_0 = 2$, $\varepsilon = 8.33 \quad 10^{-4}$, and $\delta = 0.006$, with $\gamma_{11} = \gamma_{12} = 0.5$ while increasing the coupling coefficient $\gamma_{21} = 1 - \gamma_{22}$: $\gamma_{21} = 0.45$ [(a) and (b)], $\gamma_{21} = 0.55$ [(c) and (d)], $\gamma_{21} = 0.6$ [(e) and (f)], and $\gamma_{21} = 0.65$ [(g) and (h)]. The solid black line corresponds to $x_1$ and the red dashed line to $x_2$. Panels (a), (c), (e) and (g) display the fundamental square wave (with period $T = 1$). Panels (b), (d), (f) and (h) show the first harmonic.

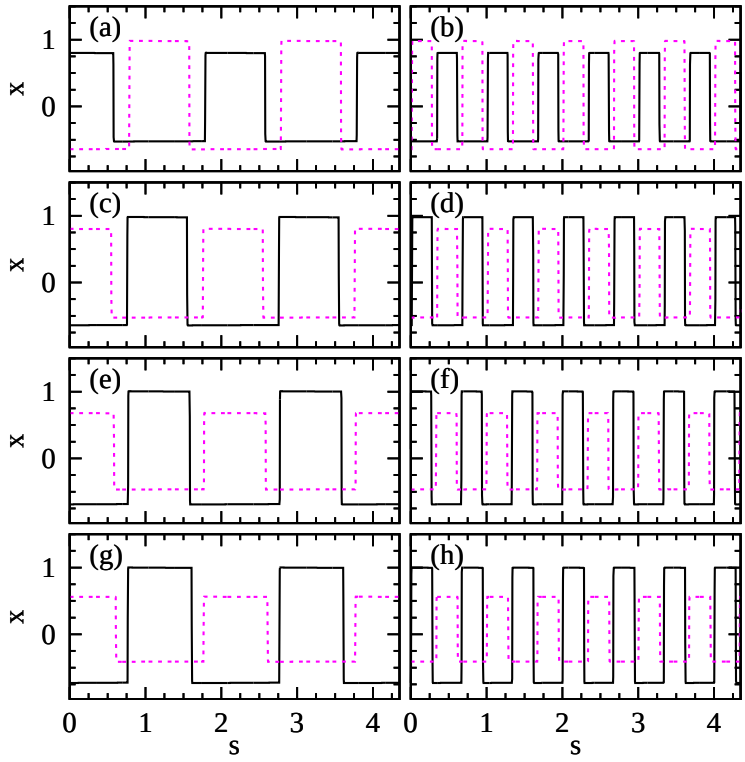


**Figure 7.11:** Out-of-phase periodic solutions for the same parameter values than in Fig. 7.10 while increasing the coupling coefficient $\gamma_{21} = 1 - \gamma_{22}$: $\gamma_{21} = 0.45$ [(a) and (b)], $\gamma_{21} = 0.55$ [(c) and (d)], $\gamma_{21} = 0.6$ [(e) and (f)], and $\gamma_{21} = 0.65$ [(g) and (h)]. Panels (a), (c), (e) and (g) display the fundamental square wave (with period $T = 2$). Panels (b), (d), (f) and (h) show the first harmonic.

### 7.4.3 Microsecond oscillations

We now focus on the microsecond oscillations associated to $j = 0$ ($k' = \tilde{k} = 0$). Neglecting $\varepsilon$ and $\delta$, according to Eq. (7.7), $\omega = 0$. For finite $\varepsilon$ and $\delta$, $\omega$ is slightly shifted from Eq. (7.7):

$$\omega_{k'} = \frac{k'\pi}{s_0} + \alpha_{k'}. \tag{7.17}$$

For $k' \neq 0$, $\alpha'_k$ is small compared to $\frac{k'\pi}{s_0}$, and thus can be neglected. For $k' = 0$, expanding Eq. (7.6) to first order in $\alpha_0$, one has

$$0 = P_c(F_1 + F_2)\left(\varepsilon\alpha_0 - \frac{\delta}{\alpha_0} - \alpha_0 s_0\right) - 2P_c^2\alpha_0\left(F_1F_2s_0 - K_1K_2\right) + 2\left(\varepsilon\alpha_0 - \frac{\delta}{\alpha_0}\right), \tag{7.18}$$

which leads to

$$\alpha_0^2 = \frac{[P_c(F_1 + F_2) + 2]\delta}{P_c(F_1 + F_2)(\varepsilon - s_0) - 2P_c^2(F_1F_2s_0 - K_1K_2) + 2\varepsilon}. \tag{7.19}$$

This result is an extension of Eq. (4.27) to the case of non-identical OEOs, and indicates that $\omega_0 = \alpha_0 \quad \delta^{1\ 2}$, which is typically in the MHz regime. As shown in Fig. 7.7, these solutions have a threshold value that is practically independent of $s_0$ (green line) and that takes place at a value slightly larger than the minimum threshold for square waves, in agreement with the results of subsection 6.3.3. Fig. 7.12 shows the shape of a microsecond solution with asymmetric duty cycle for different pump values. Increasing the pump, the asymmetry of the duty cycle increases and the solution shows a tilted plateau; however, instead of taking a full square-wave shape, it becomes chaotic. The period of these solutions increases with the pump, as clearly seen in the figure. For identical $\gamma_{ij}$ and offset phases, microsecond solutions are in phase and have exactly the same amplitude. When offset phases differ, as in Fig. 7.12, they have a small dephasing as shown in panel (d). The dephasing is so small that, at the scale of the other panels, the traces for $x_1$ and $x_2$ overlap.

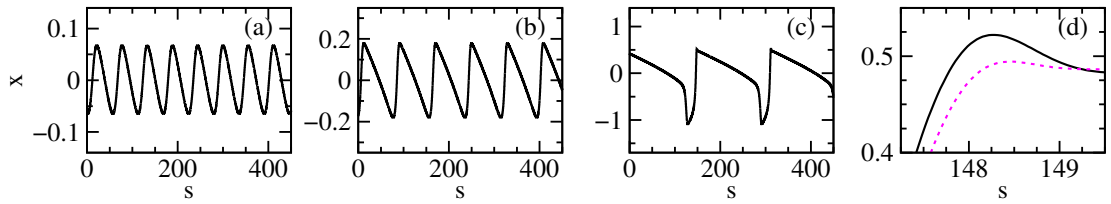


**Figure 7.12:** Microsecond solution obtained for $\Phi_1 = -0.15\pi$, $\Phi_2 = -0.1\pi$, $P = 1.444768$ (a), $P = 1.4538$ (b), and $P = 1.454$ (c). Panel (d) shows a zoom of (c) close to the maximum. Other parameters as in Fig. 7.8. The threshold is $P_c = 1.4392$ and at threshold $\omega_0 = 0.1215$. Time traces for $x_1$ and $x_2$ overlap in panels (a)-(c).

We now study the effect of mismatch in the feedback strength coefficients in the microsecond periodic solutions. As it can be seen in Fig. 7.13, if the mismatch is not too large, synchronized microsecond oscillations are stable. The mismatch in the feedback strength coefficients leads to an asymmetry on the feedback strength arriving at each OEO and, as consequence, the amplitude of $x_1$ and $x_2$ is different. If the mismatch is large, microsecond oscillations can develop fast oscillations on top of the part of the period with larger amplitude, as shown in panels (m)-(o). These fast oscillations are more prominent when the strong mismatch is in the direction of having a large self-feedback ($\gamma_{22} = 0.9$ and $\gamma_{21} = 0.1$) than when it is in the opposite way ($\gamma_{22} = 0.1$ and $\gamma_{21} = 0.9$) [compare panels (a)-(c) with (m)-(o)]. These fast oscillations are reminiscent of those encountered for a single OEO as the pump is increased leading to chaotic breathers [61, 104]. Fast oscillations appear typically only in one of the plateaus, except for the particular value of the offset phase $\Phi = -0.25\pi$, for which the microsecond solutions are symmetric.

Finally, we note that the period and the duty cycle of the microsecond pulses also change with the mismatch of the feedback strength coefficients. In particular, increasing the asymmetry of the coupling, the period increases and the duty cycle tends to be half of the period.

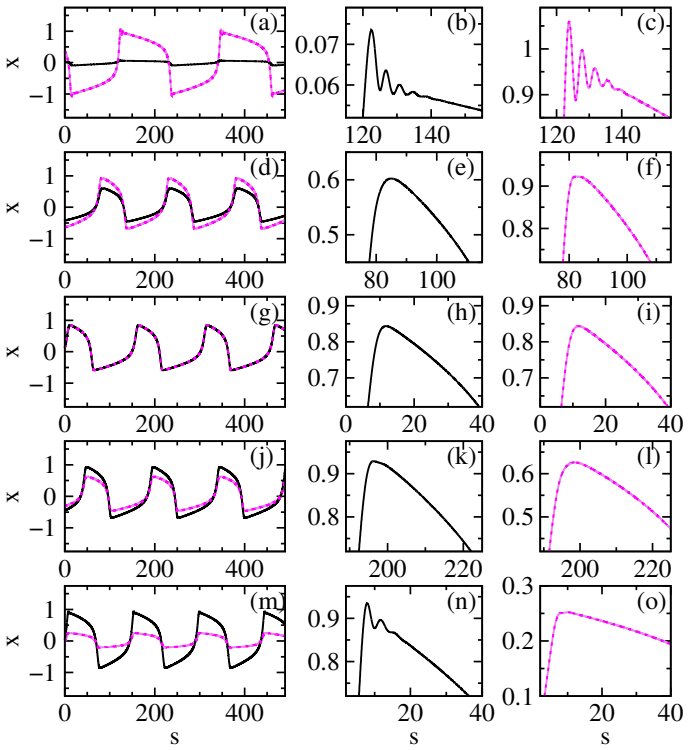


**Figure 7.13:** Microsecond oscillations with $\Phi = -0.3\pi$, $P = 1.3$, $T_f = 60\,\text{ns}$ and $T_c = 30\,\text{ns}$, so $s_0 = 2$, $\varepsilon = 8.33 \quad 10^{-4}$, and $\delta = 0.006$, with $\gamma_{11} = \gamma_{12} = 0.5$ while increasing the coupling coefficient $\gamma_{21} = 1 - \gamma_{22}$: $\gamma_{21} = 0.1$ [(a)-(c)], $\gamma_{21} = 0.4$ [(d)-(f)], $\gamma_{21} = 0.5$ [(g)-(i)], $\gamma_{21} = 0.6$ [(j)-(l)], and $\gamma_{21} = 0.9$ [(m)-(o)]. Panels (e), (f), (h), (i), (k), (l), (n) and (o) are zooms of the panels on the left.

## 7.5 Onset of T/4 dephased periodic square waves

Here we consider the parameter regions for which the instabilities of the steady state associated to odd $\tilde{k}$ dominate. As shown in Figs. 7.2 and 7.3, in the ($\Phi_1$, $\Phi_2$) parameter space, this typicality occurs in the second and fourth quadrants, where offset phases have opposite signs; more precisely, in the regions plotted as blue or orange in Fig. 7.4.

### 7.5.1 Hopf bifurcations

To illustrate the scenario, let us consider $\gamma_{ij} = 0.5$, $\Phi_1 = -0.25\pi$ and $\Phi_2 = 0.15\pi$, parameter values for which increasing the pump the first instabilities are those associated to odd $\tilde{k}$ and even $k'$ ($P_c = 1.1188$) [Fig. 7.2(d)] followed by those with odd $\tilde{k}$ and $k'$ at $P_c = 1.2526$ [Fig. 7.2(c)]. Instabilities with even $\tilde{k}$ are not relevant (either are not allowed or have a very large threshold [Figs. 7.2(a),7.2(b)]). Figure 7.14 shows the Hopf bifurcations in the range $\omega < 8\pi$ and $0 < P_c < 1.8$. In addition to $P_c$ and $\omega$ obtained solving Eqs. (7.5) and (7.6) numerically, we have plotted the phase difference $\varphi_2 - \varphi_1$ obtained from Eq. (7.16). Families of Hopf bifurcation lines are born at irreducible rational values of the delay ratio $s_0 = q'/\tilde{q}$. The members of a family can be identified by $j$, such that $2k' = jq'$ and $\tilde{k} = j\tilde{q}$. Since $\tilde{k}$ is odd, $\tilde{q}$ and $j$ must be odd; and since $2k'$ is even, $q'$ must be even. Thus, Hopf lines are born at even-odd rational values for $s_0$ and only odd harmonics are allowed. The stability analysis also predicts that instabilities

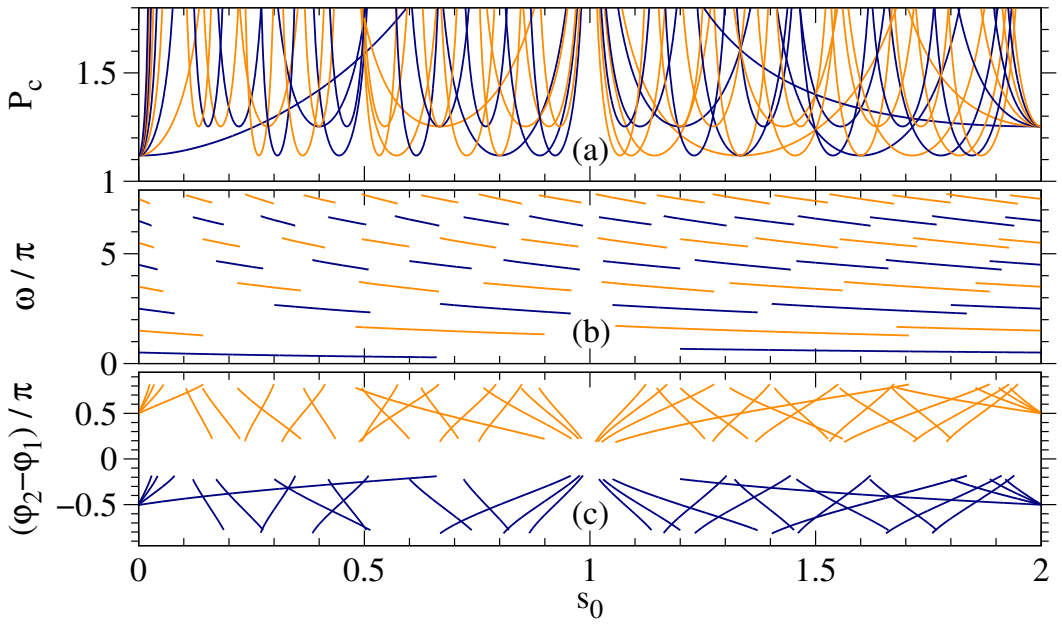


**Figure 7.14:** Hopf lines for $\Phi_1 = -0.25\pi$ and $\Phi_2 = 0.15\pi$. Other parameters as in Fig. 7.5. Yellow and blue lines correspond to bifurcations leading to synchronized solutions dephased $+T/4$ and $-T/4$, respectively.

arising at doubly even $q'$ (even $k'$) have a lower threshold than those at singly even $q'$ (odd $k'$), as shown in Fig. 7.14(a).

The amplitude ratio and dephasing between $x_1$ and $x_2$ are given by the amplitude and phase of $Q$. At the onset of the Hopf lines, from Eq. (7.14), $Q$ is purely imaginary, so there are two kinds of solutions: those where $\varphi_2 - \varphi_1 = \pi/2$, for which $x_2$ is delayed a quarter of the period with respect to $x_1$ (dephasing $T/4$), and those where $\varphi_2 - \varphi_1 = -\pi/2$, for which $x_2$ advances $x_1$ by a quarter of the period (dephasing $-T/4$). For the parameter values considered in Fig. 7.14, $Q = 0.448$ for doubly even $q'$ while $Q = 2.621$ for singly even $q'$. In both cases $[1 + P_c F_1(-1)^{k'}]/(P_c K_1) > 0$, thus the phase of $Q$ is $\pi/2$ for $\tilde{k} \pmod 4 = 3$ and $-\pi/2$ for $\tilde{k} \pmod 4 = 1$. As a consequence, fundamental solutions born at $s_0$ with $\tilde{q} = 3, 7, 11, ...$ are dephased $T/4$, while those born at $s_0$ with $\tilde{q} = 1, 5, 9, ...$ are dephased $-T/4$, and successive harmonics born at a given $s_0$ have alternatively positive and negative detunings as shown in Fig. 7.14. According to Eq. (7.16), changing $s_0$ with respect to the rational $q'/\tilde{q}$ leads to a change in the dephasing, as shown in Fig. 7.14.

### 7.5.2 Numerical results

$T/4$ square waves have a symmetric duty cycle and multiple stable harmonics can coexist, as illustrated in Fig. 7.15 for $s_0 = 4/3$ (doubly even $q'$ with lower threshold) and for $s_0 = 2/3$ (singly even $q'$ with larger $P_c$). In agreement with the stability analysis, for $s_0 = 4/3$, the amplitude of $x_2$ is smaller than that of $x_1$, while the opposite occurs for $s_0 = 2/3$. Also, while $P$ is the same, owing to the lower threshold, the overall amplitude of the square waves for $s_0 = 4/3$ is larger. Nevertheless, in both cases the fundamental solution corresponds to $\tilde{k} = 3$ and, according to Eq. (7.10), has a period $T = 4/3$ (80 ns since $T_c = 60\,\text{ns}$). First and second harmonics correspond, respectively, to $j = 3$ ($\tilde{k} = 9$) and $j = 5$ ($\tilde{k} = 15$), with period $T = 4/9$ (26.6 ns) and $4/15$ (16 ns). For the fundamental and second harmonic, $x_2$ is delayed $T/4$ with respect to $x_1$, while for the first, $x_1$ is delayed $T/4$ with respect to $x_2$ (dephasing $-T/4$).

Higher-order harmonics are also found provided the duration of the plateau is longer than the transition time, which, as discussed before, depends on $\tau$. Figures 7.15(d) and (h) show the $30^{\text{th}}$ harmonic, $j = 61$ ($\tilde{k} = 183$), with a period $T = 4/183$ (1.31 ns). For $\tau = 25\,\text{ps}$ as used in Fig. 7.15, harmonics above the $40^{\text{th}}$ are unstable. However, for smaller $\tau$, one can generate $T/4$ synchronized square waves with a subnanosecond period, as shown in Fig. 7.16.

$T/4$ oscillatory solutions are born supercritically with a sinusoidal shape, as shown in Fig. 7.17(a) for the fundamental solution born at $s_0 = 4/3$. Increasing the pump, the solution soon becomes square-wave shaped as it can be seen in Figs. 7.17(b) and 7.17(c).

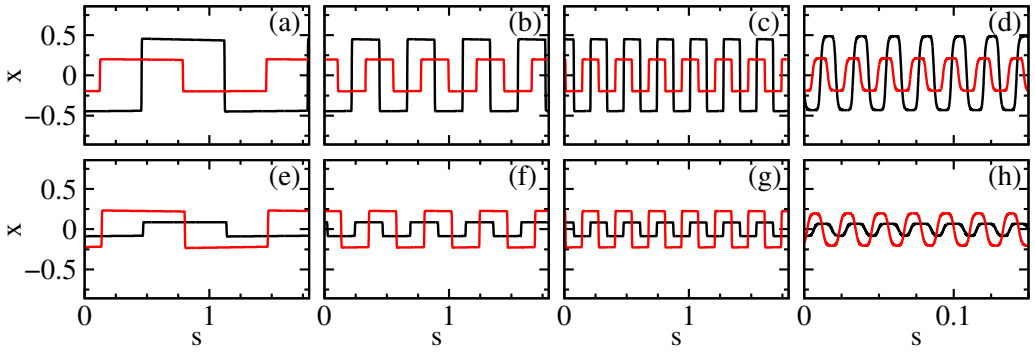


**Figure 7.15:** Coexistence of $T/4$ square waves for the parameter values of Fig. 7.14, $P = 1.3$, and $T_c = 60\,\text{ns}$. Fundamental, $1^{\text{st}}$, $2^{\text{nd}}$ and $30^{\text{th}}$ harmonics for $T_f = 80\,\text{ns}$ ($s_0 = 4/3$) are shown in (a)-(d) while (e)-(f) show the corresponding ones for $T_f = 40\,\text{ns}$ ($s_0 = 2/3$). Black and red lines correspond to $x_1$ and $x_2$ respectively.

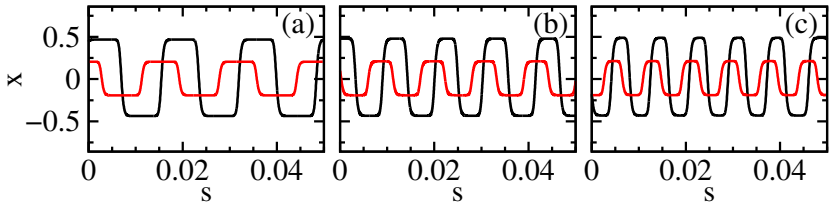


**Figure 7.16:** Higher harmonics for the parameter values of Fig. 7.15 but $\tau = 10\,\text{ps}$ and $s_0 = 4/3$: (a) $40^{\text{th}}$, $T = 4/243$ (0.99 ns), (b) $60^{\text{th}}$, $T = 4/363$ (0.66 ns) and (c) $80^{\text{th}}$, $T = 4/483$ (0.50 ns).

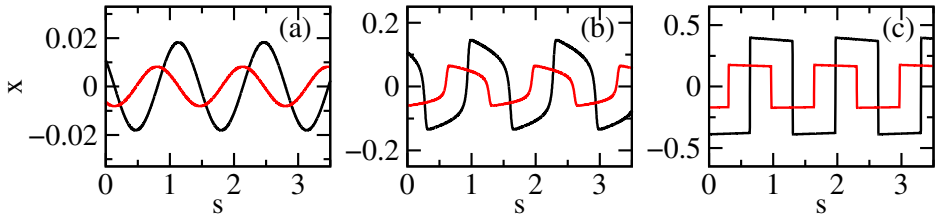


**Figure 7.17:** Square waves dephased $T/4$ for $T_c = 60\,\text{ns}$, $T_f = 80\,\text{ns}$, $P = 1.119$ (a), $P = 1.13$ (b), and $P = 1.25$ (c). Other parameters as in Fig. 7.15.

## 7.6 Robustness of $T/4$ dephased square waves to delay time mismatch

We have shown that the Hopf lines leading to different kinds of synchronized square waves originate at suitable rational values for the ratio between the delay times. Thus, from a practical point of view, it is important to assess the robustness of the synchronized square waves to small mismatches in the delay times with respect to the ideal ratio. For in- and out-of-phase square waves arising for identical offset phases, in Chapters 5 and 6 we have shown that, while synchronization is robust to mismatches up to a 5%, solutions with asymmetric duty cycle born for positive feedback are more robust than those with symmetric duty cycle arising for negative feedback, and that the larger the period of the solution the higher the robustness of the synchronization. In this section, we focus on the effect of a small mismatch in the delay times on the period, the shape and the synchronization of the $T/4$ dephased square waves.

As an example, we consider the fundamental and the first harmonic square waves originated from the Hopf lines that in Fig. 7.14 exhibit a minimum at $s_0 = 4/3$ (plotted in yellow and blue, respectively). The left panels in Figs. 7.18 and 7.19 show the time traces obtained integrating numerically Eqs. (4.11) for $P = 1.25$, keeping fixed $T_c$ and changing $T_f$. Figure 7.18 has been obtained using the fundamental square wave ($T = 4/3$) as initial condition, while the first harmonic ($T = 4/9$) has been used for Fig. 7.19. With a 1% mismatch [Figs. 7.18(b) and 7.19(c)], the solutions exhibit longer transition times between the two plateaus while the plateau lengths are reduced. Furthermore, the slope of the positive jump (transition from the negative to the positive plateau) is different than the slope of the negative jump (transition from the positive to the negative plateau). For a positive mismatch with respect to the ideal ratio, as in Fig. 7.18, the duration of the positive jump is larger than that of the negative jump, whereas for a negative mismatch is the other way around. Increasing the mismatch, the duration of the jumps becomes larger, the plateaus shorten and the difference between the positive and negative jumps becomes more apparent. Through this mechanism, $T/4$ have a large degree of flexibility, making them more robust to delay-time mismatches than in- and out-of-phase square waves with symmetric duty cycle arising for negative feedback, where already for a 2% mismatch the transition jumps develop intermediate plateaus [111]. Note that, since self- and cross-coupling delays correspond to fiber lengths of several meters, mismatches below 1% are easily achievable in practice.

Figures 7.18(e) and 7.18(f) show the frequency of $x_1$ and the phase difference between $x_2$ and $x_1$ as a function of $s_0$ for the fundamental square wave. The solid line corresponds to the prediction of Eq. (7.16), whereas red dots have been obtained integrating Eqs. (4.11) numerically and applying the Poincaré section technique. The synchronized fundamental square wave has a practically constant frequency up to a 5% mismatch, value at which it becomes unstable and the system jumps to a square wave of higher frequency. Within this range, the phase difference changes in a practically linear way, as predicted theoretically. Higher harmonics are more sensible to mismatches in the delay times. For instance, as shown in Figs. 7.19(e) and 7.19(f), the first harmonic becomes unstable with a 2%

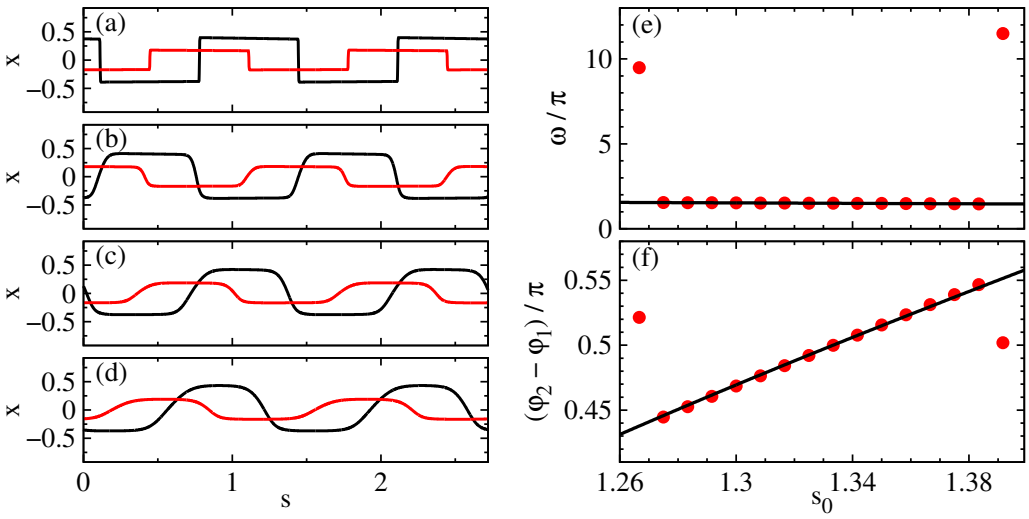


**Figure 7.18:** (a)-(d): Robustness of the $T/4$ dephased fundamental solution changing $T_f$: 80 ns ($s_0 = 4/3$) (a), 81 ns ($s_0 = 1.350$) (b), 82 ns ($s_0 = 1.367$) (c), and 83 ns ($s_0 = 1.383$) (d). $P = 1.25$, other parameters as in Fig. 7.15. We also show the frequency of $x_1$ (e) and the phase difference between $x_2$ and $x_1$ (f) as a function of $s_0$. Red dots correspond to numerical simulations of (4.11) and solid black lines to the theoretical prediction from (7.5) and (7.6).

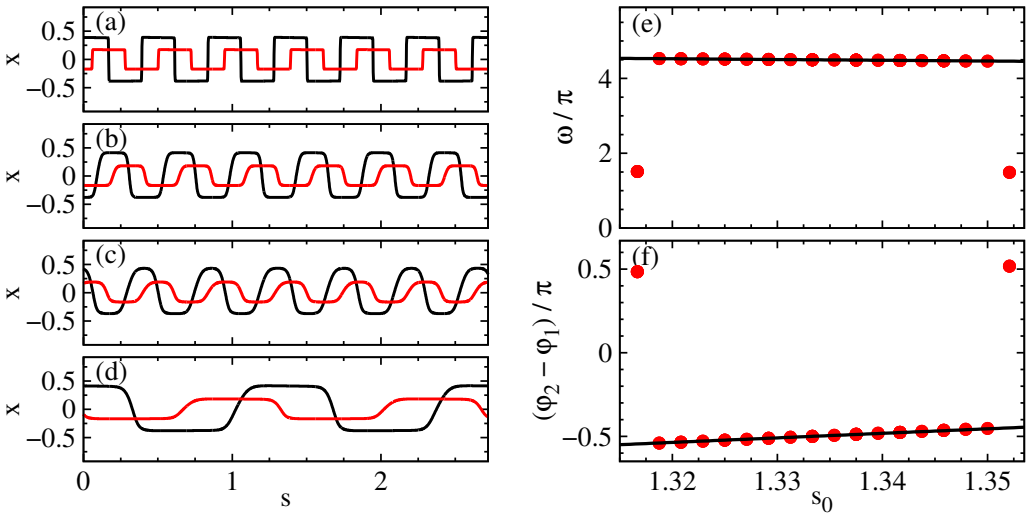


**Figure 7.19:** As Fig. 7.18 for the first harmonic with $T_f = 80$ ns ($s_0 = 4/3$) (a), $T_f = 80.5$ ns ($s_0 = 1.342$) (b), $T_f = 81$ ns ($s_0 = 1.350$) (c) and $T_f = 81.5$ ns ($s_0 = 1.358$) (d).

mismatch. This is in agreement with the linear stability analysis, as it can be seen from Fig. 7.14, where the Hopf bifurcation curves for the solutions of higher frequency are sharper. From Fig. 7.14, we can also argue the reason why the shape of the square waves smoothens: increasing the mismatch while keeping fixed the pump $P$ leads to an increase in $P_c$ along the Hopf branch, leading to a reduction of the distance $P - P_c$ to the Hopf bifurcation where the solution is sinusoidal. For larger values of $P$, the solutions are less robust to delay-time mismatches and even become chaotic.

## 7.7 Final discussion and remarks

We have explored the synchronized square-wave solutions generated by two delay-coupled non-identical OEOs as function of the offset phases and the ratio $s_0$ between self- and cross-feedback delay times. Despite the OEOs being different, synchronized square waves originate from Hopf instabilities of the steady state and multiple harmonics coexist.

For both OEOs with negative feedback, square waves have a symmetric duty cycle and arise supercritically, being synchronized in phase for $s_0$ being an odd/odd rational and out of phase for odd/even rational $s_0$.

For both OEOs with positive feedback, square waves have an asymmetric duty cycle and are born subcritically. In this case, for rational $s_0$ with an odd numerator, square waves are in phase, while if the numerator is even both in- and out-of-phase square waves coexist. Increasing the pump, subcritical asymmetric square waves are also found beyond the parameter regions where they are born, including regions of negative feedback, as described in Chapter 6 for identical OEOs.

We have also shown that, for mixed feedback, the OEOs show an interesting dynamical regime in which synchronized square waves dephased by a quarter of the period are stable. Furthermore, we have shown that this type of synchronization, which does not arise for identical OEOs, exists for a broad range of parameter values and is robust to small mismatches in the delay times.

Altogether this system displays a very large degree of flexibility, allowing for instance to select the period of the square waves without changing parameters by choosing a suitable initial condition, to tune the duty cycle while keeping the period constant just changing the offset phase or the pump level, and to tune the dephasing between the synchronized square waves by changing the offset phases or the delay times.

# Part III

# Photonic systems with state-dependent delays

Chapter 8

# State-dependent delay photonics

## 8.1 Introduction

As discussed in Chapter 1, time delays in coupling and feedback naturally appear in many dynamical systems in which the propagation time of a signal can induce important changes on the dynamical properties of the system, generally giving rise to complex behaviour [11]. In certain systems, these delay times are not constant but depend on the state of the system. An example of such a system was already introduced in Chapter 1 when considering the shower temperature control, in which the dependence of the water viscosity with temperature gives rise to a temperature-dependent delay as discussed in the subsection 1.3.1. Other examples of systems exhibiting state-dependent delay (SDD) dynamics are internet traffic [174], space communication [175], control theory [176], economics [177], turning processes [178], deep drilling [179], predator-prey systems [180], blood-flow [181], and neural systems [182].

Despite their relevance and attractive properties, the understanding of SDD systems remains poor. From a theoretical point of view, modeling those systems has found substantial interest in mathematics and control theory [175, 183, 184]. However, problems with SDD are challenging to tackle, both analytically and numerically. From the experimental side, very few implementations and studies have been realized. Recently, SDD dynamics was demonstrated with periodic square-wave oscillators programmed within field-programmable gate arrays [185]. Such Boolean oscillators have a feedback delay which switches between two different values depending on an external control voltage ($V_c$) that oscillates in time with a square-wave profile; when $V_c$ crosses a given threshold, the feedback delay switches to a different value inducing a switch in frequency in the Boolean oscillator. By coupling two Boolean oscillators with low coupling strength, it was shown that the frequency adjustment in the switching is associated with a proportional variation of the effective coupling strength, which could be useful for applications requiring controllable coupling strength [185].

In this chapter, we present a photonic implementation of a dynamical system with a feedback delay time $\tau$ which switches between two different values depending on the state of the system. More specifically, we present a state-dependent switch resulting

from the combination of a semiconductor laser and filtered feedback from two different cavities of different length and center frequency. We consider delay time values much larger than the characteristic dynamical time scale of the laser. Although this configuration represents one of the simplest SDD systems that can be realized, in which the delay time can only take two different discrete values, their dynamical properties have not been studied in detail yet, in particular in the chaotic domain. Based on experiment and modeling on semiconductor lasers with frequency-selective feedback loops, we demonstrate instabilities resulting in erratic jumps between states defined by the individual loops. Our approach opens new perspectives for the study of SDD systems and enables the development of applications that would benefit from erratic switching.

### 8.1.1 Outline

This chapter is organized as follows. In Sec. 8.2, we introduce a scheme of our system and two quantifiers of SDD dynamics. Sec. 8.3 contains the experimental setup and some experimental results demonstrating SDD dynamics in an irregular switching regime. Secs. 8.4-8.8 are devoted to the theoretical analysis of the system: in Sec. 8.4 we introduce a theoretical model of a semiconductor laser with lorentzian filtering from different filters; after that, in Sec. 8.5 we compute the relative equilibria of the system, and in Sec. 8.6 we show numerical results obtained by mimicking the experimental conditions; then, in Sec. 8.7 we analyse the effect of changing key parameters in the dynamics of the system; and finally, in Sec. 8.8 we show numerical results demonstrating SDD dynamics in a more regular switching regime. In Sec. 8.9, the switching between the two different values of the delay time is characterized by computing the sequential and probability distributions of the time intervals during which the delay time takes a given value. Finally, in Sec. 8.10 we summarize our results and discuss possible applications and future investigations.

## 8.2 SDD scheme and quanti ers

### 8.2.1 Scheme of the SDD feedback con guration

A simplified scheme of the considered configuration is shown in Fig. 8.1. It consists of an oscillator, the dynamics of which is described by a dynamical variable $x(t)$, a switch $S(x(t))$, and two feedback branches respectively described by functions $g_1(x)$ and $g_2(x)$ and delay times $\tau_1$ and $\tau_2$. Depending on the state $x(t)$, the switch $S(x(t))$ routes the dynamics to one of the two branches.

This scheme belongs to a class of SDD systems described by the following equation,

$$\mathbf{x}(t) = f(\mathbf{x}(t)) + \sum_{k=1}^{2} {}_k(\mathbf{x}(t-\tau_k))g_k(\mathbf{x}(t-\tau_k)), \tag{8.1}$$

with ${}_1(\mathbf{x}(t))$, ${}_2(\mathbf{x}(t))$ $0, 1$ and ${}_1(\mathbf{x}(t))$ ${}_2(\mathbf{x}(t)) = 0$. The functions ${}_1(\mathbf{x}(t))$ and ${}_2(\mathbf{x}(t))$ represent the state-dependent switch $S(x(t))$.

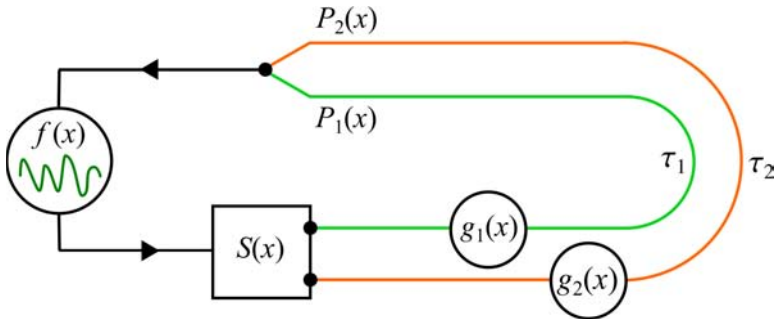


**Figure 8.1:** Simplified scheme of the SDD feedback configuration. An oscillator described by the function $f(x)$ and the dynamical variable $x(t)$ is directed to branch 1 or branch 2 depending on the state $x(t)$. The two feedback branches are respectively described by functions $g_1(x)$ and $g_2(x)$ and delay times $\tau_1$ and $\tau_2$. The power of light travelling trough branches 1 and 2 is represented by the variables $P_1(x)$ and $P_2(x)$, respectively. Figure modified from [10].

The second condition guarantees that the switch selects one branch at any time. Since the switch is located before the delay loops and the delay loops correspond to different delay times, the oscillator can receive feedback either from cavity 1, from cavity 2, from both cavities or from neither of them. More specifically, the oscillator receives feedback from cavity 1 if $_1(\mathbf{x}(t-\tau_1)) \neq 0$ and $_2(\mathbf{x}(t-\tau_2)) = 0$, from cavity 2 if $_1(\mathbf{x}(t-\tau_1)) = 0$ and $_2(\mathbf{x}(t-\tau_2)) \neq 0$, from both cavities if $_1(\mathbf{x}(t-\tau_1)) \neq 0$ and $_2(\mathbf{x}(t-\tau_2)) \neq 0$ and from none if $_1(\mathbf{x}(t-\tau_1)) = \ _2(\mathbf{x}(t-\tau_2)) = 0$.

If the switch were placed at the end of the delay loops instead, the oscillator would receive feedback from a single cavity selected by the switch. In this case, the dynamics would be given by

$$\mathbf{x}(t) = f(\mathbf{x}(t)) + \sum_{k=1}^{2} {}_k(\mathbf{x}(t))g_k(\mathbf{x}(t-\tau_k)). \tag{8.2}$$

### 8.2.2 Contrast function

The signature of the SDD dynamics can be quantified with the following *contrast function*, defined in the interval $[-1,1]$ as the normalized difference in power between the two filtered signals in the reference frame of the laser,

$$C(t) = \frac{P_1(t) - P_2(t)}{P_1(t) + P_2(t)}, \tag{8.3}$$

where $P_1 \quad {}_1(\mathbf{x}(t-\tau_1))g(\mathbf{x}(t-\tau_1))^{\ 2}$ and $P_2 \quad {}_1(\mathbf{x}(t-\tau_2))g(\mathbf{x}(t-\tau_2))^{\ 2}$. The definition of the contrast function given by Eq. (8.3) is valid provided that $P_1$ and $P_2$ do not vanish simultaneously.

The analysis of the contrast function allows us to detect the switches between the two different values of the delay time, as well as to identify the delay loop from which is mainly coming the feedback at a given time. Therefore, this function makes possible to identify which value takes the delay time at a given time.

According to Eq. (8.3), if $C > 0$ and $C < 0$, the delay time takes the values $\tau_1$ and $\tau_2$, respectively; if $C$ jumps from $C = 1$ to $C = -1$, there is a switch from $\tau_1$ to $\tau_2$, and viceversa; whereas if there is a plateau with $C = 0$, it is not possible to know only from the contrast function whether both delay times are active or neither of them is acting.

### 8.2.3 Residence times

The switching between the two different values of the delay time can be further characterized by computing the *residence-time* distributions, as it will be done in Sec. 8.9. The residence times $T_i(\tau_1)$ and $T_j(\tau_2)$ are the durations of the time intervals at which the delay time takes values $\tau_1$ and $\tau_2$, respectively.

The residence times can be computed from the contrast function, by detecting the time intervals between successive crossings through $C(t) = 0$. With this method, according to Eq. (8.3), the residence times $T_i(\tau_1)$ are given by the duration of the time intervals in which $C(t) > 0$, whereas the residence times $T_j(\tau_2)$ are given by the duration of the time intervals in which $C(t) < 0$.

For the system considered here, consisting of a semiconductor laser with filtered feedback from two cavities of different length and center frequency, the residence times can alternatively be computed from the time series of the instantaneous optical frequency, $\omega_{\mathrm{i}}(t)$. This can be done if the separation of the center frequencies as compared to the filters bandwidth is large enough, so that the switches between states around center frequencies $\ _1$ and $\ _2$ correspond to switches between delay time values $\tau_1$ and $\tau_2$. Then, the residence times can be computed considering that $\tau = \tau_1$ if $\omega \quad [\ _1 - \delta\omega, \ _1 + \delta\omega]$ and $\tau = \tau_2$ if $\omega \quad [\ _2 - \delta\omega, \ _2 + \delta\omega]$, with $0 < \delta\omega \quad _1 - \ _2\ /2$.

## 8.3 State-dependent delay experiment

In this section, we present the experimental configuration of the SDD photonic system considered here and some experimental results obtained with it. All the results shown in this section were obtained in experiments carried out by Dr. X. Porte in the nonlinear photonics laboratory of IFISC lead by Prof. Ingo Fischer.

### 8.3.1 State-dependent delay experimental design

The experimental design consists of a semiconductor laser with frequency-selective delayed optical feedback [10]. Instead of a mirror or fibre loop with fixed delay, as in conventional experiments with delayed optical feedback [186], the configuration considered here uses two feedback loops with disjunct spectral reflection ranges and different lengths, resulting in two different values of the delay time, $\tau_1$ and $\tau_2$. These delay time values are long compared to the characteristic dynamical time scales of the laser. These systems have recently been theoretically studied in terms of their relative equilibria structure and stability [187, 188]. In a recent experiment, it was demonstrated that the

addition of a second frequency-selective feedback loop allows to control the frequency of the laser light [189].

Semiconductor lasers exhibit a characteristic amplitude-phase coupling [138], in such a way that variations in amplitude are associated to changes in the optical frequency. Since amplitude-related nonlinearities typically induce very small relative changes in the delay time, especially in the large-delay limit considered here, it is more convenient to act on the spectral characteristics of the state rather than on its amplitude. For this reason, loops based on the use of spectrally selective mirrors to provide optically filtered feedback are considered.

The semiconductor laser used in the experiment is discrete-mode (DM) quantum-well and emits at 1543 nm with a threshold current of $I_{\mathrm{th}} = 12.00\,\mathrm{mA}$ [190]. The DM laser exhibits single-mode behaviour with a side-mode suppression ratio larger than 35 dB and a longitudinal mode separation of 150 GHz. The linewidth enhancement factor value, $\alpha$ 2, has been measured by using the Henning-Collins approach [191]. The current and temperature of the laser have been stabilised to an accuracy of 0.01 mA and 0.01 K, respectively.

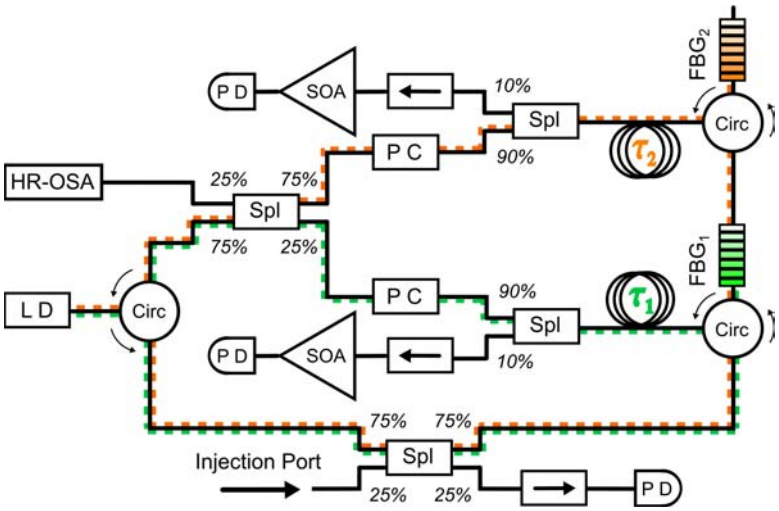


**Figure 8.2:** Scheme of the experimental setup for the SDD experiment. LD: laser diode, Circ: optical circulator, PC: polarization controller, 75/25 and 90/10: two by two optical couplers, FBG: fibre Bragg grating, : optical isolator, SOA: semiconductor optical amplifier, PD: photodiode, and HR-OSA: high-resolution optical spectrum analyser. The two delay time values, $\tau_1$ and $\tau_2$, are represented by the fibre spools after the respective FBG reflection. The delay loops closing filters 1 and 2 are highlighted in green and orange dashed lines, respectively. The fibre port labeled as *Injection Port* is used to inject trains of short pulses to measure the deskew and round trip times of each external cavity. Figure modified from [10].

A scheme of the experimental setup is shown in Fig. 8.2. The experimental configuration contains standard telecommunications components. The laser is subject to filtered optical feedback (FFB) from two cavities of different length and with disjunct spectral reflection ranges. The frequency-selective reflection is implemented on each cavity with a fibre Bragg grating (FBG) contained in the feedback loop. The FBGs have center frequency detunings with respect to the solitary laser frequency $_1/(2\pi) = -4$ 0.01

GHz and $\quad_2/(2\pi) = -11 \quad 0.01$ GHz, and reflection bandwidths $\delta \quad_1/(2\pi) = 4.63 \quad 0.02$ GHz and $\delta \quad_2/(2\pi) = 5.69 \quad 0.02$ GHz, in such a way that there is no spectral overlap between the reflection bandwidths of the two FBGs. The polarisation of each filtered-feedback cavity is independently aligned with polarisation controllers. It is assumed linear propagation for the fibre transmission within the delay loops. In this design, the laser represents the nonlinear element, which, in combination with the FBGs, acts as the state-dependent switch, as it will be discussed in the context of the experimental and numerical results.

### 8.3.2 State-dependent delay experimental results

This section summarizes some experimental results obtained with the SDD photonic system shown in Fig. 8.2. More experimental results with this SDD system can be found in [192].

The optical spectra of the LD emission changes with the injection current, as shown in Fig. 8.3 for pump currents from 4% below the solitary laser threshold to 10% above. In this figure, a range of pump currents below threshold is included because the laser threshold current of the laser is reduced with respect to the solitary laser threshold due to the feedback from the external reflectors.

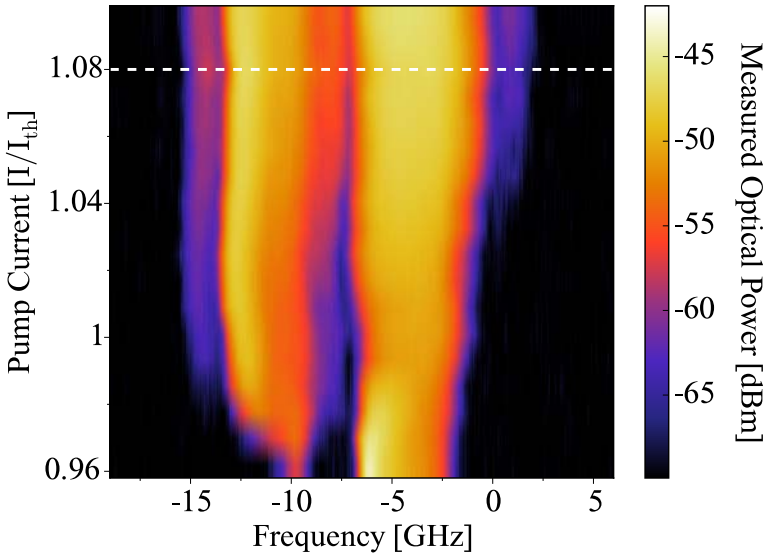


**Figure 8.3:** Dependence of the optical spectrum on the pump current of the laser. The frequency axis is centered to the value of the solitary laser frequency, $f_L = 194350$ GHz. $FBG_1$ and $FBG_2$ are detuned $-4 \quad 0.01$ GHz and $-11 \quad 0.01$ GHz from $f_L$, respectively. The dashed horizontal line represents the maximum current for which there is a gap larger than 10 dB between the two spectral bands corresponding to the two filters. The relative amplitudes of the two spectral components are affected by the coupling ratio of the coupler at which the spectra are measured. Figure reproduced from [10].

The horizontal dashed line in Fig. 8.3 indicates the limit value of pump current, $1.08I_{th}$, below which there is a spectral gap larger than 10 dB between the two filters, and thus

they can be considered as isolated. For pump currents above $1.08I_{\mathrm{th}}$, this gap gradually disappears and, therefore, the two filters cannot be considered spectrally separated. Close to threshold, the spectra exhibit comparable spectral amplitudes and bandwidths in both filters; therefore, similar contributions to the dynamics are expected from both filters. As a result of the chosen geometry and for sufficiently low pump current, this system belongs to the family of SDD systems described by Eq. (8.1).

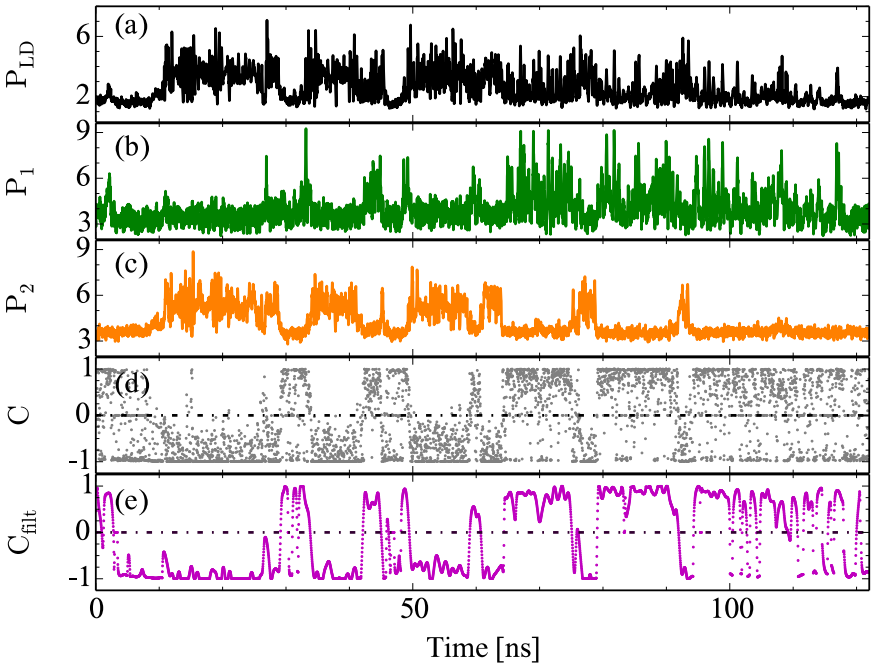


**Figure 8.4:** Experimental time series for the pump current of $I = 1.01I_{\mathrm{th}}$: (a) laser intensity dynamics, (b) and (c) filter-resolved intensity dynamics for $\mathrm{FBG}_1$ and $\mathrm{FBG}_2$, respectively, (d) contrast function, and (e) contrast function of the 1 GHz low-pass filtered intensity dynamics. Intensities are plotted in arbitrary units. Figure reproduced from [10].

The temporal evolution of the laser emission and the intensity in the two feedback loops for a pump current of $I = 1.01I_{\mathrm{th}}$ is shown in Figure 8.4. The total intensity dynamics is depicted in Fig. 8.4(a). Fig. 8.4(b) and Fig. 8.4(c) show the filter-resolved dynamics for $\mathrm{FBG}_1$ and $\mathrm{FBG}_2$, respectively. The state-dependent nature of the dynamics consists of alternating periods of emission in the frequency bands corresponding to $\mathrm{FBG}_1$, $\mathrm{FBG}_2$ or in none of both filters resulting in no feedback. The complementary nature of the laser intensity dynamics, based on mostly exclusive contributions either from $\mathrm{FBG}_1$ or $\mathrm{FBG}_2$, is already visible by eye.

The signature of this SDD dynamics can further be characterized using the contrast function introduced in the subsection 8.2.2. However, the experimental time series contain fluctuations due to detection noise, which have to be removed because they do not represent actual switches between states. Thus, the power measured on loop $i$, $P_i(t)$, is considered significative only if it is above an offset $P_{i\,\mathrm{o}}$, which is determined from the

noise characterization. Namely, experimentally, the contrast function is calculated as

$$C(t) = \frac{P_1^*(t) - P_2^*(t)}{P_1^*(t) + P_2^*(t) + \varepsilon}, \tag{8.4}$$

with $P_i^*(t) = max[(P_i(t) - P_{i\,\mathrm{o}}), 0]$, $i = 1, 2$ and $\varepsilon$ an infinitesimal parameter that avoids the indetermination zero divided by zero if $P_1^* = P_2^* = 0$.

Figures 8.4(d) and 8.4(e) show the contrast function (8.4) obtained from the fully resolved and the 1 GHz low-pass filtered intensity time traces, respectively. Erratic switches between the states corresponding to the two filters can be clearly recognised from both time traces of the contrast function. In the contrast function in Fig. 8.4(d), one can also see the fluctuations due to the influence of detection noise. Those fluctuations do not represent actual switches between states and are mostly removed by the low-pass filtering, giving rise to the much smoother contrast function in Fig. 8.4(e).

The switching properties between the two filter states and the zero-feedback state can also be characterized by the cross-correlation coefficient between $P_1$ and $P_2$: $C_\mathrm{c} = -0.4$ for the unfiltered time traces, and $C_{\mathrm{c\,f}} = -0.65$ for the filtered ones. Therefore, the intensity dynamics in the two filters is anticorrelated.

Increasing the injection current results in dynamics with faster transitions between the two different values of the delay and, thus, shorter characteristic residence times in each state, as shown in Fig. 8.5 for an injection current of $I = 1.07 I_\mathrm{th}$. The contrast function again indicates clear switches between the different filter states, providing evidence for SDD dynamics.

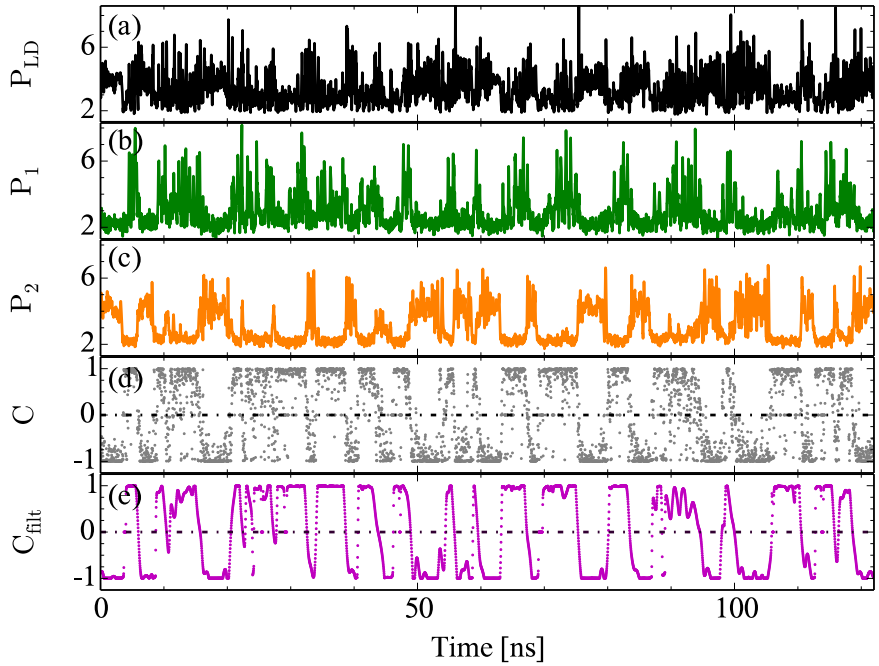


**Figure 8.5:** Experimental time series as in Fig. 8.4 but for a pump current of $I = 1.07 I_\mathrm{th}$. Figure reproduced from [10].

Increasing the injection current further results in an increasing bandwidth of the laser dynamics, related to the increase of the relaxation oscillations frequency. This ultimately gives rise to a spectral overlap, as illustrated in Fig. 8.3 and, therefore, to the loss of a clear distinction between two separate states. Nevertheless, for pump currents below $I = 1.08 I_{\mathrm{th}}$, the laser indeed acts as nonlinear element, which, in combination with the FBGs, acts as a state-dependent switch that determines which delayed feedback loop will be active at any time. The statistics of the switchings between different filter states will be discussed in more detail in Sec. 8.9. In the next sections, we introduce a model for the system using a rate equation approach and compare its properties with the experiments.

## 8.4 Theoretical model

We consider a simple model for a semiconductor laser subject to the feedback from $m$ frequency-selective external cavities. The dynamics is analysed through the extended Lang-Kobayashi [193] model, which consists of $2 + m$ equations in its simplest form. The first two, for the slowly varying complex amplitude of the electric field $E(t)$ (in the reference frame of the solitary laser frequency) and the carrier number $N(t)$, are given by

$$\begin{aligned} E(t) &= \frac{1+i\alpha}{2}[G(N,E)-\gamma]E(t) + \sum_{k=1}^{m} {}_k e^{i\ {}^k} F_k(t-\tau_k), \\ N(t) &= \frac{I}{e} - \gamma_n N(t) - G(N,E)\ E(t)\ ^2, \end{aligned} \tag{8.5}$$

where $F_k(t)$ is the slowly varying complex amplitude of the filtered electric field that is fed back to the laser after spectral filtering from filter $k$, $\alpha$ is the linewidth enhancement factor, $\gamma = 0.2\,\mathrm{ps}^{\ 1}$ is the photon decay rate, $\gamma_n = 1\,\mathrm{ns}^{\ 1}$ is the decay rate for the carriers, $I$ is the injection current, $e$ is the electron charge and $\tau_k$, ${}_k$ and $\varphi_k$ are the feedback delay time, the feedback strength and the accumulated phase of filter $k$, respectively. In the long-cavity limit, as considered here, the phases do not play a significant role [186], so we choose $\varphi_k = 0$. The Lang-Kobayashi approach is valid for a single longitudinal mode of the internal cavity. We consider a nonlinear gain

$$G(N,E) = g\frac{N(t)-N_0}{1+s\ E(t)\ ^2}, \tag{8.6}$$

where $g = 1.5\ \ 10\ ^{8}\,\mathrm{ps}^{\ 1}$ is the differential gain coefficient, $N_0 = 1.8\ \ 10^8$ the carrier number at transparency, and $s = 10\ ^{7}$ the gain saturation coefficient. The threshold current of the solitary laser, $I_{\mathrm{th}} = e\gamma_n\,(N_0 + \gamma/g)$, is 30.98 mA. For convenience, we define the adimensional carrier number as

$$n = (N - N_0)g/\gamma - 1. \tag{8.7}$$

For ease of analytic and numerical tractability, we consider Lorentzian linear filters with center frequency ${}_k$ and half-width at half-maximum ${}_k$ [149, 194]. Then, the extended

Lang-Kobayashi equations (8.5) are completed with $m$ equations, one for each filter,

$$F_k(t) = \ _kE(t) + (i \ _k - \ _k)F_k(t), \quad k = 1, m, \tag{8.8}$$

and the whole $(m+2)$-dimensional system reads

$$E(t) = \frac{1+i\alpha}{2} \ g\frac{N(t)-N_0}{1+s\ E(t)^{\ 2}} - \gamma \ E(t) + \sum_{k=1}^{m} \ _ke^{i \ _k}F_k(t-\tau_k), \tag{8.9}$$

$$N(t) = \frac{I}{e} - \gamma_n N(t) - g\frac{N(t)-N_0}{1+s\ E(t)^{\ 2}}\ E(t)^{\ 2}, \tag{8.10}$$

$$F_k(t) = \ _kE(t) + (i \ _k - \ _k)F_k(t), \quad k = 1, m. \tag{8.11}$$

The aim of this approach is to provide a simple model that allows for qualitative comparison with the experiments and for a detailed study of the underlying mechanisms. Precise quantitative agreement between theory and experiment cannot be expected, since the Lorentzian filter profile does not reflect the detailed filter characteristics of the fibre Bragg gratings. Nevertheless, we can choose similar parameters values, which give rise to similar physical conditions and dynamical behaviour.

The relative equilibria of the system (8.9)-(8.11) can be calculated depending on laser and filter parameter values, as detailed in Sec. 8.5.

## 8.5 Relative equilibria of a semiconductor laser with Lorentzian filtered feedback

The relative equilibria of the system (8.9)-(8.11) are filtered cavity modes (FCMs), which are rotating wave solutions with constant frequency, carrier number and field amplitude; namely, they can be written as

$$\begin{aligned} E(t) &= \mathcal{E}_{\rm st}e^{i \ _{\rm st}t}, \\ N(t) &= N_{\rm st}, \\ F_k(t) &= \mathcal{F}_{{\rm st}_k}e^{i(\ _{\rm st}t + \ _{{\rm st}_k} + \ _{\rm st} \ _k \quad _k)}, \end{aligned} \tag{8.12}$$

where $\mathcal{E}_{\rm st}$, $\mathcal{F}_{{\rm st}_k}$, $N_{\rm st}$, $\omega_{\rm st}$ and $\phi_{{\rm st}_k}$ are real positive constants. Inserting this ansatz into (8.9) and (8.10) yields

$$i\omega_{\rm st}\mathcal{E}_{\rm st} = \frac{1+i\alpha}{2} \ g\frac{N_{\rm st}-N_0}{1+s\mathcal{E}_{\rm st}^2} - \gamma \ \mathcal{E}_{\rm st} + \sum_{k=1}^{m} \ _k\mathcal{F}_{{\rm st}_k}e^{i \ _{{\rm st}_k}}, \tag{8.13}$$

$$0 = \frac{I}{e} - \gamma_n N_{\rm st} - g\frac{N_{\rm st}-N_0}{1+s\mathcal{E}_{\rm st}^2}\mathcal{E}_{\rm st}^2. \tag{8.14}$$

For Lorentzian filtering, inserting the ansatz (8.12) into (8.11) gives rise to

$$i\omega_{\rm st}\mathcal{F}_{{\rm st}_k} = (i \ _k - \ _k)\mathcal{F}_{{\rm st}_k} + \ _k\mathcal{E}_{\rm st}e^{i(\ _k \quad _{\rm st} \ _k \quad _{{\rm st}_k})}. \tag{8.15}$$

Real and imaginary part of Eq. (8.15),

$$\cos(\varphi_k - \phi_{\mathrm{st}_k} - \omega_{\mathrm{st}}\tau_k) = \frac{\mathcal{F}_{\mathrm{st}_k}}{\mathcal{E}_{\mathrm{st}}}, \tag{8.16}$$

$$\sin(\varphi_k - \phi_{\mathrm{st}_k} - \omega_{\mathrm{st}}\tau_k) = \frac{\mathcal{F}_{\mathrm{st}_k}}{\mathcal{E}_{\mathrm{st}}}\ {}_k(\omega_{\mathrm{st}}), \tag{8.17}$$

can be combined to get an equation for $\phi_{\mathrm{st}_k}$,

$$\tan(\varphi_k - \phi_{\mathrm{st}_k} - \omega_{\mathrm{st}}\tau_k) = \ {}_k(\omega_{\mathrm{st}}), \tag{8.18}$$

where

$${}_k(\omega_{\mathrm{st}}) = \frac{\omega_{\mathrm{st}} - \ {}_k}{{}_k}. \tag{8.19}$$

Since in (8.16) $\mathcal{F}_{\mathrm{st}_k}$ and $\mathcal{E}_{\mathrm{st}_k}$ are positive, the argument $\varphi_k - \phi_{\mathrm{st}_k} - \omega_{\mathrm{st}}\tau_k$ must be either in the first or in fourth quadrant. Then, (8.18) is equivalent to

$$\phi_{\mathrm{st}_k} = \varphi_k - \omega_{\mathrm{st}}\tau_k - \arctan\left[\ {}_k(\omega_{\mathrm{st}})\right]. \tag{8.20}$$

Substitution of (8.20) into (8.16) gives rise to

$$\frac{\mathcal{F}_{\mathrm{st}_k}}{\mathcal{E}_{\mathrm{st}}} = \cos\ \arctan\left[\ {}_k(\omega_{\mathrm{st}})\right]\ = \frac{1}{\sqrt{1 + \ {}^2_k(\omega_{\mathrm{st}})}}. \tag{8.21}$$

With the purpose to obtain an equation for $\omega_{\mathrm{st}}$, we separate (8.13) into its real and imaginary parts, yielding

$$0 = \frac{1}{2}\ g\frac{N_{\mathrm{st}} - N_0}{1 + s\mathcal{E}_{\mathrm{st}}^2} - \gamma\ + \sum_{k=1}^{m}\ {}_k\frac{\mathcal{F}_{\mathrm{st}_k}}{\mathcal{E}_{\mathrm{st}}}\cos\phi_{\mathrm{st}_k}, \tag{8.22}$$

$$\omega_{\mathrm{st}} = \frac{\alpha}{2}\ g\frac{N_{\mathrm{st}} - N_0}{1 + s\mathcal{E}_{\mathrm{st}}^2} - \gamma\ + \sum_{k=1}^{m}\ {}_k\frac{\mathcal{F}_{\mathrm{st}_k}}{\mathcal{E}_{\mathrm{st}}}\sin\phi_{\mathrm{st}_k}. \tag{8.23}$$

Substitution of Eq. (8.22) into Eq. (8.23) gives rise to

$$\omega_{\mathrm{st}} = \sum_{k=1}^{m}\ {}_k\frac{\mathcal{F}_{\mathrm{st}_k}}{\mathcal{E}_{\mathrm{st}}}\left[\sin\phi_{\mathrm{st}_k} - \alpha\cos\phi_{\mathrm{st}_k}\right]. \tag{8.24}$$

Writing the square braquet as

$$\begin{aligned}
&\sqrt{1+\alpha^2}\ \ \frac{1}{\sqrt{1+\alpha^2}}\sin\phi_{\mathrm{st}_k} - \frac{\alpha}{\sqrt{1+\alpha^2}}\cos\phi_{\mathrm{st}_k}\\
&= \sqrt{1+\alpha^2}\left[\sin\phi_{\mathrm{st}_k}\cos\ \arctan\alpha\ - \cos\phi_{\mathrm{st}_k}\sin\ \arctan\alpha\ \right]\\
&= \sqrt{1+\alpha^2}\left[\sin\left(\phi_{\mathrm{st}_k} - \arctan\alpha\right)\right],
\end{aligned} \tag{8.25}$$

Eq. (8.24) reads

$$\omega_{\mathrm{st}} = \sum_{k=1}^{m}\ {}_k\frac{\mathcal{F}_{\mathrm{st}_k}}{\mathcal{E}_{\mathrm{st}}}\sqrt{1+\alpha^2}\sin[\phi_{\mathrm{st}_k} - \arctan\alpha]. \tag{8.26}$$

The $\mathcal{F}_{\mathrm{st}_k}/\mathcal{E}_{\mathrm{st}}$ dependence in Eq. (8.26) can be eliminated using Eq. (8.21),

$$\omega_{\mathrm{st}} = \sum_{k=1}^{m} \frac{k\sqrt{1+\alpha^2}}{1+\ ^2_k(\omega_{\mathrm{st}})} \sin[\phi_{\mathrm{st}_k} - \arctan\alpha], \tag{8.27}$$

whereas inserting Eq. (8.20) into Eq. (8.27) we eliminate the $\phi_{\mathrm{st}}$ dependence in Eq. (8.27) and get a transcendental equation for the frequency $\omega_{\mathrm{st}}$:

$$\omega_{\mathrm{st}} = \sum_{k=1}^{m} K^{\mathrm{e}}_k\ (\omega_{\mathrm{st}}) \sin\ \ \varphi_k - \omega_{\mathrm{st}}\tau_k - \arctan[\ _k(\omega_{\mathrm{st}})] - \arctan\alpha\ \ , \tag{8.28}$$

where

$$K^{\mathrm{e}}_k\ (\omega_{\mathrm{st}}) = \frac{K_k}{\sqrt{1+\ ^2_k(\omega_{\mathrm{st}})}} \tag{8.29}$$

and $K_k = \ _k\ \sqrt{1+\alpha^2}$ is the dressed feedback strength. For a single single filter ($k = 1$) and $\mathcal{F}_{\mathrm{st}} = \mathcal{E}_{\mathrm{st}}$, which corresponds to the case of conventional optical feedback (COF), this parameter is a measure of the number of relative equilibria of the system and it separates the region of monostable operation ($K < 1/T$) from the region of multistable operation ($K > 1/T$) [149].

Equation (8.28) can be solved numerically to find the frequencies of the relative equilibria. Each solution of (8.28) corresponds to the intersection of the straight line $\omega_{\mathrm{st}}$ with the oscillating right-hand side of (8.28). It should be noticed that the argument of the sine is $\omega_{\mathrm{st}}$ dependent itself, and it exhibits an additional $\omega_{\mathrm{st}}$ dependence in the argument of the *arctan* function that is not present in COF.

In the case of a single filter ($k = 1$), the number of solutions of (8.28) increases with the effective feedback strength $K^{\mathrm{e}}\ (\omega_{\mathrm{st}})$, which is proportional to the feedback strength . As it can be deduced from Eq. (8.29), the number of relative equilibria with FFB is reduced as compared to the case of COF; nevertheless, for FFB with a single filter centered at $\omega_{\mathrm{st}}$, i.e. with $= \omega_{\mathrm{st}}$, Eq. (8.28) takes the same form than for COF.

For $s = 0$, the carrier number at the relative equilibrium can be obtained substituting (8.16) and (8.20) into (8.22),

$$N_{\mathrm{st}} = N_0 + \frac{1}{g}\ \ \gamma - 2\sum_{k=1}^{m}\ _k \frac{K^{\mathrm{e}}_k\ (\omega_{\mathrm{st}})}{K_k} \cos\ \ \varphi_k - \omega_{\mathrm{st}}\tau_k - \arctan[\ _k(\omega_{\mathrm{st}})]\ \ \ . \tag{8.30}$$

In this case, the field amplitude $\mathcal{E}_{\mathrm{st}}$ can be obtained from Eq. (8.14),

$$\mathcal{E}_{\mathrm{st}} = \ \ \sqrt{\frac{J-\gamma_n N_{\mathrm{st}}}{g(N_{\mathrm{st}}-N_0)}}, \tag{8.31}$$

and $\mathcal{F}_{\mathrm{st}_k}$ can be derived from substitution of Eq. (8.29) into (8.21),

$$\mathcal{F}_{\mathrm{st}_k} = \frac{K^{\mathrm{e}}_k\ (\omega_{\mathrm{st}})}{K_k}\mathcal{E}_{\mathrm{st}}. \tag{8.32}$$

For $s \neq 0$, the results for low laser intensity can be approximated by those obtained for $s = 0$.

8.6

## Numerical simulations

We have performed numerical simulations of (8.9)-(8.11) using different parameter values mimicking the experimental conditions qualitatively.

First, we consider a laser with a linewidth enhancement factor of $\alpha = 3$ and two cavities with $_1 = \ _2 = 40\,\text{ns}$ $^1$, $_1/(2\pi) = \ _2/(2\pi) = 0.5\,\text{GHz}$, $\tau_1 = 106.075\,\text{ns}$, $\tau_2 = 121.625\,\text{ns}$, $_1/(2\pi) = -5\,\text{GHz}$ and $\ _2/(2\pi) = -15\,\text{GHz}$, for several values of the injection current.

For injection currents sufficiently below threshold, $I/I_{\text{th}} < 0.99$, and neglecting noise in the simulations, the system gets trapped at the most stable FCM, with lowest carrier number and frequency close to the center frequency of the more detuned filter.

For injection currents in the interval $I/I_{\text{th}} = 0.99 - 1.1$, the system exhibits switching dynamics between the two islands of FCMs corresponding to the two solitary filters with different delay times. Remarkably enough, for large delays the switching regime can start even below the solitary laser threshold. As an example, Fig. 8.6 shows a 15.5 ns trajectory of the system for $I/I_{\text{th}} = 0.99$ together with the FCMs in the $(\omega_{\text{i}}, n)$ plane. The corresponding instantaneous optical angular frequency $\omega_i$, relative to the solitary laser frequency, is plotted in the inset as function of time. In Fig. 8.6, one can recognise how the system jumps from a state centered in the more detuned filter (blue region) towards the less detuned one (green region). Despite of the tails of the filter functions, the FCMs of the system with two filters lie very close to the FCMs of a corresponding system with a single filtered feedback. One can therefore conclude that the dynamics indeed exhibits SDD properties.

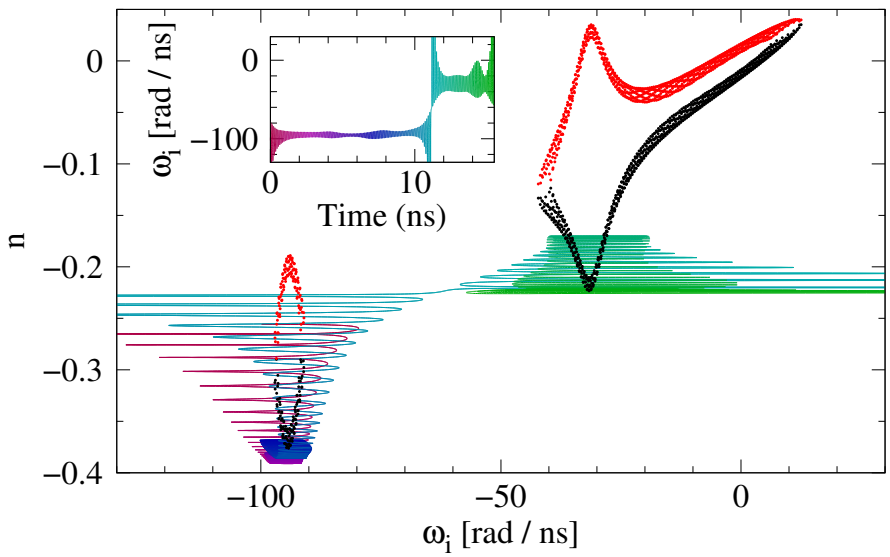


**Figure 8.6:** 15.5 ns trajectory of (8.9)-(8.11) with two filters around modes (black points) and antimodes (red points) for $\alpha = 3$, $I = 0.99 I_{\text{th}}$, $_1/(2\pi) = -5\,\text{GHz}$, $\ _2/(2\pi) = -15\,\text{GHz}$, $_1 = \ _2 = 40\,\text{ns}$ $^1$ and $s = 0$. The inset shows the instantaneous optical angular frequency as function of the time.

The instantaneous optical angular frequency of a larger trajectory with several jumps is shown as a function of time in Fig. 8.7(e), together with the intensity of the electric field (a), the intensity of the filtered fields $P_1(t) = F_1(t)^2$ (b) and $P_2(t) = F_2(t)^2$ (c) and the filter contrast (d). In Fig. 8.7(e), the center frequencies of the two filters are plotted as dashed lines to illustrate the time intervals in which the trajectories oscillate around the relative equilibria of each filter. The time intervals during which the trajectories are concentrated in one of the filters are shorter than the delay times.

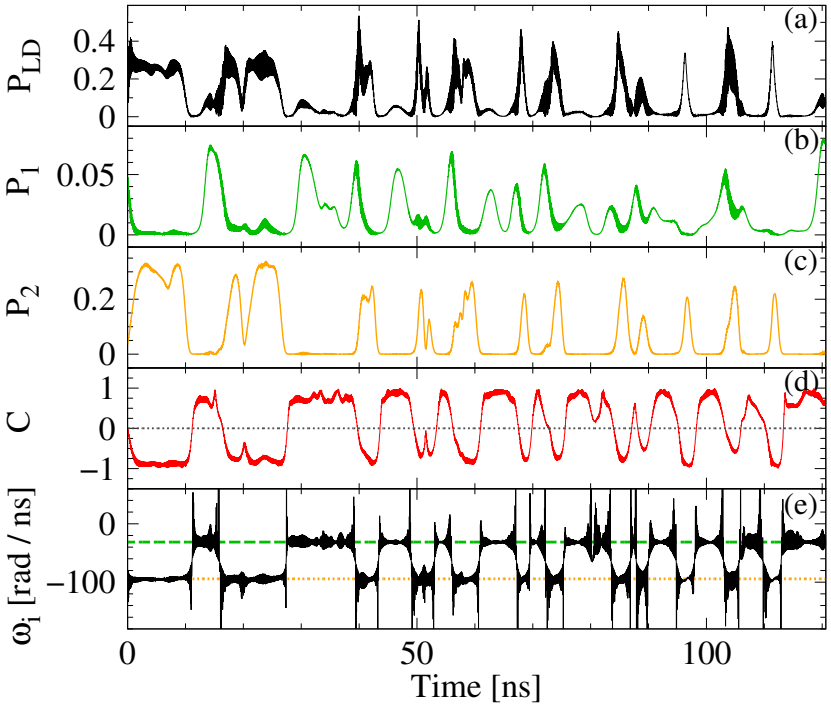


**Figure 8.7:** Numerical time traces for the same parameter values than in Fig. 8.6: (a) intensity of the electric field, (b) $P_1(t) = F_1(t)^2$, (c) $P_2(t) = F_2(t)^2$, (d) filter contrast and (e) instantaneous optical angular frequency of the electric field. In the last panel, the dashed lines indicate $_1$ (green) and $_2$ (orange).

The signature of SDD dynamics can also be recognised from the optical spectra of the laser emission. Examples of optical spectra plots are shown in Fig. 8.8 for different values of the injection current. For $I/I_{\text{th}} = 0.98$ [panel (a)] and lower values of $I/I_{\text{th}}$, the optical spectrum shows a single peak centered at the center frequency of the more detuned filter, indicating that the system operates in a stable FCM. In the interval $I/I_{\text{th}} = 0.99 - 1.1$ there is a competition between the two frequencies corresponding to the two different values of the delay, as shown in panels (b), (c), (d), (e), and (f) for increasing values of $I/I_{\text{th}}$ in this range, corresponding to the different values of the delay. In the next section we will show that the range of currents in which SDD dynamics is found in numerical simulations for the configuration considered here is robust against small changes in the values of the other parameters.

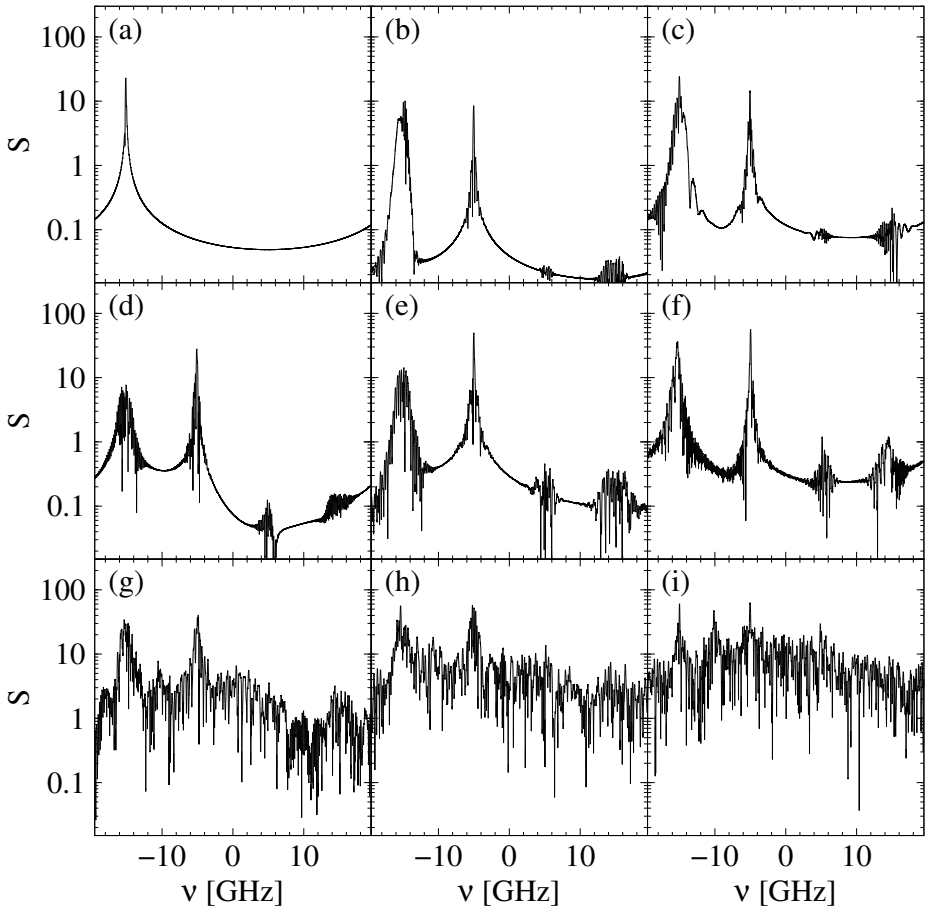


**Figure 8.8:** Optical spectra of the laser emission for the same parameter values than in Fig. 8.6 but different values of the injection current: (a) $I/I_{\rm th} = 0.98$, (b) $I/I_{\rm th} = 0.99$, (c) $I/I_{\rm th} = 1.001$, (d) $I/I_{\rm th} = 1.01$, (e) $I/I_{\rm th} = 1.05$, (f) $I/I_{\rm th} = 1.1$, (g) $I/I_{\rm th} = 1.2$, (h) $I/I_{\rm th} = 1.5$, and (i) $I/I_{\rm th} = 1.8$.

For $I/I_{\rm th} > 1.1$, the dynamical evolution of the system converges to a global chaotic attractor, in which distinct jumps between the two different filters can no longer be identified. In the optical spectra shown in Figs. 8.8(g), 8.8(h) and 8.8(i) for $I/I_{\rm th} = 1.2$, $I/I_{\rm th} = 1.5$ and $I/I_{\rm th} = 1.8$, respectively, the two peaks centered at the center frequencies of the two filters overlap so much that the filters cannot be considered as isolated.

Figure 8.9 depicts a situation nominally even closer to the experimental conditions with $\alpha = 2$, $_1/(2\pi) = -4.5\,\text{GHz}$, $_2/(2\pi) = -13\,\text{GHz}$, $_1 = 30\,\text{ns}^{\ 1}$ and $_2 = 50\,\text{ns}^{\ 1}$. The figure illustrates that one finds similar switching dynamics between the filter states as depicted in Fig. 8.7.

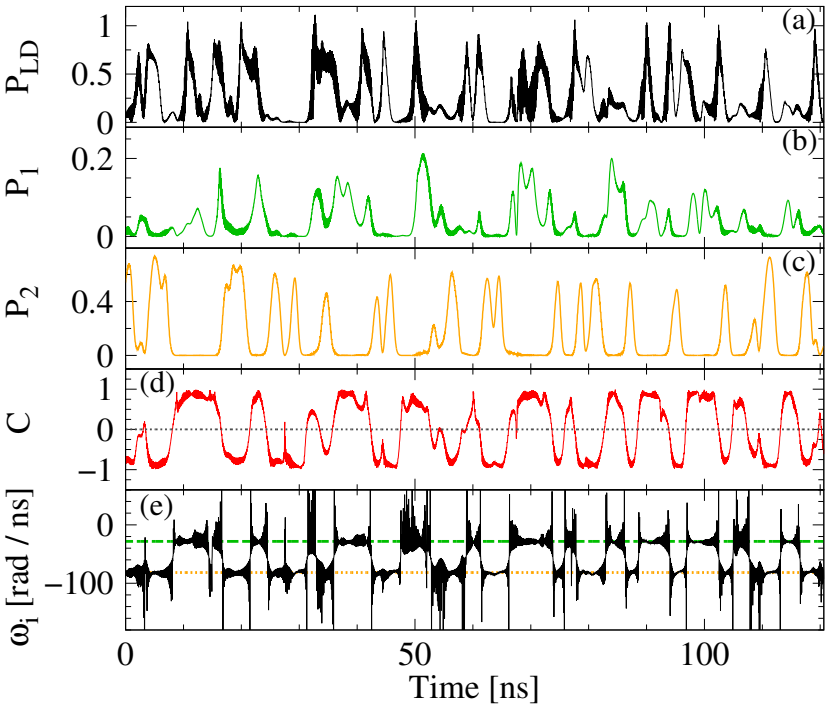


**Figure 8.9:** Numerical time traces for $\alpha = 2$, $I = 0.999 I_{\mathrm{th}}$, $\quad {}_1/(2\pi) = -4.5\,\mathrm{GHz}$, $\quad {}_2/(2\pi) = -13\,\mathrm{GHz}$, $\quad {}_1 = 30\,\mathrm{ns}$ $^1$ and $\quad {}_2 = 50\,\mathrm{ns}$ $^1$: (a) intensity of the electric field, (b) $P_1(t) = \ F_1(t)\ ^2$, (c) $P_2(t) = \ F_2(t)\ ^2$, (d) filter contrast and (e) instantaneous optical angular frequency of the electric field. In the last panel, the dashed lines indicate $\quad {}_1$ (green) and $\quad {}_2$ (orange).

## 8.7 Dependence on key parameters

We have performed systematic numerical studies to investigate the influence of key parameters on the dynamical behaviour. Keeping fixed $\tau_1 = 106.075\,\mathrm{ns}$ and $\tau_2 = 121.625$ ns, we find SDD dynamics for considerable parameter regimes covering intervals for the injection current of $[I/I_{\mathrm{th}} = 0.99 - 1.1]$, the studied range of $\alpha \quad [2, 3]$, filter detunings of $\Delta \ /(2\pi) \quad [8\,\mathrm{GHz}, 12\,\mathrm{GHz}]$ and some variation of the absolute filter positions by a few GHz. The fact that we find SDD dynamics in a considerable parameter range and for different filter characteristics proves the robustness of the observed phenomena.

The first insight into the limit values of the feedback strength coefficients and center frequencies for SDD dynamics has been obtained plotting the FCMs in the $(\omega_{\mathrm{i}}, n)$ plane. The FCM plots represent a convenient tool to get insight into the parameter regions for which SDD is not allowed, either because the more detuned filter has not FCMs or because the two filters spectrally overlap. Nevertheless, they are not a mathematical proof of existence of SDD dynamics. In order to determine whether the dynamics has SDD nature or not, we have integrated the dynamical system with different values of the injection current, computed the filter contrast and the optical spectra for different values of the injection current.

Examples of plots of the FCMs in the $(\omega_i, n)$ plane are shown in Figs. 8.10 and 8.11, where we can see the effect of changing the position of the filters.

In Fig. 8.10, we have taken $\alpha = 3$ and $\quad_1 = \quad_2 = 40\,\text{ns}^{\ 1}$. With these parameter values, we obtain SDD dynamics for $\quad_1/(2\pi) \quad [-4\,\text{GHz}, -6\,\text{GHz}]$, $\quad_2/(2\pi) \quad [-13\,\text{GHz}, -17$ GHz] provided that $\quad_1/(2\pi) - \quad_2/(2\pi) \quad [8\,\text{GHz}, 12\,\text{GHz}]$.

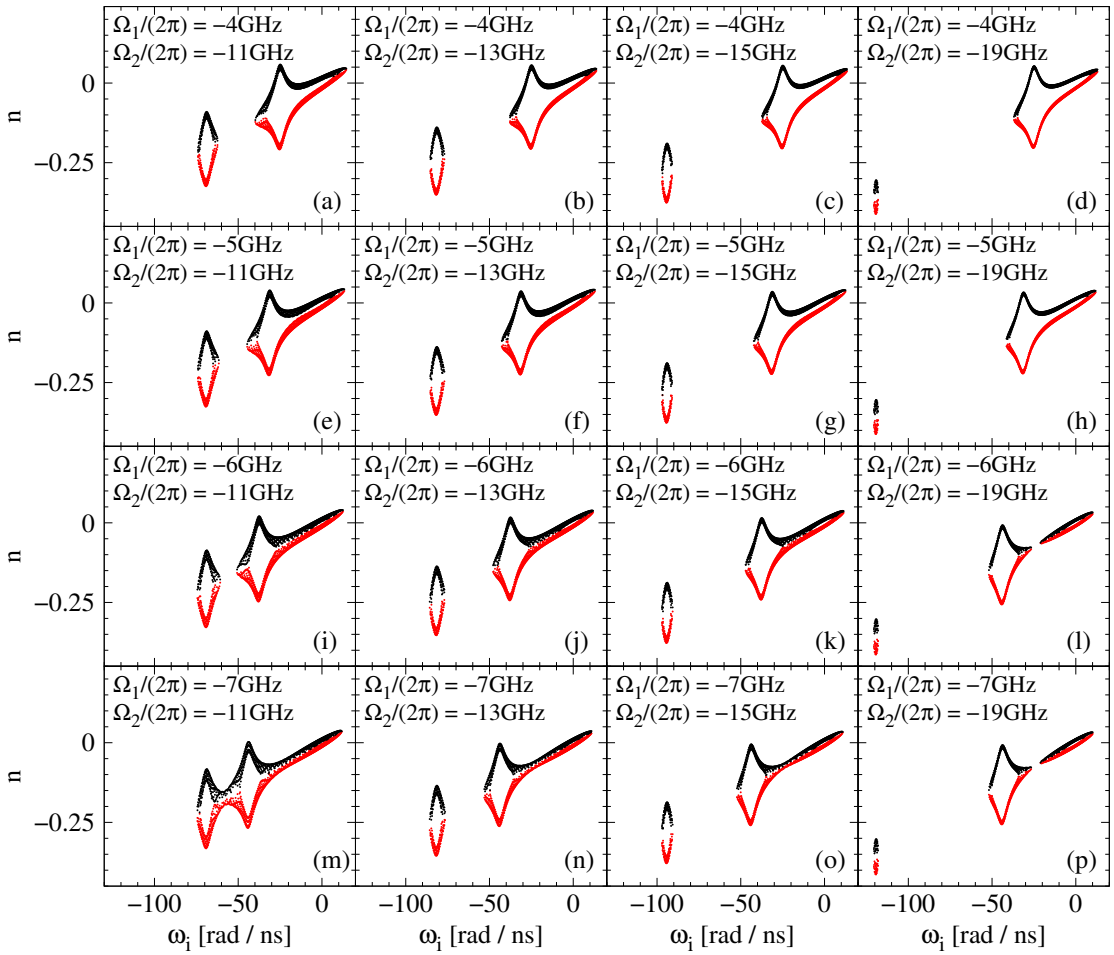


**Figure 8.10:** FCMs in the $(\omega_i, n)$ plane with $\alpha = 3$, $\tau_1 = 106.075\,\text{ns}$, $\tau_2 = 121.625\,\text{ns}$, $\quad_1/(2\pi) = \quad_2/(2\pi) = 0.5\,\text{GHz}$, $\quad_1 = \quad_2 = 40\,\text{ns}^{\ 1}$, and different values of the filter center frequencies.

With decreasing $\alpha$, the more detuned filter loses gain whereas the less detuned one is amplified, leading to a reduction of the region of SDD dynamics. In order to increase the number of FCMs in the more detuned filter, and thus obtain SDD dynamics for a large range of parameter values, without increasing $\alpha$, we can either decrease the detuning of the more detuned filter or use asymmetric feedback strengths with $k_2 > k_1$.

Figure 8.11 corresponds to $\alpha = 2$ and asymmetric feedback strength coefficients $\quad_1 = 30$ ns $^{1}$ and $\quad_2 = 40\,\text{ns}^{\ 1}$. For these values of the parameters, the limit values of the

center frequencies of the filters for SDD dynamics are $_1/(2\pi)$ $[-4\,\mathrm{GHz}, -5\,\mathrm{GHz}]$ and $_2/(2\pi)$ $[-12\,\mathrm{GHz}, -15\,\mathrm{GHz}]$.

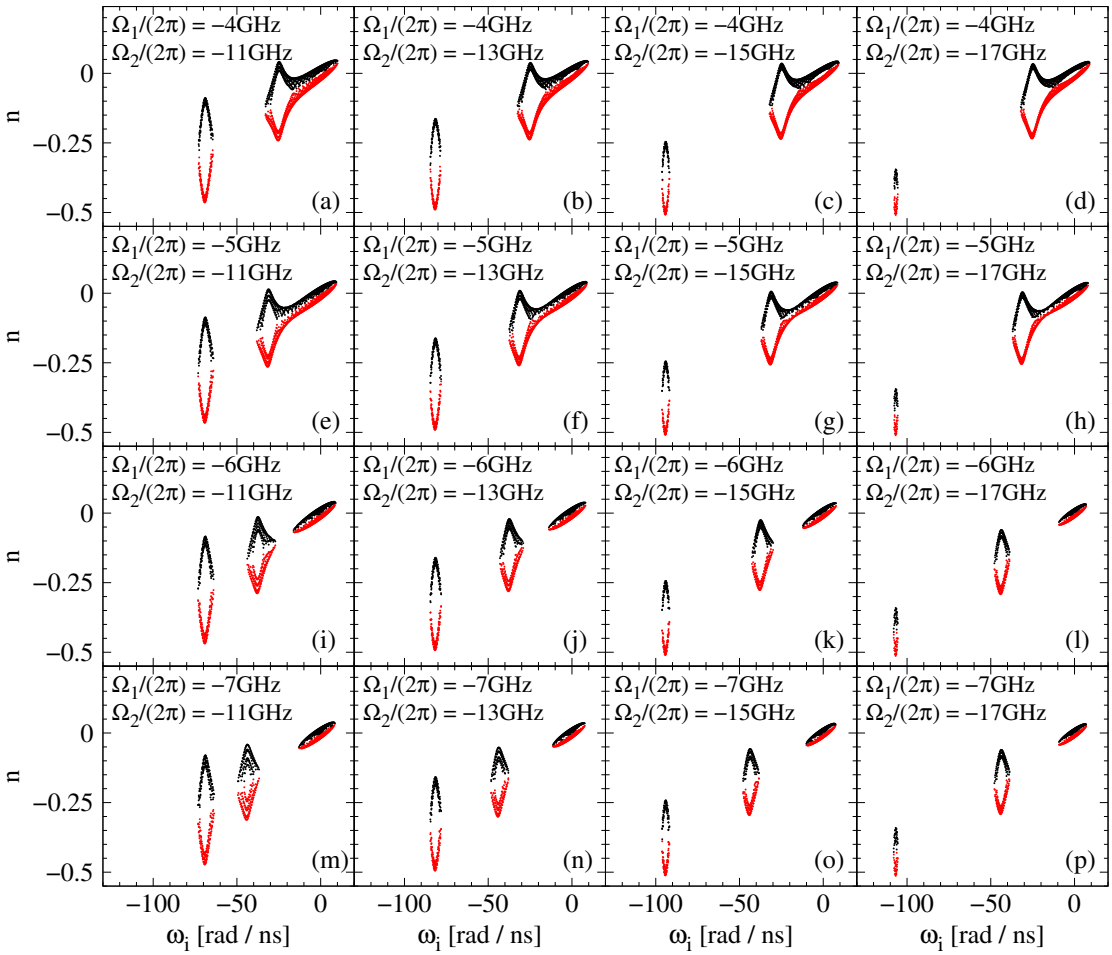


**Figure 8.11:** FCMs in the $(\omega_i, n)$ plane with $\alpha = 2$, $\tau_1 = 106.075\,\mathrm{ns}$, $\tau_2 = 121.625\,\mathrm{ns}$, $_1/(2\pi) = _2/(2\pi) = 0.5\,\mathrm{GHz}$, $_1 = 30\mathrm{ns}^{-1}$, $_2 = 50\mathrm{ns}^{-1}$, and different values of the filter center frequencies.

Beyond these ranges, the SDD dynamics is not mantained: for a fixed value of the center frequency of filter 2, $_2$, approaching $_1$ to $_2$ (compare the panels along a vertical column of Fig. 8.11), the quality of the contrast decreases. For a fixed value of the center frequency of filter 1, $_1$, moving away $_2$ from $_1$ (compare the panels along a horizontal row of Fig. 8.11) reduces the number of FCMs in filter 2 and, as a result, the dynamics takes place mainly around filter 1. Finally, for $_2$ too close to $_1$, the ECMs associated to the two filters are no longer isolated and the system operates in a stable ECM.

The effect of changing the feedback strength coefficients has also been analysed by keeping fixed the delay time values, the center frequencies of the filters and the filter bandwidth. As regards the limit values of the feedback strength coefficients, on the one hand

we need enough feedback strength in both filters. With $_1$ 20 ns $^1$ and $_2$ 30 ns $^1$, the strength of the feedback is not enough and the dynamics is, in general, centered around zero. On the other hand, although SDD dynamics can be obtained even in the case of larger feedback strength for the less detuned filter, the range of values for which SDD dynamics exists is centered around $_1$ $_2$. Choosing $\alpha = 3$, $_1/(2\pi) = -5$ GHz and $_2/(2\pi) = -15$ GHz, or $\alpha = 2$, $_1/(2\pi) = -4.5$ GHz and $_2/(2\pi) = -13$ GHz, we obtain SDD dynamics for $_1$ [30 ns $^1$, 50 ns $^1$] and $_2$ [40 ns $^1$, 50 ns $^1$] ( $_1 -$ $_2$ 20 ns $^1$).

As a proof of existence of SDD dynamics in the aforementioned parameter regions, the contrast function is shown in Figs. 8.12 and 8.13 for $\alpha = 3$ and $\alpha = 2$, respectively, for fixed values of the feedback strength coefficients and different values of the filter center frequencies. We note that, changing $_1$ and $_1$ and keeping fixed $_1$ and $_2$ we obtain similar results for the contrast function.

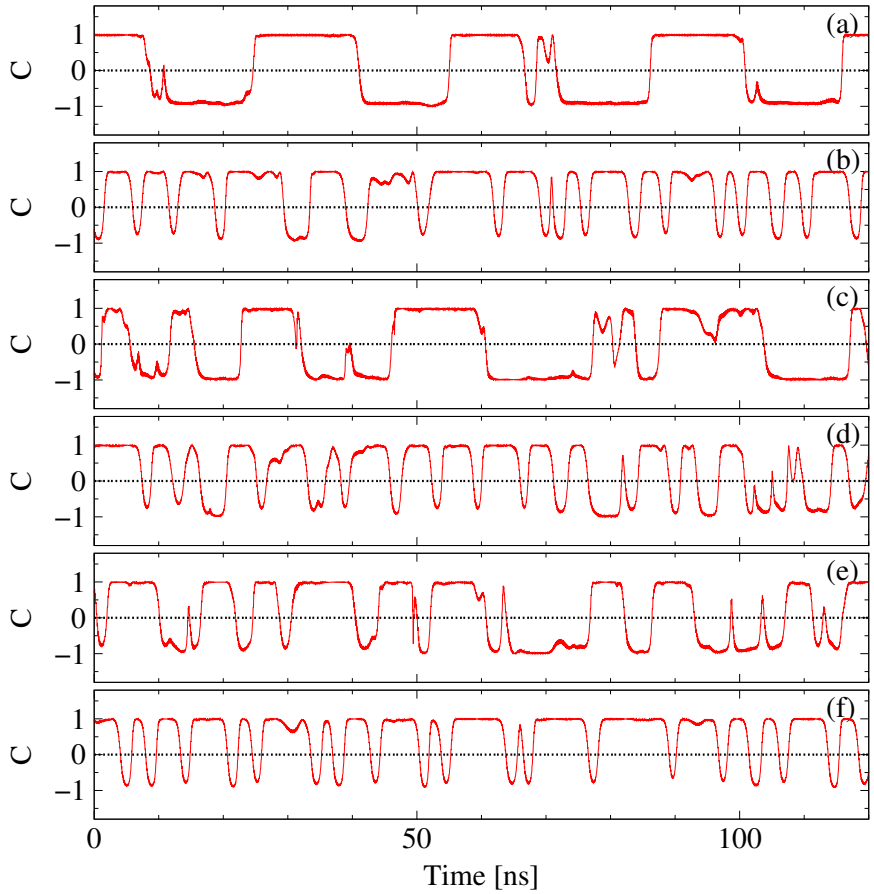


**Figure 8.12:** Contrast function with $\alpha = 3$, $I = 0.999 I_{\rm th}$, $\tau_1 = 106.075$ ns, $\tau_2 = 121.625$ ns, $_1/(2\pi) = _2/(2\pi) = 0.5$ GHz, $_1 = _2 = 40$ ns $^1$, and different values of the filter center frequencies: (a) $_1 = -4$ GHz and $_2 = -13$ GHz, (b) $_1 = -5$ GHz and $_2 = -13$ GHz, (c) $_1 = -4$ GHz and $_2 = -15$ GHz, (d) $_1 = -5$ GHz and $_2 = -15$ GHz, (e) $_1 = -6$ GHz and $_2 = -15$ GHz, (f) $_1 = -5$ GHz and $_2 = -17$ GHz.

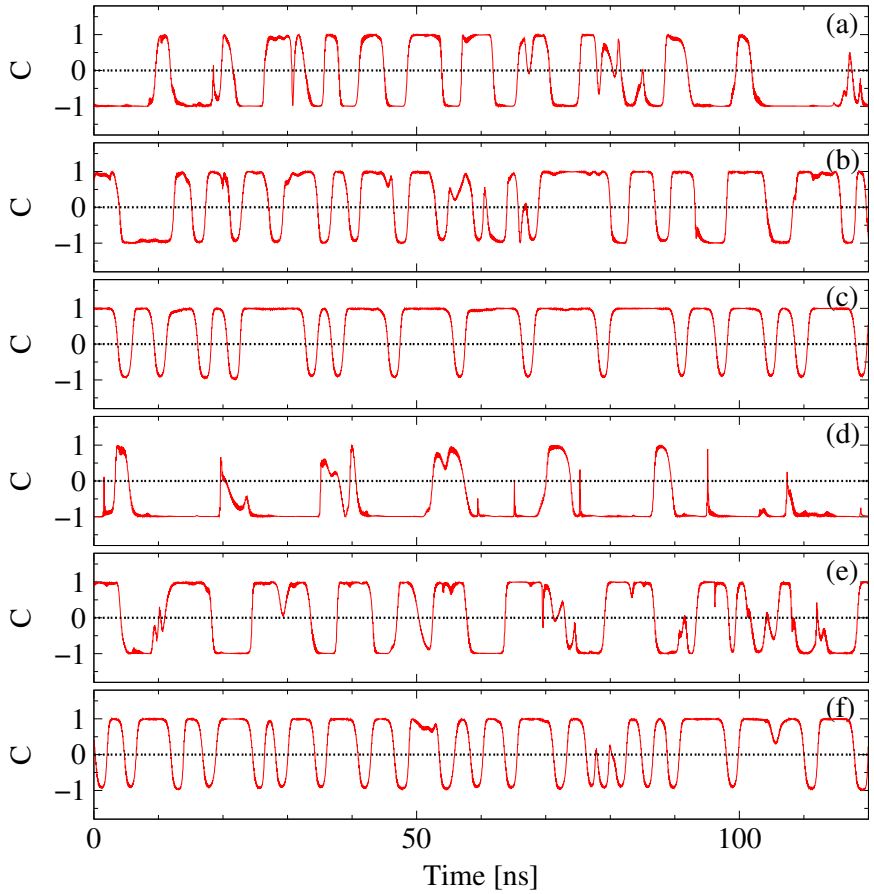


**Figure 8.13:** Contrast function with $\alpha = 2$, $I = 0.999 I_{\rm th}$, $\tau_1 = 106.075\,$ns, $\tau_2 = 121.625\,$ns, $_1/(2\pi) = \ _2/(2\pi) = 0.5\,$GHz, $_1 = 30\,$ns $^1$, $_2 = 50\,$ns $^1$, and different values of the filter center frequencies: (a) $_1 = -4\,$GHz and $_2 = -12\,$GHz, (b) $_1 = -4\,$GHz and $_2 = -13\,$GHz, (c) $_1 = -4\,$GHz and $_2 = -15\,$GHz, (d) $_1 = -5\,$GHz and $_2 = -12\,$GHz, (e) $_1 = -5\,$GHz and $_2 = -13\,$GHz, (f) $_1 = -4\,$GHz and $_2 = -15\,$GHz.

So far we have shown numerical simulations with $s = 0$. Nevertheless, as it was noted in Sec. 8.5, the approximation $s = 0$ used for computing the FCMs is only valid for low values of the laser intensity. Comparing Fig. 8.14(a) with Fig. 8.14(b), obtained with the same parameter values but with different saturation coefficient values [$s = 0$ in (a) and $s = 10^{\ 7}$ in (b)], we can see that the effect of a non-zero value of $s$ basically consists of a slightly increase of the carrier number. For lower values of $I$, this effect is smaller. In any case, in the range of currents $I/I_{\rm th} = 0.99 - 1.1$ for which we find SDD dynamics, this effect is small and it does not change the SDD nature of the dynamics.

Finally, we note that if the filter configuration is changed such that the longer delay is assigned to the less-detuned filter, we find a larger pump current region close to threshold in which the system operates in a stable FCM. As a consequence, the region of SDD dynamics is smaller or can even become negligible in parameter space.

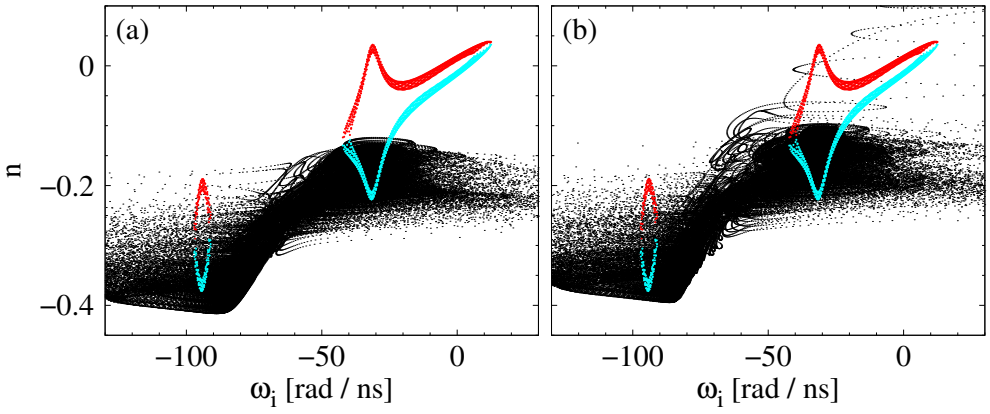


**Figure 8.14:** Black dots correspond to a 120 ns series of the dynamics projected in the $(\omega_{\rm i}, n)$ plane and obtained with delay times $\tau_1 = 106.075$ ns and $\tau_2 = 121.625$ ns, half-width at half maximum $_1/(2\pi) = \ _2/(2\pi) = 0.5$ GHz, center frequencies $_1/(2\pi) = -5$ GHz and $_2/(2\pi) = -15$ GHz, feedback strengths $_1 = \ _2 = 40$ ns $^{1}$, injection current $I = 1.1\, I_{\rm th}$, alpha parameter $\alpha = 3$, and saturation coefficient $s = 0$ (a) and $s = 10^{\ 7}$ (b). Color points indicate the FCMs obtained for $s = 0$ (blue points correspond to modes, while red points to antimodes).

## 8.8 Almost square-wave switching with state-dependent delay

In addition to SDD dynamics with irregular switching, it is also possible to observe SDD dynamics in which the switchings between the two filter states take place at more regular time intervals. This regularity is enhanced if the delay times are shorter. For instance, for delay times $\tau_1 = 30$ ns and $\tau_2$ close to 36 ns and pump currents around $I/I_{\rm th} = 0.99$, one gets periodic switchings with a periodicity close to the difference in the delay time values but larger than it, as it can be seen in Fig. 8.15 [(a)-(c)].

This kind of dynamics resembles the square-wave behaviour disussed in Parts I and II of this thesis. The peculiarity of the system considered here is twofold. First, the two states are not individual modes, but are dynamical states which can involve many external cavity modes. Second, the two states involved in the switching correspond to two different values of the delay time.

Almost square-wave switching with a periodicity of the order of the difference in the delay time values is not restricted to specific ratios $\tau_1/\tau_2$, but can be found over small windows of ratios $(\tau_1/\tau_{2_M}, \tau_1/\tau_{2_m})$. The size $\tau_1/\tau_{2_M} - \tau_1/\tau_{2_m}$ of these windows is of the order of $10^{\ 1}$ for the values of the parameters considered here. Remarkably, these regular windows are not centered around the ratio $\tau_1/\tau_2 = 1$ but at a ratio $\tau_1/\tau_2$ slightly smaller than 1. In the example of Fig. 8.15, almost square-wave switching with a periodicity of the order of the difference in delay time values is found for $\tau_2$ [35 ns, 36.5 ns] [(a)-(c)]. For $\tau_2 = 37$ ns the time traces do not have a square-wave shape and have a periodicity of the order of $\tau_2$, as shown in Fig. 8.15(d).

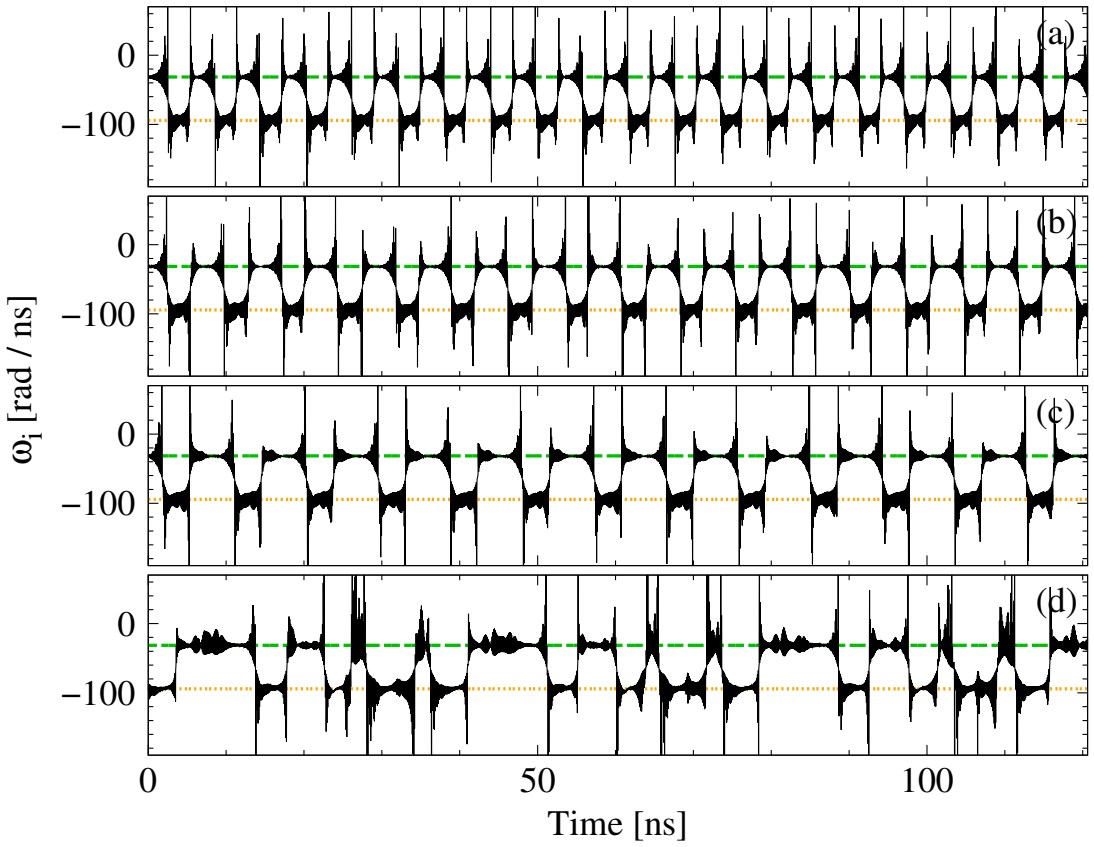


**Figure 8.15:** Instantaneous optical angular frequency of the electric field for $I/I_{\mathrm{th}} = 0.99$, $\tau_1 = 30\,\mathrm{ns}$, and different values of $\tau_2$: (a) $\tau_2 = 35\,\mathrm{ns}$, (b) $\tau_2 = 36\,\mathrm{ns}$, (c) $\tau_2 = 36.5\,\mathrm{ns}$, and (d) $\tau_2 = 37\,\mathrm{ns}$. The remaining parameters are the same as in Fig. 8.6.

Almost square-wave dynamics can also be found with a periodicity of the order of $\tau_2$, as shown in Fig. 8.16 for the same parameter values than Fig. 8.15 but $\tau_2 = 32\,\mathrm{ns}$.

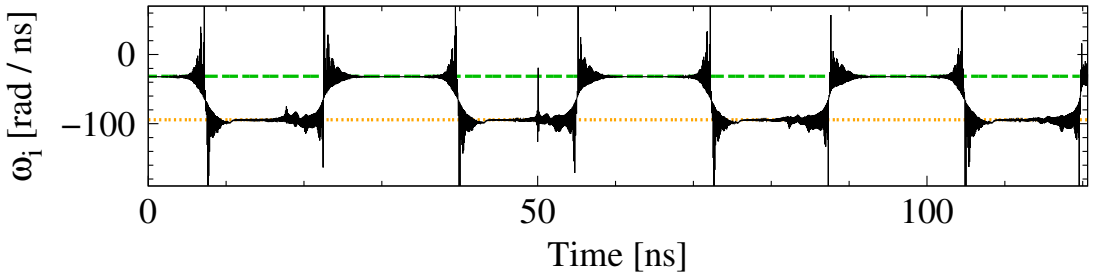


**Figure 8.16:** Instantaneous optical angular frequency of the electric field for $\tau_1 = 30\,\mathrm{ns}$, $\tau_2 = 32\,\mathrm{ns}$, $I/I_{\mathrm{th}} = 0.99$. The remaining parameters are the same as in Fig. 8.6.

Increasing the injection current, we also find regular switching but with a shorter periodicity. For instance, for $I/I_{\mathrm{th}} = 1.1$, $\tau_1 = 30\,\mathrm{ns}$, and the remaining parameters as in Fig. 8.15, we find a regular window close to $\tau_2 = 31.5\,\mathrm{ns}$, as shown in Fig. 8.17.

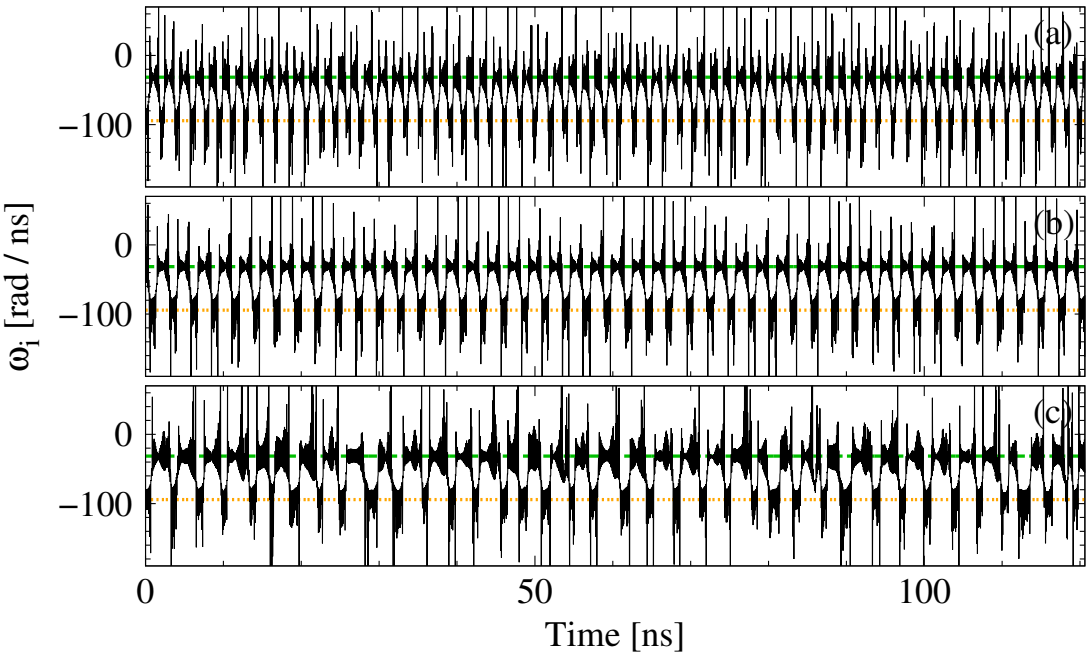


**Figure 8.17:** Instantaneous optical angular frequency of the electric field for $I/I_{\rm th} = 1.1$, $\tau_1 = 30\,$ns, and different values of $\tau_2$: (a) $\tau_2 = 31\,$ns, (b) $\tau_2 = 31.5\,$ns, and (c) $\tau_2 = 32\,$ns$\tau_1 = 30\,$ns. The remaining parameters are the same as in Fig. 8.6.

## 8.9 Switching characteristics

Experiments and numerics show the existence of different regimes where the dynamics can exhibit SDD. We now aim to further characterize the switchings between the different values of the delay time. To do so, we first compute the residence times, and then analyse their regularity and probability distributions. The residence times have been obtained from the contrast function computed for 195 s long time series averaged over windows of 0.1 ns. The experimental time series have been low-pass filtered with a cutoff frequency of 1 GHz with the aim to remove the fastest noisy oscillations, which are unrelated to switches in delay states.

The regularity in the dynamics can be characterized from the sequential distributions of the residence times, namely by plotting each residence time with a given delay time value, $T_{i+1}(\tau_j)$, as a function of the previous residence time with the same delay time value, $T_i(\tau_j)$. Examples of such plots in the regular and irregular regimes obtained from numerical simulations are shown in Figs. 8.18 and 8.19, respectively. In the regular almost square-wave switching regime, the residence times are organized in compact regions in the diagrams $T_{i+1}(\tau_j)$ *vs* $T_i(\tau_j)$, as shown in Fig. 8.18 for $\tau_1 = 30\,$ns, $\tau_2 = 36\,$ns [(a), (d)], and $\tau_2 = 36.5\,$ns [(b), (e)]. Changing the delay times, the switching becomes less regular and there is a diagonal line in the diagrams, as it it can be seen in Fig. 8.18 [(c), (f)] for $\tau_1 = 30\,$ns and $\tau_2 = 37\,$ns. This diagonal line is an indicator that there is still some regularity. Increasing the delay time values, as the dynamics gets irregular, the

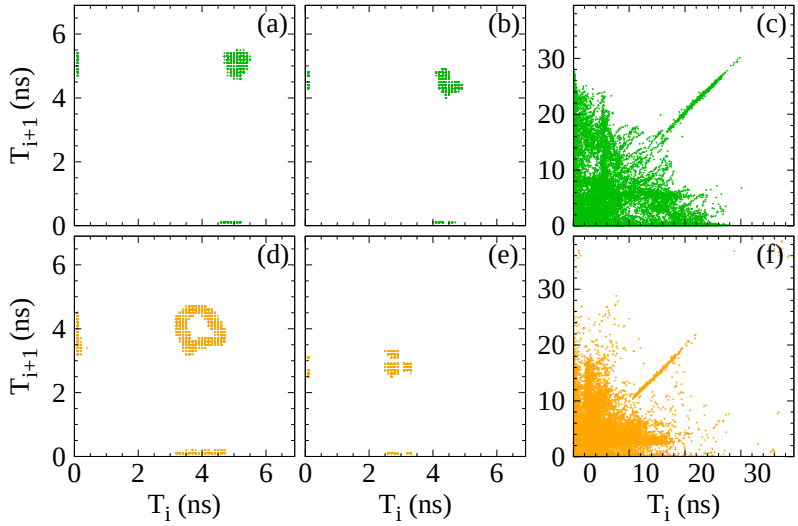


**Figure 8.18:** Numerical residence times $T_{i+1}(\tau_j)$ as function of $T_i(\tau_j)$ in filters 1 [(a)-(c)] and 2 [(d)-(f)] in the regular regime with $I/I_{\rm th} = 0.99$, $\tau_1 = 30\,$ns, and different values of $\tau_2$: [(a) and (d)] $\tau_2 = 36\,$ns, [(b) and (e)] $\tau_2 = 36.5\,$ns, and [(c) and (f)] $\tau_2 = 37\,$ns. The values of the remaining parameters are the same than in Fig. 8.6.

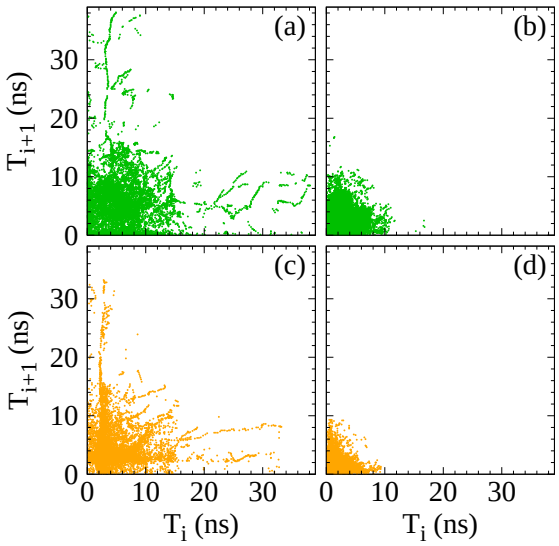


**Figure 8.19:** Numerical residence times $T_{i+1}(\tau_j)$ as function of $T_i(\tau_j)$ in filters 1 [(a)-(b)] and 2 [(c)-(d)] in the irregular regime with $\tau_1 = 106.075\,$ns and $\tau_2 = 121.625\,$ns for $I/I_{\rm th} = 0.99$ [(a) and (c)] and $I/I_{\rm th} = 1.1$ [(b) and (d)]. The values of the remaining parameters are the same than in Fig. 8.6.

diagrams $T_{i+1}(\tau_j)$ *vs* $T_i(\tau_j)$ don't have either compact regions or diagonal lines, as it can be seen in the example of Fig. 8.19 for $\tau_1 = 106.075\,$ns and $\tau_2 = 121.625\,$ns.

In Figs. 8.18 and 8.19, we can see that the time intervals $T_i(\tau_1)$ and $T_i(\tau_2)$ during which the delay time takes respective values $\tau_1$ and $\tau_2$ are always shorter than the delay time. Additional insights imply a detailed characterization of the switching statistics.

Examples of experimental and numerical residence-time distributions in the irregular switching regime are shown in Fig. 8.20 for two different values of the pump current, corresponding to $I = 1.0I_{\rm th}$ and $I = 1.1I_{\rm th}$.

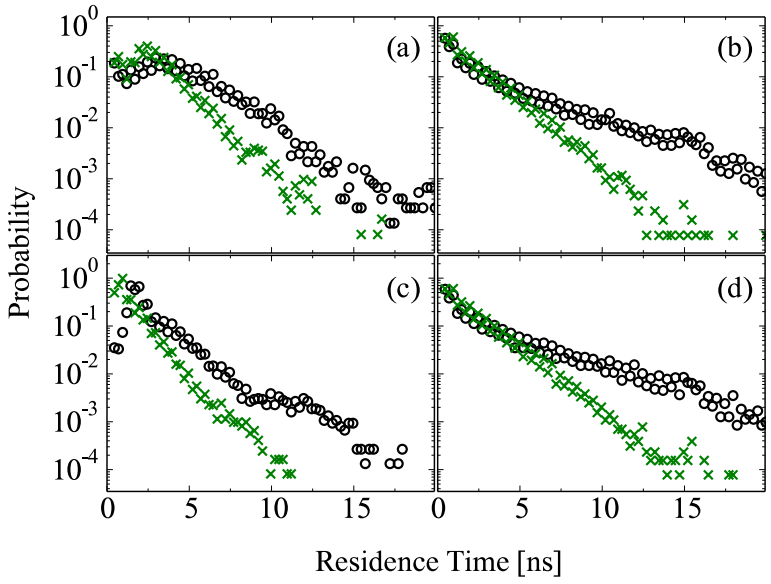


**Figure 8.20:** Numerical, (a) and (c), and experimental, (b) and (d), residence-time distributions in the states corresponding to the two delay-time values $\tau = \tau_1 = 106.075\,\text{ns}$ and $\tau = \tau_2 = 121.625$ ns. Dots correspond to $I = 1.0I_{\rm th}$ and crosses to $I = 1.1I_{\rm th}$. Other parameters as in Fig. 8.7. Panels (a) and (b) show the residence times with $\tau = \tau_1$ while (c) and (d) correspond to filter state with $\tau = \tau_2$. Figure reproduced from [10].

In Fig. 8.20, it can be seen that the residence-time distributions show maximum residence times on fast time scales of few nanoseconds or less. Moreover, the residence-time distributions exhibit almost exponential tails that decay for times smaller than 20ns. Two conclusions can be drawn from the comparison of experiment and numerics: first, the residence times are typically smaller than the difference between the two values of the delay time; and second, the lower the bias current the higher the typical residence times that the system exhibits. This can be understood by considering that the switches between the two filter states, corresponding to the two different values of the delay time, can have two possible origins: they can either occur spontaneously because of the dynamics within one filter state, or be induced by a previous filter jump being fed back into the laser. With a significant probability, such perturbations will make change the filter state and therefore the delay. Due to Eq. (8.1), the induced events take place with intervals smaller than the larger delay time and even smaller than the difference in delay times. Spontaneous jumps turn out to be much less frequent. In spite of the difference in filter shapes, the residence-time distributions have a similar decay in numerics and experiment. A deeper understanding of the residence-time distributions and their dependence on the different system parameters is left for future investigations.

## 8.10 Final discussion

We have studied a semiconductor laser system with frequency-selective feedback from two different cavities, as prototypical to understand SDD dynamics. We note that SDD dynamics has a different nature than the dynamics arising in systems with time dependent delays. In the latter ones, the delay time is externally modulated [195]; while in the former ones, the effective delay is intrinsically determined by the state of the system which, in turn, depends on the delay time value which is active at each time. Therefore, in SDD systems, the changes in delay times emerge in a self-organised fashion. In our system, the delay time switches between two different values, in such a way that the delay-time value at a any time is determined by the state of the system.

The two delay-time values have been implemented as two fibre delay loops of different length, each containing a frequency-selective Bragg filter centered at a different frequency. Therefore, the frequency of the optical field, that is associated to the state of the system, determines which delay-time value is active at any time. In this system, the SDD dynamics results from the interplay between the laser bandwidth and the spectral parameters of the filters. The two filters must slightly overlap in order to interact with each other. Nevertheless, the overlap between the filters has to be sufficiently small in order to clearly distinguish the two states. From a theoretical point of view, this means that the stationary rotating wave states (FCMs) of the system are located in two separated regions in phase space. The FCMs in each region are similar to those that appear in a semiconductor laser with a single delayed feedback.

SDD dynamics has been found close to the laser emission threshold when the delay times are chosen such that the longer delay corresponds to the more detuned filter. We have shown that the relative intensity difference or filter contrast is a suitable quantifier to identify SDD dynamics. We observe the existence of time intervals in which the feedback is mainly coming from one of the two filters. From a theoretical point of view, these time intervals of feedback from a single filter are associated to trajectories in phase space which remain around the FCMs corresponding to a given delay loop. The observation of SDD dynamics requires that the jumps between the regions in phase space associated to the two delay loops do not take place too frequently. Increasing the pump leads to more frequent jumps, and for high enough injection current the dynamics mixes the two states of the system. In this case, experimentally one sees a significant amount of feedback coming simultaneously from both delay loops.

Although this system belongs to a conceptually simple class of SDD systems in which the delay time can take only two discrete values, its flexibility allows for a detailed experimental and theoretical exploration of SDD systems and their possible applications. Our system represents a well-controllable and reconfigurable platform built from standard telecom components in which the dynamics can be precisely measured. Therefore, our approach represents a prototypical study of SDD dynamics. In fact, it opens major opportunities to investigate different implementations and classes of SDD systems. One can, for instance, reverse the order of the filters or increase the number of them. Another possibility would be the extension from discrete to continuous delay, for instance

by using continuously chirped Fiber Bragg gratings, with either positive or negative chirp. For most of these situations, there exist mathematical models that allow to fit the system in an appropriate general background. Finally, a more precise correspondence between experiment and modelling could be obtained by considering a travelling wave model, which would allow us to better mimick the FFB filter characteristics.

Direct characterization of the SDD dynamics in systems with controllable parameters is relevant in a variety of scientific fields well behond optics. For instance, SDDs play a crucial role in the dynamics of age-structured biological or physiological processes such as erythropoiesis [196, 197] and state-dependent population growth [198, 199]. But also technological applications exploiting the self-organized erratic switching between different delay states can be envisaged. In particular, control and encryption systems could benefit from such switching. Recently, key exchange protocols that utilise the synchronisation of delay-coupled systems [200, 201] have been introduced. For some of them, the irregular switching regime has been suggested to enhance security [201]. Irregular jumps between states induced by SDD dynamics could play this role without the need of externally controlled switching. For control systems, the self-organised switching between different loops performing different transformations provides new possibilities. One could, for instance, implement specific control loops for multiple possible states or different control loops depending on the distance from a target state.

# Part IV

# Summary and future work

Chapter 9

# Summary and future work on part II

We have theoretically and numerically studied the dynamics of two delay-coupled optoelectronic loops subject to delayed feedback. Synchronized square waves originate from Hopf instabilities of the steady state and multiple harmonics coexist, even if the OEOs are different.

For both OEOs with negative feedback, the square waves have a symmetric duty cycle and arise supercritically, synchronized in phase if the ratio $s_0$ between self- and cross-delay times is an odd/odd rational, and out-of-phase if $s_0$ is an odd/even rational.

For both OEOs with positive feedback, the square waves have an asymmetric duty cycle and are born subcritically. In this case, for $s_0$ rational with an odd numerator, square waves are in phase; while if the numerator is even, both in- and out-of-phase square waves coexist. Increasing the pump, subcritical asymmetric square waves are also found beyond the parameter regions where they are born, including regions of negative feedback.

The square waves born at positive feedback are more robust and flexible with respect to parameter changes than those born with negative feedback: by changing the feedback phase, the square waves with a symmetric duty cycle undergo a period doubling route to chaos, whereas those with asymmetric duty cycle mantain their period by adapting their shape in response to changes of the offset phase. In addition, for positive feedback, besides the fast square-wave oscillations, which for typical parameter values are at nanosecond time scale, there are in-phase microsecond periodic solutions for which the period and the asymmetry can also be tuned with the offset phase. Concerning robustness to mismatch in the delay times with respect to the ideal ratio, the square waves with negative feedback develop secondary plateaus whereas those with positive feedback don't. The mechanism leading to the formation of this secondary plateaus is still an open question.

Besides in- and out-of-phase synchronization, delay-coupled oscillators subject to mixed feedback, namely positive for one OEO and negative for the other one, can generate stable synchronized square waves dephased by a quarter of the period ($T/4$ solutions). These $T/4$ square waves exist for a broad range of parameter values and are robust to small mismatches in the delay times.

## CHAPTER 9. SUMMARY AND FUTURE WORK ON PART II

We have derived analytical expressions for the period of the solutions. For identical oscillators, both for positive and negative feedback, we have also obtained approximate maps for the amplitude of the square-wave oscillations. The maps turn out to be same for in-phase and out-of-phase solutions. In addition, for the positive feedback case, the map also allows to determine the asymmetry of the duty cycle. For negative feedback, we have also obtained a more general map to predict the secondary instabilities of the periodic square waves. The map derivation for the square-waves synchronized at a quarter of the period is left for future investigations.

A detailed analysis of the period of the solutions using Poincaré sections shows that the square waves can undergo a splitting in the duration of the period. For the fundamental square wave, the splitting only arises in the negative feedback case and if there is a sufficienly large mismatch in the delay-times ratio with respect to a rational ratio. The higher harmonics show a temporal splitting for both positive and negative feedback, even in the case of perfect matching, although the differences in the duration of the periods are enhanced by mismatch in the delay-times ratio. For negative feedback and for sufficiently large mismatch, higher harmonics undergo a secondary splitting. This secondary splitting does not happen for positive feedback. In all the cases, we have found that the number of different values for the period is determined by the rational fraction $s_0$ and the order of the harmonic. The origin of the splitting seems to be related to the asymmetry between the rising and falling edges of the square waves; however, the precise mechanism leading to the splitting has not been determined. The theoretical analysis of this phenomenon is left for future investigations.

Altogether this system displays a very large degree of flexibility allowing for instance to select the period of the square waves without changing parameters by choosing a suitable initial condition, to tune the duty cycle while keeping the period constant by changing the offset phase or the pump level, and to tune the dephasing between the synchronized square waves by changing the offset phases or the delay times. The rich dynamics of the system allows for the coexistence of multiple stable periodic solutions synchronized in-, out-of-phase, or at a quarter of the period, or with two kinds of synchronization (in- and out-of-phase, or $T/4$ and in-phase, or $T/4$ and out-of-phase) with different periods for the same values of the parameters. Such a system turns out to be interesting for applications such as information encoding, which benefits from high-frequency oscillations of controllable period. The theoretical predictions have been confirmed with numerical simulations of the full dynamical model and bifurcation diagrams obtained with continuation techniques. The methodology and results presented here can be generalized to other systems composed by several oscillators subject to negative, positive or mixed feedback.

Future possible investigations with this system include the map derivation for the square-waves synchronized at a quarter of the period, the analytical demonstration of the splitting of the period in different intervals, and the experimental demonstration of the analytical and numerical results. Finally, it would be interesting to study the dynamics, robustness and resilience of systems involving a larger number of delay-coupled OEOs, from small motifs to networks of OEOs.

Chapter 10

# Summary and future work on part III

We have studied, from a theoretical point of view and in collaboration with experimentalists, the SDD dynamics in a prototypical system composed of a semiconductor laser with frequency-selective feedback from two different cavities. In this system, the delay time switches between two different values, and at any time it is determined by the state of the system. The two delay-time values have been implemented as two fibre delay loops of different lengths and center frequencies, in such a way that the frequency of the optical field determines the value of the delay time at any time. Since the SDD dynamics results from the interplay between the laser bandwidth and the spectral parameters of the filters, it requires the two filters to slightly overlap spectrally in order to interact with each other, but not too much in order to clearly distinguish the two states.

SDD dynamics has been found close to the laser emission threshold in the case where the longer delay corresponds to the more detuned filter. We observe the existence of time intervals in which the feedback is mainly coming from one of the two filters. These time intervals are associated to trajectories in phase space which remain around the filtered cavity modes corresponding to a given delay loop. Increasing the pump leads to more frequent jumps, and for high enough injection current the two states get mixed in the dynamics.

Such a system represents a well-controllable and reconfigurable platform in which the dynamics can be precisely measured. Its flexibility allows for a detailed experimental and theoretical exploration of other SDD systems and their possible applications. Besides the fundamental interest that the study of such SDD system has, the self-organized erratic switching between different delay-time values could be exploited in technological applications, for instance to enhance security without the need of externally controlled switching in control and encryption protocols.

Future extensions of our system include reversing the order of the filters, increasing the number of them, and considering a continuous delay. From a theoretical point of view, the physical mechanism at the onset of SDD dynamics in this system is still unknown. In collaboration with Prof. Thomas Erneux, we are currently working on this topic. Preliminary results with smaller delay times changing one of the feedback strengths while keeping constant the other one indicate that a possible mechanism for the origin of SDD dynamics is the appearance of high-frequency solutions or bridges connecting

ECMs corresponding to different filters. To simplify the analysis, we are also working with a two-mode model in the limit of narrow filter widths in which the two filters become independent. Finally, a more precise correspondence between experiment and modelling could be obtained by considering a travelling wave model, which could better mimick the FFB filter characteristics.

# Bibliography


[1] T. Heil, I. Fischer, and W. Elsä er, Stabilization of feedback-induced instabilities in semiconductor lasers, *J. of Optics B: Quantum and Semiclassical Optics*, vol. 2, pp. 413 420, 2000.

[2] T. Heil, I. Fischer, W. Elsä er, and A. Gavrielides, Dynamics of semiconductor lasers subject to delayed optical feedback: The short cavity regime, *Phys. Rev. Lett.*, vol. 87, p. 243901, 2001.

[3] M. L. Huber, R. A. Perkins, A. Laesecke, D. G. Friend, J. V. Sengers, M. J. Assael, I. N. Metaxa, E. Vogel, R. Mare , and K. Miyagawa, New international formulation for the viscosity of h2o, *Journal of Physical and Chemical Reference Data*, vol. 38, pp. 101 125, 2009.

[4] `http://www.viscopedia.com/viscosity-tables/substances/water/#c2269`.

[5] `http://ddbonline.ddbst.de/VogelCalculation/VogelCalculationCGI.exe`.

[6] K. Ikeda and K. Matsumoto, High-dimensional chaotic behavior in systems with time-delayed feedback, *Physica D*, vol. 29, pp. 223 235, 1987.

[7] A. Gavrielides, T. Erneux, D. W. Sukow, G. Burner, T. McLachlan, J. Miller, and J. Amonette, Square-wave self-modulation in diode lasers with polarization-rotated optical feedback, *Opt. Lett.*, vol. 31, pp. 2006 2008, 2006.

[8] L. Weicker, T. Erneux, D. P. Rosin, and D. J. Gauthier, Multirhythmicity in an optoelectronic oscillator with large delay, *Phys. Rev. E*, vol. 91, p. 012910, 2015.

[9] T. Yoshida, L. E. Jones, S. P. Ellner, G. F. Fussmann, and N. G. H. Jr, Rapid evolution drives ecological dynamics in a predator prey system, vol. 424, pp. 303 306, 2003.

[10] J. Martínez-Llinàs, X. Porte, M. C. Soriano, P. Colet, and I. Fischer, Dynamical properties induced by state-dependent delays in photonic systems, *Nature Communications*, vol. 6, p. 8425, 2015.

[11] T. Erneux, Introduction, in *Applied Delay Di erential Equations*, vol. 3, pp. 1 27, New York: Springer, 2009.

[12] M. Kalecki, A macrodynamic theory of business cycles, *Econometrica*, vol. 3, pp. 327 344, 1935.

[13] R. Haberman, *Mathematical models*. Prentice-Hall, Englewood Cliffs, New Jersey, 1977; reprinted by SIAM, Philadelfia (1998).

[14] M. Brackstone and M. McDonald, Car-following: a historical review, *Transportation Research Part F: Tra c Psychology and Behaviour*, vol. 2, pp. 181 196, 1999.

[15] S. Logghe and L. Immers, Multi-class kinematic wave theory of traffic flow, *Transportation Research Part B: Methodological*, vol. 42, pp. 523 541, 2008.

[16] A. Soh, M. Marhaban, M. Khalid, and R. Yusof, Modelling and optimisation of a traffic intersection based on queue theory and markov decision control methods, in *Modelling Simulation, 2007. AMS 07. First Asia International Conference on*, pp. 478 483, 2007.

[17] P. Fleurquin, J. J. Ramasco, and V. M. Eguiluz, Systemic delay propagation in the US airport network, *Scienti c Reports*, vol. 3, p. 1159, 2013.

[18] G. E. Hutchinson, Circular causal systems in ecology, *Annals of the New York Academy of Sciences*, vol. 50, pp. 221 246, 1948.

[19] T. Faria, Stability and bifurcation for a delayed predator prey model and the effect of diffusion, *J. of Mathematical Analysis and Applications*, vol. 254, pp. 433 463, 2001.

[20] I. Fischer, G. H. M. van Tartwijk, A. M. Levine, W. Elsässer, E. Göbel, and D. Lenstra, Fast pulsing and chaotic itinerancy with a drift in the coherence collapse of semiconductor lasers, *Phys. Rev. Lett.*, vol. 76, pp. 220 223, 1996.

[21] G. H. M. van Tartwijk and D. Lenstra, Semiconductor lasers with optical injection and feedback, *Quantum and Semiclassical Optics: J. of the European Optical Society Part B*, vol. 7, p. 87, 1995.

[22] J. D. Murray, A. Bernacchia, D. J. Freedman, R. Romo, J. D. Wallis, X. Cai, C. Padoa-Schioppa, T. Pasternak, H. Seo, D. Lee, and X.-J. Wang, A hierarchy of intrinsic timescales across primate cortex, *Nat Neurosci*, vol. 17, p. 1661 1663, 2014.

[23] H. Eichenbaum, Time cells in the hippocampus: a new dimension for mapping memories, *Nat Rev Neurosci*, vol. 15, p. 732 744, 2014.

[24] L. Appeltant, *Reservoir Computing Based On Delay-Dynamical Systems. PhD Thesis*. Vrije Universiteit Brussel, Universitat de les Illes Balears, 2012.

[25] S. D. Poisson, Sur les équations aux différences melées, *J. de l École Royal Polytech.*, vol. 6(13), pp. 126 147, 1806.

[26] H. O. Walther, On Poisson's state dependent delay, *Discret Contin. Dyn. Syst.,Ser A*, vol. 33, pp. 365 379, 2013.

[27] H. O. Walther, Stable periodic motion of a system using echo for position control, *J. Dynamics and Di erential Equations*, vol. 15, no. 1, pp. 143 223, 2003.

[28] R. D. Driver, A "backwards" two-body problem of classical relativistic electrodynamics, *Phys. Rev.*, vol. 178, pp. 2051 2057, 1969.

[29] R. D. Driver, A neutral system with state dependent delay, *J. Di er. Equ.*, vol. 54, pp. 73 86, 1984.

[30] J. A. Wheeler and R. P. Feynman, Interaction with the absorber as the mechanism of radiation, *Rev. Mod. Phys.*, vol. 17, p. 157, 1945.

[31] J. A. Wheeler and R. P. Feynman, Classical electrodynamics in terms of direct interparticle action, *Rev. Mod. Phys.*, vol. 21, pp. 425 433, 1949.

[32] T. Insperger, T. Stepan, and J. Turi, State-dependent delay model for regenerative cutting processes, *Proc.of the Fifth EUROMECH Nonlinear Dynamics Conf.,Eindhoven, The Netherlands*, pp. 1124 1129, 2005.

[33] R. D. Driver, Linear differential systems with small delays, *J. Di er. Equ.*, vol. 21, pp. 148 166, 1976.

[34] A. D. Mishkis, General theory of differential equations with retarded arguments, *Uspekhi Mat. Nauk*, vol. 4, pp. 99 141, 1949.

[35] R. E. Bellman and J. M. Danskin, *A Survey of the Mathematical Theory of Time Lag, Retarded Control, and Hereditary Processes.* 1954.

[36] R. E. Bellman and K. Cooke, *Di erential-Di erence Equations.* New York: Academic Press, 1963.

[37] A. Krasovskii, *Stability of Motion Translation.* Stanford, CA: Stanford University Press, 1963.

[38] J. Hale, *Theory of functional di erential equations.* Springer Verlag, New York, 1977.

[39] B. Bolarinwa, R. A. Ademiluyi, A. P. Oluwagunwa, and B. O. Awomuse, Scheme for solving ordinary differential equations with derivative discontinuities: A new class of semi- implicit rational, runge-kutta., *African Journal of Mathematics and Computer Science Research*, vol. 5, pp. 193 199, 2012.

[40] C. Paul, *The Treatment of Derivative Discontinuities in Di erential Equations.* University of Manchester, 1999.

[41] L. F. Shampine and S. Thompson, Solving delay differential equations with dde23, *Appl. Numer. Math*, pp. 441 458, 2001.

[42] Z. Qing-Chang, *Robust Control of Time-delay Systems*. Springer-Verlag London, 2006.

[43] M. L. Ferreira Nascimento and C. Aparicio, Viscosity of strong and fragile glass-forming liquids investigated by means of principal component analysis, *Journal of Physics and Chemistry of Solids*, vol. 68, pp. 104 110, 2007.

[44] A. Messaâdi, N. Dhouibi, H. Hamda, F. B. M. Belgacem, Y. H. Adbelkader, N. Ourfelli, and A. H. Hamzaoui, A new equation relating the viscosity arrhenius temperature and the activation energy for some newtonian classical solvents, *Journal of Chemistry*, vol. 2015, pp. pp. 1 12, 2015.

[45] K. Ikeda, Multiple-valued stationary state and its instability of the transmitted light by a ring cavity system, *Opt. Comm.*, vol. 30, pp. 257 261, 1979.

[46] K. Ikeda, H. Daido, and O. Akimoto, Optical turbulence: chaotic behavior of transmitted light from a ring cavity, *Phys. Rev. Lett.*, vol. 45, pp. 709 712, 1980.

[47] K. Ikeda, K. Kondo, and O. Akimoto, Successive higher-harmonic bifurcations in systems with delayed feedback, *Phys. Rev. Lett.*, vol. 49, pp. 1467 1470, 1982.

[48] T. Aida and P. Davis, Oscillation modes of laser diode pumped hybrid bistable system with large delay and application to dynamical memory, *IEEE J. Quantum Electronics*, vol. 28, pp. 686 699, 1992.

[49] T. Aida and P. Davis, Oscillation mode selection using bifurcation of chaotic mode transitions in a nonlinear ring resonator, *IEEE J. Quantum Electronics*, vol. 30, pp. 2986 2997, 1994.

[50] G. Giacomelli and A. Politi, Relationship between delayed and spatially extended dynamical systems, *Phys. Rev. Lett.*, vol. 76, pp. 2686 2689, 1996.

[51] G. Giacomelli, F. Marino, M. A. Zaks, and S. Yanchuk, Coarsening in a bistable system with long-delayed feedback, *EPL (Europhysics Letters)*, vol. 99, p. 58005, 2012.

[52] B. Sartorius, C. Bornholdt, O. Brox, H. Ehrke, D. Hoffmann, R. Ludwig, and M. Mohrle, All-optical clock recovery module based on self-pulsating dfb laser, *Electronics Letters*, vol. 34, pp. 1664 1665, 1998.

[53] S. Ura, S. Shoda, K. Nishio, and Y. Awatsuji, In-line rotation sensor based on VCSEL behavior under polarization-rotating optical feedback, *Opt. Express*, vol. 19, pp. 223688 236833, 2011.

[54] D. W. Sukow, A. Gavrielides, T. Erneux, B. Mooneyham, K. Lee, J. McKay, and J. Davis, Asymmetric square waves in mutually coupled semiconductor lasers with orthogonal optical injection, *Phys. Rev. E*, vol. 81, p. 025206(R), 2010.

[55] C. Masoller, D. Sukow, A. Gavrielides, and M. Sciamanna, Bifurcation to square-wave switching in orthogonally delay-coupled semiconductor lasers: Theory and experiment, *Phys. Rev. A*, vol. 84, p. 23838, 2011.

[56] E. A. Viktorov, A. M. Yacomotti, and P. Mandel, Semiconductor lasers coupled face-to-face, *J. Opt. B: Quantum Semiclass. Opt.*, vol. 6, pp. L9 L12, 2004.

[57] J. Mulet, M. Giudici, J. Javaloyes, and S. Balle, Square-wave switching by crossed-polarization gain modulation in vertical-cavity semiconductor lasers, *Phys. Rev. A*, vol. 76, p. 43801, 2007.

[58] L. Mashal, G. V. d. Sande, L. Gelens, J. Danckaert, and G. Verschaffelt, Square-wave oscillations in semiconductor ring lasers with delayed optical feedback, *Opt. Express*, vol. 20, pp. 22503 22516, 2012.

[59] X. Zhang, C. Gu, G. Chen, B. Sun, L. Xu, A. Wang, and H. Ming, Square-wave pulse with ultra-wide tuning range in a passively mode-locked fiber laser, *Opt. Lett.*, vol. 37, pp. 1334 1336, 2012.

[60] M. Marconi, J. Javaloyes, S. Barland, M. Giudici, and S. Balle, Robust square-wave polarization switching in vertical-cavity surface-emitting lasers, *Phys. Rev. A*, vol. 87, p. 13827, 2013.

[61] Y. C. Kouomou, P. Colet, L. Larger, and N. Gastaud, Chaotic breathers in delayed electro-optical systems, *Phys. Rev. Lett.*, vol. 95, p. 203903, 2005.

[62] L. Weicker, T. Erneux, O. D'Huys, J. Danckaert, M. Jacquot, Y. Chembo, and L. Larger, Strongly asymmetric square waves in a time-delayed system, *Phys. Rev. E*, vol. 86, p. 055201(R), 2012.

[63] L. Weicker, T. Erneux, O. D'Huys, J. Danckaert, M. Jacquot, Y. Chembo, and L. Larger, Slow fast dynamics of a time-delayed electro-optic oscillator, *Phil. Trans. R. Soc. A*, vol. 371, p. 20120459, 2013.

[64] L. Mei, G. Chen, L. Xu, X. Zhang, B. S. C. Gu, and A. Wang, Width and amplitude tunable square-wave pulse in dual-pump passively mode-locked fiber laser, *Opt. Lett.*, vol. 39, pp. 3235 3237, 2014.

[65] W. H. Loh, Y. Ozeki, and C. L. Tang, High-frequency polarization self-modulation and chaotic phenomena in external cavity semiconductor lasers, *Applied Physics Letters*, vol. 56, 1990.

[66] G. Friart, L. Weicker, and J. Danckaert, Relaxation and square-wave oscillations in a semiconductor laser with polarization rotated optical feedback, vol. 22, pp. 3545 3547, 2014.

[67] J. C. Maxwell, On governors, *Proceedings of the Royal Society of London*, vol. 16, pp. pp. 270 283, 1868.

[68] R. Vicente, *Nonlinear Dynamics and Synchronization of Bidirectionally Coupled Semiconductor Lasers*. Universitat de les Illes Balears, 2006.

[69] T. S. Parker and L. O. Chua, *Practical Numerical Algorithms for Chaotic Systems*. Springer New York, 1989.

[70] S. H. Strogatz, *Nonlinear dynamics and chaos: with applications to Physics, Biology, Chemistry, and Engineering.* Perseus Books Publishing, New York, 1994.

[71] E. Hopf, Abzweigung einer periodischen Lösung von einer stationären Lösung eines Differentialsystems, *Berichte Math.-Phyis. Kl. Sächs. Akad. Wiss. Leipzig*, vol. 94, pp. 3 32, 1942. A translation of this paper can be found in: J.E. Marsden and M. McCraken, "The Hopf fiburcation and its applications", *Appl. Math. Sci.* **19**, Springer-Verlag, New York, 1976.

[72] Y. A. Kuznetsov, *Elements of Applied Bifurcation Theory. Second Edition.* New York: Springer-Verlag, 1998.

[73] M. Henon, On the numerical computation of Poincaré maps, *Physica D: Nonlinear Phenomena*, vol. 5, pp. 412 414, 1982.

[74] K. Engelborghs, T. Luzyanina, and D. Roose, Numerical bifurcation analysis of delay-differential equations using DDE-BIFTOOL, *ACM Trans. Math. Softw.*, vol. 28, pp. 1 21, 2002.

[75] J. Sieber, K. Engelborghs, T. Luzyanina, G. Samaey, and D. Roose, DDE-BIFTOOL v. 3.0 Manual - Bifurcation analysis of delay differential equations, *arXiv:1406.7144*, 2015.

[76] B. Wage, *Normal form computations for delay di erential equations in DDE-BIFTOOL. Master s thesis.* Utrecht University (NL).

[77] K. Engelborghs, T. Luzyanina, and G. Samaey, Technical Report TW-330, *Department of Computer Science, K.U. Leuven.*

[78] B. E. A. Saleh and J. Wiley, *Fundamentals of Photonics, Second Edition.* Wiley-Interscience, 2nd ed ed., 2007.

[79] R. Gray, The rev. john kerr, f.r.s., inventor of the kerr cell, *Nature*, vol. 136, pp. 245 247, 1935.

[80] P. Weinberger, John kerr and his effects found in 1877 and 1878, *Philosophical Magazine Letters*, vol. 88, pp. 897 907, 2008.

[81] P. A. Franken, A. E. Hill, C. W. Peters, and G. Weinreich, Generation of optical harmonics, *Phys. Rev. Lett.*, vol. 7, pp. 118 119, 1961.

[82] T. H. Maiman, Stimulated Optical Radiation in Ruby, *Nature*, vol. 187, pp. 493 494, 1960.

[83] E. Wooten, K. Kissa, A. Yi-Yan, E. Murphy, D. Lafaw, P. Hallemeier, D. Maack, D. Attanasio, D. Fritz, G. McBrien, and D. Bossi, A review of lithium niobate modulators for fiber-optic communications systems, *IEEE J. Selected Topics in Quantum Electronics*, vol. 6, no. 1, pp. 69 82, 2000.

[84] S. Kasap, *Optoelectronics and Photonics: Principles and Practices, Second Edition.* Pearson Education, 2nd ed ed., 2013.

[85] A. Neyer and E. Voges, High [U+2010] frequency electro [U+2010] optic oscillator using an integrated interferometer, *Applied Physics Letters*, vol. 40, pp. 6 8, 1982.

[86] M. F. Lewis, Novel rf oscillator using optical components, *Electronics Letters*, vol. 28, no. 1, pp. 31 32, 1992.

[87] X. S. Yao and L. Maleki, Optoelectronic microwave oscillator, *J. Opt. Soc. Am. B*, vol. 13, pp. 1725 1735, 1996.

[88] X. S. Yao and L. Maleki, Optoelectronic oscillator for photonic systems, *IEEE J. of Quantum Electronics*, vol. 32, pp. 1141 1149, 1996.

[89] K. Saleh, R. Henriet, S. Diallo, G. Lin, R. Martinenghi, I. V. Balakireva, P. Salzenstein, A. Coillet, and Y. K. Chembo, Phase noise performance comparison between optoelectronic oscillators based on optical delay lines and whispering gallery mode resonators, *Opt. Express*, vol. 22, pp. 32158 32173, 2014.

[90] E. Salik, N. Yu, and L. Maleki, An ultralow phase noise coupled optoelectronic oscillator, *Photonics Technology Letters, IEEE*, vol. 19, no. 6, pp. 444 446, 2007.

[91] H. K. Sung, X. Zhao, E. K. Lau, D. Parekh, C. J. Chang-Hasnain, and M. C. Wu, Optoelectronic oscillators using direct-modulated semiconductor lasers under strong optical injection, *IEEE J. Selected Topics in Quantum Electronics*, vol. 15, no. 3, pp. 572 577, 2009.

[92] P. Zhou, S. Pan, D. Zhu, R. Guo, F. Zhang, and Y. Zhao, A compact optoelectronic oscillator based on an electroabsorption modulated laser, *IEEE Photonics Technology Letters*, vol. 26, no. 1, pp. 86 88, 2014.

[93] D. Strekalov, D. Aveline, N. Yu, R. Thompson, A. B. Matsko, and L. Maleki, Stabilizing an optoelectronic microwave oscillator with photonic filters, *J. Lightwave Technology*, vol. 21, pp. 3052 3061, 2003.

[94] A. B. Matsko, L. Maleki, A. A. Savchenkov, and V. S. Ilchenko, Whispering gallery mode based optoelectronic microwave oscillator, *Journal of Modern Optics*, vol. 50, pp. 2523 2542, 2003.

[95] A. Coillet, R. Henriet, P. Salzenstein, K. P. Huy, L. Larger, and Y. Chembo, Time-domain dynamics and stability analysis of optoelectronic oscillators based on whispering-gallery mode resonators, *IEEE J. Selected Topics in Quantum Electronics*, vol. 19, no. 5, pp. 1 12, 2013.

[96] K. Volyanskiy, P. Salzenstein, H. Tavernier, M. Pogurmirskiy, Y. K. Chembo, and L. Large, Compact optoelectronic microwave oscillators using ultra-high q whispering gallery mode disk-resonators and phase modulation, *Opt. Express*, vol. 18, pp. 22358 22363, 2010.

[97] X. S. Yao and L. Maleki, Multiloop optoelectronic oscillator, *IEEE J. Quantum Electronics*, vol. 36, no. 1, pp. 79 84, 2000.

[98] R. M. Nguimdo, Y. K. Chembo, P. Colet, and L. Larger, On the phase noise performance of nonlinear double-loop optoelectronic microwave oscillators, *IEEE J. Quantum Electronics*, vol. 48, pp. 1415 1423, 2012.

[99] S. García and I. Gasulla, Multi-cavity optoelectronic oscillators using multicore fibers, *Opt. Express*, vol. 23, pp. 2403 2415, 2015.

[100] J. P. Goedgebuer, P. Levy, L. Larger, C.-C. Chen, and W. T. Rhodes, Optical communication with synchronized hyperchaos generated electrooptically, *IEEE J. Quantum Electronics*, vol. 38, pp. 1178 1183, 2002.

[101] Y. C. Kouomo, *Nonlinear Dynamics of Semiconductor Laser Systems with Feedback: Applications to Optical Chaos Cryptography, Radar Frequency Generation, and Transverse Mode Control*. Universitat de les Illes Balears, 2006.

[102] Y. K. Chembo, L. Larger, and P. Colet, Nonlinear Dynamics and Spectral Stability of Optoelectronic Microwave Oscillators, *IEEE J. Quantum Electronics*, vol. 44, pp. 858 866, 2008.

[103] L. Larger and I. Fischer, *Optical delay dynamics and its applications, Chap.4, in The Complexity of Dynamical Systems*. 2011.

[104] M. Peil, M. Jacquot, Y. K. Chembo, L. Larger, and T. Erneux, Routes to chaos and multiple time scale dynamics in broadband bandpass nonlinear delay electrooptic oscillators, *Phys. Rev. E*, vol. 79, p. 26208, 2009.

[105] T. Erneux and P. Glorieux, *Laser Dynamics*. New York: Cambridge University Press, 2010.

[106] Y. K. Chembo, L. Larger, H. Tavernier, R. Bendoula, E. Rubiola, and P. Colet, Dynamic instabilities of microwaves generated with optoelectronic oscillators, *Opt. Lett.*, vol. 32, pp. 2571 2573, 2007.

[107] Y. Kouomou Chembo, L. Larger, R. Bendoula, and P. Colet, Effects of gain and bandwidth on the multimode behavior of optoelectronic microwave oscillators., *Optics express*, vol. 16, pp. 9067 72, 2008.

[108] G. R. G. Chengui, A. F. Talla, J. H. T. Mbé, A. Coillet, K. Saleh, L. Larger, P. Woafo, and Y. K. Chembo, Theoretical and experimental study of slow-scale hopf limit-cycles in laser-based wideband optoelectronic oscillators, vol. 31, pp. 2310 2316, 2014.

[109] J. H. Talla Mbé, A. F. Talla, G. R. G. Chengui, A. Coillet, L. Larger, P. Woafo, and Y. K. Chembo, Mixed-mode oscillations in slow-fast delayed optoelectronic systems, *Phys. Rev. E*, vol. 91, p. 012902, 2015.

[110] Y. K. Chembo, K. Volyanskiy, L. Larger, E. Rubiola, and P. Colet, Determination of Phase Noise Spectra in Optoelectronic Microwave Oscillators: A Langevin Approach, *IEEE J. Quantum Electronics*, vol. 45, pp. 178 186, 2009.

[111] J. Martínez-Llinàs, P. Colet, and T. Erneux, Tuning the period of square-wave oscillations for delay-coupled optoelectronic systems, *Phys. Rev. E*, vol. 89, p. 42908, 2014.

[112] J. Martínez-Llinàs, P. Colet, and T. Erneux, Synchronization of tunable asymmetric square-wave pulses in delay-coupled optoelectronic oscillators, *Phys. Rev. E*, vol. 91, p. 032911, 2015.

[113] J. Martínez-Llinàs and P. Colet, In-phase, out-of-phase and T/4 synchronization of square waves in delay-coupled non-identical optoelectronic oscillators, *Opt. Express*, vol. 23, pp. 24785 24799, 2015.

[114] J. P. Goedgebuer, L. Larger, and H. Porte, Optical cryptosystem based on synchronization of hyperchaos generated by a delayed feedback tunable laser diode, *Phys.Rev. Lett.*, vol. 80, pp. 2249 2252, 1998.

[115] L. Larger, J. P. Goedgebuer, and F. Delorme, An optical encryption system using hyperchaos generated by an optoelectronic wavelength oscillator, *Phys. Rev. E*, vol. 57, pp. 6618 6624, 1998.

[116] A. Argyris, D. Syvridis, L. Larger, V. Annovazzi-Lodi, P. Colet, I. Fischer, J. García-Ojalvo, C. R. Mirasso, L. Pesquera, and K. A. Shore, Chaos-based communications at high bit rates using commercial fiber-optic links, *Nature*, vol. 438, p. 343, 2005.

[117] L. Larger, M. C. Soriano, D. Brunner, L. Appeltant, J. M. Gutierrez, L. Pesquera, C. R. Mirasso, and I. Fischer, Photonic information processing beyond Turing: an optoelectronic implementation of reservoir computing, *Optics Express*, vol. 20, pp. 3241 3249, 2012.

[118] M. C. Soriano, S. Ortín, D. Brunner, L. L., M. C. R., I. Fischer, and L. Pesquera, Asymmetric square waves in mutually coupled semiconductor lasers with orthogonal optical injection, *Optics Express*, vol. 21, pp. 12 20, 2013.

[119] Z. Gao, Z. Wu, L. Cao, and G. Xia, Chaos synchronization of optoelectronic coupled semiconductor lasers ring, *Applied Physics B*, vol. 97, no. 3, pp. 645 651, 2009.

[120] A. Einstein, Zur quantentheorie der strahlung, *Phys. Z. A translation of the paper appears in: A. Engel "The Collected Papers of Albert Einstein", vol.* **6***, 434, Princeton U. Press, Princeton, NJ, 1997*, vol. 18, pp. 121 128, 1917.

[121] W. E. Lamb and R. C. Retherford, Fine structure of the hydrogen atom by a microwave method, *Phys. Rev.*, vol. 72, pp. 241 243, 1947.

[122] J. P. Gordon, H. J. Zeiger, and C. H. Townes, The maser-new type of microwave amplifier, frequency standard, and spectrometer, *Phys. Rev.*, vol. 99, pp. 1264 1274, 1955.

[123] A. L. Schawlow and C. H. Townes, Infrared and optical masers, *Phys. Rev.*, vol. 112, pp. 1940 1949, 1958.

[124] H. Kogelnik and T. Li, Laser beams and resonators, *Appl. Opt.*, vol. 5, pp. 1550 1567, 1966.

[125] G. Smith, P. C. Shardlow, and M. J. Damzen, High-power near-diffraction-limited solid-state amplified spontaneous emission laser devices, *Opt. Lett.*, vol. 32, pp. 1911 1913, 2007.

[126] R. H. Dicke, Coherence in spontaneous radiation processes, *Phys. Rev.*, vol. 93, pp. 99 110, 1954.

[127] D. A. G. Deacon, L. R. Elias, J. M. J. Madey, G. J. Ramian, H. A. Schwettman, and T. I. Smith, First operation of a free-electron laser, *Phys. Rev. Lett.*, vol. 38, pp. 892 894, 1977.

[128] J. M. J. Madey, Wilson prize article: From vacuum tubes to lasers and back again1, *Phys. Rev. ST Accel. Beams*, vol. 17, p. 074901, 2014.

[129] J. Neumann, Notes on the photon-disequilibrium-amplification scheme (JvN), september 16, 1953, *IEEE J. Quantum Electronics*, vol. 23, no. 6, pp. 659 673, 1987.

[130] R. N. Hall, G. E. Fenner, J. D. Kingsley, T. J. Soltys, and R. O. Carlson, Coherent light emission from GaAs junctions, *Phys. Rev. Lett.*, vol. 9, pp. 366 368, 1962.

[131] N. Holonyak and S. F. Bevacqua, Coherent (visible) light emission from Ga(As−xPx) junctions, *Applied Physics Letters*, vol. 1, pp. 82 83, 1962.

[132] M. I. Nathan, W. P. Dumke, G. Burns, F. H. Dill, and G. Lasher, Stimulated emission of radiation from GaAs p-n junctions, *Applied Physics Letters*, vol. 1, pp. 62 64, 1962.

[133] T. M. Quist, R. H. Rediker, R. J. Keyes, W. E. Krag, B. Lax, A. L. McWhorter, and H. J. Zeigler, Semiconductor maser of GaAs, *Applied Physics Letters*, vol. 1, pp. 91 92, 1962.

[134] G. P. Agrawal and N. K. Dutta, *Semiconductor lasers, 2nd edn.* New York: International Thomson Publishing, London, 1993.

[135] G. Grynberg, A. Aspect, and C. F., *Introduction to Quantum Optics. From the Semi-classical Approach to Quantized Light.* New York: Cambridge University Press, 2010.

[136] F. T. Arecchi, G. L. Lippi, G. P. Puccioni, and J. R. Tredicce, Deterministic chaos in laser with injected signal, *Optics Communications*, vol. 51, pp. 308 314, 1984.

[137] G. Agrawal and C. Bowden, Concept of linewidth enhancement factor in semiconductor lasers: its usefulness and limitations, *Photonics Technology Letters, IEEE*, vol. 5, no. 6, pp. 640 642, 1993.

[138] C. Henry, Theory of the linewidth of semiconductor lasers, *IEEE J. Quantum Electronics*, vol. 18, pp. 259 264, 1982.

[139] K. Lang, R.and Kobayashi, External optical feedback effects on semiconductor injection laser properties, *IEEE J. Quantum Electronics*, vol. 16, pp. 347 355, 1980.

[140] M. Wolfrum and D. Turaev, Instabilities of lasers with moderately delayed optical feedback, *Optics Communications*, vol. 212, pp. 127 138, 2002.

[141] D. Lenstra, Full Rate-Equation Description of Multi-mode Semiconductor Lasers, *IFISC Seminar*, 2013.

[142] H. Olesen, J. Osmundsen, and B. Tromborg, Nonlinear dynamics and spectral behavior for an external cavity laser, *IEEE J. Quantum Electronics*, vol. 22, no. 6, pp. 762 773, 1986.

[143] N. Schunk and K. Petermann, Numerical analysis of the feedback regimes for a single-mode semiconductor laser with external feedback, *IEEE J. Quantum Electronics*, vol. 24, no. 7, pp. 1242 1247, 1988.

[144] J. Mork and B. Tromborg, The mechanism of mode selection for an external cavity laser, *Photonics Technology Letters, IEEE*, vol. 2, no. 1, pp. 21 23, 1990.

[145] J. Mork, B. Tromborg, and P. L. Christiansen, Bistability and low-frequency fluctuations in semiconductor lasers with optical feedback: a theoretical analysis, *IEEE J. Quantum Electronics*, vol. 24, no. 2, pp. 123 133, 1988.

[146] T. Sano, Antimode dynamics and chaotic itinerancy in the coherence collapse of semiconductor lasers with optical feedback, *Phys. Rev. A*, vol. 50, pp. 2719 2726, 1994.

[147] G. Van Tartwijk, A. Levine, and D. Lenstra, Sisyphus effect in semiconductor lasers with optical feedback, *IEEE J. Selected Topics in Quantum Electronics*, vol. 1, no. 2, pp. 466 472, 1995.

[148] M. Yousefi and D. Lenstra, Rate-equation description of multi-mode semiconductor lasers, *Proc. SPIE 8980, Physics and Simulation of Optoelectronic Devices XXI*, p. 89800B, 2014.

[149] M. Yousefi and D. Lenstra, Dynamical Behavior of a Semiconductor Laser with Filtered External Optical Feedback, *IEEE J. Quantum Electronics*, vol. 35, pp. 970 976, 1999.

[150] I. Fischer, O. K. Andersen, M. Yousefi, S. Stolte, and D. Lenstra, Experimental and theoretical study of filtered optical feedback in semiconductor lasers, *IEEE J. Quantum Electronics*, vol. 36, pp. 375 384, 2000.

[151] A. P. A. Fischer, M. Yousefi, D. Lenstra, M. W. Carter, and G. Vemuri, Filtered optical feedback induced frequency dynamics in semiconductor lasers, *Phys. Rev. Lett.*, vol. 92, p. 023901, 2004.

[152] F. Rogister, D. W. Sukow, A. Gavrielides, P. Mégret, O. Deparis, and M. Blondel, Experimental demonstration of suppression of low-frequency fluctuations and stabilization of an external-cavity laser diode, *Opt. Lett.*, vol. 25, pp. 808 810, 2000.

[153] H. Yasaka and H. Kawaguchi, Linewidth reduction and optical frequency stabilization of a distributed feedback laser by incoherent optical negative feedback, *Applied Physics Letters*, vol. 53, pp. 1360 1362, 1988.

[154] E. Lacot, O. Hugon, and F. Stoeckel, Hopf amplification of frequency-shifted optical feedback, *Phys. Rev. A*, vol. 67, p. 053806, 2003.

[155] V. Rottschäfer and B. Krauskopf, The ECM-backbone of the Lang Kobayashi equations: A geometric picture, *International Journal of Bifurcation and Chaos*, vol. 17, pp. 1575 1588, 2007.

[156] T. Heil, I. Fischer, and W. Elsä er, Coexistence of low frequency fluctuations and stable emission on a single high-gain mode in semiconductor lasers with external optical feedback, *Phys. Rev. A*, vol. 58, 1997.

[157] T. Heil, I. Fischer, and W. Elsä er, Influence of amplitude-phase coupling on the dynamics of semiconductor lasers subject to optical feedback, *Phys. Rev. A*, vol. 60, pp. 634 641, 1999.

[158] K. Otsuka, Self-induced phase turbulence and chaotic itinerancy in coupled laser systems, *Phys. Rev. Lett.*, vol. 65, pp. 329 332, 1990.

[159] T. Sano, Antimode dynamics and chaotic itinerancy in the coherence collapse of semiconductor lasers with optical feedback, *Phys. Rev. A*, vol. 50, pp. 2719 2726, 1994.

[160] B. Haegeman, K. Engelborghs, D. Roose, D. Pieroux, and T. Erneux, Stability and rupture of bifurcation bridges in semiconductor lasers subject to optical feedback, *Phys. Rev. E*, vol. 66, p. 046216, 2002.

[161] A. Tager and K. Petermann, High-frequency oscillations and self-mode locking in short external-cavity laser diodes, *IEEE J. Quantum Electronics*, vol. 30, no. 7, pp. 1553 1561, 1994.

[162] D. Pieroux, T. Erneux, B. Haegeman, K. Engelborghs, and D. Roose, Bridges of periodic solutions and tori in semiconductor lasers subject to delay, *Phys. Rev. Lett.*, vol. 87, no. 19, p. 193901, 2001.

[163] D. Pieroux, T. Erneux, T. Luzyanina, and K. Engelborghs, Interacting pairs of periodic solutions lead to tori in lasers subject to delayed feedback, *Phys. Rev. E*, vol. 63, p. 036211, 2001.

[164] T. Erneux, F. Rogister, A. Gavrielides, and V. Kovanis, Bifurcation to mixed external cavity mode solutions for semiconductor lasers subject to optical feedback, *Optics Communications*, vol. 183, pp. 467 477, 2000.

[165] M. Zigzag, M. Butkovski, A. Englert, W. Kinzel, and I. Kanter, Zero-lag synchronization and multiple time delays in two coupled chaotic systems, *Phys. Rev. E*, vol. 81, p. 36215, 2010.

[166] N. Gastaud, S. Poinsot, L. Larger, J. Merolla, M. Hanna, J. P. Goedgebuer, and F. Malassenet, Electro-optical chaos for multi-10 Gbit/s optical transmissions, *Electronics Letters*, vol. 40, pp. 898 899, 2004.

[167] M. Golubitsky, I. Stewart, P.-l. Buono, and J. J. Collins, Symmetry in locomotor central, vol. 401, pp. 693 695, 1999.

[168] C. Zhang, R. D. Guy, B. Mulloney, Q. Zhang, and T. J. Lewis, Neural mechanism of optimal limb coordination in crustacean swimming., *Proceedings of the National Academy of Sciences of the United States of America*, vol. 111, pp. 13840 5, 2014.

[169] T. Morbiato, R. Vitaliani, and A. Saetta, Numerical analysis of a synchronization phenomenon: Pedestrian structure interaction, *Computers & Structures*, vol. 89, pp. 1649 1663, 2011.

[170] L. E. Jones and S. P. Ellner, Effects of rapid prey evolution on predator-prey cycles., *Journal of mathematical biology*, vol. 55, pp. 541 73, 2007.

[171] R. Gobbelé, T. D. Waberski, H. Simon, E. Peters, F. Klostermann, G. Curio, and H. Buchner, Different origins of low- and high-frequency components (600 Hz) of human somatosensory evoked potentials., *Clinical neurophysiology : o - cial journal of the International Federation of Clinical Neurophysiology*, vol. 115, pp. 927 37, 2004.

[172] S. A. Campbell, R. Edwards, and P. van den Driessche, Delayed Coupling Between Two Neural Network Loops, *SIAM J. Applied Mathematics*, vol. 65, pp. 316 335, 2004.

[173] T. Wang, L. Ofman, J. M. Davila, and Y. Su, Growing Transverse Oscillations of a Multistranded Loop Observed by SDO/AIA, *The Astrophysical Journal Letters*, vol. 751, p. L27, 2012.

[174] C. Briat, H. Hjalmarsson, K. Johansson, U. Jonsson, G. Karlsson, and H. Sandberg, Nonlinear state-dependent delay modeling and stability analysis of internet congestion control, in *49th IEEE Conference on Decision and Control (CDC)*, pp. 1484 1491, IEEE, 2010.

[175] H.-O. Walther, On a model for soft landing with state-dependent delay, *J. Dynamics and Di erential Equations*, vol. 19, pp. 593 622, 2007.

[176] G. Kozyreff and T. Erneux, Singular Hopf bifurcation in a differential equation with large state-dependent delay, *Proceedings of the Royal Society A-Mathematical Physical and Engineering Sciences*, vol. 470, no. 2162, 2014.

[177] M. C. Mackey, Commodity price fluctuations: Price dependent delays and nonlinearities as explanatory factors, *J. Economic Theory*, vol. 48, pp. 497 509, 1989.

[178] T. Insperger, D. A. Barton, and G. Stépán, Criticality of Hopf bifurcation in state-dependent delay model of turning processes, *International Journal of Non-Linear Mechanics*, vol. 43, pp. 140 149, 2008.

[179] T. Richard, C. Germay, and E. Detournay, A simplified model to explore the root cause of stick slip vibrations in drilling systems with drag bits, *Journal of Sound and Vibration*, vol. 305, pp. 432 456, 2007.

[180] J. L. Mitchell and T. W. Carr, Effect of state-dependent delay on a weakly damped nonlinear oscillator, *Phys. Rev. E*, vol. 83, 2011.

[181] Blood flow in microvascular networks: A study in nonlinear biology, *Chaos*, vol. 20, 2010.

[182] C. W. Eurich, M. C. Mackey, and H. Schwegler, Recurrent inhibitory dynamics: the role of state-dependent distributions of conduction delay times., *Journal of theoretical biology*, vol. 216, pp. 31 50, 2002.

[183] H. O. Walther, Algebraic-delay differential systems, state-dependent delay, and temporal order of reactions, *Journal of Dynamics and Di erential Equations*, vol. 21, pp. 195 232, 2009.

[184] J. Sieber, Finding periodic orbits in state-dependent delay differential equations as roots of algebraic equations, *Discrete and Continuous Dynamical Systems - Series A*, vol. 32, pp. 2607 2651, 2012.

[185] D. P. Rosin, D. Rontani, and D. J. Gauthier, Synchronization of coupled Boolean phase oscillators, *Phys. Rev. E*, vol. 89, p. 42907, 2014.

[186] M. C. Soriano, J. García-Ojalvo, C. R. Mirasso, and I. Fischer, Complex photonics: Dynamics and applications of delay-coupled semiconductors lasers, *Reviews of Modern Physics*, vol. 85, pp. 421 470, 2013.

[187] P. Slowi ski, B. Krauskopf, and S. M. Wieczorek, Solution structure and dynamics of a semiconductor laser subject to feedback from two external filters, in *Semiconductor Lasers and Laser Dynamics IV*, vol. 7720, Proceedings of SPIE Europe, 2010.

[188] P. Slowi ski, B. Krauskopf, and S. M. Wieczorek, Mode structure of a semiconductor laser with feedback from two external filters, *Discrete and Continuous Dynamical Systems - Series B*, 2014.

[189] V. Pal, J. S. Suelzer, A. Prasad, G. Vemuri, and R. Ghosh, Semiconductor laser dynamics with two filtered optical feedbacks, *IEEE J. Quantum Electronics*, vol. 49, pp. 340 349, 2013.

[190] B. Kelly, R. Phelan, D. Jones, C. Herbert, J. O'Carroll, M. Rensing, J. Wendelboe, C. Watts, A. Kaszubowska-Anandarajah, P. Perry, C. Guignard, L. Barry, and J. O'Gorman *Electronics Letters*, vol. 43, pp. 1282 1284, 2007.

[191] I. D. Henning and J. V. Collins *Electronics Letters*, vol. 19, p. 927, 1983.

[192] X. Porte, *Complex dynamics of delay-coupled semiconductor lasers: fundamentals and applications. PhD Thesis.* Universitat de les Illes Balears, 2015.

[193] R. Lang and K. Kobayashi, External optical feedback effects on semiconductor injection laser properties, *IEEE J. Quantum Electronics*, vol. 16, pp. 347 355, 1980.

[194] M. C. Soriano, F. Ruiz-Oliveras, P. Colet, and C. R. Mirasso, Synchronization properties of coupled semiconductor lasers subject to filtered optical feedback, *Phys. Rev. E*, vol. 78, pp. 1 8, 2008.

[195] W.-H. Kye, M. Choi, S. Rim, M. Kurdoglyan, C.-M. Kim, and Y.-J. Park, Characteristics of a delayed system with time-dependent delay time, *Phys. Rev. E*, vol. 69, p. 055202, 2004.

[196] J. Bélair, Age-structured and two-delay models for erythropoiesis, *Mathematical Biosciences*, vol. 128, pp. 317 346, 1995.

[197] J. M. Mahaffy, J. Bélair, and M. C. Mackey, Hematopoietic model with moving boundary condition and state dependent delay: applications in erythropoiesis., *Journal of theoretical biology*, vol. 190, pp. 135 146, 1998.

[198] A. Fathallah and O. Arino, On a Model Representing Stage-Structured Population Growth with State-Dependent Time Delay, 1997.

[199] W. G. Aiello, H. I. Freedman, and J. Wu, Analysis of a Model Representing Stage-Structured Population Growth with State-Dependent Time Delay, *SIAM J. Applied Mathematics*, vol. 52, pp. 855 869, 1992.

[200] R. Vicente, C. R. Mirasso, and I. Fischer, Simultaneous bidirectional message transmission in a chaos-based communication scheme, *Optics Letters*, vol. 32, p. 403, 2007.

[201] I. Kanter, E. Kopelowitz, and W. Kinzel, Public Channel Cryptography: Chaos Synchronization and Hilbert's Tenth Problem, *Phys. Rev. Lett.*, vol. 101, p. 084102, 2008.

# Appendix

Appendix A

# Temporal splitting in identical delay-coupled OEOs with negative feedback

In Sec. 5.7, the effect of a mismatch in the delay-times ratio on the period of the square waves generated by identical delay-coupled OEOs subject to negative feedback was investigated from numerical simulations of the full dynamical model (4.11). By using the Poincaré section technique, we observed a nonlinear effect consisting of the temporal splitting in different intervals. We considered $s_0$ to be close to $s_0 = 1/3$ for in-phase solutions and to $s_0 = 3/4$ for out-of-phase solutions. We now show that similar results can be obtained for $s_0$ close to other rational values.

## A.1 Temporal splitting of in-phase solutions

### A.1.1 $s_0$ near $s_0 = 1/5$ ($n_0 = 3$)

For $s_0 = 1/5$, the minimum values of $l$ and $m$ that satisfy Eq. (5.1) are $l_0 = 2$ and $m_0 = 1$; thus, $n_0 = l_0 + m_0 + 1 = 3$. For the ideal ratio $s_0 = 1/5$ [Fig. A.1(a)], the fundamental solution has a period $T_0^{\text{in}} = 0.400152$, in good agreement with the prediction (4.25), $T_3^{\text{in}} = 0.400113$, taking into account the correction $\alpha_3^{\text{in}}$ of order $\varepsilon$ and $\delta$ given by Eq. (4.29) for $n = 3$. With a 1% mismatch with respect to the ideal ratio [Fig. A.1(b)], the period of the fundamental solution is also in agreement with the prediction given by Eq. (4.25). With a 2% mismatch [Fig. A.1(c)], there is splitting in $n_0 = 3$ different Poincaré return times, although the mean value of the three different intervals is in good agreement with the prediction given by Eq. (4.25). With a 3% mismatch, this splitting increases, as shown in Fig. A.1(d).

For perfect matching the delay times ratio $s_0 = 1/5$, the harmonic of order $j$ has a small splitting in $2j + 1$ different intervals, as shown in panels (e) and (i) of Fig. A.1 for the first ($j = 1$) and second ($j = 2$) harmonics. Introducing a 1% mismatch with respect to the ideal ratio, this splitting increases, as it can be seen in panels (f) and (j) of Fig. A.1 for the first and second harmonics, respectively. With a 2% mismatch, the

## APPENDIX A. TEMPORAL SPLITTING IN IDENTICAL DELAY-COUPLED OEOS WITH NEGATIVE FEEDBACK

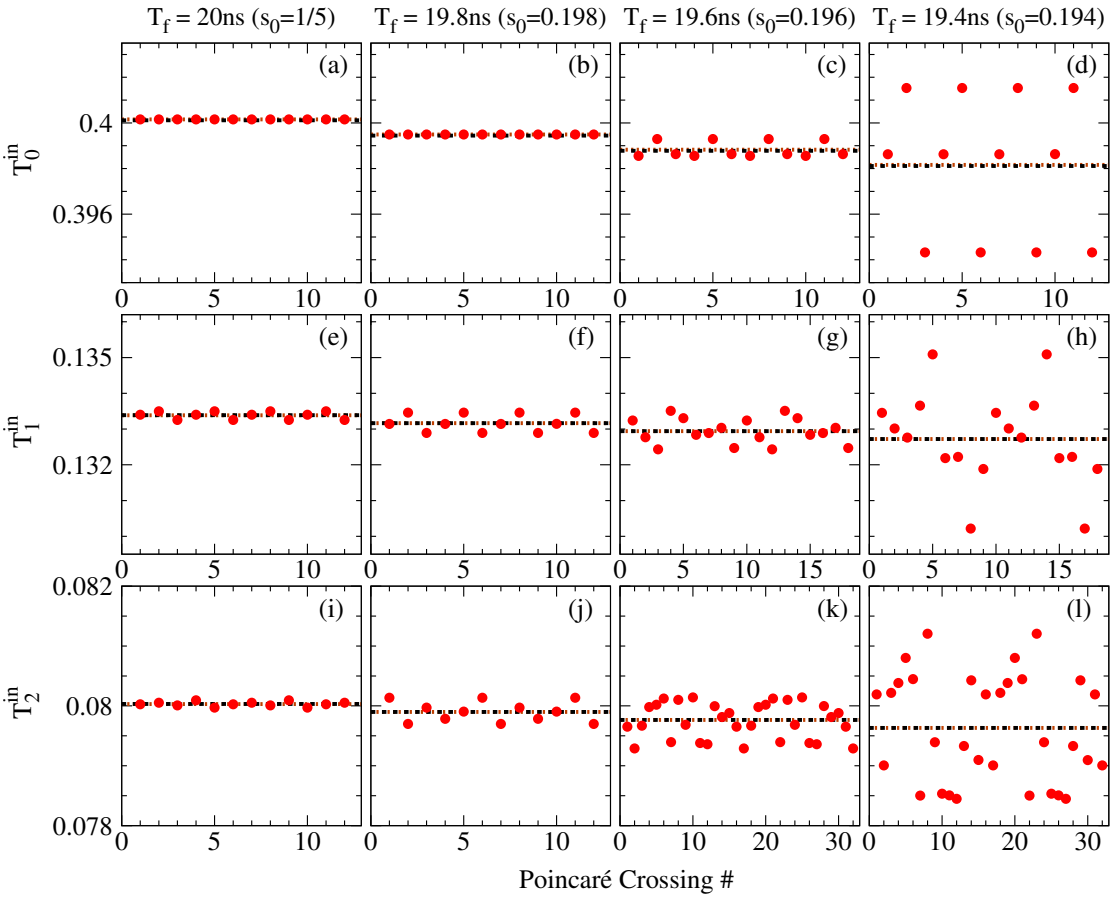


**Figure A.1:** Poincaré return times for in-phase square waves with $\phi = 0.25\pi$, $P = 1.5$, $\gamma = 0.5$, $T_c = 100\,\text{ns}$, $\varepsilon = 2.5\ \ 10^{\ -4}$, $\delta = 2\ \ 10^{\ -2}$ and different values of $T_f$: 20 ns ($s_0 = 1/5$) in (a), (e) and (i); 19.8 ns ($s_0 = 198$) in (b), (f) and (j); 19.6 ns ($s_0 = 0.196$) in (c), (g) and (k); and 19.4 ns ($s_0 = 0.194$) in (d), (h) and (l).

harmonic of order $j$ has a splitting in $n_j = (2j+1)n_0 = 6j+3$ values, namely 9 and 15 different intervals for $j = 1$ [Fig. A.1(g)] and $j = 2$ [Fig. A.1(k)], respectively. With a 3% mismatch, the splitting is larger, as shown in Figs. A.1(h) and Fig. A.1(k). The mean value of all the different intervals is very similar to the prediction given by Eq. (4.25) for $n = 9$ and $n = 15$, for the first and second harmonics, respectively.

### A.1.2 $s_0$ near $s_0 = 1/7$ ($n_0 = 4$)

For $s_0 = 1/7$, the minimum values of $l$ and $m$ that satisfy Eq. (5.1) are $l_0 = 0$ and $m_0 = 3$; thus, $n_0 = 4$.

The fundamental solution for the ideal ratio $s_0 = 1/7$ [Fig. A.2(a)] has a period $T_0^{\text{in}} = 0.285832$, in good agreement with the prediction (4.25), $T_4^{\text{in}} = 0.285822$, taking into account the correction $\alpha_4^{\text{in}}$ of order $\varepsilon$ and $\delta$ given by Eq. (4.29) for $n = 4$. With a 1% mismatch with respect to the ideal ratio [Fig. A.2(b)], the period of the fundamental so-

lution is also in agreement with the prediction given by Eq. (4.25). With a 3% mismatch [Fig. A.2(c)], there is splitting in $n_0 = 4$ different Poincaré return times, although the mean value of the three different intervals is in good agreement with the prediction given by Eq. (4.25). With a 4% mismatch, this splitting increases, as shown in Fig. A.2(d).

The harmonic of order $j$ for $s_0 = 1/7$ has a small splitting in $2j + 1$ different intervals, as shown in panels (e) and (i) of Fig. A.2 for the first ($j = 1$) and second ($j = 2$) harmonics. Introducing a 1% mismatch with respect to the ideal ratio, this splitting increases, as it can be seen in panels (f) and (j) of Fig. A.2 for the first and second harmonics, respectively. With a 3% mismatch, the harmonic of order $j$ has already a splitting in $n_j = (2j+1)n_0 = 8j+4$ values, namely 12 and 20 different intervals for $j = 1$ [Fig. A.2(g)] and $j = 2$ [Fig. A.2(k)], respectively. With a 4% mismatch, the splitting of the first harmonic is larger, as shown in Fig. A.2(h), whereas the second harmonic is not stable. The mean value of all the different intervals is very similar to the prediction given by Eq. (4.25) for $n = 6$ and $n = 10$, for the first and second harmonics, respectively.

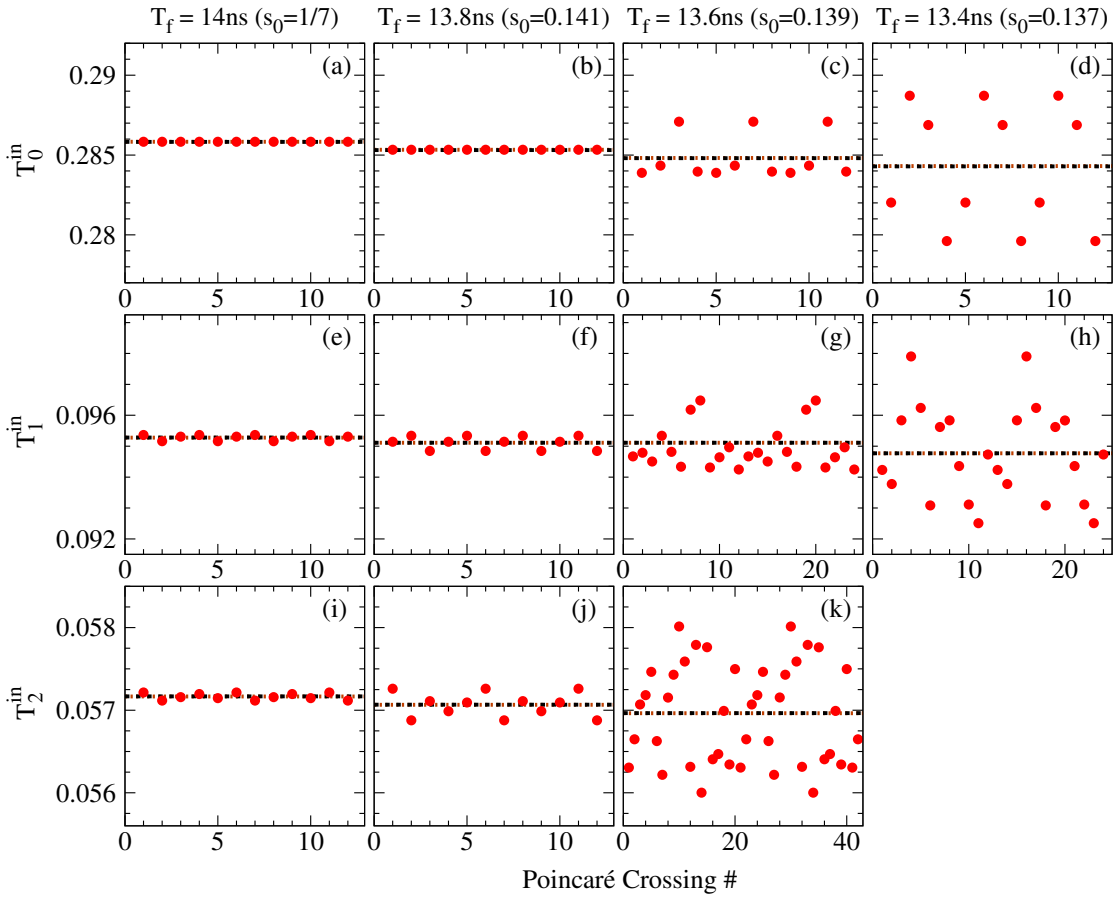


**Figure A.2:** Poincaré return times for in-phase square waves with $\phi = 0.25\pi$, $P = 1.5$, $\gamma = 0.5$, $T_c = 98\,\text{ns}$, $\varepsilon = 2.55\ \ 10^{\ -4}$, $\delta = 1.96\ \ 10^{\ -2}$ and different values of $T_f$: 14 ns ($s_0 = 1/7$) in (a), (e) and (i); 13.8 ns ($s_0 = 0.141$) in (b), (f) and (j); 13.6 ns ($s_0 = 0.139$) in (c), (g) and (k); and 13.4 ns ($s_0 = 0.137$) in (d) and (h).

## APPENDIX A. TEMPORAL SPLITTING IN IDENTICAL DELAY-COUPLED OEOS WITH NEGATIVE FEEDBACK

### A.1.3 $s_0$ near $s_0 = 3/5$ ($n_0 = 4$)

For $s_0 = 3/5$, the minimum values of $l$ and $m$ that satisfy Eq. (5.1) are $l_0 = 1$ and $m_0 = 2$; thus, $n_0 = 4$.

The fundamental solution for the ideal ratio $s_0 = 3/5$ [Fig. A.3(a)] has a period $T_0^{\text{in}} = 0.400111$, in good agreement with the prediction given by Eq. (4.25), $T_4^{\text{in}} = 0.400084$, taking into account the correction $\alpha_4^{\text{in}}$ of order $\varepsilon$ and $\delta$ given by Eq. (4.29) for $n = 4$. With a mismatch lower than 1% with respect to the ideal ratio [Fig. A.3(b) and A.3(c)], the period of the fundamental solution is also in agreement with the prediction given by Eq. (4.25). With a 1% mismatch [Fig. A.3(d)], there is splitting in $n_0 = 4$ different Poincaré return times, although the mean value of the three different intervals is in good agreement with the prediction given by Eq. (4.25).

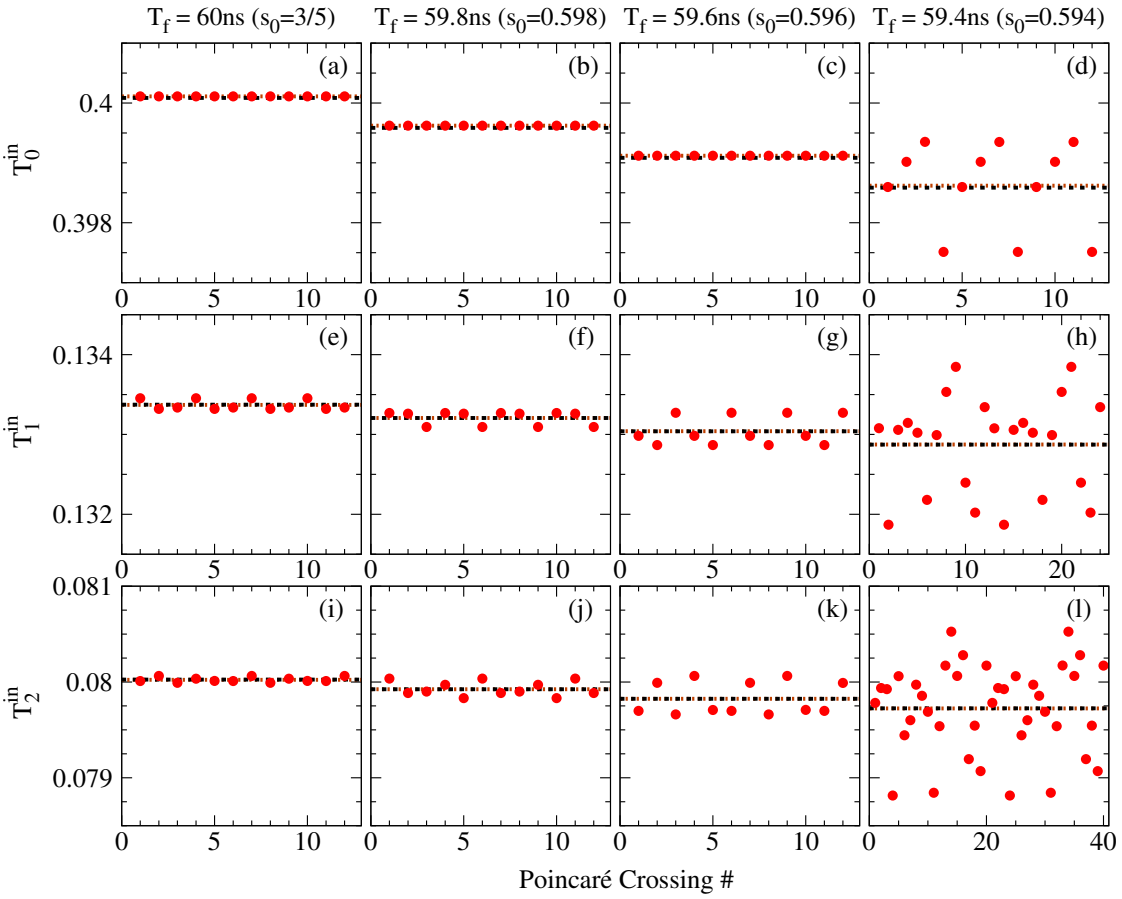


**Figure A.3:** Poincaré return times for in-phase square waves with $\phi = 0.25\pi$, $P = 1.5$, $\gamma = 0.5$, $T_c = 90\,\text{ns}$, $\varepsilon = 2.78\ \ 10^{\ -4}$, $\delta = 1.8\ \ 10^{\ -2}$ and different values of $T_f$: 60 ns ($s_0 = 3/5$) in (a), (e) and (i); 59.8 ns ($s_0 = 0.598$) in (b), (f) and (j); 59.6 ns ($s_0 = 0.596$) in (c), (g) and (k); and 59.4 ns ($s_0 = 0.594$) in (d), (h) and (l).

The harmonic of order $j$ for $s_0 = 3/5$ has a small splitting in $2j + 1$ different intervals, as shown in panels (e) and (i) of Fig. A.3 for the first ($j = 1$) and second ($j = 2$) harmonics. Introducing mismatches of the order of 0.3-0.7% with respect to the ideal ratio, this splitting increases, as it can be seen in panels (f)-(g) and (j)-(k) of Fig. A.3 for the first and second harmonics, respectively. With a 1% mismatch, the harmonic of order $j$ has already a splitting in $n_j = (2j + 1)n_0 = 8j + 4$ values, namely 12 and 20 different intervals for $j = 1$ [Fig. A.3(h)] and $j = 2$ [Fig. A.3(l)], respectively. The mean value of all the different intervals is very similar to the prediction given by Eq. (4.25) for $n = 12$ and $n = 20$, for the first and second harmonics, respectively.

## A.2 Temporal splitting of out-of-phase solutions

### A.2.1 $s_0$ near $s_0 = 5/2$ ($n_0 = 3$)

For $s_0 = 5/2$, the minimum values of $k$ and $m$ that satisfy Eq. (5.6) are $k_0 = 2$ and $m_0 = 1$; thus, $n_0 = 3$.

The fundamental solution for the ideal ratio $s_0 = 5/2$ [Fig. A.4(a)] has a period $T_0^{\text{in}} = 1.00032$, in good agreement with the prediction given by Eq. (4.36), $T_4^{\text{in}} = 1.00024$, taking into account the correction $\alpha_3^{\text{out}}$ of order $\varepsilon$ and $\delta$ given by Eq. (4.39) for $n = 3$. With a mismatch lower than 5% with respect to the ideal ratio [Figs. A.4(b) and A.4(c)], the period of the fundamental solution is also in agreement with the prediction given by Eq. (4.36). With a 6% mismatch [Fig. A.4(d)], there is splitting in $2n_0 + 1 = 7$ different Poincaré return times, although the mean value of the three different intervals is in good agreement with the prediction given by Eq. (4.36).

The harmonic of order $j$ for $s_0 = 5/2$ has a small splitting in $(2j + 1)$ different intervals, as shown in panels (e) and (i) of Fig. A.4 for the first ($j = 1$) and second ($j = 2$) harmonics. Introducing a mismatch lower than 5% with respect to the ideal ratio, this splitting increases, as it can be seen in panels (f)-(g) and (j)-(k) of Fig. A.4 for the first and second harmonics, respectively. With a 6% mismatch, the harmonic of order $j$ has already a splitting in $2n_j + 1 = (2j + 1)(2n_0 + 1) = 14j + 7$ values, namely 21 and 35 different intervals for $j = 1$ [Fig. A.4(h)] and $j = 2$ [Fig. A.4(l)], respectively. The mean value of all the different intervals is very similar to the prediction given by Eq. (4.36) for $n = 21$ and $n = 35$, for the first and second harmonics, respectively.

### A.2.2 $s_0$ near $s_0 = 1/2$ ($n_0 = 1$)

For $s_0 = 1/2$, the minimum values of $k$ and $m$ that satisfy Eq. (5.6) are $k_0 = 0$ and $m_0 = 1$; thus, $n_0 = 1$.

The fundamental solution for the ideal ratio $s_0 = 1/2$ [Fig. A.5(a)] has a period $T_0^{\text{in}} = 1.00049$, in good agreement with the prediction given by Eq. (4.36), $T_1^{\text{in}} = 1.00015$, taking into account the correction $\alpha_1^{\text{out}}$ of order $\varepsilon$ and $\delta$ given by Eq. (4.39) for $n = 1$. With a

## APPENDIX A. TEMPORAL SPLITTING IN IDENTICAL DELAY-COUPLED OEOS WITH NEGATIVE FEEDBACK

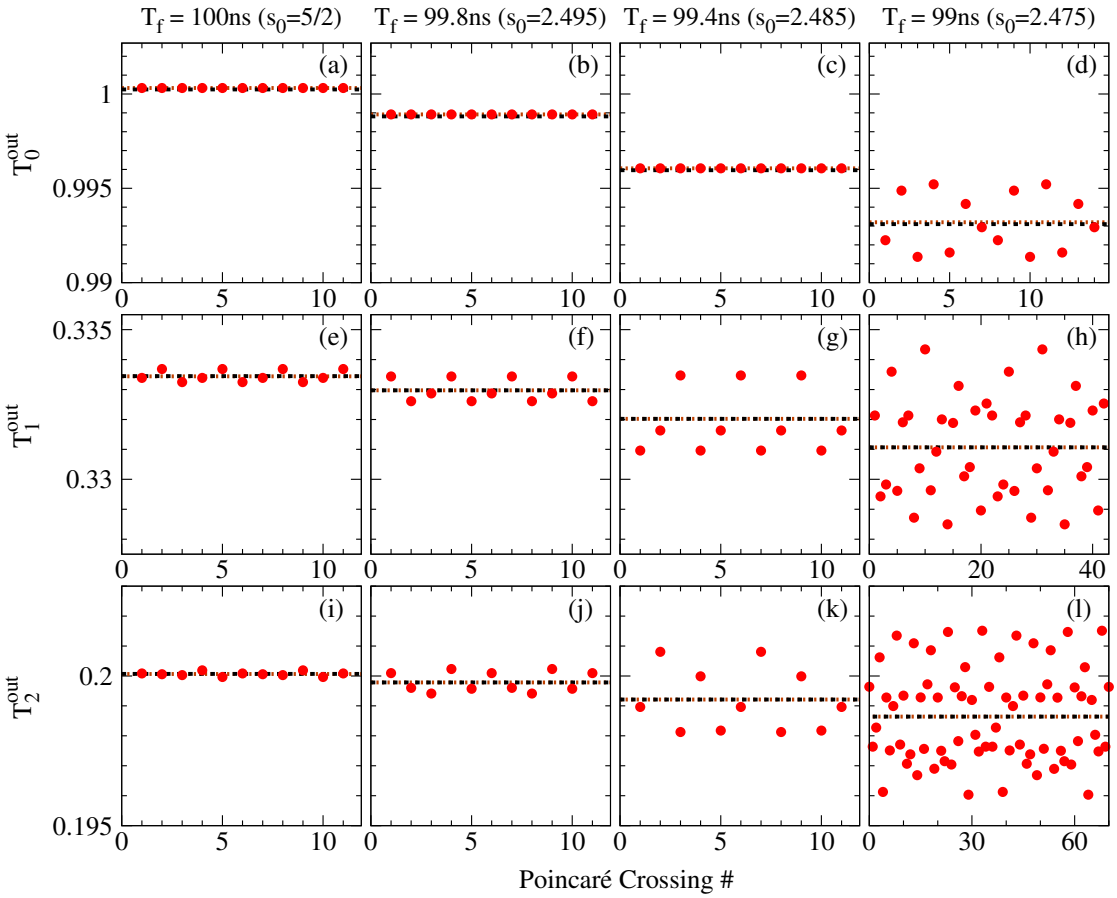


**Figure A.4:** Poincaré return times for out-of-phase square waves with $\phi = 0.25\pi$, $P = 1.5$, $\gamma = 0.5$, $T_c = 40\,\text{ns}$, $\varepsilon = 6.25\ \ 10^{\ 4}$, $\delta = 0.8\ \ 10^{\ 2}$ and different values of $T_f$: 100 ns ($s_0 = 5/2$) in (a), (e) and (i); 99.8 ns ($s_0 = 2.495$) in (b), (f) and (j); 99.4 ns ($s_0 = 2.485$) in (c), (g) and (k); and 99 ns ($s_0 = 2.475$) in (d), (h) and (l).

1% mismatch with respect to the ideal ratio [Figs. A.5(b) and A.5(c)], the period of the fundamental solution is also in agreement with the prediction given by Eq. (4.36). With a 2% mismatch [Fig. A.5(d)], there is splitting in $2n_0 + 1 = 3$ different Poincaré return times, although the mean value of the three different intervals is in good agreement with the prediction given by Eq. (4.36).

The harmonic of order $j$ for $s_0 = 1/2$ has a small splitting in $(2j+1)$ different intervals, as shown in panels (e) and (i) of Fig. A.5 for the first ($j = 1$) and second ($j = 2$) harmonics. Introducing a 1% mismatch with respect to the ideal ratio, this splitting increases, as it can be seen in panels (f)-(g) and (j)-(k) of Fig. A.5 for the first and second harmonics, respectively. With a 2% mismatch, the harmonic of order $j$ has already a splitting in $2n_j + 1 = (2j+1)(2n_0+1) = 6j+3$ values, namely 9 and 15 different intervals for $j = 1$ [Fig. A.5(h)] and $j = 2$ [Fig. A.5(l)], respectively. The mean value of all the different intervals is very similar to the prediction given by Eq. (4.36) for $n = 9$ and $n = 15$, for the first and second harmonics, respectively.

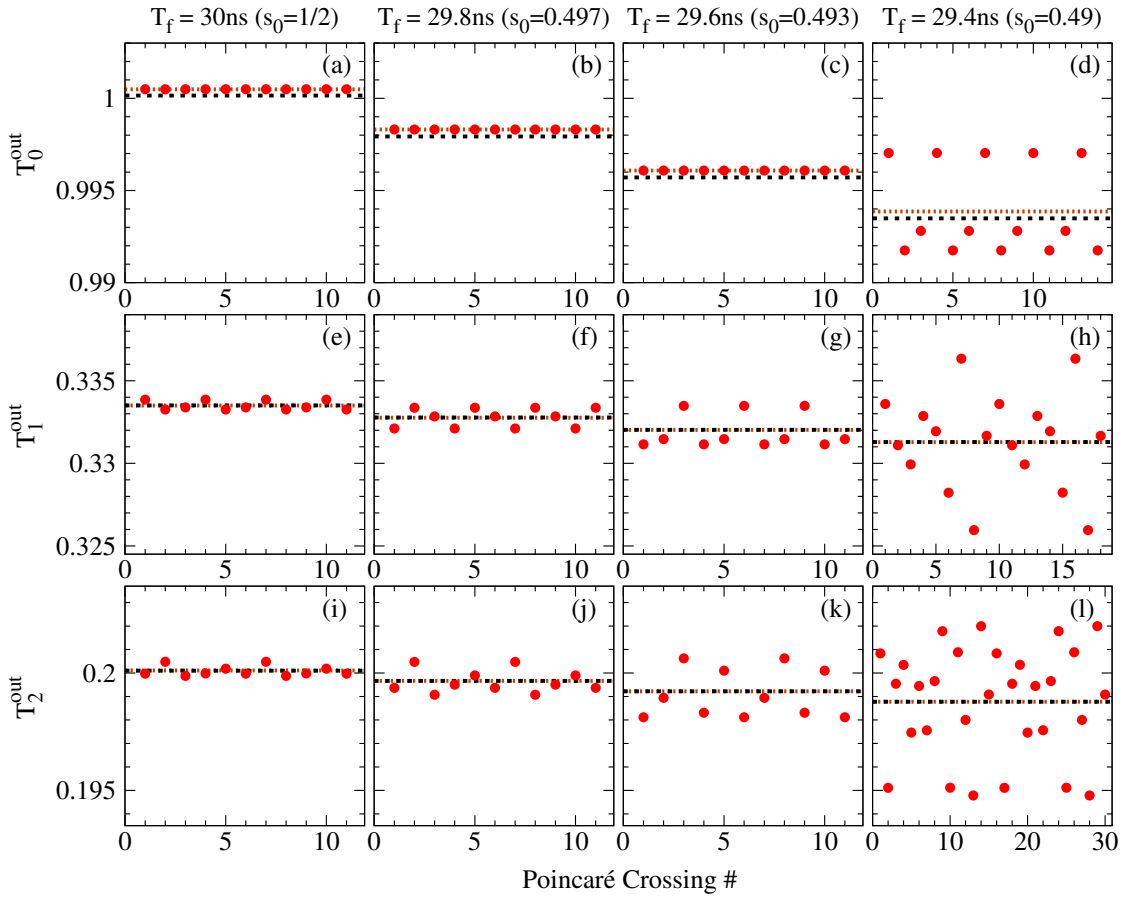


**Figure A.5:** Period of out-of-phase square waves with $\phi = 0.25\pi$, $P = 1.5$, $\gamma = 0.5$, $T_c = 60\,\text{ns}$, $\varepsilon = 4.17\ \ 10^{\ 4}$, $\delta = 1.2\ \ 10^{\ 2}$ and different values of $T_f$: 30 ns ($s_0 = 1/2$) in (a), (e) and (i); 29.8 ns ($s_0 = 0.497$) in (b), (f) and (j); 29.6 ns ($s_0 = 0.493$) in (c), (g) and (k); and 29.4 ns ($s_0 = 0.49$) in (d), (h) and (l).

### A.2.3 $s_0$ near $s_0 = 1/6$ ($n_0 = 3$)

For $s_0 = 1/6$, the minimum values of $k$ and $m$ that satisfy Eq. (5.6) are $k_0 = 0$ and $m_0 = 3$; thus, $n_0 = k_0 + m_0 = 3$.

The fundamental solution for the ideal ratio $s_0 = 1/6$ [Fig. A.6(a)] has a period $T_0^{\text{in}} = 0.333479$, in good agreement with the prediction given by Eq. (4.36), $T_4^{\text{in}} = 0.333463$, taking into account the correction $\alpha_3^{\text{out}}$ of order $\varepsilon$ and $\delta$ given by Eq. (4.39) for $n = 3$. With a 2% mismatch with respect to the ideal ratio [Fig. A.6(b)], the period of the fundamental solution is also in agreement with the prediction given by Eq. (4.36). With a 3% mismatch [Fig. A.6(c)], there is splitting in $2n_0 + 1 = 7$ different Poincaré return times, although the mean value of the three different intervals is in good agreement with the prediction given by Eq. (4.36). This splitting increases with a 4% mismatch, as shown in Fig. A.6(d).

## APPENDIX A. TEMPORAL SPLITTING IN IDENTICAL DELAY-COUPLED OEOS WITH NEGATIVE FEEDBACK

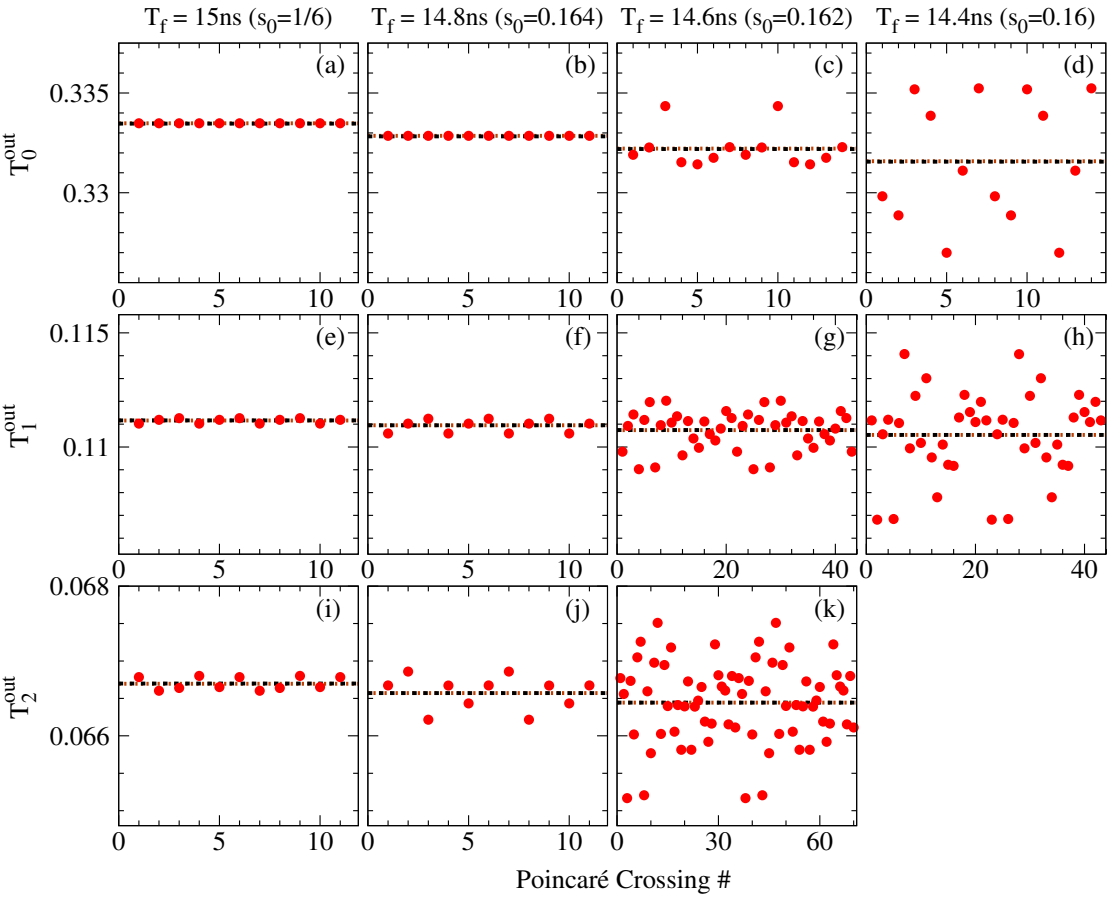


**Figure A.6:** Poincaré return times for out-of-phase square waves with $\phi = 0.25\pi$, $P = 1.5$, $\gamma = 0.5$, $T_c = 90\,\text{ns}$, $\varepsilon = 2.78\ \ 10^{-4}$, $\delta = 1.8\ \ 10^{-2}$ and different values of $T_f$: 15 ns ($s_0 = 1/6$) in (a), (e) and (i); 14.8 ns ($s_0 = 0.164$) in (b), (f) and (j); 14.6 ns ($s_0 = 0.162$) in (c), (g) and (k); and 14.4 ns ($s_0 = 0.16$) in (d) and (h).

The harmonic of order $j$ for $s_0 = 1/6$ has a small splitting in $(2j+1)$ different intervals, as shown in panels (e) and (i) of Fig. A.6 for the first ($j = 1$) and second ($j = 2$) harmonics. With a 2% mismatch with respect to the ideal ratio, this splitting increases, as it can be seen in panels (f) and (j) of Fig. A.6 for the first and second harmonics, respectively. With a 3% mismatch, the harmonic of order $j$ has already a splitting in $2n_j + 1 = (2j+1)(2n_0+1) = 14j + 7$ values, namely 21 and 35 different intervals for $j = 1$ [Fig. A.6(g)] and $j = 2$ [Fig. A.6(k)], respectively. With a 4% mismatch, the splitting of the first harmonic increases, as shown in Fig. A.6(h), whereas the second harmonic becomes unstable. The mean value of all the different intervals is very similar to the prediction given by Eq. (4.36) for $n = 21$ and $n = 35$, for the first and second harmonics, respectively.